Appendices

NCHRP Research Report 933 is accompanied by eight appendices. Appendix A, which provides the proposed specifications and test methods, is included with the report and may be downloaded with the report's PDF file. Seven additional appendices accompany the report and are presented together in this downloadable PDF file, titled "Appendices," which can be accessed from www.trb.org by searching "NCHRP Research Report 933".

Contents

APPENDIX B

Experimental Plan for Phase III Field Activities

This document contains a brief explanation of field protocols recommended for implementation in support of the activities of the NCHRP 24-45.

Goal of Study. The goal of this study is to develop a robust means of extracting stiffness parameters from Intelligent Compaction (IC) rollers.

Objective of Study. The short-term objective is to develop a test procedure that rapidly and rigorously will supplant the design verification given the design parameters. The long-term objective is to recommend a robust field test protocol and associated equipment that can evaluate whether the design modulus of a given layer is achieved. The following field devices will be carried out when appropriate:

1. Light Weight Deflectometer (LWD)
2. Dynamic Cone Penetrometer (DCP)

Field Testing: The following steps will be followed in the field to achieve the objective:

1. Install instrumentation in the subgrade as discussed below.
2. Map the completed subgrade with an intelligent compaction (IC) roller after compaction.
3. Conduct field tests with nuclear density gauge (NDG), LWD and DCP on prepared subgrade.
4. Prepare and compact the unbound aggregate base (UAB).
5. Install instrumentation in the base as discussed below.
6. Map the completed base with an IC roller after compaction.
7. Conduct field tests with NDG, LWD and DCP on prepared base.

Lab Testing: To support the goals of this project, UTEP will conduct laboratory resilient modulus tests on the samples of the subgrade and UAB materials at several moisture contents. In addition, UTEP will carry out index tests (gradation and Atterberg limits) and moisture-density tests if necessary.

Detail Information: Table B-1 contains a summary of the activities and an approximate schedule at each site. Each activity is briefly explained below.

1. **Identification of Test Section.** The team members from UTEP, DOT and Contractor will coordinate and identify a 250 ft (minimum) long and full width (or minimum of 25 ft) wide test section.
2. **Set up of GPS.** As much as possible, DOT or contractor's base station will be used. If necessary UTEP will set up a base station.
3. **Set up of IC Roller.** UTEP will setup the IC roller. The IC roller will be checked for proper data collection and all settings including roller speed, and vibration frequency and amplitude.
4. **Carry out Construction as normally done.** It is at the discretion of the contractor to use a regular or an IC roller. UTEP team may observe the construction but will not become involved in or interfere with the operation.

5. **Carry out Tests**[1]**.** UTEP will map the test section using one forward pass of the IC roller. UTEP will carry out spot tests at a minimum of twenty (20) points for correlation testing shortly after compaction. These activities will be carried out at a time that is least disruptive to the Contractor. The proposed NDT devices for these tests include:
   - Nuclear Density Gauge (NDG) by DOT
   - Dynamic Cone Penetrometer (DCP) by UTEP/ DOT
   - Light Weight Deflectometer (LWD) by UTEP/DOT
   - Moisture sample (five random locations) for validation of NDG by UTEP/DOT

Instrumentation. A data acquisition system (DAQ) has been developed at UTEP to collect vibration data and ground response during IC operations. A schematic of the system is depicted in Figure B-1. The system consists of two accelerometers that are mounted on the roller (drum), a data acquisition box, a GPS antenna and receiver, a power supply and a laptop computer to monitor the data collection process.

A similar data acquisition system has been developed to monitor the propagation of roller vibration within the geomaterials by embedding geophones at different depths in the subsurface layers (see Figures B-1 and B-2). A second GPS system is used to synchronize the geophone data with the accelerometers mounted on the rollers. The geophones are embedded in the existing ground layer (before placement of the new test layers) to monitor the soil layer responses during the IC operation. The geophones record the vertical, transversal and/or longitudinal amplitudes of vibration, with the longitudinal response being in the same direction as the roller movement and the transversal response being perpendicular to the moving direction.

Table B-1. Test activity and approximate schedule.

Time	Tasks	Activities
2 days before Field Tests	Coordination and Initial Set up	• Sample representative subgrade and base (UTEP) • Arrange for field instrumentation (DOT, UTEP) • Obtain GPS coordinates for spot test locations • Coordinate with IC roller operator on how to collect, record, save, download and transfer data for this project (Contractor, DOT and UTEP)
First Visit	Subgrade	• Prepare and compact subgrade within the test section (Contractor, UTEP) • Install geophones at a depth of 24 in. and 6 in. from the top of subgrade (UTEP) • Map the top of subgrade with IC roller (Contractor, UTEP) • Carry out in-situ testing with LWD/DCP (UTEP) • Carry out NDG tests (DOT) and obtain moisture samples for validation of NDG (UTEP)
Second Visit	Unbounded Aggregate Base (UAB)	• Pre-map subgrade within the test section (Contractor, UTEP) • Prepare and compact UAB within the test section (Contractor, UTEP) • Install geophone at a depth of 6 in. from the top of the aggregate base (UTEP) • Map the top UAB with IC roller (Contractor, UTEP) • Carry out in-situ testing with LWD/DCP (UTEP) • Carry out NDG tests (DOT) and obtain moisture samples for validation of NDG (UTEP)

[1] DOT and contractor staff are more than welcome to participate.

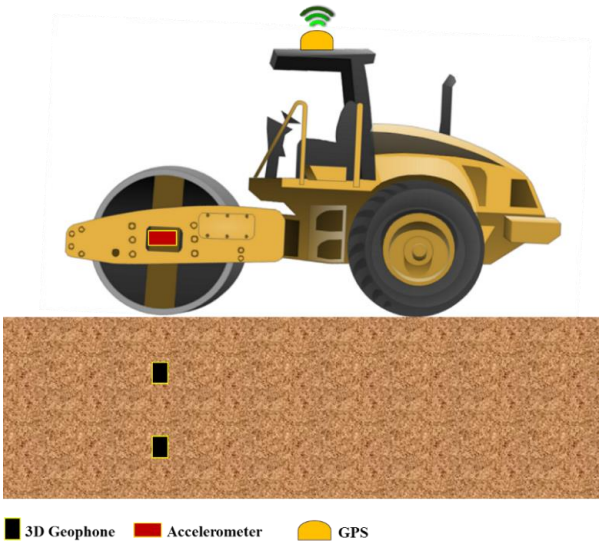

Figure B-1. Schematic of IC system.

Figure B-2. Components of IC and data acquisition system.

APPENDIX C

Review of Literature

Estimation of Modulus of Compacted Materials

Lekarp et al. (2000) includes a comprehensive review of the concepts and definitions regarding the resilient response of the unbound aggregates. The stresses beneath a rolling wheel load could be defined in terms of the time-dependent vertical, horizontal and shear components. Although a resilient response has been assumed satisfactory to represent the behavior of the unbound geomaterials under the repeated loads, the true nature of such behavior could be the result of the consolidation, distortion and attrition (Loung 1982).

The behavior of the unbound materials under repeated loading is quite complex and involves many different factors. Werkmeister (2003) used the shakedown concept to demonstrate that the resilient behavior of the unbound granular materials was a result of the temporary deformation of the individual particles. Tutumluer (2013), as a part of a synthesis of the current practices related to the unbound aggregates pavement layers, summarized the evolution of the characterization of the unbound aggregates for pavement design. Figure C-1 differentiates between the concepts of elastic and resilient modulus in terms of the stress-strain correlations considering the principal stresses σ_1 and σ_3. While it is desirable to minimize the deviation of the pavement layers from the elastic region, it is fully expected that these layers will exercise the resilient and plastic behaviors during their construction and modulus testing with most NDT devices.

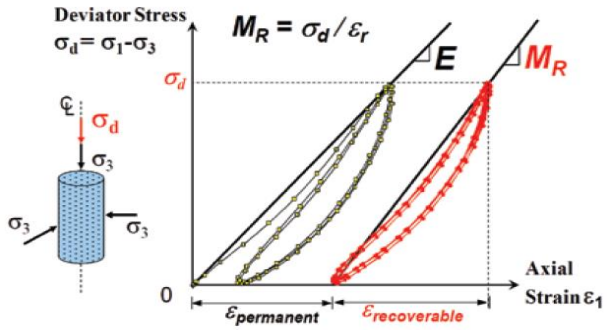

Figure C-1. Difference between elastic and resilient modulus (Tutumluer 2013).

Puppala (2008) and Tutumluer (2013) synthesized the body of literature regarding the estimation of the resilient modulus of the unbound geomaterials. Tables C.1 and C.2 summarize the laboratory and field approaches to estimate the stiffness/modulus of the compacted geomaterials. Aside from these test methods and devices, several direct and indirect correlations have been developed to determine the resilient modulus parameters from the basic soil properties and some compaction-related parameters.

Laboratory tests are essential to study the parameters that affect the properties of materials. The behavior of a material in terms of variation in modulus with stress level, strain amplitude, and the strain rate is best established by conducting laboratory tests such as the resilient modulus test. However, moduli from laboratory tests are moderately or significantly different than the in-situ results.

Table C-1. Summary of laboratory methods to estimate the stiffness of geomaterials.

Methods and Devices	Standard	Strengths	Limitations
California Bearing Ratio (CBR)	AASHTO T-193 ASTM D1883	- Relatively easy and inexpensive to perform - Well known among pavement professionals - Established correlations with some in situ test devices (e.g. DCP and LWD)	- Not used directly in Mechanistic-Empirical (ME) design - Not dependent of state of stress and therefore not representing the actual response of geomaterial layers under repeated wheel loads
Static Triaxial	ASTM D4767 ASTM D2850	- Common among DOTs	- Does not measure the moduli at the strain levels associated with NDT
Resonant Column	ASTM D4015	- Directly correlated to field seismic moduli without the need for transfer functions - Relatively easy and inexpensive to perform	- Estimates the low-strain linear-elastic modulus of geomaterials and is not representative of nonlinear behavior
Resilient Modulus (MR)	AAHTO T307 NCHRP 1-28A	- Directly used in M-E design process - The test is performed under various ranges of confining pressure and deviatoric stress - Different models are available to correlate MR to the state of stress - Correlation to the material properties have been under continuous investigation	- Relatively complicated and expensive - The test device requires comprehensive training to perform the test

Von Quintus et al. (2009) as part of the NCHRP Project 10-65 investigated the application of the existing NDT technologies for measuring the quality of the flexible pavements. They assessed a number of promising NDT technologies on actual field projects for their ability to evaluate the quality of pavement layers during or immediately after the placement. That project identified the practical NDT technologies that were appropriate for the implementation in routine QC/QA operations.

A review of the literature on the recent efforts in studying the fundamental differences between the laboratory and field moduli is summarized in Table C-3. Due to the complexity and time-consuming nature of the resilient modulus (MR) tests, simple methods have been proposed for estimating the modulus of the geomaterials in the laboratory. As reflected in Puppala (2008), these simple tests include the free-free resonant column (FFRC) and the bender elements that measure the low-strain linear-elastic moduli of specimens. It is also common to use strength tests, such as the unconfined compressive strength or laboratory California Bearing Ratio (CBR), to estimate the modulus.

Table C-2. Summary of field methods to estimate the stiffness of geomaterials.

Methods and Devices	Standard	Strengths	Limitations
Falling Weight Deflectometer (FWD)	ASTM D4694	- Provides a reasonable estimation of layer moduli - Well known among pavement professionals	- Requires backcalculation of test results to determine layer moduli - The backcalculated results are uncertain due to the variation in layer thickness
Light Weight Deflectometer (LWD)	ASTM 2583 ASTM 2835	- Equipment is readily available - Community is familiar with concept of deflection-based testing	- Moduli can be influenced by the underlying layers, resulting in more variable moduli
Portable Seismic Property Analyzer (PSPA)	NA	- Measures layer-specific modulus independent of thickness of layer - No backcalculation necessary - Results can be calibrated to specific material being tested prior to construction when M-D relationship is measured in lab	- Need to calibrate the test results to the material and site conditions under evaluation - Requires more sophisticated training of technicians - Low repeatability, with a high standard deviation due to capability to detect anisotropic conditions
Soil Stiffness Gauge (SSG) - Geogauge	ASTM D6758	- Training and technical requirements are similar to nuclear density gauge - Provides a reasonable estimate of laboratory measured moduli with proper calibration	- Proper intimate contact between Geogauge and soil is difficult to achieve in practice without preparation - Underlying materials can influence results especially for relatively thin unbound layers
Dynamic Cone Penetrometer (DCP)	ASTM D6951	- Several correlations have been established to correlate DCP test results to CBR and modulus/stiffness - Widely used among state highway agencies - Relatively inexpensive and easy to use	- It requires intruding a metal rod into compacted layer - The correlations between DCP index and stiffness are empirical

Field tests are more practical and more desirable because they are rapid to perform, and because they test a large volume of material in its in situ natural or engineered state, the state in which the material will perform. Field tests typically fall into two categories: material characterization and design simulation. In material characterization one attempts to determine the engineering properties of a material (such as modulus) in a way that is the most theoretically correct. The material properties measured in that way are fundamental material properties that are not related to a specific modeling scenario. To use these material properties in a certain design methodology, they should be combined with an appropriate analytical or numerical model (and often additional laboratory tests) to obtain the design output. In the design simulation, one tries to her/his best ability to simulate the design condition experimentally and then back-figure some material parameter that is relevant to that condition. These methods usually measure the response (typically the stiffness) of the pavement system. Both approaches have advantages and disadvantages. In the design simulation, the state of stress applied to the geomaterials ideally should be similar to those from the actual scenario they are attempting to simulate. However, since the state of stress in the pavement depends on the modulus of the layers, it would be difficult to use a measured modulus from one pavement structure to another with different layer thicknesses or underlying layers. The moduli that resemble the material characterization can be used universally, but they have to be tied to a pavement design model.

Table C-3. Summary of Studies Correlating Differences between Laboratory and Field Resilient Moduli

Reference	Objectives and Approach	Concluding Remarks	Devices and Test Methods
Nazarian et al. (2014)	To investigate laboratory-field transfer functions as a part of developing modulus-based construction quality control of unbound geomaterials	The seismic methods were employed to develop the laboratory-field transfer functions since the field moduli estimated by PSPA could be directly correlated to laboratory moduli values determined from Free-Free Resonant Column (FFRC) test	Lab MR and FFRC tests; field LWD and PSPA
Oh et al. (2011)	To determine correlation factors (CFs) between laboratory resilient moduli and moduli from in situ tests for unbound geomaterials	A reasonable correlation was found between the backcalculated FWD moduli and the corresponding CFs to correlate to laboratory MR values. However, the backcalculated FWD moduli were not realistic due to uncertainties associated with layer thickness	DCP; FWD; lab MR
Mohammad et al. (2007)	To correlate resilient modulus of subgrade geomaterials from NDT, in situ and laboratory methods	- A reasonable correlation found between the predicted MR results using DCP index and the actual laboratory results - The DCP soil-property model found to be the most reliable approach to correlate the laboratory and field test results as compared to other field test deices	DCP; FWD; Continuous Intrusion Miniature Cone Penetrometer (CIMCPT); lab MR
Gudishala (2005)	To investigate the correlations between in situ and laboratory resilient moduli	- Correlations developed for specific soil types between in situ and laboratory resilient moduli - Developed models were associated with some level of uncertainty	DCP; LWD; lab MR
Ping et al. (2002)	To investigate correlations between laboratory and field moduli of granular subgrade materials	- Field backcalculated moduli were about 60% greater than those from laboratory tests - A reasonable correlation between lab MR and in situ plate load test was not found	FWD; In Situ Plate Load Test (PLT); lab MR
Tanyu et al. (2003)	To compare the elastic moduli from lab MR tests to those obtained from backcalculation of FWD deflections	- The minimum bulk stress in the laboratory resilient modulus test can be higher than the bulk stress under field conditions - The low-strain elastic modulus from laboratory tests were lower than the elastic moduli backcalculated from field data	Lab MR test, Large Scale Model Experiment (LSME), FWD

The correlations developed by various studies in the literature predict the moduli only within the range of the geomaterial types used for the model development. However, most models exhibit poor predictive power when they are tested on different soils not used to develop the relationships (Von Quintus and Killingsworth 1998; Yau and Von Quintus 2002; Wolfe and Butalia 2004; Malla and Joshi 2006). Such problems should be expected because correlations are developed from the data that may have shown large variations for similar types, similar compaction, and stress conditions. Practically speaking, it may never be possible to develop a universal correlation that can be used universally. However, it may be feasible for each highway agency to develop their soil-specific relationships for their most common geomaterials.

Review of Estimation of Mechanical Properties of Geomaterials

The resilient modulus of the compacted geomaterials is dependent on the applied stress state and it can be as high as the initial tangent modulus for stiff materials (see Figure C-2). For less stiff materials under

different stress conditions, the resilient moduli can be the secant moduli marked as E_1 though E_3 in Figure C-2. Stiffness is defined as the resistance to deformation of a material under an applied load. As such, stiffness is not a unique material property but the response of a pavement system to the load. With different levels of approximation, the modulus can be estimated from the stiffness given the knowledge of the layers in the pavement system, the dimensions of the applied load and a model that estimates the response of the pavement system. Due to the complexity and nonlinearity of the behavior of the unbound pavement geomaterials under the repeated wheel loads, it is crucial to investigate the parameters affecting the resilient responses of such materials (Lekarp et al. 2000). Significant research efforts have been dedicated to studying these parameters.

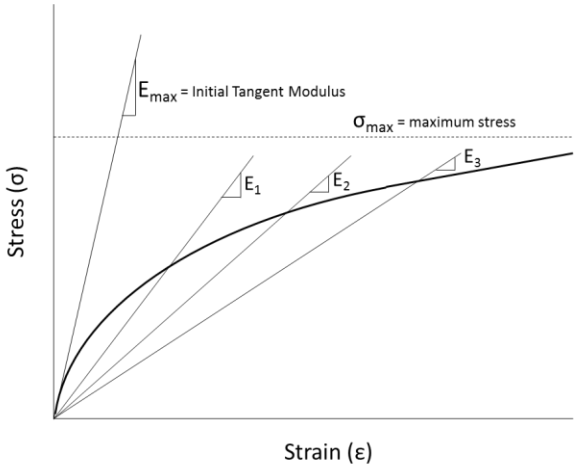

Figure C-2. Definitions of modulus dependent of stress state and material stiffness.

Residual Stresses during Compaction

Tutumluer (2013) contains a summary of research body regarding the consideration of initial stress states induced by compaction. D'Appolonia et al. (1969) and Duncan et al. (1991) have investigated the residual stresses as a result of the compaction process. Due to such stresses locked in the geomaterial layers, the separation/loosening of the materials could happen towards the final stages of the compaction (Mooney and Reinhart 2009).

State of Stress

Table C-4 summarizes the different constitutive models using the various definitions of the stress state to explain the nonlinear behavior of the compacted geomaterials. Different forms of the stress state have been implemented to explain the stress dependency of the resilient modulus models. These forms include: the repeated stress, confining pressure, bulk stress, deviatoric stress, mean stress and octahedral shear stress. The state of stress is bound between two extremes, when no external loads are applied and under external loads imparted by a truck or the roller. When no external load is applied the initial confining pressure, σ_{c_init}, is:

$$\sigma_{c\_init} = \frac{1+2k_0}{3}\sigma_v \tag{C.1}$$

where σ_v is the vertical geostatic stress and k_o is the coefficient of lateral earth pressure at rest. The initial deviatoric stress, σ_{d_init} can be written as:

Table C-4. Summary of resilient modulus constitutive models based on stress states.

Reference	Model Form	Stress Parameter
Dunlap (1963)	$MR = k_1 (\sigma_3/P_a)^{k2}$	$S_{u1.0\%}$ = stress causing 1% strain in conventional unconfined compressive test Confining stress (σ_3) Effective confining stress (σ'_3) Atmospheric pressure (P_a) Bulk stress (θ) Deviatoric stress (σ_d)
Seed et al. (1967)	$MR = k_1 (\theta/P_a)^{k2}$	
Moossazadeh and Witczak (1981)	$MR = k_1 (\sigma_d/P_a)^{k2}$	
Shackel (1973)	$MR = k (\sigma^n_{oct} / \tau^m_{oct})$	
Brown et al. (1975)	$MR = k_1 (\sigma_d/\sigma'_3)^n$	
Thompson and Robnett (1976)	$MR = k_1 + k_2(\sigma_d)$, when $\sigma_d < \sigma_{di}$ $MR = k_3 + k_4(\sigma_d)$, when $\sigma_d > \sigma_{di}$	
Fredlund et al. (1977)	$MR = 10^{(k-n\sigma d)}$	
Thompson and Elliot (1985)	$MR = k_2 + k_3(k_1 - \sigma_d)$ $MR = k_2 + k_4(\sigma_d - k_1)$	
Drumm et al. (1990)	$MR = (k + n\sigma_d) / \sigma_d$	
Lee et al. (1997)	$MR = 695.4 (S_{u1.0\%}) – 5.93(S_{u1.0\%})^2$	
Witczak and Uzan (2004)	$MR = k_1 P_a (\theta/P_a)^{k2} (\sigma_d/P_a)^{k3}$	
Wolfe and Butalia (2004)	$MR = k_1 P_a [P_a \sigma_{oct}/\tau^2_{oct}]^{k2}$	
SHRP (2001)	$MR = k_1 P_a [(\theta-3k_6)/P_a)]^{k2} (\tau_{oct}/P_a)^{k3}$	
Andrei et al. (2004) NCHRP 1-28A	$MR = k_1 P_a (\theta/P_a)^{k2} (\tau_{oct}/P_a+1)^{k3}$	
Ooi et al. (2004)	$MR = k_1 P_a (\theta/P_a+1)^{k2} (\tau_{oct}/P_a+1)^{k3}$	
Pezo et al. (1991)	$MR = k_1 P_a (\sigma_3/P_a)^{k2} (\sigma_d/P_a)^{k3}$	
Ni et al. (2002)	$MR = k_1 P_a (\sigma_3/P_a+1)^{k2} (\sigma_d/P_a+1)^{k3}$	

$$\sigma_{d\_init} = \frac{2-2k_0}{3}\sigma_v . \tag{C.2}$$

When the external loads are present, additional stresses, σ_x, σ_y and σ_z, are induced in two horizontal and one vertical directions under the application of an external load. A multi-layer algorithm can conveniently compute these additional stresses. The ultimate confining pressure, σ_{c_ult} is:

$$\sigma_{c\_ult} = \frac{1+2k_0}{3}\sigma_v + \frac{\sigma_x + \sigma_y + \sigma_z}{3} \tag{C.3}$$

and the ultimate deviatoric stress, σ_{d_ult}, is equal to:

$$\sigma_{d\_ult} = \frac{2-2k_0}{3}\sigma_v + \frac{2\sigma_z - \sigma_x - \sigma_y}{3} . \tag{C.4}$$

Under a truckload or for that matter a roller or an NDT device, the modulus can become nonlinear depending on the amplitude of the confining pressure, σ_{c_ult}, and the deviatoric stress, σ_{d_ult}. Even though simple in concept, the dependency of the modulus on the state of stress brings about several practical complications in the context of this study. These complications can be summarized into the following items:

- The representative modulus of a given geomaterial placed in a pavement section is not a unique value and depends on the underlying and/or overlying layers.
- The state of the stress of a given geomaterial placed in a pavement section can only be estimated if the moduli of all layers are known. As such, the estimation of the target modulus based on the design modulus has to be carried out iteratively using an analytical layered structural model (based on the linear-elastic layered theory or the nonlinear finite element).
- The sophistication of the selected analytical structural model impacts the design and target moduli.

Moisture Content

The behaviors of geomaterials under saturated conditions were also investigated in a number of studies such as Wolfe and Butalia (2004), Hopkins et al (2004) and Ooi et al. (2006). In general, the studies regarding the impact of moisture variation on modulus of compacted geomaterials under the unsaturated conditions can be divided into the models based on the matric suction, models based on the gravimetric/volumetric moisture content, and models based on the degree of saturation. The soil may be subjected to variation in stiffness due to interaction with the atmosphere, leading to repeated cycles of infiltration and evaporation, referred to as hydraulic hysteresis, which in turn can lead to a change in soil stiffness (McCartney and Khosravi 2013). A comprehensive synthesis of such studies were previously reviewed in Puppala (2008) and Tutumluer (2013).

Drumm et al. (1997) investigated the variation in the resilient modulus with the moisture variations after compaction. They proposed an approach to consider the effect of the moisture changes in terms of the degree of saturation as a correction factor for the gradient of resilient modulus.

Hossain (2008) investigated the use of the resilient moduli at different moisture contents with respect to the optimum conditions for design purposes. Sawangsuriya et al. (2008) studied matric suction, small-strain shear modulus and compaction properties of various soils to present various empirical relations. Various compaction moisture content regimes including dry to wet of optimum with Proctor and reduced Proctor energies were studied. A generalized relationship among modulus-suction-compaction conditions was developed. Cox et al. (2009) developed an in situ testing technique that uses the field shakers to evaluate the coupled response between excess pore water pressure generation and nonlinear shear modulus behavior. The research resulted in the design of a new in situ liquefaction sensor to measure dynamic soil particle motion and pore water pressure. Nazzal and Mohammad (2010) developed a methodology for estimating the resilient modulus of the subgrade soils at various compaction moisture contents. Several local correlations were developed which showed better modulus prediction capabilities than the Long-Term Pavement Performance (LTPP) models. McCartney and Khosravi (2013) developed a field-monitoring system to evaluate changes in matric suction and temperature profiles in subgrade soil layers. This system consisted in the placement into boreholes of sensors capable of inferring the volumetric water content and temperature of soils. High-permeability silica flour was used to backfill the borehole around the sensors so that changes in matric suction with depth in the subgrade can be inferred through the soil-water retention curve of the silica flour.

The research efforts in these areas are summarized in Table C-5.

Nazarian et al. (2014) measured soil suction measured before and after resilient modulus testing using the filter paper method. They found matric suctions before and after MR tests to be similar, indicating that no major change in soil suction occurred during the testing process. They also observed no excess pore pressure development as the applied deviatoric loads were small as compared to the ultimate loads at which soil specimens fail. Khosravi et al. (2016) studied the impact of suction-induced hardening on the dynamic shear modulus of unsaturated compacted soils. They used a series of resonant column tests on compacted soil specimens to measure the small-strain shear modulus values under successive cycles of drying and wetting, and isotropic compression tests were utilized to characterize the evolution of the yield surface with matric suction changes.

Table C-5. Summary of studies including the evaluation of moisture variation on modulus.

Reference	Objectives and Approach	Concluding Remarks	Approaches and Concepts
Von Quintus and Killingsworth (1998)	Investigating the performance of cohesive and granular subgrade soils.	Moisture content of cohesive subgrades increases after compaction of the layer which affects the resilient modulus of compacted layer.	The data were extracted from long-term pavement performance (LTPP) database.
Maher et al. (2000)	Investigating the parameters affecting resilient modulus including moisture variation. Proposing statistical approached to predict resilient modulus from soil properties.	Initiation and dissipation of pore pressure significantly impacts the strength of subgrade geomaterials. Statistical models were developed and calibrated to predict the resilient modulus of subgrade geomaterials at different moisture contents and stress states.	A number of subgrade materials were selected to perform the resilient modulus tests under different water contents to investigate their sensitivity to moisture variation and cyclic stress ratio.
Yuan and Nazarian (2003)	Seismic non-destructive testing approaches were utilized to evaluate the variation of resilient modulus and moisture content.	The variations in seismic modulus with moisture seems to be different for subgrade soils compared to base materials. Moisture susceptibility of geomaterials are dependent of their fine content and soil type. The effect of moisture content variation on design modulus should be considered.	Drying and wetting cycles were applied to both fine- and coarse-grained materials. Laboratory seismic tests were performed to evaluate the sensitivity to moisture variations.
Kung et al. (2006)	Evaluating the variation of resilient modulus and plastic strain with post-compaction moisture content.	An increase in matric suction would result in decrease in resilient deformation and hence increase in resilient modulus. higher moisture content of subgrade materials as well as the lower matric suction results in decline of resilient modulus.	Resilient modulus and plastic strain were investigated on two types of cohesive subgrade soils under different moisture content and suction conditions. A prediction model using matric suction and deviatoric stress was proposed to estimate resilient modulus.
Zaman and Khoury (2007)	Investigating the effect of post-compaction moisture content on resilient modulus.	Resilient modulus exhibited a hysteric loop with changes of moisture content The initial moisture content affects the drying/wetting loop from both suction-based and moisture content-based models. The increase in resilient modulus with increase in soil suction was dependent of the soil type.	Resilient modulus tests performed during wetting and drying cycles for a number of subgrade soils both matric suction and moisture content were evaluated during the experiments.
Pacheco and Nazarian (2011)	Investigating the impact of compaction and testing moisture content and density on modulus of compacted geomaterials.	Modulus of samples compacted at dry side of optimum showed higher values For higher compaction moisture contents and constant density, the modulus is lower compared to optimum conditions. The modulus of compacted geomaterials is dependent of the difference between time of compaction and testing.	A number of subgrade geomaterial samples were prepared under different moisture and density conditions in the laboratory. The seismic modulus of compacted samples were evaluated during wetting and drying cycles. Impact of relative density on modulus were also evaluated.

Table C-5, cont. Summary of studies including the evaluation of moisture variation on modulus.

`Reference	Objectives and Approach	Concluding Remarks	Approaches and Concepts
Khoury et al. (2013)	Evaluate the variation in resilient modulus, unconfined compressive strength and modulus of elasticity with changes in moisture content after compaction.	The resilient and elastic modulus as well as the unconfined compression strength of the compacted subgrade samples decreased when subjected to wetting and increased after drying. The variation of materials strength and modulus is affected by soil type and stabilizing agent. Modulus-moisture models were developed to be implemented in the design process. Parameters for MEPDG environmental adjustment factor have been estimated for modulus and strength tests.	Both untreated and stabilized soils were evaluated during resilient modulus, unconfined compression strength and modulus of elasticity.
Nazarian et al. (2014)	Developing specifications for modulus-based construction quality control of soils and unbound aggregate geomaterials.	The moisture content of geomaterials at the time of compaction affects the modulus-moisture correlations. The rate of modulus change with respect to moisture variation is not the same for different geomaterials. The modulus-moisture correlations developed under laboratory conditions are different than those developed under field conditions. Transfer functions are needed to correlate field and laboratory modulus-moisture correlations. The variability of moisture measurement devices affects the modulus-moisture correlations.	A number of subgrade soils and unbound granular materials were evaluated under laboratory, small-scale and field conditions. The materials were compacted at different moisture contents and then modulus-based tests were performed during drying and wetting cycles. A number of modulus-moisture correlations were developed under laboratory, small-scale and field conditions.
Li and Sun (2015)	Investigating the impact of moisture fluctuation on resilient modulus of compacted clay using simulation and laboratory experiments.	The amplitude of moisture fluctuation has inverse correlation with resilient modulus of compacted clay. The reduction factor for moisture fluctuation was proposed to reflect its impact on long-term resilient modulus changes.	Wetting and drying cycles with respect to optimum and equilibrium moisture content.
Abu-Farsakh et al. (2015)	Developing/modifying a resilient modulus constitutive model to incorporate the impact of moisture content for unsaturated subgrade geomaterials.	Nonlinearity of the relationship between resilient modulus and matric suction. Due to the complexities associated with the existing models in the literature, a modified constitutive model was proposed to consider the nonlinearity of the modulus-suctions correlation by incorporating normalized moisture content and including the effect of soil type.	Four subgrade soil types were selected to perform the laboratory tests. The soil-water characteristic curves (SWCC) were evaluated using axis-translation and chilled hygrometer.

Nazarian et al. (2015) investigated the employment of the intelligent compaction retrofit kits during the compaction of the earthwork and subgrade geomaterials. In situ soil samples were extracted after the compaction of the soil layers to measure their moisture contents. The results from the modulus-based devices (LWD and PSPA) and ICMVs from different IC rollers were compared with the in situ moisture

contents. Some relationships were observed between the modulus-based moduli and moisture contents. However, the moisture dependencies of the ICMVs could not be established.

Many other studies have also focused on developing correlations to predict the resilient modulus of the compacted geomaterials using the moisture/suction variables. A summary of these relationships is included in Table C-6.

Table C-6. Summary of models developed to predict modulus based on moisture/suction variations.

Reference	Model Form	Model Parameters
Oloo and Fredlund (1998)	$(Mr)_{us} = k\sigma^{n}_{b}+k_s(u_a - u_w)$, for coarse-grained materials $(Mr)_{us} = k_2 - k_3(k_1 - \sigma_d)+k_s(u_a - u_w)$, when $k_1>\sigma_d$ for fine-grained materials $(Mr)_{us} = k_2 - k_4(\sigma_d - k_1)+k_s(u_a - u_w)$, when $k_1<\sigma_d$ for fine-grained materials	σ_b = *bulk stress* σ_d = deviatoric stress k_i = *regression* parameter M_r = resilient modulus Mr_{us}= unsaturated resilient modulus J_1 = first stress invariant θ_w = volumetric water content θ_s = saturated water content χ = function of degree of saturation u_a = pore air pressure T_s = soil surface tension S_r = degree of saturation T_s = total suction γ_d = dry density θ = volumetric water content β = model parameter χ_w = bishop's parameter $(u_a\text{-}u_w)_b$ = air entry value $(u_a\text{-}u_w) = \Psi_m$ u_a = pore air pressure u_w = pore water pressure p_a = atmospheric pressure σ_{eb} = external bulk stress τ_{oct} = octahedral shear stress θ_{net} = θ-3u_a = net bulk stress $\Delta u_{w\text{-}sat}$ = pore water pressure under saturated conditions Ψ_m = matric suction Ψ = total soil suction Ψ_{m0} = initial matric suction $\Delta\Psi_m$= relative change in matric suction P = net mean stress P_r = reference pressure q_{cyc} = cyclic shear stress α and β = model parameters $\Theta = \frac{\theta - \theta_r}{\theta_s - \theta_r}$ = normalized water content θ = water content θ_r = water content at residual condition θ_s = water content at saturated condition k = 1/n = fitting parameter m = fitting parameter MC = moisture content
Johnson et al. (1986)	$M_r = 1.35\times10^{6}(101.36 - \Psi)^{-2.36}(J_1)^{-3.25}(\gamma_d)^{-3.06}$	
Fredlund and Xing (1994)	$\theta_w = \left[1 - \frac{\ln(1+\frac{\psi}{\psi_r})}{\ln(1+\frac{10^6}{\psi_r})}\right]\frac{\theta_s}{\left[\ln(e+\left(\frac{\psi}{a}\right)^{n}\right]^{m}}$	
Drumm et al. (1997)	$M_r = k_3\,(\sigma_d + \chi\Psi_m)^{k4}$	
Yang et al. (2005)	$M_r = k_3\,(\sigma_d - u_a + \chi\Psi_m)^{k4}$	
Ling et al. (2006)	$S_r = -0.5913\,T_s + 95.2$, when $T_s \geq 24$ kPa $S_r = -0.47847\,\ln(T_s) + 95.2$, when $T_s < 24$ kPa $M_r = 8\,e^{0.0437Ts}$	
Drumm and Meier (2003)	$M_r = 27.06 - 0.526\theta$, if $\gamma_d > 100$ pcf $M_r = 18.18 - 0.404\theta$, if $\gamma_d < 100$ pcf	
Gupta et al. (2007)	$M_r = k_1 P_a\left[\frac{\theta_b - 3k_4}{P_a}\right]^{k2}\left[\frac{\tau_{oct}}{P_a} + k_5\right]^{k3} + \alpha(u_a - u_w)^{\beta}$	
Liang et al. (2008)	$M_r = k_1 P_a\left[\frac{\theta + \chi_w\psi_m}{P_a}\right]^{k2}\left[\frac{\tau_{oct}}{P_a} + 1\right]^{k3}$ $\chi_w = \left[\frac{(u_a - u_w)_b}{u_a - u_w}\right]^{0.55}$	
Siekmeier (2011)	$M_r = k_1 \times p_a \times \left(\frac{\sigma_{eb} + f_s\,\theta_w\,\psi}{p_a}\right)^{k_2} \times \left(\frac{\tau_{oct}}{p_a} + 1\right)^{k_3}$	

Table C-6, cont. – Summary of models developed to predict modulus based on moisture/suction variations.

Reference	Model Form	Model Parameters
Cary and Zapata (2011)	$M_r = k_1 P_a \left[\frac{\theta_{net} - 3\Delta u_{w-sat}}{P_a}\right]^{k2} \left[\frac{\tau_{oct}}{P_a}\right]^{k3} \left[\frac{\psi_{m0} - \Delta\psi_m}{P_a} + 1\right]$	σ_b = bulk stress σ_d = deviatoric stress k_i = regression parameter M_r = resilient modulus Mr_{us}= unsaturated resilient modulus J_1 = first stress invariant θ_w = volumetric water content θ_s = saturated water content χ = function of degree of saturation u_a = pore air pressure T_s = soil surface tension S_r = degree of saturation T_s = total suction γ_d = dry density θ = volumetric water content β = model parameter χ_w = Bishop's parameter $(u_a\text{-}u_w)_b$ = air entry value $(u_a\text{-}u_w) = \Psi_m$ u_a = pore air pressure u_w = pore water pressure p_a = atmospheric pressure σ_{eb} = external bulk stress σ_{oct} = octahedral shear stress $\theta_{net} = \theta - 3u_a$ = net bulk stress $\Delta u_{w\text{-}sat}$ = pore water pressure under saturated conditions Ψ_m = matric suction Ψ = total soil suction Ψ_{m0} = initial matric suction $\Delta\Psi_m$= relative change in matric suction P = net mean stress P_r = reference pressure q_{cyc} = cyclic shear stress α and β = model parameters $\Theta = \frac{\theta - \theta_r}{\theta_s - \theta_r}$ = normalized water content θ = water content θ_r = water content at residual condition θ_r = water content at saturated condition $k = 1/n$ = fitting parameter m = fitting parameter MC = moisture content
Ng et al. (2013)	$M_r = M_0 \left[\frac{P}{P_r}\right]^{k1} \left[1 + \frac{q_{cyc}}{P_r}\right]^{k2} \left[1 + \frac{u_a - u_w}{P}\right]^{k3}$	
Nazarian et al. (2014)	$Modulus_{Testing} / Modulus_{Compaction} = EXP[0.18(MC_{Compaction} - MC_{Testing})]$, for subgrade materials $Modulus_{Testing} / Modulus_{Compaction} = EXP[1.19(MC_{Compaction} - MC_{Testing})]$, for GP Base materials $Modulus_{Testing} / Modulus_{Compaction} = EXP[0.66(MC_{Compaction} - MC_{Testing})]$, for GW Base materials	
Han and Vanapali (2014)	$M_r = M_{rsat} + \alpha(u_a - u_w)S^{\beta}$	
Abu-Farsakh et al. (2015)	$M_r = k_1 P_a \left[\frac{\theta + \Theta^{k\psi}}{P_a}\right]^{k2} \left[\frac{\tau_{oct}}{P_a}\right]^{k3}$ $\theta_w = \frac{\theta_s}{\left[\ln(e + \left(\frac{\psi}{a}\right)^n\right]^m}$	
Sawangsuriya et al. (2009)	$M_r / M_{rsat} = -5.61 + 4.54 \log(u_a - u_w)$ $M_r / M_{ropt} = -0.24 + 0.25 \log(u_a - u_w)$	

There are a limited number of studies with regards to the impact of the moisture content variation on the stiffness and ICMVs of the compacted geomaterials during IC process. Thompson and White (2007) investigated the variability of the roller-integrated compaction data with respect to the moisture content to

estimate the stiffness of the compacted geomaterials. They used test strips constructed at the optimum and two additional moisture contents to evaluate the impact of the moisture content on the ICMVs. Regression equations relating the moisture content to the compaction meter value (CMV) and Machine Drive Power (MDP) showed strong correlation coefficients. They also discussed that the inherent variation in the moisture content of the compacted geomaterials in construction scale is inevitable, and can affect the roller-integrated quality management of earthwork and unbound geomaterials. Variation of MDP, as well as the variation of in-situ measurements, were found generally higher for cohesive soil than for granular soil.

Density

Most of the studies involved using the intelligent compaction for the earthwork and unbound geomaterials evaluated the possible correlations between any of the ICMVs and the in situ dry density from an NDG. Table C-7 summarizes the most recent studies regarding the correlation of density and intelligent compaction measurement values for earthworks and unbound geomaterials.

Gradation and Plasticity

Indirect modulus models exist that can estimate the resilient modulus of the geomaterials using the index properties such as the gradation parameters and plasticity indices. Such models have been evolved during the past two decades. Richter (2006), Puppala (2008) and Tutumluer (2013) include reviews of the impact of the gradation parameters and plasticity indices on modulus. Other attempts to develop these models could be found in Santha (1994), Titus-Glover and Fernando (1995), Mohammad (1999), Amber and Von Quintus (2002), Malla and Joshi (2007, 2008), Nazzal and Tatari (2013), Kim et al. (2014) and Gu et al. (2014).

Modeling of Geomaterials Subjected to Compaction

Geomaterials, both in their natural or man-made composite forms, are heterogeneous. However, for characterization and numerical modeling purposes, geomaterials are often considered as macroscopically homogeneous and isotropic. Constitutive and material models have been developed for describing the mechanical properties of geomaterials. Several researchers have used forward modeling to investigate the relationship between the roller ICMVs and layer moduli. Different numerical modeling techniques have been attempted in the forward modeling.

Lumped-Parameter

The lumped-parameter approach models both the roller and the soil as discrete mass-spring-dashpot elements to characterize the dynamic drum-soil interaction. One concept of a non-rocking 3DOF model is illustrated in Figure C-3 where the model represents the soil with a Kelvin-Voigt spring-dashpot model. Parameters k and c are the ground stiffness and damping, respectively. The soil spring element is a composite spring that represents both the stiffness of the lift being compacted and the underlying layers within the depth of influence (Anderegg and Kaufmann 2004).

Quibel (1980), Machet (1980), and Kröber (1988) experimentally demonstrated the drum-soil decoupling. Adam (1996) and Anderegg (1997) used lumped-parameter modeling to explore the various operational modes of the roller vibration, including the nonlinear and chaotic vibration. Anderegg (1997) described the jump mode and rocking mode of vibration as chaotic. Using chaos theory, he showed that the rocking and jump states occur above a certain combinations of centrifugal force and soil stiffness states.

Table C-7. Summary of studies including the correlation between ICMVs and density.

Reference	Objectives and Approach	Concluding Remarks
White et al. (2007)	Evaluated the use of intelligent compaction for quality control and quality assurance of earthwork and soils Developing correlations between ICMVs and in situ soil properties such as dry density during field evaluations and laboratory compaction of soil samples	ICMVs may not reflect the actual soil compaction in terms of density for unbound granular soils Not a clear correlation was found between different ICMVs and in situ dry unit weight of the compacted geomaterials
White et al. (2008)	ICMVs and spot tests were performed on test sections to establish possible correlation	At project scale, the ICMVs and spot test could be correlated using average values. However, such correlations revealed lower correlation coefficient for density tests compared to modulus tests
White and Thompson (2008)	Two types of ICMVs were collected on test sections to establish their correlations with in situ spot tests	Correlations between ICMVs and in situ dry density were established as a function of soil type Not a significant correlation was observed between ICMVs and dry unit weights
Mooney et al. (2010)	Reviewed and evaluated different intelligent soil compaction systems Evaluated the correlations between in situ spot tests and ICMVs Recommended specifications for roller-integrated Continuous Compaction Control	A common quality control/quality assurance approach utilizing ICMVs to identify weak areas to further perform spot tests such as density Areas with low ICMV did not necessarily represent areas with low density Measured ICMVs are more sensitive to compaction process as compared to density values
Cao et al. (2010)	Conducted theoretical analysis to develop a dynamic model of roller vibration and its impact on degree of compaction of the soil A number of clayey soils were selected to perform experimental study A test section was selected to perform vibratory tests on subgrade geomaterials	A linear correlation found between degree of compaction of subgrade and acceleration of vibratory drum Results of experimental evaluations showed that there was a correlation between vibration acceleration harmonic ratio and degree of compaction
Xu et al. (2012)	A systematic approach was developed to analyze and manage data from IC operations for HMAs and unbound geomaterial layers	The linear correlation between ICMVs and moduli of in situ spot tests were more consistent compared to density
Siddagangaiah et al. (2014)	A number of field evaluation along with a series of laboratory tests were performed under different moisture and density conditions ICMVs were compared to the results of modulus-based spot tests as well as the in-situ density and moisture test results	Some correlations were observed between ICMV and in situ modulus from LWD or DCP but not a clear correlation was found between ICMV and density from NDG

An important yet difficult parameter to estimate in this approach is the mass of the involved soil m_s. This was ignored in early modeling efforts, e.g., Yoo and Selig (1979), but shown to play an important role in more recent studies (Anderegg and Kaufmann 2004; van Susante & Mooney 2008). Van Susante and Mooney (2008), Facas et al. (2010), and Mooney et al. (2010) were successful in capturing the behavior of the roller during the coupled drum/soil vibration and during the decoupling of the drum, i.e. loss of contact between soil and drum. Van Susante and Mooney (2008) presented a 3DOF nonlinear model to reflect the roller vibration behavior on a compacted soil, considering the curvature of the drum and the stress dependency of the soil stiffness, in addition to the drum/soil decoupling.

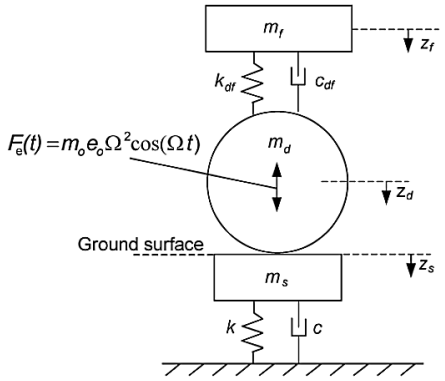

Figure C-3. Lumped-parameter approach as proposed by van Susante and Mooney (2008).

In a 3DOF model that considers vertical motion and no rocking, Mooney et al. (2010) following the steady-state dynamic behavior models of the soil-machine system proposed by Adam (1996) and Anderegg and Kaufmann (2004), recommended the following relationship for the determination of the force transmitted to the soil, i.e. contact force F_c, as

$$F_c = F_e(t) + \left(m_f + m_d\right) g - m_d \ddot{z}_d - m_f \ddot{z}_f \tag{C.5}$$

where $F_e(t)$ is the vertical component of the excitation force produced by an eccentric mass configuration within the drum, as defined in Equation C.1, g is the acceleration of gravity, $\ddot{z}_f$ and $\ddot{z}_d$ are the accelerations of the frame and the drum, respectively. The resulting drum/soil contact force in that equation is comprised of four elements: drum inertia, frame inertia, eccentric force and machine weight.

Roller-based measurement of the soil stiffness is based on the measurement of the vertical drum vibration with the accelerometers mounted on the nonrotating roller components. This arrangement assumes rocking motion of the drum to be negligible. Facas et al. (2010) developed a multidegree of freedom lumped-parameter model to capture not only the translation by the rocking motion but also to account for the observed differences attributed to the rocking in the single-location accelerometers when traveling in different directions. The authors validated their model with field and laboratory data collected from a Sakai smooth drum vibratory roller. Building upon this, Neff et al. (2015) developed a center of gravity ICMV that is independent of the influence of rocking.

Capatana (2013) proposed a lumped-continuous model of terrain compaction and related machine-terrain interaction based on a rheological approach with a predominantly dynamic behavior. The author developed a multi-layer continuous-lumped system by making use of the linear-elastic and the dissipative friction elements that simulated the compaction phenomenon by taking into account the discrete linkages between the adjacent layers. The dissipative friction element considered the Coulomb friction force, F_c,

Stribeck friction law coefficient of proportionality, c_v, the relative velocity between the two points of the connection, v, and the viscous friction coefficient, f_v.

$$F = \begin{cases} \left[F_C + \left(F_{brk} - F_C\right) e^{-c_v|v|}\right] sign(v) + f_v v, & \text{when } |v| \geq v_{th} \\ v \dfrac{f_v v_{th} + \left[F_C + \left(F_{brk} - F_C\right) e^{-c_v|v|}\right]}{v_{th}}, & \text{when } |v| < v_{th} \end{cases} \tag{C.6}$$

where F is the total friction force, F_{brk} is the force of static friction at detachment, i.e. at velocity threshold v_{th}. The author concluded the model was able to simulate the compaction process of the terrain under a vibratory roller compactor.

Table C-8 summarizes the objectives and findings of the latest studies that made use of the lumped-parameter approach for modeling roller compaction.

Table C-8. Summary of studies using lumped-parameter for modeling of roller compaction.

Reference	Objective and Approach	Concluding Remarks	Roller/Pavement Contact Model	Loading Type
van Susante and Mooney (2008)	Studied ability of nonlinear lumped-parameter model to capture complex nonlinear behavior.	Model captured salient roller response during contact and partial loss of contact.	3DOF and 4DOF model with rotational degree of freedom. Nonlinear k_s accounts for drum curvature. Stress-dependent hardening.	Low and high eccentric excitation with wide frequency range 10-45 Hz.
Facas et al. (2010)	Multidegree of freedom model developed to predict rotational kinematics of vibratory roller during contact and loss of contact. Machine parameters for model tuned from suspended drum testing isolated from the ground.	Rotational motion found to influence significantly MVs of soil stiffness in single position drum vibration data. Dual-sided measurement proposed to account for heterogeinity.	Roller-soil rocking model	Sakai SV510D CCC Roller: - Drum mass: 4,466 kg - Frame mass: 2,534 kg - Drum inertia: 1696 kg·m^2 - Frame inertia: 2174 kg·m^2 - Moment: 4.21 kg·m (low), 9.74 kg·m (high) - Frequency: 20-35 Hz - Sitffness: 1,266 kN/m
Beainy et al. (2013)	Proposed Viscoelastic-plastic (VEP) model based on Burger's rheological model.	Static compaction resulted in minimal reduction in air voids. Model captured asphalt thickness and temperature cooling effects on compaction outcome.	Asphalt mat modeled using VEP Burger's model.	Vibratory static compaction - Ingersoll Rand DD118HF Vibratory Compactor - Frame mass: 4,225 kg - Drum mass: 2,371 kg - Frequency: 314 rad/s - Moment: 1.45 kg·m - Contact area: 0.016 m^2
Capatana (2013)	Include dissipative friction element in rheological model.	Model was able to simulate the compaction process of terrain under vibratory roller compactor.	Multiple layer continuous-lumped system using linear-elastic and dissipative friction elements.	Harmonic excitation function.
Jiao et al. (2015)	Identify soil stiffness and damping during soil compaction using harmonic balance identification method (HBIM).	Algorithm proposed for identifying compacted soil parameters.	Used classic vibratory roller-soil dynamics model (VRSDM).	LG520A6 vibratory compactor - Frame mass: 9,419 kg - Drum mass: 10,500 kg - Eccentric mass: 81 kg - Frequency: 125.6 rad/s - Soil stiffness: 61 MN/m - Soil damping: 410 kN·s/m

Boundary Element (BE)

The boundary element method (BEM) is a tool used for the stress and displacement analysis of layered continua. Mooney and Facas (2013) used BEM to model drum/soil interaction during post-compaction vibratory proof rolling. Based on the Rinehart et al. (2008) experimental results that indicated the plane-strain conditions existed beneath the center of a 2.1 m long roller drum. They developed a two-layered, quasi-static model with elastic geomaterials subjected to a parabolic surface loading. The authors employed an iterative process was employed to determine the applied force and its contact width. As shown in Figure C-4, the contact force, F_c, was applied as a parabolic surface traction, $p(x)$, consistent with the predictions of Hertz contact theory for a cylinder on a half-space. The force was distributed over a contact width $2a$ and drum length L_d.

Musimbi et al. (2010) described an iterative process for determining the contact width $2a$, which they found to agree reasonably well with the Hertz predictions for granular materials. The authors concluded the drum-soil contact problem for the stiffer materials can be modeled with as plane strain, using BE or 2D FE models, and recommended the use of the 3D analyses for the softer clayey materials.

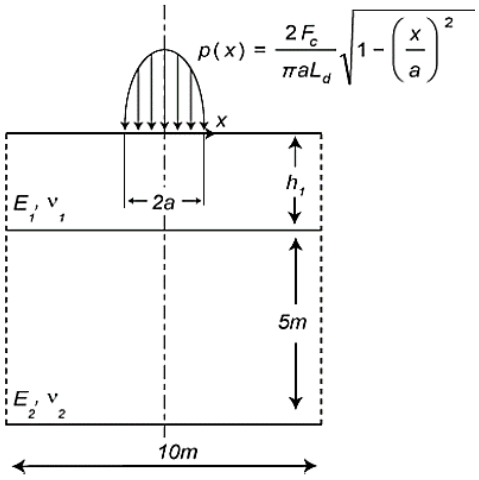

Figure C-4. BE model of two-layered system as proposed by Mooney and Facas (2013).

Discrete Element Modeling (DEM)

Discrete Element Modeling (DEM) is another numerical simulation technique that allows the researchers to gain insight into the interaction of the distinct constituents of mixed, heterogeneous materials. DEM was introduced by Cundall (1971) for applications in rock mechanics. DEM has been used by the researchers for studying the behavior of granular materials at the microscopic level, particularly when the internal structure of the material can be properly represented through the use of image analysis techniques. The granular medium is represented by an assembly of discrete blocks that can be considered as rigid or deformable.

The DEM is based on the formulation and solution of the equations of motion or deformation of discrete blocks and the contacts between them. The contact between the blocks must be identified by proper constitutive models during the entire deformation or motion process. A simple linear spring-dashpot model of the contact between two material particles is shown in Figure C-3. The contact is modeled by a spring with stiffness k and a dashpot with damping c in both the normal n and tangential s directions and an additional slider with friction μ in tangential direction. Researchers have used DEM to provide a fundamental understanding of the particle kinematics during the compaction as shown in Figure C-5.

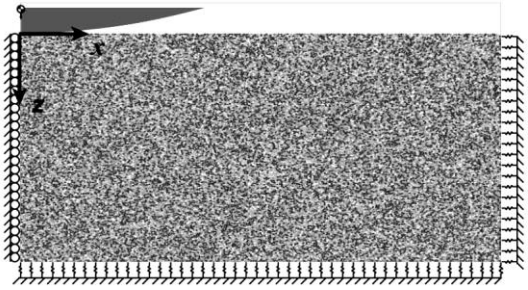

Figure C-5. DEM model with drum roller loading by Buechler et al. (2012).

Table C-9 provides a summary of the latest studies using DEM for the simulating roller compaction of pavement materials.

Table C-9. Summary of studies using discrete element modeling (DEM) for the modeling of roller compaction of pavement materials.

Reference	Objective and Approach	Concluding Remarks	Loading Type and Model
Wang et al. (2007)	Evaluated compaction mechanisms using PFC3D and studied the effect of particle shape, particle contact and temperature on the compaction process.	Provided fundamental understanding of particle kinematics, and relative binder/ mastics to aggregate stiffness.	• Roller weight of 5- 20 kN plus vibration force (sinusoidal) with smaller magnitude. • Rigid roller
Micaelo et al. (2010)	2D DEM used to simulate field compaction.	• DEM results agreed reasonably with field data. • Dynamic mode achieved higher densities than static mode.	• Circular wall with prescribed drum displacement. • Static and vibratory modes.
Buechler et al. (2012)	Studied the effect of tensile stiffness on the contact stress and strain distributions, contact widths, and centerline properties for 2D plate and static drum roller contact problems.	DEM was cable of modeling transition from inversely parabolic contact stress distributions of cohesive soils to parabolic nature of cohensionless granular soils.	• Drum roller radius: 750 mm Solid density ρ = 2700 kg/m^3 • Soil size: 450 m, with length of Winkler springs of 300 mm

Finite Element Modeling (FEM)

The Finite Element Method (FEM) has been widely used for modeling the soil response due to the roller compaction. A 2-D, plain strain, linearly elastic FE modeling approach was attempted by Mooney and Facas (2013) to investigate the relative influence of the layer properties (layer modulus and thickness) on the roller-measured composite soil stiffness. They developed their model using ABAQUS, discretizing the soil as shown in Figure C-5. The infinite elements were included at the boundaries to capture the effects of the radiation damping. They used Rayleigh damping constants α = 25 and β = 0.0002 to minimize the dilatational and shear wave reflections. The vibratory drum was modeled as a 1.5 m diameter rigid cylinder with a combined drum and frame weight of 16.35 kN as a single, static vertical load acting at the center of the rigid cylinder. Kenneally (2015) used this model to quantify the relationships between the ICMVs and the subgrade and base lift moduli. They used a 2-D FE model, which is computationally less expensive than the 3-D models, to forward model the responses as a part of an inverse analysis to develop a real-time modulus prediction.

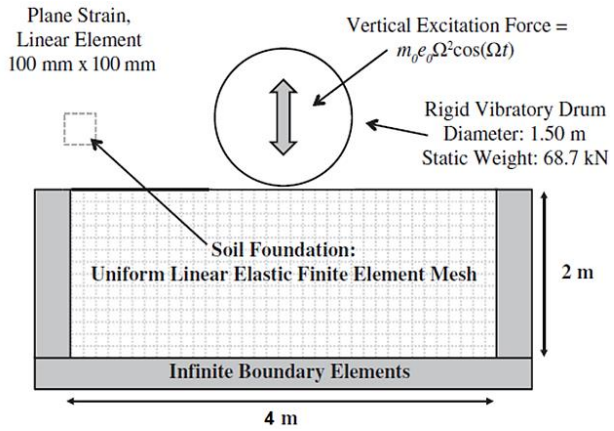

Figure C-6. 2-D FE model with infinite boundary elements by Mooney and Facas (2013).

Capraru et al. (2014) developed a 2-D plane-strain FE model of a two-layer pavement system consisting of 0.50 m sandy soil compacted on top of a 6.0 m gravel subsoil to study the dynamic roller-soil interaction in soil compaction with vibratory rollers. The model was bounded with infinite elements to dampen the incident waves. In addition, they considered geostatic state of stress and the contact initialization between the drum and the soil. The authors used the modified Drucker–Prager/Cap model for modeling the behavior of the sandy soil, while the subsoil was assumed to be linearly elastic. The viscous damping of the soil was modeled using the Rayleigh damping approach, in which the discrete damping is accounted as a linear combination of the mass and stiffness of the material. The two Rayleigh coefficients α and β for the soil were computed according to the double frequency method suggested by Lanzo et al. (2004) assuming a constant soil damping ratio ζ=20%. The authors defined the contact between the drum and the soil based on the surfaces of the two bodies, and a prescribed dry friction with a coefficient of friction μ of 0.30. The drum was connected through a spring-dashpot system to a reference point with a boundary prescribed motion. The authors estimated the energy loss between the two bodies based on the shear stresses and the relative slip velocities developed at the contact area, and the observed soil dilation due to the shearing during the compaction process.

Since a 2-D FE model considers a uniform distribution of the responses along the length of the drum, a number of researchers have favored the 3-D modeling of the drum. Kim (2010) modeled various drum types (cylindrical, triangular, Landpac's rounded triangular, pentagonal and Bomag's octagonal) to study their influence depths of compaction. He concluded that the depth of influence varied depending on the stiffness of the soil. Though no vibratory loading was considered, the drums were allowed to rotate by friction force between the drum and the soil. Carrasco et al. (2014) developed 3-D FE models for the simulation of the soil compaction by vibratory drums, as shown in Figure C-7.

FEM allows the inclusion of nonlinear material models for the base and subgrade materials. Chiroux et al. (2005), Wang et al. (2007), Kim (2010), Kuo et al. (2013), Capraru et al. (2014) and Yesuf (2014) considered the Drucker–Prager/cap model for modeling soils, whereas Hügel et al. (2008), Patrick and Werkmeister (2010) and Erdmann and Adam (2014) preferred the viscoplastic models. Similarly, the resilient modulus, developed as a means to characterize the resilient behavior of soils under repeated loading, can be used with the IC given the vibratory nature of the repeated loading applied to the underlying soils during the compaction process (Rinehart et al. 2009).

Xia and Pan (2010) focused on asphalt compaction by implementing a vibratory drum and a crushable foam model with volumetric hardening for asphalt; yet, the base and subgrade were modeled as linearly elastic. They used the FE model to predict the spatial density change due to the rolling compaction. McAdams (2014) and Carrasco et al. (2014) developed dynamic FE models to predict the behavior of the pavement systems based on the stress-dependent resilient moduli.

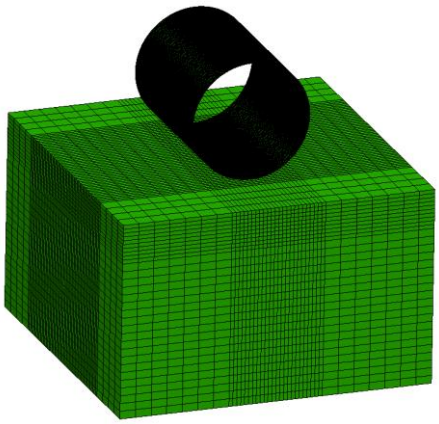

Figure C-7. 3-D FE model with cylindrical vibrating drum by Carrasco et al. (2014).

Xu et al. (2012) developed a 3-D FE model using ANSYS® to study the effect of the compaction uniformity on the pavement performance. The heterogenous HMA moduli obtained from the field IC measurements was spatially distributed through the layer. All pavement materials were assumed linearly elastic. Their model simulated a 770 ft long by 10 ft wide compaction lane following the conditions of an IC construction project located on US-52 in Lafayette, IN. A total of 105,798 elements and 117,100 nodes were used. The roller vibrational force was simulated as a sinusoidal pulse with a cycling period of 0.6 s, a peak magnitude of 9000 lb, a pressure of 100 psi, and a contact area of 5.8 in. × 15.6 in. To simulate the load movement at a constant speed of 60 mph, the authors applied step loading element by element. Peak pavement responses were used for pavement performance prediction using the Mechnical-Empirical Pavement Design Guide (MEPDG) distress models. They determined the Bomag ICMV measurement of the vibration (dynamic) modulus of elasticity, E_{vib}, for pavement materials. The authors found rutting of the nonuniform HMA model was deeper than that of the homogeneous HMA, while a nonuniform HMA caused a reduction in the fatigue life. They further indicated that a pavement section with lower mean layer moduli did not necessarily mean inferior performance since the effects from the uniformity of the material property might dominate other factors.

Chi and Zhang (2012) developed an advanced FE compaction model using the Coupled Eulerian-Lagrangian (CEL) method to simulate the landfill compaction with a CAT compactor. They implemented this method in ABAQUS as a user-defined material subroutine (VUMAT) with Eulerian elements. They found the CEL method outperforms the traditional Lagrangian method due to the excessive mesh distortions in the simulations that require multiple machine passes. The authors implemented an elasto-plastic model for the highly compressible waste material. They concluded that the CEL model failed to predict the responses for the landfill compactor model, thus recommending further improvements to their material subroutine.

Erdmann and Adam (2014) simulated the dynamic compaction process of the vibratory rollers using a 3-D FE elastic model to study the influence of the drum stiffness and elasticity on the gradient of the force-displacement curve. They found the variation of the drum thickness resulted in a different deformation of the drum due to the interaction with the subgrade. They also found the elastic deformation increased as the drum shell thickness decreased. Moreover, the authors found that the tangential stiffness decreased with the increase in the thickness of the drum shell. The drum stiffness affected the stress propagation in the subgrade causing a decrease in the depth of influence with the thinner drum shell.

Based on the review of existing documents, relatively little work has been done toward developing comprehensive approaches that tie the design moduli of the compacted geomaterials to the moduli measured in the field for acceptance.

The existing approaches are summarized in Table C-10 along with the concerns with each one. One weakness of most of these methods is relating the design and target moduli.

Table C-10. Summary of finite element studies for the modeling of roller compaction.

Reference	Objective and Approach	Concluding Remarks	FE Model	Loading Type and Model	Roller/Pavement Contact Model
ter Huerne (2004)	Proposed an FEM for HMA rolling problem	Recommendations to Rock material model available in DiekA code.	• FEM code DiekA • 400 mm long model • Sub-base of infinite material length • HMA modeled using Arbitrary Lagrangian Eulerian method	HAMM DV6.42 roller modeled as a free rotating rolling drum.	• Drum modeled as rigid rotating boundary. • 4-node contact elements using Coulomb friction model.
Chiroux et al. (2005)	• Soil interaction with a rigid wheel. • Compared soil compaction wheel rut depth, and octahedral normal and shear stress of laboratory testing.	Modeled air void reduction process with FEM with reasonable accuracy in terms of deflections and stresses.	• ABAQUS/Explicit • Two models: soil-bed and rigid rotating wheel • Soil was 7.2 m in length, 0.5 m height and 1.0 m in width • Relatively fine mesh density in the first 5 cm of soil under the wheel • Soil used Drucker–Prager/cap model • Hydrostatic pressure considered	• Rigid wheel, using “R3D4” elements. • Dimension: Diam.: 54 in. Width: 6 in. • Weight applied along perimeter of wheel. • 5.8 and 11.6 kN loadings. • Translational velocity of 16.74 and 18.45 cm/s, respectively.	• Contact surfaces at top of soil and outer surface of rigid wheel were defined as a “contact pair”. • Rigid wheel. • Load gradually applied with linear ramp. • Friction interaction $\mu = 0.6$.
Wang et al. (2007)	• Provided an overview of fundamental mechanisms of asphalt compaction. • Evaluated compaction mechanisms using FEM and DEM, using Evolution of Element Volume (EVOL) and Void Volume Fraction (VVF).	• Modeled air void reduction process with reasonable accuracy. • Both methods serve as guides for selection of compaction parameters.	• ABAQUS • Gurson-Tvergaard (1981) porous viscoplasticity model (Guler et al. 2002), considers hydrostatic components of stresses and strains and takes into account effect void nucleation and growth	• Rigid roller. • Constant load (5-20 kN) applied to roller, vibrational (sinusoidal) force included with smaller magnitude.	• Rigid roller with contact model.
Hügel et al. (2008), referring to a study carried by Kelm (2003)	• Modeling of compaction of soil by vibratory rollers on dry non-cohesive soils. • Calculate distribution of void ratio e of soil after single vehicle crossing.	• Simulations helped optimize compaction and homogenization of non-cohesive soils.	• ABAQUS/Explicit • Soil is modeled using hypoplastic constitutive models • Subsoil section is discretized using continuum elements (C3D8R) with displacement degree of freedom, and far field uses infinite elements (CIN3D8)	• Vibratory roller modeled as rigid surface linked with a point mass. • Predefined horizontal velocity and vertical harmonic excitation.	• Roller drum modeled as rigid plate.

Table C-10, cont. – Summary of finite element studies for the modeling of roller compaction.

Reference	Objective and Approach	Concluding Remarks	FE Model of Pavement	Loading Type and Model	Roller/Pavement Contact Model
Kim (2010)	• Modeling of IC rollers to estimate influence depth of soil compaction. • Various drum types evaluated: cylindrical, triangular, Landpac's (rounded triangular), pentagonal and Bomag's octagonal.	• Width of contact area between drum and soil controls depth of compaction. • Depth of compaction larger for IC rollers. • Depth of compaction depends on stiffness of soil. • Surface pressure controls degree of compaction (uneven for impact rollers).	• 3-D FE LS-DYNA • Soil length: 52.5 ft • Planned compaction test length: 42 ft • 4 in. element size underneath roller • Drucker–Prager (simplified elastic perfectly plastic model) • Contact friction of drum and soil based on soil external friction angle of 30°~35°	• Drum size: Diam. 1.50 m Width 2.20 m Weight 24,000 lb with 4 in. thick rigid shell elements • Beam element located axially in the middle of drum mesh moves at 10 km/h • Different drum shapes: cylindrical, triangular, etc.	• Roller shell and beam elements coupled as constrained rigid bodies. • Contact automatic surface to surface coupling added for contact between drum and soil mesh. • Soil treated as master material coupled drum and axis defined as slave material.
Patrick and Werkmeister (2010)	• Compaction of thick granular bases. • Compared theoretical stress and strain distribution under a vibratory roller and a standard heavy vehicle. • Evaluated thin AC surface granular pavements.	• Initial post-construction deformation of thin-surfaced granular pavement is affected by compaction level in the field, though rut would be relatively small. • Degree of compaction of 88% max. dry density (MDD) would not result in significant rutting of pavement.	• ReFEM, 3-D FE • Used quarter model: FE section 2.4 m long × 4.0 m wide • HMA and subgrade modeled as linear-elastic • Base course modeled using Dresden model	• Smooth drum, Caterpillar CD 563C, 3000 kg. • Dimensions: Diam.: 1.5 m, Width: 2.1 m. • Contact area: 2.66 m width for high amplitude dynamic load 1.33 m width for low amplitude dynamic load. • High amplitude dynamic load 15.2 ton.	• Roller drum modeled as rigid plate (high stiffness E = 320,000 MPa in transversal and vertical direction).
Xia and Pan (2010)	• Modeling of vibratory asphalt compaction. • Different compactor operations modeled to understand impact on compacted density. • FE model used to predict spatial density change due to rolling compaction.	• Vibratory asphalt compaction delivers better compaction to HMA layers. • Vibration frequency is an important parameter for influencing final asphalt compaction.	• ABAQUS, 3-D FE • Model Size: Length 10 m, Width: 3 m • 3 layer system: 0.125 m HMA layer, 0.3 m base, and 2.0 m subgrade • Crushable foam model with volumetric hardening to model asphalt compaction • Base and subgrade assumed to deform elastically	• Non-vibratory and vibratory roller • Rigid roller • Roller dimensions: Base: 3.44 m Diam. 1.30 m Width 1.72 m • Load 10.8 k (48 kN) Freq.: 40 Hz • Eccentric mass moment m_0e_0 = 1.585 kg·m	• ABAQUS general contact model.

Table C-10, cont. – Summary of finite element studies for the modeling of roller compaction.

Reference	Objective and Approach	Concluding Remarks	FE Model of Pavement	Loading Type and Model	Roller/Pavement Contact Model
Xia (2011)	• Tire/terrain interaction for off-road vehicle design • Predict soil compaction and tire mobility	• Effects of tire inflation pressure, rolling speed and frictional property of tire/terrain interface on rolling radius, acceleration, torque and traction were obtained • Proved that numerical model can serve as robust tool on predicting soil compaction	• ABAQUS/Explicit • 3-D FE, 2-layer system • 12 m long, 3 m wide, 2 m deep • Upper soil using Drucker–Prager/Cap model for soil compaction • Stiffer lower soil modeled linear-elastic	• Modeling of a tire with 981 mm diameter and 327 mm tread width • Tire rubber modeled as compressible hyperelastic material and fiber reinforcement as linear-elastic	• Simulation in two steps: first static followed by tire rolling over a deformable soil with an angular velocity at the tire axle • Coulomb's friction law used to define friction between tire and ground
Chi and Zhang (2012)	Compare Coupled Eulerian–Lagrangian (CEL) to traditional Lagrangian elements (ALE)	• Found CEL outperforms Lagragian elements when excessive mesh distortion • CEL failed to predict full landfill compaction, but proved effective in barrel compaction	• ABAQUS/Explicit 6.11-1 • Developed CEL in VUMAT subroutine • Elasto-plastic model for highly compressible waste material • Fine mesh: 420,305 elements, 445,521 nodes • 520,000 time increments to model 4 passes • 16 hr computation with 24 CPUs	• Caterpillar SEM6020 landfill compactor with tip-wheels • Wheels modeled with solid material	• ABAQUS general contact model between compactor wheels and refuse materials • Friction model with constant friction coefficient for interface behavior
Roudgari (2012)	Develop model for compaction of thin sand layer over deep deposit	• Factors dictating compaction of top layer are stiffness of lower layer deposit, magnitude of load, load repetitions and thickness of top layer • Stiffness of lower layer provides more compaction to subgrade layer when lower layer has higher stiffness than subgrade	• Plaxis 2D, static analysis • Plain strain FE, 4^{th} order triangular elements of 15 nodes for accuracy • Soil width 25 m • Lower layer using Mohr-Coulomb model • Upper layer using Stress Hardening model	• Static roller simulated with uniform distributed load applied directly on stiff weightless plate on top of soil surface • Contact width of 0.4 m	• None, load directly applied on stiff plate, attached to soil surface elements

Table C-10 (Continued)

Reference	Objective and Approach	Concluding Remarks	FE Model of Pavement	Loading Type and Model	Roller/Pavement Contact Model
Xu et al. (2012)	• Study effect of compaction uniformity on pavement performance. • Compared effect of heterogeneity to homogeneous HMA material. • Peak pavement responses used for performance prediction using MEPDG distress models. • Determined Bomag ICMV and E_{vib}.	• Rutting of the nonuniform HMA model was higher than that of homogeneous HMA. • Fatigue life reduced in nonuniform HMA model. • A pavement section with lower mean value of layer moduli does not necessarily mean inferior performance since the effects from uniformity of material properties may dominate other factors.	• ANSYS 12.1® • 3-D model with heterogeneous HMA moduli as obtained from field IC measurements • All pavement materials assumed linear-elastic • Spatially distributed moduli for heterogeneous HMA • Dimensions: 770 ft long by 10 ft wide compaction lane similar to an IC construction project on US-52 in Lafayette, IN • The FE model: 105,798 elements, 117,100 nodes	• Sinusoidal pulse with cycling period of 0.6 s, peak value of 9000 lb and pressure of 100 psi. • Contact area of 5.8 in. × 15.6 in., comprised by 3 elements. • Moved at a constant speed of 60 mph.	None, pressure applied directly on AC layer.
Kuo et al. (2013)	• Quantify effectiveness of Rolling Dynamic Compaction (RDC) by means of field studies and numerical modeling.	• Shear modulus, Poisson's ratio and cohesion were significant on effect of RDC. • Mass and roller width significantly affect depth of influence. • FE model had reasonable predictions of soil settlement and soil stresses with field study.	• LS-DYNA • 3D dynamic FE • Non-reflecting boundaries • MAT_005 Soil and Foam and MAT_193 Drucker– Prager models evaluated	• 4-sided impact roller, similar to Broons BH-1300 8-ton roller. • Roller is steel encased concrete block. • Shell elements.	• Contact automatic surface to surface. • Rolling motion using prescribed rigid motion.
Liang and Xin (2013)	• Quantify effectiveness of Rolling Dynamic Compaction (RDC) by means of field studies and numerical modeling.	• Higher stress develop at higher frequencies and constant amplitude	• LS-DYNA • 3D dynamic FE • Soil modeled using Drucker–Prager • Soil dimensions: Depth 0.8 m, Width 1.0 m, and Length 2.0 m • Mesh consisting of 508,100 elements	• Smooth cylinder vibrating roller using solid elements. • Roller with 2754 elements. • Rotation speed 314 rad/s.	Contact automatic surface to surface.
Mooney and Facas (2013)	• Investigate the influence of layer properties on roller-measured composite soil stiffness. • Develop real-time approach to modulus prediction.	• Recommended statistical regression analysis for backcalculation of prediction of modulus.	• ABAQUS • 2-D FE, plane strain • Included infinite elements to minimize reflections • Linear-elastic geomaterials with varying modulus	• Rigid vibratory 1.5 m diameter drum. • Drum and frame weight of 16.35 kN.	General contact model.

Table C-10, cont. – Summary of finite element studies for the modeling of roller compaction.

Reference	Objective and Approach	Concluding Remarks	FE Model of Pavement	Loading Type and Model	Roller/Pavement Contact Model
Capraru et al. (2014)	• Describe the numerical modeling of dynamic roller-soil interaction in soil compaction with oscillatory rollers.	• Estimated shear stresses and relative slip velocities developed at the contact area and estimated energy lost between the two bodies.	• ABAQUS Standard. • 2-D FE, plane-strain, two-layer system. • Dimensions: length 15 m, depth 6.5 m, use of infinite elements. • Upper sandy soil using Drucker–Prager/Cap model, linear-elastic subgrade.	• Rigid drum with 4.4 ton weight, 0.6 diameter. • Speed 4 km/h, Freq.: 39 Hz.	• General contact model. • Friction of $\mu = 0.30$.
Carrasco et al. (2014)	• Study influence depth of IC roller and LWD.	• Depth of influence increases with more clayey materials • Influence depth of 1.0-1.8 m with stress criterion, and ~2.0 m on deflection • Use of MEPDG representative modulus, as determined by NCHRP 1-28A recommended state of stress, significantly underpredicts the soil response when compared to nonlinear response	• LS-DYNA • 3D dynamic FE • Soil modeled using MEPDG model for determining resilient modulus • Soil dimensions: Depth 2.5 m, Width 4.0 m, and Length 4.0 m • Mesh consisting of 63,840 elements	• Rigid roller, using shell elements. • Roller dimensions: Diam. 0.75 m, Length 2.0 m, Weight 6000 kg. • Peak load of oscillating load of 350 kN. Freq.: 30 Hz.	Contact automatic single surface model.
Erdmann and Adam (2014)	• Study the influence of drum stiffness and elasticity on force-displacement curve. • Static roller, vertical and oscillatory rollers considered.	• Drum thickness influence affects elastic deformation, force-displacement curve and E_{vib}. • Thinner drum thickness reduces depth of influence.	• ABAQUS and MSC.MARC • 3-D static and dynamic FE. • UMAT with hypoplastic law with integranular strain material model.	• Drum modeled using shell elements. • Diam. 1.5 m. • Frame mass 1720 kg, drum mass 2700 kg. • 150 kN vertical force, with 30 Hz freq. • 140 kN oscillatory force, with 30 Hz freq. • Speed 4 km/h.	General contact model.
Li and Su (2014)	• Studied the influence of large power compacting machine on subgrade.	• Study recommended a gravel thickness layer of 90 cm.	• ABAQUS • 3-D FE model: Length 10 m, width 10 m, height 4 m + compacted layer • Used linear-elastic and Drucker–Prager models.	• ZHONG-DA YZ32Y2 20 ton vibratory roller • Drum size: Diam. 1.53 m, Width 2.18 m • 59 ton excitation force, with freq. 28 Hz • Speed 2 km/h	General contact model.

Table C-10, cont. – Summary of finite element studies for the modeling of roller compaction.

Reference	Objective and Approach	Concluding Remarks	FE Model of Pavement	Loading Type and Model	Roller/Pavement Contact Model
McAdams (2014)	Develop an iterative stress-dependent procedure to specify resilient modulus values under compacted soil.	• Soil stiffness determined using the resilient modulus procedure were somewhat similar to values found from field data. • Force-displacement maxima do not necessarily relate to field conditions.	• ABAQUS • 2-D FE, plane strain using CPE4R elements • Included infinite elements to minimize reflections • Soil modeled using MEPDG model for determining resilient modulus	• Sakai SV510D • Rigid vibratory 1.5 m diameter drum • Drum mass 4466 kg, frame mass 2534 kg. • Mass moment 1.0–4.25 kg·m. Freq. 20-35 Hz	General contact model.
Yesuf (2014)	Proposes a method for optimizing effective depth of compaction of subgrade.	Lift thickness can be chosen as a function of strength parameters depending on weight of roller and required relative density.	• ABAQUS/Explicit • 3-D FE model size • 5 m × 3 m × 3 m • Drucker–Prager model	• Rigid roller using shell elements, with fillet of radius 0.07 m in outer edge • Diam. 1.2 m., length 1.0 m • Roller mass of 100 kg. • Speed 4 km/h. Freq.: 1.85 rad/s	• General contact model. • Friction coefficient defined as tangent of friction angle of soil.
Kenneally et al. (2015)	Quantify the relationships between Continuous Compaction Control (CCC) roller-soil stiffness and subgrade and base lift moduli and thickness for quality control of compacted soils.	• Stiffness is sensitive to increases in lower layer modulus E_2 at $E_2/E_1 < 2.5$, recommending to avoid very stiff materials over soft materials ($E_2/E_1 > 3$). • Stiffness sensitive to 1 m, after which the stiffness is not sensitive to underlying layers and only depends on top layer.	• ABAQUS • 2-D FE, plane strain using CPE4R elements • Included infinite elements to minimize reflections • Linear-elastic geomaterials with varying modulus • 2-layer system with different moduli to study effect of contact area on MVs	• Sakai SV510D • Rigid vibratory 1.5 m diameter drum • Drum mass 4466 kg, frame mass 2534 kg. • Mass moment 3.0 kg·m, freq. 30 Hz	General contact model.

Constitutive Models of Geomaterials

Researchers have developed an increasing number of stress-strain relationships to account for the behavior of geomaterials. These models can be grouped into the linear-elastic, nonlinear elastic, elasto-plastic, visco-elasto-plastic, cap models and hypoplastic materials. Finite element (FE) modeling is built upon the concept of continuum mechanics. Various constitutive models have been proposed in the literature for capturing the properties and features of the numerous soil types from their stress-strain characteristics. The nonlinear and stress sensitive structural response models have been incorporated into the finite element codes for the iterative calculation of the stiffness properties of the granular layers. This information is instrumental for accurate calculations of the pre-yield responses beneath the drum roller.

Linear-Elastic

Because of the computational and theoretical limitations, the linear-elastic assumption has been mostly used to analyze soil compaction with mixed success. A linear-elastic model is based on Hooke's law of linear stress-strain relation. The stress-strain relationships can be expressed in terms of two soil parameters, namely modulus of elasticity, *E*, and Poisson's ratio, *v*. These parameters may vary depending on the moisture content, loading, texture, etc. Nonetheless, soils only behave truly elastically at very small strains (Simpson et al. 1979).

Resilient Modulus

The two constant confining pressure (CCP) stress path testing protocols, namely NCHRP 1-28A and AASHTO T307, are commonly used by practitioners for the determination of the resilient modulus in the laboratory. The general consensus of the material model in the M-E pavement design guide is given by

$$M_r = k_1 P_a \left(\frac{\theta}{P_a}\right)^{k_2} \left(\frac{\tau_{oct}}{P_a} + 1\right)^{k_3} \tag{C.7}$$

where M_r is the resilient modulus, θ is the bulk normal stress, and τ_{oct} is the octahedral shear stress, P_a is the normalizing stress (atmospheric pressure), k_1, k_2, and k_3 are model parameters (determined form fitting the laboratory data to the model). The bulk normal stress and the octahedral shear stress are defined as

$$\theta = \sigma_1 + \sigma_2 + \sigma_3 \text{ , and} \tag{C.8}$$

$$\tau_{oct} = \frac{1}{3}\sqrt{(\sigma_1 - \sigma_2)^2 + (\sigma_2 - \sigma_3)^2 + (\sigma_1 - \sigma_3)^2} \text{ , respectively,} \tag{C.9}$$

where σ_i is one of the principal stresses. Generally, the *k*-values are determined by using a best-fit regression analysis of the applied stresses and the measured strains in the laboratory. A proper set of constraints should be considered for the coefficients and exponents of the model, so that the hardening term and the softening term are physically meaningful.

Other resilient modulus models have been proposed implementing different forms of stress state to explain the nonlinear behavior of geomaterials. Taciroglu (1998), Hjelmstad and Taciroglu (2000), and Ke et al. (2002) utilized stress-dependent constitutive models to determine the resilient modulus for simulations using finite element (FE) modeling in statically loaded pavement systems.

Rinehart et al. (2009) compared the in situ stress states and paths induced beneath a low amplitude vibratory roller during proof rolling to the stress states and paths used in the laboratory resilient modulus testing using the AASHTO T307 protocol. As shown in Figure C-8, their measured responses followed their numerical responses. They used a boundary element (BE) model with the stress-dependent constitutive model proposed by Witczak and Uzan (1988) with k_1-k_3 parameters determined by Santha (1994). The authors also documented the disagreements between the traditional resilient modulus loading protocols and the stresses imparted by drum rollers. Even during the low excitation forces associated with the proof rolling of the compacted lifts, the deviatoric stresses were at least three times greater than the stresses in the traditional resilient modulus loading protocols, as shown in Figure C-9. Despite the fact that the authors provided a compelling argument as the stress states in the AASHTO T307 protocol are not representative of the stress states induced by drum rollers on the granular layers, they overlooked the significance of this finding in the post processing of the field data.

More recently, the MEPDG stress-dependent constitutive model has been implemented in several finite element models by Carrasco et al. (2014) and McAdams (2014) to simulate the vibratory roller compaction of the soils. They used an iterative process to determine the stress-dependent resilient moduli for unbound granular bases and subgrades undergoing dynamic loading induced by the vibratory roller compactors.

Simulation results by McAdams (2014) showed similarities to the results obtained from the field data, indicating that the proposed algorithm might be a feasible modeling procedure.

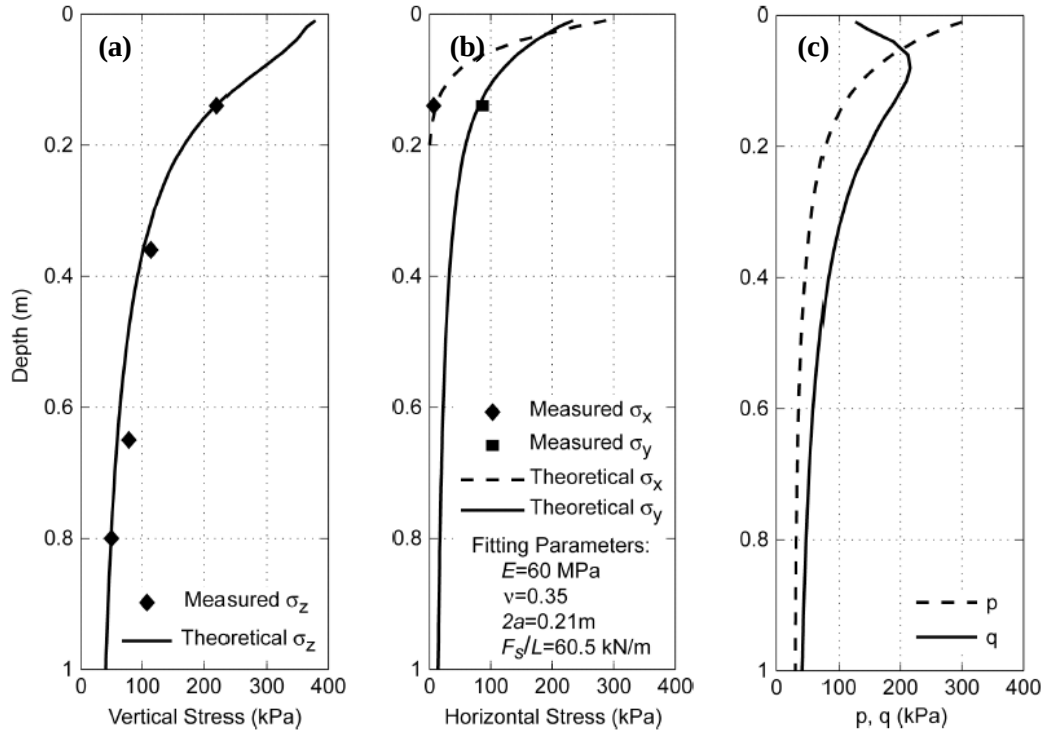

Figure C-8. Comparison of measured stresses to theoretical stress in clayey sand A-6(1) subgrade type due to vibratory roller loading at depths z = 0-1.0 m in terms of (a) vertical component σ_z, (b) longitudinal σ_x and transversal σ_y components and (c) mean stress p and von Mises deviator stress q [f = 30 Hz, Fev = 88 kN, v = 0.5 m/s], by Rinehart et al. (2009).

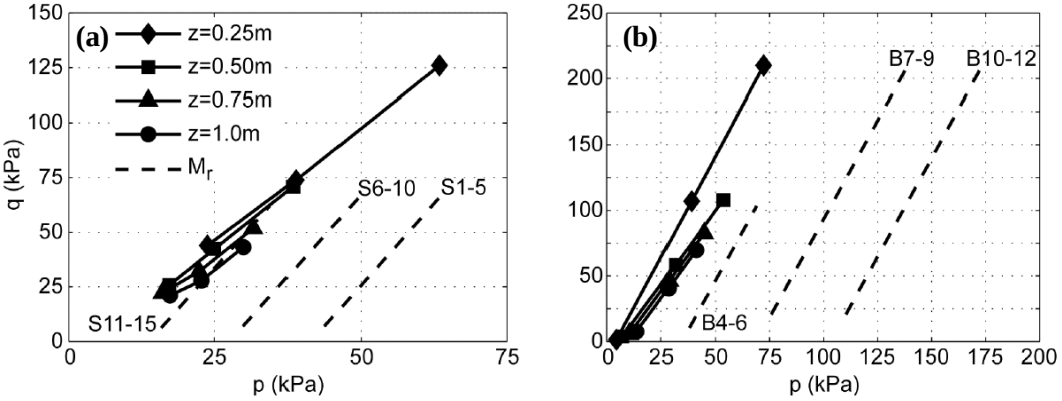

Figure C-9. Vibratory roller loading response in terms of mean stress p and von Mises deviator stress q in comparison with AASHTO T307 at depths z = 0-1.0 m in (a) clayey sand A-6(1) type subgrade [f = 30 Hz, Fev = 88 kN, v = 0.5 m/s] and (b) base material A-1-b type over sandy silt A-4 subgrade [f = 28 Hz, Fev = 88 kN, v = 1.0 m/s], by Rinehart et al. (2009).

Elasto-plastic Models and Yield Criteria

The implementation of the Mohr-Coulomb yield function in the finite element code is cumbersome due to the singularity issues at the six vertices in the octahedral planes. The Drucker–Prager criterion has been considered for minimizing the stability problems. The Drucker–Prager model is a modification of the von Mises criterion where an extra term is included to introduce pressure sensitivity.

The plastic yielding begins when the second stress invariant and the mean stress reach a critical combination. The onset equation for plastic yielding is given by

$$f\left(I_1, J_2\right) = \alpha I_1 + \sqrt{J_2} - k \tag{C.10}$$

where α and k are model parameters determined from the triaxial shear tests, I_1 is the first invariant (bulk) stress tensor, J_2 is the second invariant (deviatoric) stress, defined as

$$I_1 = \sigma_1 + \sigma_2 + \sigma_3, \text{ and} \tag{C.11}$$

$$J_2 = \frac{1}{2}\sigma_{ij}^{dev}\sigma_{ji}^{dev} = \frac{1}{6}\left[\left(\sigma_1 - \sigma_2\right)^2 + \left(\sigma_2 - \sigma_3\right)^2 + \left(\sigma_3 - \sigma_1\right)^2\right], \tag{C.12}$$

in terms of the principal stresses σ_i. The stress tensor is defined as

$$\sigma_{ij}^{dev} = \sigma_{ij} - \frac{I_1}{3}\delta_{ij}, \tag{C.13}$$

where δ_{ij} is the Kronecker delta. Figure C-10 shows the different approximations of the Mohr-Coulomb yield criterion by the Drucker–Prager yield function in the 3D space. The model parameters α and k can be estimated by finding the intersections of the two yield functions in the 3D space, and can be expressed in terms of the cohesion c and friction angle φ corresponding to the outer vertex Drucker–Prager circle as,

$$\alpha = \frac{2\sin\phi}{\sqrt{3}\left(3-\sin\phi\right)} \quad \text{and} \quad k = \frac{6c\cos\phi}{\sqrt{3}\left(3-\sin\phi\right)}. \tag{C.14}$$

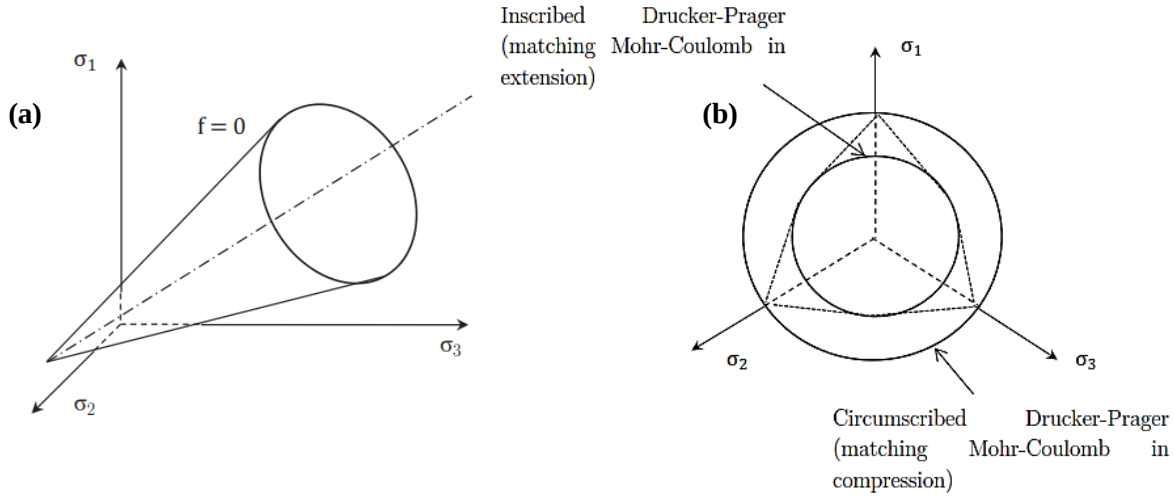

Figure C-10. (a) Drucker–Prager yield surface in principal stress and (b) Mohr-Coulomb yield function (Yesuf, 2014).

These constants can also be determined based on the equivalent or the inner vertex of the Mohr-Coulomb criterion (Kim 2010). Researchers, such as Kim (2010), Kuo et al. (2013), Liang and Xin (2013), Li and Su (2014) and Yesuf (2014), have used the Drucker–Prager failure criterion for modeling vibratory compaction of geomaterials.

The modified Drucker–Prager/Cap plasticity model has been widely used in the finite element analysis programs for different geotechnical applications, including the compaction of the geomaterials using vibratory rollers. This model adds an elliptical cap to the Drucker–Prager yield surface to provide for the pressure-dependent yielding, adding a transition surface between the shear failure surface, and the cap to provide for a smooth yield surface. The model is assumed to be isotropic, and its yield surface is described then by three segments in the deviatoric *p-t* plane as shown in Figure C-11 a shear failure surface F_s, providing dominantly shearing flow; a cap F_c, providing an inelastic hardening mechanism for plastic

compaction, and a transition region F_t between the first two segments, meant to provide a smooth surface that facilitates only the numerical implementation of the model (Pistrol et al. 2012).

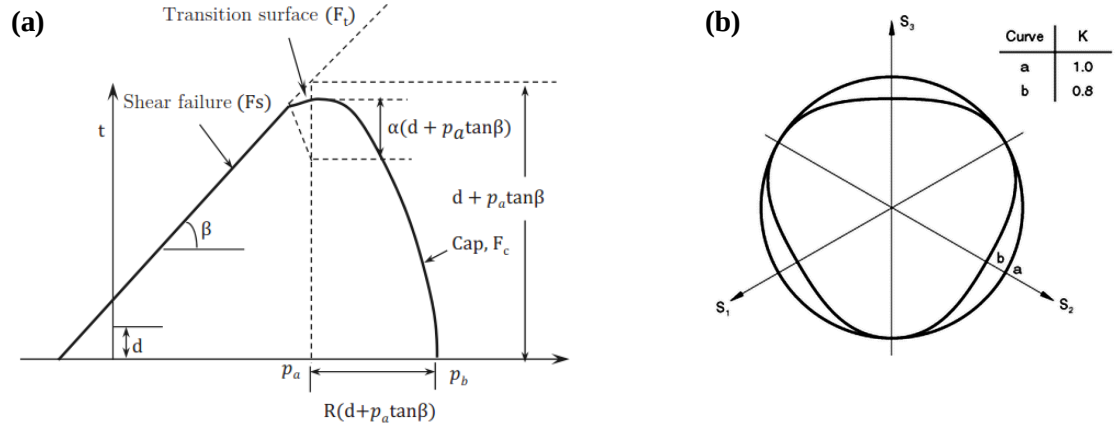

Figure C-11. Drucker–Prager/Cap model (a) yield surface in the p-t plane and (b) typical yield/flow surfaces of the linear model in the deviatoric plane (ABAQUS User's Manual 2000).

Table C-11 summarizes the Drucker–Prager/cap model parameters and their respective equations. Pistrol et al. (2012) provides a more detailed derivation of the equations involved in the Drucker–Prager/Cap plasticity constitutive model, including the equations for plastic flow omitted for brevity in this report.

Table C-11. Drucker–Prager/cap model parameters, adapted from Pistrol et al. (2012).

Model Form	Model Parameters
Yield condition: $F_s = t - p\tan\beta - d = 0$ $p = \frac{1}{3}tr(\sigma_{ij}) = \frac{1}{3}(\sigma_1+\sigma_2+\sigma_3)$ $t = \frac{1}{2}q\left[1+\frac{1}{K}-\left(1-\frac{1}{K}\right)\left(\frac{r}{q}\right)^3\right]$ $q = \sqrt{3J_2} = \sqrt{\frac{3}{2}s_{ij}s_{ij}} = \sqrt{\frac{1}{2}\left[(\sigma_1-\sigma_2)^2+(\sigma_2-\sigma_3)^2+(\sigma_3-\sigma_1)^2\right]} = \frac{3\tau_{oct}}{\sqrt{2}}$ $r = \left(\frac{27}{2}J_3\right)^{\frac{1}{3}} = \left(\frac{9}{2}s_{ij}s_{jk}s_{ki}\right)^{\frac{1}{3}} = \left(\frac{27}{2}J_3 - 9J_1J_2 + J_1^3\right)^{\frac{1}{3}}$ Cap yield surface: $F_c = \sqrt{(p-p_a)^2+\left[\frac{Rt}{(1+\alpha-\alpha/\cos\beta)}\right]^2} - R(d+p_a\tan\beta) = 0$ Shape of transition surface: $F_t = \sqrt{(p-p_a)^2+\left[t-\left(1-\frac{\alpha}{\cos\beta}\right)(d+p_a\tan\beta)\right]^2} - \alpha(d+p_a\tan\beta) = 0$ $p_a = \frac{p_b - Rd}{1+R\tan\beta}$	σ_{ij} = stress deviator tensor $\sigma_{1,2,3}$ = principal stresses s_{ij} = deviatoric stress tensor p = equivalent (hydrostatic) pressure stress t = measure of the deviatoric stress d = cohesion in p-t stress plane β = friction angle in p-t stress plane q = von Mises equivalent stress r = third stress invariant dependent variable K = material parameter that controls the dependence of the yield surface on the value of the intermediate principal stress τ_{oct} = octahedral shear stress J_1 = first invariant of deviator stress J_2 = second invariant of deviator stress J_3 = third invariant of deviator stress α = transition surface model parameter p_a = evolution parameter calculated from actual intersection of the cap surface and the shear failure surface p_b = hydrostatic compression yield stress parameter calculated as a function of volumetric plastic strain required to define the cap hardening/softening law R = material parameter that controls the eccentricity of cap surface

Compaction of soils is primarily associated with the yielding on the cap surface. As the load of the roller increases, the cap surface expands accordingly (see Figure C-12). The shear failure limit increases as the load limit increases with the same rate for different loading conditions. The inclination of the yield surface is affected only when the strength parameters such as the friction angle and cohesion are changed.

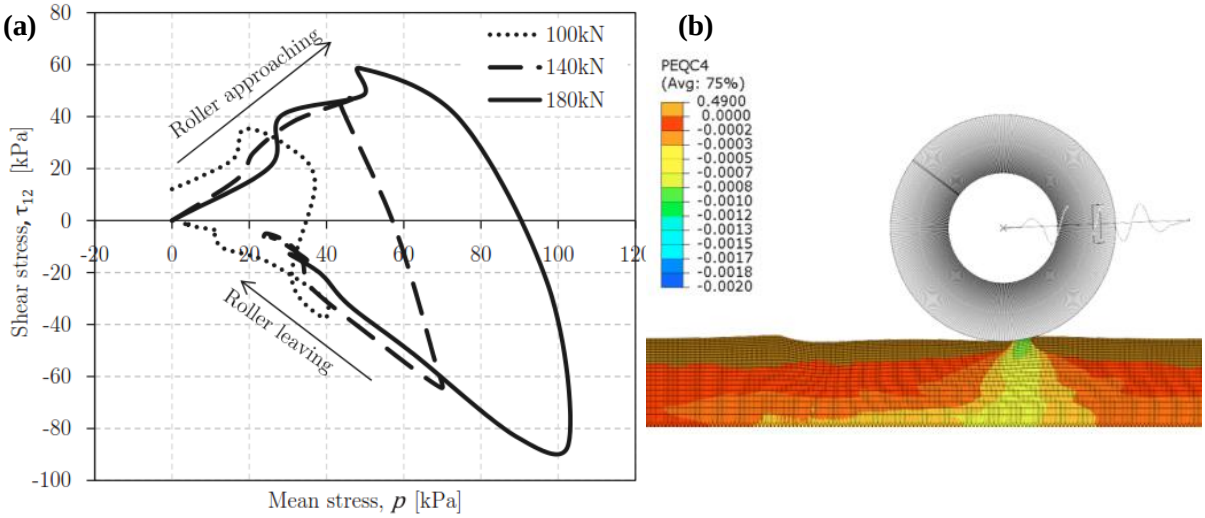

Figure C-12. (a) Stress path and evolution of the cap surface (Yesuf 2014) and (b) volumetric plastic strain distribution $\varepsilon_{vol,p}$ (compaction) based Drucker–Prager/cap model with R = 0.2.

Chiroux et al. (2005), Pistrol et al. (2012), Capraru et al. (2014) and Yesuf (2014) have used this model for simulation of the roller compaction with mixed results. Chiroux et al. (2005) compared the numerical soil response for a non-vibrating rolling wheel to corresponding experimental data. The authors pointed out that the soil rebounding not seen experimentally occurred in the numerical model. Pistrol et al. (2012) and Capraru et al. (2014) in their numerical simulations of oscillatory roller compaction of soil observed soil dilation due to the shearing during the compaction process, instead of an expected volume reduction.

Hypoplasticity

First developed by Kolymbas (1978), the existing hypoplastic models are able to describe the mechanical behaviors of the non-cohesive and cohesive soils (Gudehus, 1996; Niemunis and Herle, 1997). The hypoplasticity is a relation that associates the strain rate with the stress rate, where the nonlinear behavior of the hypoplastic law is modeled by the stress dependence of the stiffness (Erdmann and Adam 2014). The hypoplasticity assumes grains are aggregated to a *simple granular skeleton* defined by the following properties (Meißner et al. 2006; Niemunis and Herle 1997):

- state of a granular material is fully characterized by effective stress, σ, and by the void ratio only,
- grains maintain their size and general form during deformation,
- deformation of the granular skeleton is due to grain rearrangements,
- compression, abrasion and crushing of grains are negligible,
- surface effects such as capillarity, cemented bridges and osmotic pressure, are absent,
- change of the limiting void ratio with the mean pressure is related to the granular hardness,
- three pressure-dependent limiting void ratios can be distinguished, as shown in Figure C-13, where tr($\boldsymbol{\sigma}$) is the trace of the stress tensor, and h_s is the granular hardness.

The three pressure-dependent limiting void ratios, shown in Figure C-13 are:

- e_i = the upper bound of the simple granular skeleton and corresponds to maximum void ratio during the isotropic compression starting from the minimum density by pressure zero, $e > e_i$ suggests macropores and honeycomb formations;
- e_c = the critical void ratio; and
- e_d = the lower bound of the simple granular skeleton and corresponds to the minimum void ratio after a cyclic shearing with a small amplitude, $e < e_d$ suggest a masonry-like granular skeleton.

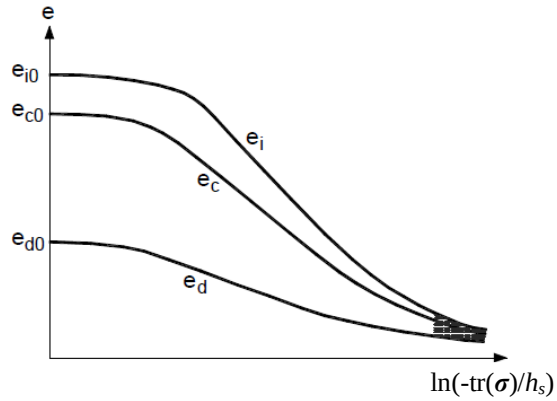

Figure C-13. Pressure-dependent void ratio by Meißner et al. (2006).

Change of the limiting void ratios with the mean pressure is related to a so-called granular hardness, h_s, which represents a reference pressure-independent stiffness of the soil and is the only dimensional constant in the hypoplastic equation.

This hypoplastic constitutive model is formulated as a single nonlinear tensor equation that yields the stress rate , called the Jaumann stress tensor, based on the rate of deformation tensor, d, and the current effective stress, σ, and void ratio, e, defined as

$$\dot{\sigma} = h(\sigma, d, e) = L(\sigma, e) : d + N(\sigma, e)\|d\| . \tag{C.15}$$

The hypoplastic model is decomposed in a linear or hypoelastic constitutive tensor L and a nonlinear constitutive tensor N. The derivations of these tensors are available in Niemunis and Herle (1997) and in Niemunis (2002).

Hügel et al. (2008) and Erdmann and Adam (2014) used a hypoplastic model for modeling the granular materials by incorporating it into a user-defined material subroutines UMAT for finite element (FE) modeling in ABAQUS. The constitutive model they implemented is based on the extended hypoplastic law with the intergranular strain proposed by Niemunis and Herle (1997) who introduced the concept of intergranular strains to model cyclic and dynamic problems. The extended hypoplastic model was developed to improve the small-strain performance after changes in the direction of the stress or strain path. A comparison of the extended to the traditional hypoplastic models for compaction of sand is provided in Figure C-14.

The extended hypoplastic constitutive model was adapted by Kelm (2003) for modeling the compaction of dry, non-cohesive soils using vibratory rollers. In his study, the vibratory roller left a zone of homogenized and compacted soil with a certain depth depending on the machine parameters and the initial state variables of the soil. His studies led to further implementation in the finite element (FE) modeling by Hügel et al. (2008) and Erdmann and Adam (2014). Erdmann and Adam (2014) compared the FE responses of a subgrade subjected to an 8,000 kg roller compactor under three modes of vibration: (1) static, i.e. non-vibrating compaction, (2) vertically excited roller compaction and (3) oscillatory excited roller compaction.

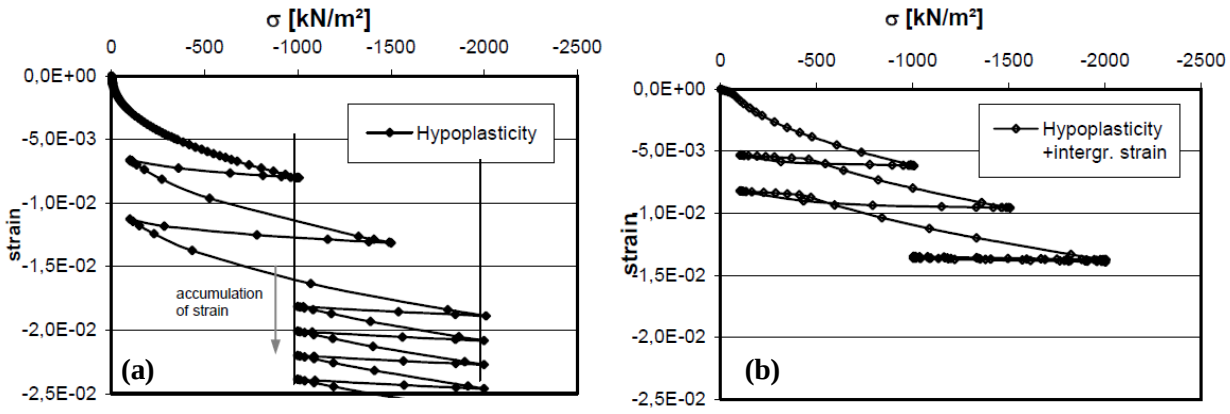

Figure C-14. Comparative of cyclic compression test with hypoplasticity (a) without integranular strain, and (b) with intergranular strain for cyclic loads by Meißner et al. (2006).

They found the vertically excited drum induced the highest stresses and caused the largest settlement in the subgrade, whereas the static and the oscillatory excited drums produced approximately similar stress values and pressure bulbs. They also found simulation calculations with an elastic soil provided comparable stress magnitudes and stress bulbs; yet, the point of load incidence in the contact area between drum and subgrade was different: the pressure bulb in soil modeled as an elastic material was located nearly right underneath the drum axis, whereas simulations with hypoplastic soils resulted in pressure bulbs occurring ahead of the vertical drum center plane due to the bow wave occurring in front of the drum-soil contact. Using the hypoplastic model, the drum provoked a material loosening in the top layer of the subgrade, a phenomenon that commonly appears in non-cohesive soils or in materials with a closely graded granulometric distribution.

Soil-Drum Contact Mechanics

The contact interaction between a rigid rolling cylinder (drum) and the soil surface depends mostly on the soil type and dynamic behavior of the drum (Yoo and Selig 1979; van Susante and Mooney 2008). Such interactions are better explained in terms of the contact width and the stress-strain paths at the contact area. Hertz (1882) presented the fundamental contact theory by addressing the contact of two elastic masses with curved surfaces. Based on those assumptions, the maximum contact width, *b*, is expressed as:

$$b = \sqrt{\frac{4F_c R}{\pi L_d E^*}} \tag{C.16}$$

where L_d is the length of the drum, R is the drum radius, F_c is the contact force and E^* is the composite modulus as determined by:

$$\left(E^*\right)^{-1} = \frac{1-\nu_d^2}{E_d} + \frac{1-\nu_s^2}{E_s} = \frac{1-\nu_s^2}{E_s} \tag{C.17}$$

where E_d is the modulus of the drum, E_s is the modulus of the soil, where $E_d >> E_s$ (i.e., steel drum is much stiffer than soil), ν_d is Poisson's ratio for the drum and ν_s is Poisson's ratio for the soil.

Such Hertzian contact concepts are based on a number of assumptions including the isotropy, homogeneity and linearly elastic behavior of two smooth and frictionless surfaces. A parabolic stress distribution is assumed at the contact area, as shown in Figure C-15. Figure C-16a depicts a photoelastic view of the stresses at the contact area between a rigid cylinder and an elastic half-space under both

tangential and normal forces. Figure C-16b represents a schematic of the soil-drum contact in which w_1 is the displacement of the last contact point and w_{max} is the displacement under the center of the drum.

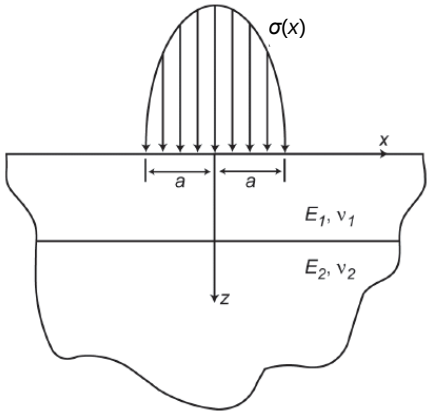

Figure C-15. Contact stress in layered media.

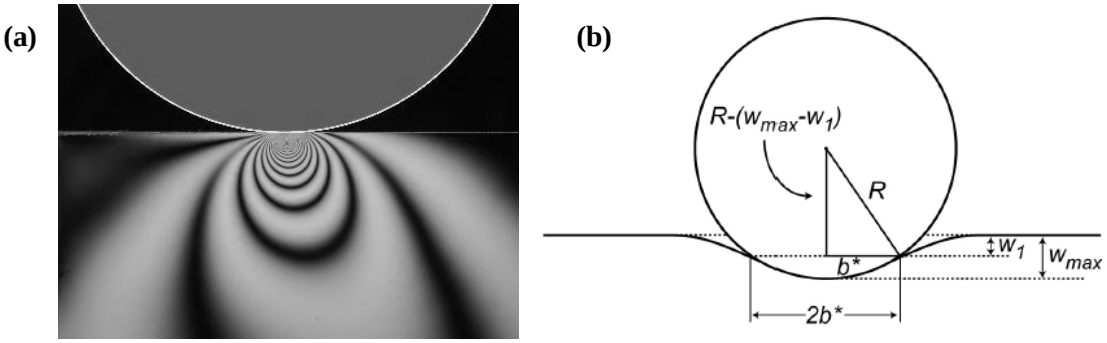

Figure C-16. (a) Visualization of stresses at contact area and (b) geometry of soil-drum contact (Musimbi et al. 2010).

Based on Hertzian contact theory, the relationship with surface contact stress distribution σ_c and the contact half-width b is given by

$$\sigma_c(x) = \frac{2F}{\pi b L}\sqrt{1-\frac{x^2}{b^2}} \cdot \tag{C.18}$$

The knowledge of the contact stress distributions and the contact width for a variety of soil types is necessary to accurately predict the stress fields (Mooney and Rinehart 2009; Rinehart et al. 2009). The forces and the motions of the soil and the drum are described by different sets of equations in the different phases. The loss of contact (i.e. decoupling of the drum from the soil) was first experimentally predicted by Quibel (1980), Machet (1980) and Kröber (1988) using the lumped-parameter modeling. Adam (1996) characterized the partial loss of contact when the drum decouples from the soil during a portion of a loading cycle, and "jump" mode (also referred to as double jump) when the drum loses contact with the soil more than once cycle of vibration.

Kopf and Erdmann (2005) used an iterative process to calculate the drum contact width, as well as stiffness and damping parameters, based on a cone-spring-damper model proposed by Kargl (1995). The relationship for determining the surface contact half-width for small depression based on the circular shape of the cross-section rolling approximated as a parabola is:

$$b = \sqrt{d \cdot z_{stat}} \ , \tag{C.19}$$

where d is the drum radius and z_{stat} is the static deflection calculated as

$$z_{stat} = \frac{\left(m_d + m_f + m_e\right) \cdot g}{k^p} \ , \tag{C.20}$$

where m_d is the drum mass, m_f is the mass frame, m_e is the eccentric mass, g is gravity, and k^p is a plastic parameter defined as

$$k^p = K \frac{\varepsilon}{1-\varepsilon} \ , \tag{C.21}$$

where ε is a ratio of the plastic z^p to cone-spring-damper model deflection elastic deformation z_0 as

$$\varepsilon = \frac{z_0}{z_0 + z^p} = \frac{k^p}{k^p + K} \ , \tag{C.22}$$

where both deformations are defined as

$$z^p = \frac{F_{\max}}{k^p} \ \text{ and } \ z_0 = \frac{F}{K} \text{, respectively.} \tag{C.23}$$

Both deformations are calculated using the contact force F, the previous cycle maximum force F_{max} and stiffness K defined as

$$K = \frac{G \cdot b}{1-\nu}\left[3.1\left(\frac{a}{b}\right)^{0.75} + 1.6\right], \tag{C.24}$$

where a is the drum length and G is the shear modulus.

Rinehart et al. (2009) studied the stress and strain paths during the vibratory soil compaction and compared them to the laboratory resilient modulus results. The study was conducted on a uniform embankment layer as well as on a two-layer soil system. The stress profile was concluded to be dependent on the soil-drum contact width. However, with the presence of a thick base layer (compared to the contact width), the contact area became less affected by the elastic modulus of the layer. Using BEM, they observed the traditional Hertzian methods underpredicted the drum-soil contact widths. Musimbi et al. (2010) compared the results of an iterative BEM approach with the results of the Hertzian theory application and a field investigation on different types of layered soils to study the drum-soil contact width. They found that, the Hertzian theory better predicted the contact width for granular materials as compared to clayey soils due to low elastic modulus of clay. Considering a layered system (consisting of base and subgrade layers), they found the base thickness has an influence on the contact width when the base material is quite soft relative to subgrade ($E_1/E_2 < 0.5$), while for stiffer (granular) base materials, the contact width is nearly independent of base thickness.

A third approach to study the drum-soil contact width using discrete element modeling (DEM) method has been recently attempted. Asaf et al. (2006) used DEM to simulate the interaction between a rigid wheel and the soil surface. They concluded that the DEM provided reasonable results on contact mechanics as compared to the other theoretical and experimental studies. Khot et al. (2007) used DEM to investigate the dynamic soil-wheel interaction. Their study focused on the surface displacement caused by a wheel passing and did not go as far as to investigate the stress fields in the contact width. Buechler et al. (2012) employed DEM to study the contact mechanism of a static drum on the soil surface. Their predicted contact widths with the DEM analyses were greater than those predicted by the Hertz theory and were close to the BEM results predicted by Rinehart et al. (2009). The authors also found that granular soils exhibited greater contact widths as compared to the cohesive soils.

Estimation of Mechanical Properties using Intelligent Compaction (IC)

In conventional construction, the earth material is compacted by a number of passes of a roller at ideally a constant speed, and at a constant vibrating frequency and amplitude. Given the nature of the construction environment, these parameters will be variable even when an experienced and conscientious roller operator is used. The heterogeneity of the final product due to the variations in the index properties of compacted material (gradation, soil composition, and moisture content), and the stiffness/condition of the underlying layer is inevitable. While some areas will be sufficiently compacted, other areas may be either insufficiently compacted or over-compacted. In the context of estimating the material properties in a practical and realistic matter, one should always be aware of these uncertainties.

The descriptions of the roller measurement values are discussed in detail in Mooney et al. (2010). The different data measurement values used for compaction control are listed in Table C-12. The ratio between the amplitude of the first harmonic and the amplitude of the excitation frequency was first correlated to the stiffness of the soil as measured by dynamic plate load tests (Thurner and Forsblad 1978). Thurner and Sandström (1980) introduced the compaction meter value (CMV). Since then, various measuring systems have been implemented by the roller manufactures. Bomag first introduced the OMEGA value and the Terrameter measuring system in 1982, followed by the vibration modulus E_{vib}, a measure of dynamic soil stiffness (Ferris 1985; Floss et al. 2001; Kröber et al. 2001). Ammann introduced the ACE (Ammann Compaction Expert) that calculated the soil stiffness parameter k_s (also called k_B) in 1999 (Anderegg and Kaufmann 2004; Anderegg 1998).

Table C-12. Commercially available roller measurement values (Mooney et al. 2010).

Measurement Value	Manufactures	Parameters Used	Relations Used
Compaction Meter Value (CMV)	Dynapac, Caterpillar, Hamm, Volvo	Ratio of vertical drum acceleration amplitudes at fundamental vibration frequency and its first harmonic	$CMV = c\frac{A_{2\Omega}}{A_{\Omega}}$ where c is constant around 300, $A_{2\Omega}$ is the amplitude of second harmonic, A_{Ω} is amplitude of fundamental frequency
Compaction Control Value (CCV)	Sakai	Algebraic relationship of multiple vertical drum vibration amplitudes, including fundamental frequency, and multiple harmonics and sub harmonics	$CCV = \left[\frac{A_1 + A_3 + A_4 + A_5 + A_6}{A_1 + A_2}\right] \times 100$ where A_i are amplitudes at the excitation frequencies
Stiffness, k_s (k_b)	Ammann	Vertical drum displacement, drum-soil contact force	$k_s = \Omega^2\left[m_d + \frac{m_0 e_0 \cos\phi}{z_d}\right]$ where m_d is drum mass, m_0e_0 is eccentric mass moment, ϕ is phase angle, z_d is drum displacement, Ω is frequency
Vibration Modulus, E_{vib}	Bomag	Vertical drum displacement, drum-soil contact force	$z_d = \frac{2(1-\nu^2)}{\pi \times E_{vib}} \times \frac{F_s}{L} \times \left(1.8864 + \ln\frac{L}{b}\right)$ where F_s is drum-soil interaction force, L is the drum length, b is contact width, ν is Poisson ratio, z_d is drum displacement
Machine Drive Power (MDP)	Caterpillar	Difference of gross power and the power associated with sloping grade and machine loss	$MDP = P_g - WV\left[\sin\theta + \frac{a}{g}\right] - (mV + b)$ where P_g is gross power, W is roller weight, a is acceleration, g is acceleration due to gravity, θ is slope angle, V is roller velocity, m and b are internal loss coefficients

Mechanistic ICMVs

The introduction of E_{vib} and k_s signaled an important evolution toward the measurement of more mechanistic, performance-related soil properties (e.g., soil stiffness/modulus). These two ICMVs are determined from the force-displacement hysteresis loops. The hysteresis loops are interpreted from the drum acceleration time histories collected by the IC rollers. The force-displacement loops are created by plotting the time-varying contact force, F_c, versus time-varying drum displacement, z_d, where contact force is calculated from the vertical response of the drum.

Ammann ACE system calculates the secant soil stiffness, k_s, from the gradient of the line passing through the point of zero dynamic displacement (i.e., displacement due to the static weight of the roller) to the point representing the maximum dynamic drum displacement, as shown in Figure C-17 (Anderegg and Kaufmann 2004; Mooney et al. 2010). To determine these parameters, the system takes advantage of the lumped-parameter model introduced in Figure C-3. That model consists of a roller and a 2DOF model representing the vertical kinematics of the drum-frame system. The drum/soil contact force F_s consists of the machine weight, the eccentric force and the drum and frame inertias. Ammann system determines the drum inertia and the eccentric force by measuring the vertical drum acceleration and eccentric mass position, while the frame inertia is neglected.

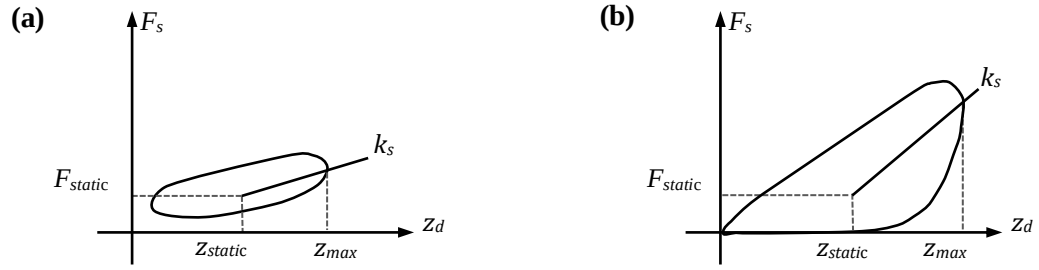

Figure C-17. Secant stiffness during (a) contact and (b) partial loss of contact (Mooney et al. 2010).

The vertical drum displacement amplitude, z_d, is determined by the spectral decomposition and integration of the measured peak drum accelerations (Anderegg and Kaufmann 2004). Secant stiffness, k_s, is calculated from

$$k_s = \Omega^2 \left[m_d + \frac{m_0 e_0 \cos\phi}{z_d} \right], \tag{C.25}$$

where m_d is the drum mass, m_0e_0 is the eccentric mass moment, Ω is the excitation frequency and ϕ is the phase lag between the eccentric mass and the drum displacement.

Similar to the Ammann's ACE system, the Bomag Variocontrol system makes use of the force-displacement hysteresis curves to determine the tangent stiffness, as shown in Figure C-18 during the process of calculating a "vibration modulus," E_{vib}. Tangent stiffness is defined as the slope to the force-displacement loop at locations of 80% and 20% of the difference between the maximum and minimum contact forces (Mooney et al. 2010).

In addition, Bomag makes use of the Lundberg's (1939) theoretical static solution for a rigid cylinder resting on a homogeneous, isotropic, elastic half-space, to develop a relationship for determining drum displacement, z_d, as

$$z_d = \frac{2\left(1-\nu^2\right)}{\pi \times E_{vib}} \times \frac{F_s}{L} \times \left(1.8864 + \ln\frac{L}{b} \right), \tag{C.26}$$

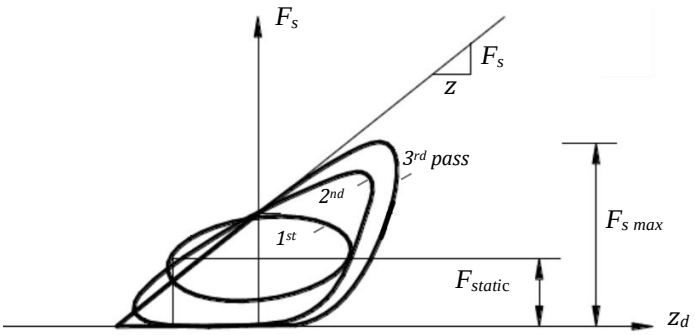

Figure C-18. Calculation of tangent stiffness at different roller passes (Mooney et al. 2010).

where F_s is the drum-soil interaction force, L is the drum contact width, v is the Poisson ratio (assumed as 0.25 for soil), and b is the drum radius as calculated by

$$b = \sqrt{\frac{16 \times R \times \left(1-\nu^2\right)}{\pi \times E \times L} \times F_s} \tag{C.27}$$

where E is the modulus of the half-space, and R is the drum radius. The Variocontrol system determines the appropriate E_{vib} via an iterative approach based on the relationship

$$\frac{\Delta F}{\Delta z_1} = \frac{\pi L E_{vib}}{2\left(1-\nu^2\right) \times \left\{2.14 + 0.5 \times \ln\left[\frac{\pi L^3 E_{vib}}{\left(1-\nu^2\right) \times 16 \times \left(m_e + m_d + m_f\right) \times R \times g}\right]\right\}}, \tag{C.28}$$

where m_e is the excitation mass, m_d is the drum's mass, and m_f is the frame mass, and g is the acceleration of gravity. The relationship between contact force and drum displacement based on E_{vib} on an elastic half-space is illustrated in Figure C-19.

Kröber et al. (2001) list the benefits of the compaction indicator value E_{vib} as being:

- relatively independent from the amplitude, frequency, and working speed of the roller.
- allows for a direct determination of the soil stiffness in the form of the vibration modulus E_{vib} during the compaction process, and
- directly related to the first and second loading modulus values (E_{v1} and E_{v2}) obtained from the two-cycle plate load tests.

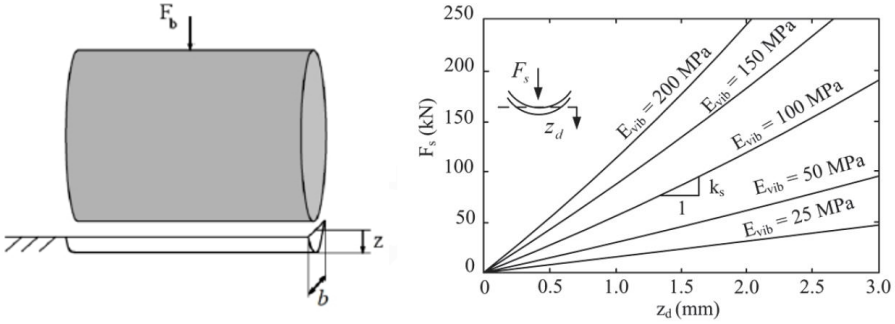

Figure C-19. Drum on elastic half-space and relationship between contact force and drum displacement on an elastic half-space (Mooney and Adam 2007; Hager 2015).

Summary of IC Measurements and Correlation Analysis Studies

Several studies have been carried out to evaluate the roller measurement values for the compaction quality management of different pavement layers and embankment soils. Research has also been carried out to correlate the roller measurement values with the in-situ point test measurements. measurements. Table C-13 summarizes the various studies and their significant findings.

Table C-13. Summary of IC measurements for quality control and in-situ correlations.

Reference	Objective and Scope	Key Findings/Comments
White et al. (2005)	Evaluated the utilization of intelligent rollers in real-time compaction monitoring. A pilot field study was carried out in Illinois on a cohesive glacial till soil. Spot measurements of density, moisture content, and DCP and Clegg impact hammer values were correlated to roller measurement values.	The variation in MDP was observed to be the result of inherent soil and moisture variations in the compacted layer. The compaction effort was found to be significant only up to a depth of 40 cm. Consideration of moisture content in the regression analysis resulted in a better understanding of measurements.
White et al. (2006)	Evaluated the relationship between machine drive power and measures of soil compaction at a test section in Peoria, Illinois. Two moisture contents were adopted. Vibratory pad foot roller was used. Well-graded silty sand was evaluated with nuclear gauge, moisture meter and DCP.	Demonstrated the use of machine drive power as a tool for compaction control. Variability of the DCP index reduced with increase in the roller passes.
Anderegg et al. (2006)	Demonstrated the compaction monitoring using single drum vibratory intelligent compactor.	Linear relation with high correlation was established between moduli from the plate bearing tests and roller measurement values.
Mooney et al. (2006)	Investigated the influence of heterogeneity on vibratory roller compactor response in Colorado. Lift thickness and moisture content were also considered along with varying depth to bedrock. A double smooth drum roller was used. The soil type was a poorly graded sand (A-1-b) and DCP was used for the point measurements.	Roller parameters found to be sensitive to the underlying stiffness when operated near resonance. At higher frequencies the roller parameters were insensitive to the changes in the underlying soil conditions.
Hossain et al. (2006)	Demonstrated intelligent compaction control concepts in identifying soft spots in Kansas. The relation of the roller-measured stiffness with density and moisture content was established. A single drum vibratory roller was used. Soil type was clayey sand and nuclear gauge, moisture meter and DCP were used for point measurements.	Poor correlation was observed between the roller measurement values and the CBR from DCP due to empirical nature. The target stiffness values needs to be function of the dry density since both high and low densities results in lower IC roller stiffness. Authors also showed the limitations of QC based on dry density alone.
Petersen and Peterson (2006)	Compared CMV with the point test measurements such as LWD, DCP and Geogauge	The roller measurements vary greatly with point measurements. The variation in the roller measurements is due to the difference in the area of the measurements between drum and sensors of spot tests, and the response is influenced by moisture, material and support
Rahman et al. (2007)	Studied the use of subgrade stiffness obtained from the IC technology using Bomag single smooth steel drum variocontrol intelligent roller. Three sections were considered in Kansas.	Demonstrated the potential benefits of the IC technology in identifying less stiff areas. Revealed the sensitivity of the roller measurements to moisture content variation.
Mooney and Rinehart (2007)	Explored relationship between vibration characteristics and soil properties in a test section in Denver. Double drum smooth intelligent compactor was used.	Heterogeneity causes significant challenge to vibration based assessment of soil properties. Roller measurements for QC/QA were found to be influenced by the stress-dependent nature of soil.

Table C-13, cont. – Summary of IC measurements for quality control and in-situ correlations.

Reference	Objective and Scope	Key Findings/Comments
White and Thompson (2008)	Evaluated compaction meter value and machine drive power with five different types of sub-base materials including RAP in Illinois. Single drum intelligent roller with Clegg Impact tester, SSG, LWD, DCP and PLT were used as compaction control tools.	Machine drive power was observed to be more variable as compared to compaction meter value. Multivariate analyses may be used to relate the roller-measured values and in-situ point test values.
White et al. (2011)	Review of the field assessment studies and examining the factors influencing roller measurement values, correlations between the spot-test measurements and spatial uniformity.	Roller measurement values are highly influenced by the variability of soil properties across the width of roller drum and moisture content. Establishing the target values, acceptance limits, correlations between field measurements being technology specific and based on local experience are the potential limitations of existing IC specifications.
Rahman et al. (2012)	Developed correlations between the in-situ measurements and roller measurement values in Kansas. Single drum intelligent roller was used along with nuclear gauge, SSG, LWD, DCP and PLT.	The change in layer modulus with depth is a potential source of problem to compare stiffness and modulus results from different test and roller measurement values.
Rinehart et al. (2012)	Evaluated the European CCC specifications on a pilot project in Colorado. Pilot study was implemented on a 30 cm thick sub-base, of 12 m width and 300 m long. Dynapac roller was used in the study.	Lowering the acceptance criteria using spot-test results on the weak areas identified through roller-based measurement values. For process and acceptance control, additional analysis beyond correlation is needed to establish roller compaction target values.
White et al. (2013)	Evaluated 16 sections of stabilized pavement foundations covering 4.8 mi, with ground conditions ranging from soft to very stiff using FWD, LWD, and roller-integrated compaction monitoring systems.	The CMV values correlated better with LWD and FWD values than with MDP values. CMV values correlated better with FWD values than with LWD values.
	CBR - California Bearing Ratio RAP - Reclaimed Asphalt Pavement CCC - Continuous Compaction Control SSG - Soil Stiffness Gauge	LWD - Light Weight Deflectometer DCP - Dynamic Cone Penetrometer PLT - Plate Load Test

Table C-14 summarizes the findings from selected studies in use of the IC in quality control and acceptance testing.

Current Backcalculation Techniques of Mechanical Properties

Table C-15 summarizes the static and dynamic backcalculation methods for prediction of pavement moduli. ANN-based pavement backcalculation models are summarized in Table C-16.

Table C-14. IC in quality control and quality acceptance testing.

Reference	Findings
White et al. (2005)	Statistical analysis of the data help to reduce the IC measurement variations, position error and explains the underlying support conditions
Hossain et al. (2006)	By continuous nature of stiffness measurements by IC rollers, it is possible to identify soft spots during production control and acceptance testing
Mooney and Rinehart (2007)	The IC roller identified the weak areas that were not identified by a static proof roll test during acceptance testing
White et al. (2008)	The variations in the RMVs are important for interpreting layered soil conditions
Gallivan et al. (2011)	Minimal or inconsistent rolled areas are easily identified when IC roller is used for production control
Rahman et al. (2012)	Variability in soil properties is reduced when IC roller is used for production process. Proof rolling using an IC roller identified poorly compacted locations. High variability in the stiffness measurements within a short distance contradicts the concept of uniform compaction using IC rollers
Heersink et al. (2013)	Improved IC and QA of compaction process using a sequential, spatial back-fitting of RMVs coupled with multiresolution scale space analysis to generate estimates of compaction level
Cai et al. (2015a)	Correlations between IC CMV and MDP to DCP, LWD and FWD, confirm the promise of IC for reducing sampling requirements for acceptance criteria but not entirely replacing current QA sampling

Table C-15. Static and dynamic backcalculation using parameter identification, database and genetic algorithms for prediction of pavement moduli.

Reference	Findings
Ledesma et al. (1994)	Used a coupled FEM and Levenberg–Marquardt optimization technique for the parameter and variance estimation in geotechnical backanalysis using prior information in static case.
Fwa et al. (1997)	Developed a GA-based backcalculation program which performed comparably against EVERCALC and EVERCALC-Alt (nonlinear least-squares optimization), MICHBACK (modified Newton's optimization) and MODULUS (database) backcalculation programs. The GA-based program was able to process a large number of possible solutions in the form of string structures and in its global search ability.
Kang (1998)	Developed a frequency domain backcalculation program (BKGREEN) based on the forward program GREEN. It models the pavement as a layered elastic system in terms of dynamic Green flexibility influence functions.
Al-Khoury et al (2001)	Used mixed spectral and poroelastic spectral element methods together with the factored Secant update, modified Levenberg–Marquardt and Powell as the three different minimization algorithms, for the dynamic parameter identification of multi-layered systems in frequency domain.
Wang et al. (2001)	Proposed a static inverse method for determining the material properties of a multi-layer medium using the boundary element and the modified Levenberg–Marquardt optimization technique.
Dong et al. (2002)	Proposed a hybrid FE and modal superposition technique for the dynamic analysis of multi-layer half-space. In addition, they used the truncated singular value decomposition method as an optimization tool to calculate the essential parameters of the problem.
Feng et al. (2004)	Used FEM and integration of evolutionary Support Vector Machines (SVM) and GA optimization techniques to introduce a static displacement backanalysis procedure for identifying the mechanical and geomaterial parameters.
Reddy et al. (2004)	Optimal GA parameters for backcalculation of pavement layer moduli were conducted based on the level of accuracy desired and the corresponding computational effort.
Alkasawneh (2007)	Developed Dynamic Parameterless Genetic Algorithm (DPGA) to study the interaction between the genetic operators and parameters and their effect on the backcalculation process. BackGenetic3D program developed for backcalculation of pavement moduli with any arbitrary number of layers, loading conditions, and loading configurations.

Table C-15, cont. – Static and dynamic backcalculation using parameter identification, database and genetic algorithms for prediction of pavement moduli.

Reference	Findings
Levasseur et al. (2009)	Used FEM and GA optimization for the identification of soil constitutive parameters from the static geotechnical measurements.
Hadidi and Gucunski (2010)	Presented a comparative study between the static and dynamic backcalculation of multi-layer half-spaces. Static backcalculation methods for parameters estimation of half-spaces in which dynamic measured response are used as input data are unreliable.
Park et al. (2010)	Developed backcalculation program, GAPAVE, using the GA coupled with FEM, to predict layer moduli from FWD deflections. Optimal GA parameters selected from sensitivity analysis for six different pavement structures.
Pekcan et al. (2010)	Developed and implemented GA and ANN with a structural pavement model based on FEM to backcalculate pavement layer properties as well as determining thickness of full depth asphalt pavements using results of FWD test.
Saltan et al. (2011)	Backcalculation of pavement layer moduli and Poisson's ratio using data mining (DM) method of asphalt pavement from synthetically derived FWD.
Kargah-Ostadi and Stoffels (2013)	Developed effective and reliable Restart Covariance Matrix Adaptation (RCMA) backcalculation (BC) strategy with attention to variable layer thicknesses. An RCMA Evolution Strategy (CMA-ES) was implemented to minimize error between ANNs (forward process) and FWD-measured deflections. RCMA-BC method proved effective and reliable in backcalculating moduli and surface layer thickness but failed to predict base thickness because the forward calculation routine does not have significant sensitivity to this parameter.
Maina et al (2013)	Evaluated static and dynamic backcalculation of FWD responses of inverted pavements structures.
Rabaiotti et al. (2013)	Levenberg–Marquardt and Mesh Adaptive Direct Search (MADS) algorithms implemented for inverse analysis procedure based on 3D deflection bowl matching. Eight to nine stiffness parameters, in particular Young's moduli and Poisson ratio for four layers, or pressure-dependent stiffness for three layers, depending on the adopted constitutive model, can be back calculated with a convergent procedure.
Senseney et al. (2013)	Conventional backcalculation of layer parameters from LWD deflections is formulated as an inverse problem where predicted vertical deflections are matched to observed vertical deflections using a dynamic FE model for the forward calculation of LWD deflection data and GA as the inverse solver. Top-layer thickness, top-layer modulus, and underlying modulus for the experimental data compare favorably with expected values.
Tang and Yang (2013)	Developed inverse analysis procedure that combines the dynamic FE analysis and GA to determine the pavement layer structural properties. An LWD was used to infer the moduli of instrumented three-layer scaled flexible pavement models. Recorded time histories of the LWD load were used as the known inputs while the measured time histories of surface and subgrade deflections measured with LVDTs were considered as outputs.
Sanggaleh et al (2014)	Presented a detailed study on two objective functions applied to a two-layer pavement model containing measurement errors. These were the Root Mean Square (RMS) and the Area Value Correction Factor (AVCF), the latter based on the AREA algorithm extensively used to analyze concrete pavement deflection basins. They found AVCF to be efficient and accurate in backcalculation of pavement modulus and thickness, even when measurement errors are present, unlike RMS which is sensitive to measurement errors.
Vosoughi et al. (2014)	Developed inverse algorithm for the estimation of dynamic surface responses using hybrid finite element (FE)–incremental differential quadrature (IDQ) method together with the discrepancy principle and the conjugate gradient method (CGM).
Xu (2014)	Developed computational method to invert dynamic moduli of multi-layer systems with applications to flexible pavements under FWD tests. Author first developed an FE and Newton-Raphson method to invert layer elastic moduli using FWD data. Then improved the moduli seeds estimation based on Monte Carlo simulations, addressing the common backcalculation issue of no unique solutions. Developed PDE-constrained Lagrangian optimization method used to invert dynamic moduli and viscoelastic properties of multi-layer systems.

Table C-15, cont. – Static and dynamic backcalculation using parameter identification, database and genetic algorithms for prediction of pavement moduli.

Reference	Findings
Cai et al. (2015b)	Developed a system identification (SID) inverse method to invert the elastic moduli in isotropic and cross-anisotropic layered pavements based on the deflection data from FWD using a forward calculation based on a propagating matrix method in terms of the cylindrical system of vector functions.

AVCF – Area Value Correction Factor
CGM – Conjugate Gradient Method
DM – Data Mining
DPGA – Dynamic Parameterless Genetic Algorithm
FEM – Finite Element Model (Method)
FWD – Falling Weight Deflectometer
ES – Evolution Strategy
GA – Genetic Algorithm
IDQ – Incremental Differential Quadrature
LVDT – Linear Variable Differential Transformers
LWD – Light Weight Deflectometer
MADS – Mesh Adaptive Direct Search
PDE – Partial Differential Equation
RCMA – Restart Covariance Matrix Adaptation
RMS – Root Means Square
SID – System Identification
SVM – Support Vector Machines

Table C-16. Adaptive methods for backcalculation of pavement responses and mechanical properties of pavement layered systems.

Reference	Findings
Meier and Rix (1994)	Applied ANN for the SASW test data inversion and backcalculation of flexible pavement layer properties.
Meier and Rix (1995)	Verified susceptibility of ANN methodology for pavement moduli backcalculation utilizing FWD data.
Tutumluer and Seyhan (1998)	Feed-forward ANN trained to predict horizontal and shear moduli responses in a repeated load triaxial test using confining pressure, applied deviator stress, measured vertical deformation, and two aggregate properties as input variables.
Ferregut et al. (1999)	Developed a methodology based on ANN techniques to estimate the remaining life of flexible pavements given the occurrence failure (rutting and fatigue cracking). ANN techniques were also used to develop models to predict the critical strains at the interfaces of the pavement. Inputs to all the models are the best estimates of the thickness of each layer and the surface deflections obtained from a FWD test.
Kim et al. (2000)	Predicted depth to a stiff layer and layer moduli using a series of ANNs using numerical solutions of a multi-layered half-space based on Hankel transforms as a forward model.
Melchor-Lucero et al. (2002)	Developed a software tool that integrates ANN technology, functional condition of pavement, uncertainty analysis and traffic information to predict a probabilistic pavement performance curve. ANN models predict critical strains at layer interfaces, using readily available data such as the best estimates of each layer thickness and surface deflections from a FWD test, eliminating backcalculation.
Saltan (2002)	Neuro-Fuzzy method used for simulation of FWD deflection basin implemented in backcalculation procedure for calculation of each pavement layer elastic modulus.
Nazarian et al. (2004)	Improved inversion process for rapid reduction of Spectral Analysis of Surface Waves (SASW) data by implementing ANN models to estimate thickness of modulus of pavement layers. Reduction algorithm proved to be robust and yielded consistent results in almost real time.
Göktepe et al (2005)	Multi-Layer Perceptron (MLP) and Adaptive Neuro-Fuzzy Inference System (ANFIS) methodologies employed for backcalculation of flexible pavements. MLP proved better choice if sufficient amount of data exists to characterize the target behavior; otherwise, ANFIS preferred due to its ability of fuzzy logic which manages uncertainty. ANFIS can be employed when considerable amount of uncertainty or having incomplete data.
Saltan and Terzi (2005)	ANN and Gene Expression Programming (GEP) used in backcalculating the pavement layer thickness from deflections measured on the surface of the flexible pavements. Though ANN gives more realistic results than GEP, the latter approach can be selected in order to obtain only one formula.

Table C-16, cont. – Adaptive methods for backcalculation of pavement responses and mechanical properties of pavement layered systems.

Reference	Findings
Sharma and Das (2008)	Backcalculated the pavement layer moduli using synthetically derived FWD normal and noisy deflections and concluded trained ANNs in backcalculation would give more reliable and accurate results than other methods.
Nazarian and Abdallah (2009)	Implemented ANN model to estimate thickness and pavement layer moduli for FWD and Seismic Pavement Analyzer (SPA).
Gopalakrishnan (2010)	Developed a hybrid ANN-PSO (Particle Swarm Optimization) approach, a population-based stochastic optimization technique, applied to inversion of pavement NDT deflection data for real-time backcalculation of flexible pavement layer moduli.
Pekcan et al. (2010)	Developed and implemented GA and ANN with a structural pavement model based on FEM to backcalculate pavement layer properties as well as determining thickness of full depth asphalt pavements using results of FWD test.
Gopalakrishnan and Papadopoulos (2011)	Employed a novel machine learning concept called Conformal Prediction (CP) in pavement backcalculation. A Neural Networks Regression-Inductive Conformal Prediction (NNR-ICP) approach is used to derive a decision rule for the inverse prediction of nonlinear pavement layer moduli from Non-Destructive Test (NDT) deflection data. A CP is then implemented for the NNR decision rule and tested on an independent data set to demonstrate its error calibration properties. CP can be used to derive reliable pavement moduli predictions without compromising the accuracy of the NNR decision rule but with control of the risk of error.
Nazarian et al. (2014)	ANN model developed to estimate the LWD target moduli for two-layer pavement systems as a function of Poisson's ratios and resilient modulus constitutive model nonlinear parameters (k_1, k_2, k_3) of both layers, surface stress, and the thickness of the top layer.
Tarawneh and Nazzal (2014)	Evaluated the use of regression analysis and ANN to develop models to accurately predict the subgrade resilient modulus design input value using FWD test results. Soil properties such as clay content, maximum dry density and liquid limit appeared as significant model predictors.

ANFIS – Adaptive Neuro-Fuzzy Inference System	LVDT – Linear Variable Differential Transformers
ANN – Artificial Neural Network	LWD – Light Weight Deflectometer
CP – Conformal Prediction	MLP – Multi-Layer Perceptron
FEM – Finite Element Model (Method)	NDT – Non-Destructive Testing
FWD – Falling Weight Deflectometer	NNR – Neural Network Regression
GA – Genetic Algorithm	PSO – Particle Swarm Optimization
GEP – Gene Expression Programming	SASW – Spectral Analysis of Surface Waves
ICP – Inductive Conformal Prediction	SPA – Seismic Pavement Analyzer

Backcalculation Methods in IC Technology

Mooney and Facas (2013) evaluated different backcalculation processes for determining layer moduli with a forward process that made use of a static boundary element (BE) model simulating roller compaction. The forward process predicted the stiffness over a wide range of two-layered pavement structures with different layer moduli and top-layer thicknesses, as shown in Figure C-20.

The secant method was used to backcalculate the top-layer modulus, E_1, by finding the zero of the difference between the measured and model-predicted stiffness given by the error function F_{err},

$$F_{err}\left(E_1\right) = k - f_1\left(E_1\right), \tag{C.28}$$

where f_1 is a function of E_1 while E_2 and h_1 are assumed known. E_1 is determined as

$$\left[E_1\right]_{i+1} = \left[E_1\right]_i - \frac{\left[E_1\right]_i - \left[E_1\right]_{i-1}}{F_{err}\left(\left[\left[E_1\right]_i\right]\right) - F_{err}\left(\left[E_1\right]_{i-1}\right)} F_{err}\left(\left[E_1\right]_i\right), \tag{C.29}$$

where i is an integer for the current iteration and $[E_1]_i$ is the value of E_1 after the i^{th} iteration.

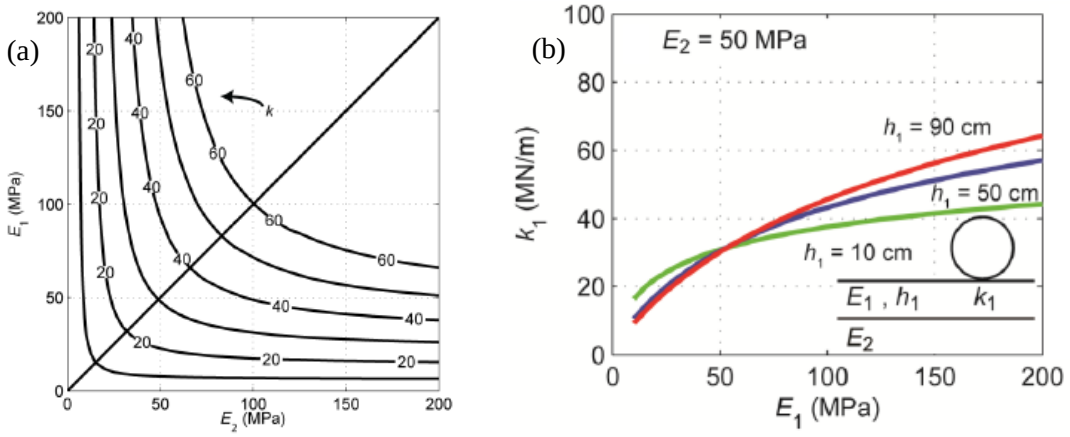

Figure C-20. Comparison of simulated stiffness, k, values from BE analysis for a two-layer system with (a) bottom layer modulus, E_2, vs. top-layer modulus, E_1, and top-layer thickness h_1 = 30 cm, and (b) k vs. top-layer modulus, E_1, for variable top-layer thickness, h_1 (Mooney and Facas, 2013).

Mooney and Facas found this approach time intensive, as each inversion required 5 to 15 iterations, and each iteration required forward modeling. To increase the efficiency of the backcalculation process, they used direct inverse models created through regression analyses to substitute the simulations in the forward model in the backcalculation process. They evaluated the following three regression models from the training data created using a BE response model: (1) a database with local tri-cubic (LTC) interpolation, (2) a 9th order polynomial fit regression model and (3) an artificial neural network (ANN). The authors found that all models were able to simulate the responses with acceptable error.

The three regression models were also used for the backcalculation of the top-layer modulus, E_1. The LTC database method yielded the lowest maximum error of 4%, though when considering the 99th percentile, the 9th order polynomial method performed better than the LTC database method. Their investigation revealed that uncertainty in backcalculated layer modulus increased as the top-layer thickness, h_1, decreased and/or as the layer modulus ratio, E_1/E_2, increased.

Approaches and Limitations in Quality Management of Compacted Geomaterials with IC Technology

A number of DOTs have been developing specifications for mainstream earthwork projects. Mooney et al. (2010) propose six options to incorporate IC in the United States as summarized in Table C-17.

According to Mooney et al. (2010), implementing these options as performance-based specifications is possible but challenging. They state that:

> "The extraction of mechanistic material parameters using roller-based measurements for performance-based specifications consistent with mechanistic-empirical-based design (e.g., AASHTO 2007 Pavement Design Guide) is possible but challenging. The extraction of appropriate parameters must account for the three-dimensional nature of the roller/soil interaction, the influence of layers, the nonlinear modulus of each involved material, and the dynamics of the drum/soil interaction."

The contractors, however, should be rewarded for adopting good construction practices, such as rigid process control on the compaction, moisture and gradation of the materials. Implementing IC in their day-to-day operation is one such good practice for the DOTs to consider.

A number of agencies in the United States has adopted specifications for quality management of geomaterials with the IC technology. Table C-18 includes a summary of these specifications.

Table C-17. Summary of specifications options (Mooney et al. 2010).

Roller-Integrated CCC QA Option	Target Measurement Value (MV-TV)	Acceptance Criteria
Option 1: Spot testing of roller-informed weakest area(s)	Not required	Spot-test measurements in roller-identified weakest area(s) satisfy contract spot-test measurement requirement (QA-TV)
Option 2a: Monitoring percentage change in mean MV	Not required	Achieving ≤ 5% change in mean MV between consecutive roller passes
Option 2b: Monitoring spatial percentage change (%Δ) in MVs	Not required	Achieving the %Δ-TV between consecutive passes over a defined percentage of an evaluation section
Option 3a: Empirically relating MVs to spot-test measurements	Based on correlation of MV to spot-test measurement: MV-TV=MV corresponding to contract QA-TV[a]	Achieving MV-TV over a set percentage of an evaluation section
Option 3b: Compaction curve based on MVs	MV-TV=mean MV when the increase in pass-to-pass mean MV in a calibration area ≤ 5%	
Option 3c: Empirically relating MVs to lab-determined properties (e.g. M_r)	Based on correlation of MV to lab soil property: MV-TV=MV corresponding to contract QA-TV[b]	

Note: [a]QA-TV is spot-test-based measurement of density, modulus, etc., [b]For example, a QA-TV based on M_r

Summary of U.S. Federal and State Specifications for the Implementation of IC Technology

A number of DOTs have been developing specifications for incorporating IC technology. These are summarized in Table C-19. Equipment specifications are summarized in Table C-20.

Summary of U.S. Federal and State Specifications for the Implementation of IC Technology

Specifications for roller-integrated measurement systems for QC/QA have been developed and implemented in Europe as national compaction standards for more than two decades under the term of Continuous Compaction Control (CCC). These specifications were first introduced in Austria in 1990 (with revisions in 1993 and 1999), and adopted in Germany in 1994 (with revisions in 1997 and 2009, see ZTVA-StB, 1997), Finland in 1994, Sweden in 1994 (with revision in 2004, see VVR VÄG 2009), and Switzerland (2006). The International Society for Soil Mechanics and Geotechnical Engineering (ISSMGE) developed specifications based primarily on the Austrian specifications (ISSMGE 2005, Adam 2007).

Spot-testing requirements varies by countries. The acceptance of earthwork materials in Europe is primarily based on using the plate load test (PLT) or the lightweight deflectometer (LWD), whereas in U.S. testing it is primarily based on the dry density measurements using NDG. The principal components of the various specifications and planned revisions are described in Ninfa (2013). Tables C.21, C.22, and C.23 summarize the Austrian, German and Swedish specifications, respectively.

Table C-18. Summary of current specifications for quality management of geomaterials using IC technology.

Agency	Specification Title	Target Materials	Use of ICMV	Year
California Department of Transportation (CalTrans)	Pavement Recycling with Intelligent Compaction	Cold In-Place Recycled Pavement	Target ICMV is not specified	2014
California Department of Transportation (CalTrans)	Intelligent Compaction for Hot Mix Asphalt	Hot Mix Asphalt (HMA)	Target ICMV is limited to target densities of test strip	2014
Federal Highway Administration (FHWA)	Intelligent Compaction Technology for Soils Applications	Soils	Target ICMV is established based on density/number of passes and is not correlated to mechanical properties	2014
Indiana Department of Transportation (INDOT)	Quality Control/Quality Assurance, QC/QA, Soil Embankment	Soils	Target ICMV is determined based on the DCP test results on the test section	2014
Kentucky Transportation Cabinet (KYTC)	Special Note for Intelligent Compaction of Aggregate Bases and Soils (draft)	Soils/Aggregate Base	Target ICMV is not specified (target value is restricted to density on test section)	2014
Minnesota Department of Transportation (MnDOT)	Quality Management Special – Intelligent Compaction (IC) Method	Soils/Asphalt	Target ICMV is not specified	2014
Texas Department of Transportation (TxDOT)	Intelligent Compaction of Soil and Flexible Base	Soils and Flexible Base	Even though construction of test strip is included, estimation of Target ICMV is not specified	2014
Michigan Department of Transportation (MDOT)	Intelligent Compaction Mapping of Sub-base and Aggregate Base	Sub-base/ Aggregate Base	Target ICMV is not specified	2013
Georgia Department of Transportation (GDOT)	Intelligent Compaction for Soils	Soils	Target ICMV is determined based on density and number of passes on a test section	2012
North Carolina Department of Transportation (NCDOT)	Intelligent Compaction (draft)	Soils	Minimum soil modulus of at least 6 ksi at a vertical stress of 15 psi is specified to establish target ICMV	2011
Iowa Department of Transportation (IDOT)	Special Provisions for Intelligent Compaction-Embankment	Soils	Target ICMV is not specified	2010

Table C-19. U.S. federal and state IC specifications.

Agencies	FHWA	AASHTO	MN
Application	Soils	Soils	Soils
Date	2015	2014	2014
Status	Generic Specification	Provisional Specification PP 81-14	Special Provision
Alignment Files	Not Required	Required	Required
Test Section	Required	Not Required	Not Required
Pre-mapping	Recommended	Recommended as “proof roll”	Recommended as “test roll”
IC Training	• Required Onsite – 4–8 mo • IC training includes Veta (Veda)	• Required • Does not include Veta	• Required • Does not include Veta
Data Submittal Requirements	• Obtain data twice per day. • Contractor analyze for uniformity and coverage. • Submit all data, proof data, and analysis results to Engineer at completion (at minimum).	• Via USB each day • Or via wireless (if available) every 15-min. or at least one time per day	• Submit to cloud every 15 min. when cell coverage available. • At least one time per day.
IC-Base Acceptance	• A minimum coverage of 90% of the individual construction area shall meet the optimal number of roller passes and 70% of the target ICMV determined from the test sections	• Project Percent Coverage of the cumulative measurement pass count completed by the instrumented rollers over the required compaction areas	• Measurement for IC based on percent coverage, certification, and approved rollers • 100% coverage is considered to be achieved when cumulative measurement pass count is ≥ 1
Basis of Payment	• Lump Sum	• Lump Sum • Partial payment based on certification of personnel (10%), certification of rollers (10%), and project percent coverage over 70% (80%).	• Lump Sum • Partial payment based on certification of personnel (10%), certification of rollers (10%), and project percent coverage over 70% (80%).

Table C-19, cont. U.S. federal and state IC specifications.

Agencies	GA	IA	IN
Application	Soils	Soils	Soils
Date	2012	2010	2014
Status	Special Provision	Special Provision 090063	Special Provision
Alignment Files	Not Required	Not Required	Not Required
Test Section	Required	Required	Required
Pre-mapping	Recommended	Not specified	Not specified
IC Training	• Required • IC training includes Veta (Veda)	• Required • Does not include Veta (Veda)	• Required Onsite – 4-8 hrs.
Data Submittal Requirements	• Submit data to Engineer twice per day. • Department will analyze the data.	• Daily (ASCII file) • Or upon request	• Via wireless every 10 minutes. • Contractor will perform analysis.
IC-Base Acceptance	• A minimum coverage of 90% of the individual construction area shall meet the optimal number of roller passes determined from the test sections. A minimum of 70% of the individual construction area shall meet the target ICMV values determined from the test sections. • Final compaction acceptances by the Engineer will be based on the Department-performed field density and moisture content readings in accordance with GDT-59 and GDT-67 and Section 208 of the specifications.	• IC-E proof area mapping is to be implemented for compacted fill within the project limits where quality acceptance follows DS-09003.	• A minimum of 70 % of the mapped construction area shall equal or exceed the target ICMV. • If the Contractor fails to comply with the QCP and IC Construction Quality Control requirements, the Engineer may require mapping of the lift in question or the next lift placed.
Basis of Payment	• Contract Unit Price; not a separate pay item	• Lump sum	• Lump sum

Table C-19, cont. U.S. federal and state IC specifications.

Agencies	KY	MI	NC
Application	Soils	Soils	Soils
Date	2014	2013	2012
Status	Special Note to Standard Specifications	Special Provision	Draft Specifications
Alignment Files	Not Required	Not Required	Not Required
Test Section	Required	Required	Required
Pre-mapping	Not specified	Not specified	Not specified
IC Training	• Required • Does not include Veta (Veda)	• Required • Does not include Veta (Veda)	• Required • Classroom and field • 1st day requires "Essential IC Workshop" • IC training includes Veta (Veda)
Data Submittal Requirements	• Twice per day. • Or as directed by the Engineer.	• After completion of the measurement pass, before placing successive layers. • Provide access to data for 6 mo. after completion required.	• Within 48 hrs. of proof rolling.
IC-Base Acceptance	• Any areas a minimum of 50 ft^2 in area not achieving the 80% of the stiffness value determined by the latest control strip shall be tested by other means approved by the Engineer. • All acceptance testing shall be as outlined in Standard Specifications sections 200 and 300.	• Proof roll the finished sub-base and aggregate base layers over the full width of the layer using the same IC rollers throughout the project. • Final compaction acceptance of sub-base and aggregate base layers based on Department-performed field density and moisture content measurements in accordance with the Manual.	• Compaction shall be accepted when a minimum of 70% of the embankment section meets or exceeds the Target ICMV requirements
Basis of Payment	• All areas with a minimum of 90% pass coverage and 80% required stiffness readings. • Payment is full compensation for all work associated with providing IC equipped rollers, transmission of electronic data files, two copies of IC roller manufacturer software, and training. • The Department will measure the total tons of aggregate base (DGA and/or CSB) and total cubic yards of soil compacted using the IC roller(s).	• Lump sum	• Not stated.

Table C-19, cont. U.S. federal and state IC specifications.

Agencies	PA	TX	VT
Application	Embankment or Sub-base	Soils	Sub-base and Reclaimed Stabilized Base (RSB)
Date	2015	2012	2014
Status	Special Provision	Special Provision	Special Provision
Alignment Files	Not Required	Not Required	Not Required
Test Section	Required	Required	Required
Pre-mapping	Not specified	Not specified	Recommended
IC Training	• Required • Does not include Veta (Veda)	• Not specified • Does not include Veta (Veda)	• Not specified • Does not include Veta (Veda)
Data Submittal Requirements	• During construction, interim copies. • At completion submit copies of the IC data files, coordinates of points of interest, and other requested information on CDs or DVDs.	• Submit both printed and electronic data files in ASCII format before placing successive courses.	• Twice per day.
IC-Base Acceptance	• Material acceptance is not based upon this IC item but is in accordance to the appropriate section of Publication 408 for the material being compacted. For bituminous materials, take additional research cores for information only in accordance with Publication 771 Section IX.	• Proof roll the finished courses over the full width of the course using the same IC rollers throughout the project.	• A minimum of 90 % of the construction area shall be mapped. A minimum of 70 % of the mapped construction area shall equal or exceed the target ICMV.
Basis of Payment	• Per square yard for Bituminous or roller compacted concrete • Per cubic yard for embankment areas or sub-base materials.	• Paid as a subsidiary to pertinent items.	• Lump sum. • Partial payments.

Table C-20. U.S. state equipment base specifications.

Agencies	Application	GPS Verbiage	GPS Verification Tolerance	Temperature Verification Tolerance	Alignment Files	Department Approval of Rollers	Approved Roller Vendors Listed	Veta (Veda)
FHWA	Soils	HPPS	12 in.	Not Required	Not Required	Not Required	No	Required
AASHTO	Soils	RTK-GPS	6 in.	5°F	Required	Required	No	Required
MN	Soils	RTK-GPS	6 in.	5°F	Required	Required	No	Required
GA	Soils	RTK-GPS	1.6 in. using rover stacked over roller GPS method	Not Required	Not Required	Required	Yes	Required
IA	Soils	RTK-GPS	1.2 in.	Not Required	Not Required	Not Required	No	Not Specified
IN	Soils	RTK-GPS	6 in.	Not Required	Not Required	Not Required	Requires reference to IC website	Required
KY	Soils	RTK-GPS	12 in.	Not Required	Not Required	Required	No	Required
MI	Soils	RTK-GPS	1.6 in. using rover stacked over roller GPS method	Not Required	Not Required	Not Required	No	Required
NC	Soils	RTK-GPS	1.6 in. using rover stacked over roller GPS method	Not Required	Not Required	Not Required	Approved vendor with 3 completed IC projects is required	Required
PA	Embankment or sub-base	RTK-GPS	Not specified but check required.	Not Required	Not Required	Not Required	No	Required
TX	Soils	GPS	Not specified and/or required	Not Required	Not Required	Required	Yes	Not Specified
VT	Sub-base and Reclaimed Stabilized Base (RSB)	RTK-GPS	1.6 in. (rover over roller GPS method) vendor alternative can be substituted	Not Required	Not Required	Not Required	No	Required

Table C-21. U.S. state equipment base specifications.

Agencies	Application	GPS Verbiage	GPS Verification Tolerance	Temperature Verification Tolerance	Alignment Files	Department Approval of Rollers	Approved Roller Vendors Listed	Veta (Veda)
FHWA	Soils	HPPS	12 in	Not Required	Not Required	Not Required	No	Required
AASHTO	Soils	RTK-GPS	6 in	5°F	Required	Required	No	Required
MN	Soils	RTK-GPS	6 in	5°F	Required	Required	No	Required
GA	Soils	RTK-GPS	1.6 in. using rover stacked over roller GPS method	Not Required	Not Required	Required	Yes	Required
IA	Soils	RTK-GPS	1.2 in	Not Required	Not Required	Not Required	No	Not Specified
IN	Soils	RTK-GPS	6 in	Not Required	Not Required	Not Required	Requires reference to IC website	Required
KY	Soils	RTK-GPS	12 in	Not Required	Not Required	Required	No	Required
MI	Soils	RTK-GPS	1.6 in. using rover stacked over roller GPS method	Not Required	Not Required	Not Required	No	Required
NC	Soils	RTK-GPS	1.6 in. using rover stacked over roller GPS method	Not Required	Not Required	Not Required	Approved vendor with 3 completed IC projects is required	Required
PA	Embankment or sub-base	RTK-GPS	Not specified but check required	Not Required	Not Required	Not Required	No	Required
TX	Soils	GPS	Not Specified and/or Required	Not Required	Not Required	Required	Yes	Not Specified
VT	Sub-base and Reclaimed Stabilized Base (RSB)	RTK-GPS	1.6 in. (rover over roller GPS method) vendor alternative can be substituted	Not Required	Not Required	Not Required	No	Required

Table C-22. Summary of Austrian specifications (Mooney et al. 2010; Briaud and Saez 2015).

QA Method	Calibration Process	Acceptance Criteria and Remarks
Acceptance based on calibration	Two main steps are performed: (1) Onsite calibration to develop correlations between ICMVs and spot-test results is performed over the entire width of the construction site and over a length of 100 m for each material (subgrade, sub-base, and base). The roller parameters are kept constant during the calibration. ICMV data are captured during each measurement run, and subsequent PLT or LWD testing is performed at values of low, medium, and high roller MV. PLT is required at a minimum of nine locations. If LWD testing is used, the average of four E_{LWD} values at a minimum of nine locations is required. The correlation coefficient, R^2, must be no less than 0.5. (2) Using the regression equation and specified E_{v1} or E_{LWD} leads to a minimum ICMV (MIN) and a mean roller MV (ME).	Minimum spot value MIN corresponds to 0.95 E_{v2} or E_{LWD}, and the ME corresponds to 1.05 E_{v1} or E_{LWD}. The maximum value MAX is defined as 1.5 MIN. According to the Austrian/ISSMGE specification: ▪ The mean ICMV (ME) must be ≥ ME ▪ 100% of ICMVs must be ≥ 0.8 MIN ▪ 90% of ICMVs must be ≥ MIN Compaction must be continued until the mean ICMV (ME) is < 5% greater than the mean value from the previous pass. The Austrian/ISSMGE specification also requires the following uniformity criteria: ▪ If 100% of ICMVs ≥ MIN, then the COV of ICMV for the entire area must be ≤ 20%. ▪ If 0.8 MIN ≤ minimum ICMV ≤ MIN, then 100% of ICMVs must be ≤ MAX = 1.5 MIN.
Acceptance based on percentage of change in measurement values	Calibration process is not performed	Compaction should be continued until the mean ICMV is < 5% greater than the mean ICMV from the previous pass. Subsequently, PLT or LWD testing is conducted at the weakest area as determined by the ICMV output. The E_{v1} or E_{LWD} must be greater than or equal to the required value. A minimum of three PLT or nine LWD tests must be performed in the weakest area

Acceptance Modulus Values for PLT and LWD Spot Tests

Level	E_{v1} (MPa)	E_{LWD} (MPa)
1 m below subgrade	15 (cohesive); 20 (cohesionless)	18 (cohesive); 24 (cohesionless)
Top of subgrade	25 (cohesive); 35 (cohesionless)	30 (cohesive); 38 (cohesionless)
Top of sub-base	60 (rounded); 72 (angular)	58 (rounded); 68 (angular)
Top of base	75 (rounded); 90 (angular)	70 (rounded); 82 (angular)

COV = Coefficient of variation
E_{v1} = Modulus from the first loop in the static plate load test
E_{LWD} = Modulus from light weight deflectometer
LWD = Light weight deflectometer
MAX = maximum spot-test measurement value
ME = mean spot-test measurement value
MIN = minimum spot-test measurement value
MV (MAX) = maximum roller measurement value
MV (ME) = mean roller measurement value
MV (MIN) = minimum roller measurement value
PLT = Plate load test

Table C-23. Summary of German specifications (Mooney et al. 2010; Briaud and Saez 2015).

QA Method	Calibration Process	Acceptance Criteria and Remarks
Calibration approach (M2 in German specifications)	Two main steps are performed: (1) Onsite calibration to develop correlations between ICMVs and spot-test results in an area equal to three 20-m-long test strips: (a) low compaction (after one pass), (b) medium compaction (after 3 or 5 passes), and (c) after high degree of compaction (i.e., multiple passes until no further compaction is achieved). Three to five static PLTs or density tests are performed on each test strip. Regression analysis is performed on the ICMV versus spot-test data. The correlation coefficient must be $R^2 \geq 0.5$. (2) Identification of target ICMV consistent with required density or reload modulus from PLT.	90% of all ICMVs must exceed the MV-TV. Variable frequency, amplitude, or jump mode is not permitted during calibration. The underlying soil must be homogeneous. Further modifications are being implemented. Minimum PLT modulus (reload modulus) for clay and silty soils is 45 MPa. For granular material, the corresponding modulus is between 80 and 100 MPa. Density requirements (typically 98% standard Proctor) exist for all layers below the top of subgrade. There are no moisture content requirements.
CCC to identified weak areas for spot testing	CCC is used to map the compacted area. The weakest spots are identified for spot testing (density or PLT). A minimum number of spot tests are specified (i.e., 4/5000 m^2).	Each density or reload modulus from the PLT must be greater or equal than the desired value. A minimum PLT modulus (reload modulus) for clay and silty soils is 45 MPa. For granular material, the corresponding modulus is between 80 and 100 MPa. Density requirements, (typically 98% standard Proctor) exist for all layers below the top of subgrade. There are no moisture content requirements.
	MV-TV = Target roller measurement value	PLT = Plate load test

Table C-24. Swedish specifications for unbound material, per 5000 m² control area (Mooney et al. 2010; Briaud and Saez 2015).

Depth below base course surface (mm)	Number of PLTs	Asphalt Pavement (1) $E_{v2(min)}$ (MPa)	Asphalt Pavement (2) E_{v2}/E_{v1} alternative if (2) is not met	Concrete Pavement (1) $E_{v2(min)}$ (MPa)	Concrete Pavement (2) E_{v2}/E_{v1} alternative if (2) is not met
0-250	1-2	125	≤ 1 + 0.0136E_{v2}	105	≤ 1 + 0.0162E_{v2}
251-500	1-2	32	≤ 1 + 0.078E_{v2}	45	≤ 1 + 0.056E_{v2}
500-550	1-2	32	NA	45	NA
551-650	1-2	20	NA	30	NA
651-750	1-2	15	NA	20	NA

Recommended Modulus Values for PLT and LWD Spot Tests

Depth Below Base Course Surface (mm)	Construction With Only Base and Sub-Base Material Above Crushed Rock		Construction With Only Base and Sub-Base Material Above Sandy Subgrade	
	$E_{v2(min)}$ (MPa)	E_{LWD} (MPa)	$E_{v2(min)}$ (MPa)	E_{LWD} (MPa)
800	12	10 - 15	16	12 - 18
900	9	8 - 12	11	10 - 14
1000	6	5 - 8	8	7 - 11
1100	4	4 - 5	5	5 - 8
1200	3	3	4	3 - 5
1300	2	2	3	3

E_{v2} = Modulus from the second loop in the static plate load test
E_{LWD} = Modulus from light weight deflectometer
LWD = Light weight deflectometer
PLT = Plate load test

References

ABAQUS User's Manual. (2000). Hibbit, Karlsson & Sorensen, Inc., Pawtucket, RI.

Abdallah, I. N., and Nazarian, S. (2009). "Rapid Interpretation of Nondestructive Testing Results Using Neural Networks." *Intelligent and Soft Computing in Infrastructure Systems Engineering*, (259), pp. 1-19.

Abu-Farsakh, M., Nazzal, M., and Mohammad, L. (2015). "Effect of Reinforcement on Resilient and Permanent Deformations of Base Course Material." *Transportation Research Record: Journal of the Transportation Research Board*, No. 2004, Transportation Research Board of the National Academies, Washington, D.C., pp. 120–131.

Adam, D. (1996). "Flächendeckende Dynamische Verdichtungskontrolle (FDVK) mit Vibrationswalzen (Continuous Compaction Control with Vibratory Rollers)." Technische Universität Wien.

Adam, D., and Kopf, F. (2004). "Operational Devices for Compaction Optimization and Quality Control (Continuous Compaction Control & Light Falling Weight Device)." *International Seminar on Geotechnic Pavement and Railway Design and Construction*, Millpress,Rotterdam, The Netherlands, Athens, Greece, pp. 97–106.

Alkasawneh, W. (2007). Backcalculation of Pavement Moduli Using Genetic Algorithms, PhD Dissertation. University of Akron, Akron, OH.

Al-Khoury, R., Kasbergen, C., Scarpas, A., and Blaauwendraad, J. (2001). "Spectral element technique for efficient parameter identification of layered media: Part II: Inverse calculation." *International Journal of Solids and Structures*, 38(48), pp. 8753-8772.

Amber, Y., & Von Quintus, H. L. 2002. "Study of LTPP Laboratory Resilient Modulus Test Data and Response Characteristics, Federal Highway Administration." Report No. FHWA- RD-02-051, Fugro-BRE, Inc. Austin, TX

Anderegg, R. (1997). "Nichtlineare Schwingungen bei dynamischen Bodenverdichtern (Nonlinear Vibrations with Dynamic Soil Compactors)." Eidgenössische Technishe Hochschule ETH Zürich, Zürich, Switzerland.

Anderegg, R., and Kaufmann, K. (2004). "Intelligent Compaction with Vibratory Rollers: Feedback Control Systems in Automatic Compaction and Compaction Control." *Transportation Research Record: Journal of the Transportation Research Board*, Transportation Research Board of the National Academies, 1868, pp. 124–134.

Andrei, D., Witczak, M. W., Schwartz, C. W., and Uzan, J. (2004). "Harmonized resilient modulus test method for unbound pavement materials." *Transportation Research Board*, 1874(1874), 29–37.

Asaf, Z., Shmulevich, I., and Rubinstein, D. (2006). "Predicting Soil-Rigid Wheel Performance Using Distinct Element Methods." *Transactions of the American Society of Agricultural and Biological Engineers*, 49(3), 607–616.

Beainy, F., Commuri, S., Zaman, M., and Syed, I. (2013). "Viscoelastic-Plastic Model of Asphalt-Roller Interaction." *International Journal of Geomechanics*, American Society of Civil Engineers, 13(5), 581–594.

Bräu, G., K. Hartman, and G. Pelz. (2004). "Flächendeckende Prufung der Verdichtung (FDVK)-Baupraktische Umsetzung und verfahrens-bezogene Verdichtungsanforderungen (CCC Testing of Compaction-Implementation in Construction Practice and Procedure-Related Compaction Specifications)." Lehrstuhl und Prüfamt für Grundbau, Bodenmechanik und Felsmechanik der Technischen Universitat München, Heft 897, München, Germany.

Brown, S. F., and Hyde, A. F. (1975). "Significance of Cyclic Confining Stress in Repeated-Load Triaxial Testing of Granular Material," *Transportation Research Record*, No. 537, Transportation Research Board, 1975.

Buechler, S. R., Mustoe, G. G. W., Berger, J. R., and Mooney, M. A. (2012). "Understanding the Soil Contact Problem for the LWD and Static Drum Roller by Using the DEM." *Journal of Engineering Mechanics*, American Society of Civil Engineers, 138(1), 124–132.

Burati, J. L., Weed, R. M., Hughes, C.S., Hill, H.S. (2003), *Optimal Procedures for Quality Assurance Specifications*, Report No. FHWA-RD-02-095, Federal Highway Administration (FHWA), pp. 57-59.

Cai, H., Kuczek, T., and Dunston, P. S. (2015a). "Field Experiment for Correlating Intelligent Compaction Data to In-Situ Soil Compaction Quality Measurements," In *Transportation Research Board 94th Annual Meeting*, No. 15-0319, Washington, D.C.

Cai, Y., Pan, E., and Sangghaleh, A. (2015b). "Inverse Calculation of Elastic Moduli in Cross-Anisotropic and Layered Pavements by System Identification Method." *Inverse Problems in Science and Engineering*, 23(4), pp. 718-735.

Cao, Y.-W., Liang, N.-X., Qin, M., and Lu, Z.-F. (2010). "Research on the Correlation between Vibration Acceleration of Roller and Compaction Degree of Subgrade Soil." *ICCTP 2010: Integrated Transportation Systems-Green, Intelligent, Reliable*, American Society of Civil Engineers, pp. 3738–3746.

Capatana, G. F. (2013). "Complex Continuous-Lumped Model for Simulation of Vibratory Compaction Process." *5th International Conference "Computational Mechanics and Virtual Engineering" COMEC 2013*, Brasov, Romania, 132–137.

Capraru, C., Pistrol, J., Villwock, S., Völkel, W., Kopf, F., and Adam, D. (2014). "Numerical Simulation of Soil Compaction with Oscillatory Rollers." *XV Danube - European Conference on Geotechnical Engineering (DECGE 2014)*, H. Brandl and D. Adam, eds., Vienna, Austria.

Carrasco, C., Tirado, C., and Wang, H. (2014). *Numerical Simulation of Intelligent Compaction Technology for Construction Quality Control*. *CAIT-UTC 029 Report*, El Paso, TX.

Cary, C. E., and Zapata, C. E. (2010), "Enhanced Model for Resilient Response of Soils Resulting from Seasonal Changes as Implemented in Mechanistic-Empirical Pavement Design Guide," *Transportation Research Record: Journal of the Transportation Research Board*, No. 2170, pp. 36-44.

Cary, C. E., and Zapata, C. E. (2011). "Resilient Modulus for Unsaturated Unbound Materials." *Road Materials Pavement Design*, 12 (3), pp. 615–638.

Chi, L., and Zhang, M. (2012). "Advanced FEA Compaction Model Using CEL Method." *SIMULIA Customer Papers*.

Chiroux, R. C., Foster, W. A., Johnson, C. E., Shoop, S. A., and Raper, R. L. (2005). "Three-Dimensional Finite Element Analysis of Soil Interaction with a Rigid Wheel." *Applied Mathematics and Computation*, 162(2), 707–722.

Cox, B. R., Stokoe, K. H., and Rathje, E. M. (2009). "An In Situ Test Method for Evaluating the Coupled Pore Pressure Generation and Nonlinear Shear Modulus Behavior of Liquefiable Soils." *Geotechnical Testing Journal*, 32(1), 1-37.

Cundall, P. A. (1971). "A computer model for simulating progressive large scale movements in blocky rock systems." *Symp. of the International Society for Rock Mechanics, Vol. II, No. 8*, Nancy, France.

D'Appolonia, D.J., R.V. Whitman, and E.D'Appolonia. (1969). "Sand Compaction with Vibratory Rollers." *Journal of Soil Mechanics & Foundations Division*, ASCE, Vol. 95, pp. 263–284.

Dintwa, E., Tijskens, E., and Ramon, H. (2007). "On the accuracy of the Hertz model to describe the normal contact of soft elastic spheres." *Granular Matter*, 10(3), pp. 209–221.

Dong, Q. X., Hachiya, Y., Takahashi, O., Tsubokawa, Y., and Matsui, K. (2002). "An Efficient Backcalculation Algorithm of Time Domain for Large-Scale Pavement Structures Using Ritz Vectors." *Finite Elements in Analysis and Design*, 38(12), pp. 1131-1150.

Drumm, E. C., Boateng-Poku, Y., and Pierce, T. J. (1990). "Estimation of Subgrade Resilient Modulus from Standard Tests." *Journal of Geotechnical Engineering*, Vol. 116, No. 5, pp. 774–789.

Drumm, E. C., and Meier, R. (2003). *LTPP Data Analysis: Daily and Seasonal Variations in In-Situ Material Properties*. NCHRP Web Document 60, Project 20-50, Transportation Research Board, National Research Council, Washington, D.C.

Drumm, E. C., Reeves, J. S., Madgett, M. R., and Trolinger, W. D. (1997). "Subgrade Resilient Modulus Correction for Saturation Effects." *Journal of Geotechnical and Geoenvironmental Engineering*, 123(7), pp. 663-670.

Duncan, J. M., Williams, G. W., Sehn, A. L., and Seed, R. B. (1991). "Estimation Earth Pressures Due to Compaction." *Journal of Geotechnical Engineering*, Vol. 117, No. 12, pp. 1833-1847.

Dunlap, W. A. (1963). "A Report on a Mathematical Model Describing the Deformation Characteristics of Granular Materials." Texas A&M University, Texas Transportation Institute, College Station, TX.

Erdmann, P., and Adam, D. (2014). "Numerical Simulation of Dynamic Soil Compaction with Vibratory Compaction Equipment." *XV Danube - European Conference on Geotechnical Engineering (DECGE 2014)*, H. B. & D. Adam, ed., Vienna, Austria, 243–248.

Facas, N. W., van Susante, P. J., and Mooney, M. A. (2010). "Influence of Rocking Motion on Vibratory Roller-Based Measurement of Soil Stiffness." *Journal of Engineering Mechanics*, American Society of Civil Engineers, 136(7), 898–905.

Feng, X. T., Zhao, H., and Li, S. (2004). "A New Displacement Back Analysis to Identify Mechanical Geo-material Parameters based on Hybrid Intelligent Methodology." *International Journal for Numerical and Analytical Methods in Geomechanics*, 28(11), pp. 1141-1165.

Ferregut, C., Abdallah, I., Melchor-Lucero, O., Nazarian, S. (1999). "Artificial Neural Network-Based Methodologies for Rational Assessment of Remaining Life of Existing Pavements: Development of a Comprehensive, Rational Method for Determination of Remaining Life of an Existing Pavement," Research Report TX-99 1711-1, Center for Highway Research Materials, The University of Texas at El Paso, El Paso, TX.

Ferris, A. J. (1985). "Developments in Compaction Control Systems." *Highways & Transportation*, 32(7), pp. 2–5.

Floss, R., G. Bräu, M. Gahbauer, N. Gruber, and J. Obermayer. (1991). "Dynamische Verdichtungsprüfung bei Erd-und Straßenbauten (Dynamic Compaction Testing in Earth and Road Construction)." Prüfamt für Grundbau, Boden-und Felsmechanik Technische Universität München, Heft 612. München, Germany.

Floss, R., Kröber, W., and Wallrath, W. (2001). "Dynamische Bodensteifigkeit als Qualitätskriterium für die Bodenverdichtung (Dynamic Soil Stiffness as a Quality Criterion for Soil Compaction)." *4. Internationales Symposium Technik und Technologie des Verkehrswegebaus (4th International Symposium and Technology Series of Transportation Infrastructures)*, BAUMA, München, Germany.

Fredlund, D. G., and Morgenstern, N. R. (1977). "Stress State Variables for Unsaturated Soils." *Journal of Geotechnical and Geoenvironmental Engineering*, Vol. 103.

Fredlund, D. G., and Xing, A. (1994), "Equations for the Soil-Water Characteristic Curve," *Canadian Geotechnical Journal*, Vol. 31, No. 4, pp. 521-532.

Fwa, T.F., Tan, C.Y., and Chan, W.T., 1997. "Backcalculation Analysis of Pavement Layer Moduli Using Genetic Algorithms." Transportation Research Record: *Journal of the Transportation Research Board, No. 1570, Transportation Research Board*, National Research Council, Washington, DC, pp. 134–142.

Gallivan, V. L., Chang, G. K., and Horan, D. R. (2011). "Intelligent Compaction for Improving Roadway Construction," *Geotechnical Special Publication* 218, American Society of Civil Engineers, pp. 117-124.

Göktepe, A. B., Ağar, E., and Lav, A. H. (2005). "Comparison of Multilayer Perceptron and Adaptive Neuro-Fuzzy System on Backcalculating the Mechanical Properties of Flexible Pavements." *ARI The Bulletin of the Istanbul Technical University*, 54(3), pp. 65-67.

Göktepe, A. B., Ağar, E., and Lav, A. H. (2006). "Advances in Backcalculating the Mechanical Properties of Flexible Pavements." *Advances in Engineering Software*, 37(7), pp. 421-431.

Gopalakrishnan, K. (2010). "Neural Network–Swarm Intelligence Hybrid Nonlinear Optimization Algorithm for Pavement Moduli Back-Calculation." *Journal of Transportation Engineering*, 136(6), pp. 528–536.

Gopalakrishnan, K., and Papadopoulos, H. (2011). "Reliable Pavement Backcalculation with Confidence Estimation." *Scientia Iranica*, 18(6), pp. 1214-1221.

Gu, F., Sahin, H., Luo, X., Luo, R., and Lytton, R. (2014). "Estimation of Resilient Modulus of Unbound Aggregates Using Performance-Related Base Course Properties." *Journal of Materials in Civil Engineering*, 27(6).

Gudehus, G. (1996). "A Comprehensive Constitutive Equation for Granular Materials." *Soils and Foundations*, 36(1), pp. 1–12.

Gudishala, R. (2005). "Development of Resilient Modulus Prediction Models for Base and Subgrade Pavement Layers From in Situ Devices Test Results." Sri Krishnadevaraya University.

Guler, M., Bosscher, P. J., and Plesha, M. E. (2002). "A Porous Elastoplastic Compaction Model for Asphalt Mixtures with Parameter Estimation Algorithm." *15th ASCE Engineering Mechanics Conference*, Columbia University, New York, NY.

Gupta, S., Ranaivoson, A., Edil, T., Benson, C., Sawangsuriya, A. (2007), *Pavement Design Using Unsaturated Soil Technology*, Report No. MN/RC-2007-11, Final Research Report submitted to Minnesota Department of Transportation, University of Minnesota, Minneapolis.

Hadidi, R., and Gucunski, N. (2010). "Comparative Study of Static and Dynamic Falling Weight Deflectometer Back-Calculations using Probabilistic Approach." *Journal of Transportation Engineering*, 136(3), pp. 196-204.

Hager, M. (2015). "Messwerte der Flächendeckenden Dynamischen Verdichtungskontrolle (FDVK) im theoretischen und experimentellen Vergleich (Observations of the Continuous Dynamic Compaction Control (CCC) in Theoretical and Experimental Comparison)." Technischen Universität Wien, Vienna, Austria.

Han, Z., and Vanapalli, S. K. (2014). "Predicting the Variation of Resilient Modulus with Respect to Suction Using the Soil-Water Characteristic Curve as a Tool." In Proc. ASCE Geo-Institute's 2014 Annual Congress, GSP 234, Atlanta, GA.

Heersink, D. K., Furrer, R., and Mooney, M. A. (2013). "Intelligent Compaction and Quality Assurance of Roller Measurement Values Utilizing Backfitting and Multiresolution Scale Space Analysis," arXiv preprint arXiv:1302.4631.

Hertz, H. R. (1882). "Ueber die Berührung fester elastischer Körper (On the Contact between Elastic Bodies)." *Journal für die reine und angewandte Mathematik*, 1882(92), pp. 156–171.

Hjelmstad, K. D., and Taciroglu, E. (2000). "Analysis and Implementation of Resilient Modulus Models for Granular Solids." *Journal of Engineering Mechanics*, American Society of Civil Engineers, 126(8), pp. 821–830.

Hossain, M., Mulandi, J., Keach, L., Hunt, M., and Romanoschi, S. (2006). "Intelligent Compaction Control." *Airfield and Highway Pavements*, American Society of Civil Engineers, pp. 304-316.

ter Huerne, H. L. (2004). "Compaction of Asphalt Road Pavements Using Finite Elements and Critical State Theory." University of Twente, Enschede, the Netherlands.

Hopkins, T., Beckham, T. L., Sun, C., and Ni, B. (2004). "Resilient Modulus of Kentucky Soils". Final Research Report for Kentucky Transportation Cabinet, Kentucky Transportation Center, University of Kentucky, Frankfort, KY.

Hopkins, T. C., Beckham, T. L., and Sun, C. (2007). *Resilient Modulus of Compacted Crushed Stone Aggregate Bases*. *Research Report KTC-05-27/SPR 229-01-1F*, Frankfort, KY.

Hossain, M. S. (2008). Characterization of Subgrade Resilient Modulus for Virginia Soils and its Correlation with the Results of Other Soil Tests, Report No. VTRC 09-R4, Virginia Transportation Research Council, Virginia Department of Transportation.

Hügel, H. M., Henke, S., and Kinzler, S. (2008). "High-Performance Abaqus Simulations in Soil Mechanics." *2008 ABAQUS Users' Conference*, Newport, RI, 1–15.

Jiao, T., Yang, M., and Xie, Y. (2015). "Continuous Identification of Soil Compaction Stiffness by Harmonic Balance-Based Method." *Electronic Journal of Geotechnical Engineering*, 20(12), 4485–4495.

Johnson, K. L. (1985). *Contact Mechanics*. Cambridge University Press, Cambridge, MA.

Johnson, T. C., Berg, R. L., Chamberlain, E. L., and Cole, D. M. (1986). "Frost Action Predictive Techniques for Roads and Airfields. A Comprehensive Survey of Research Findings." CRREL Report 86–18. U.S. Army Corps of Engineers, Cold Regions Research and Engineering Laboratory, Hanover, NH.

Kang Y. V. (1998). "Multi-Frequency Backcalculation of Pavement Layer Moduli." *Journal of Transportation Engineering*, 124(1), pp. 73–81.

Kargah-Ostadi, N., and Stoffels, S. M. (2013). "Backcalculation of Flexible Pavement Structural Properties Using a Restart Covariance Matrix Adaptation Evolution Strategy." *Journal of Computing in Civil Engineering*, 29(2), 04014035.

Kargl, G. (1995). "Modellversuche zur Ermittlung des Last-Deformationsverhaltens geschichteter Modellböden unter ebenen und zylindrisch gekrümmten Belastungsflächen und vergleichende Computerberechnungen." Technische Universität Wien.

Ke, L., Nazarian, S., Abdallah, I., and Yuan, D. (2002). *A Sensitivity Study of Parameters Involved in Design with Seismic Moduli*. *Report TX-99-1780-2*, El Paso, TX.

Kelm, M. (2003). “Numerische Simulation der Verdichtung kohäsionsloser Böden mit Vibrationswalzen.” TU Hamburg-Harburg.

Kenneally, B., Musimbi, O. M., Wang, J., and Mooney, M. A. (2015). “Finite element analysis of vibratory roller response on layered soil systems.” *Computers and Geotechnics*, 67, pp. 73–82.

Kim, Y. R., Xu, B., and Kim, Y. (2000). “A New Backcalculation Procedure Based on Dispersion Analysis of FWD Time-History Deflections and Surface Wave Measurements using Artificial Neural Networks.” In *Symposium on Nondestructive Testing of Pavements and Backcalculation of Moduli*: Third Volume, STP 1375, S. D. Tayabji, E. O. Lukanen, eds., ASTM Publication, pp. 297–312.

Khosravi, A., Salam, S., McCartney, J. S., and Dadashi, A. (2016). "Suction-Induced Hardening Effects on the Shear Modulus of Unsaturated Silt." *International Journal of Geomechanics*, D401600, 1-7.

Khoury, N. N., and Zaman, M. M. (2004), “Correlation between Resilient Modulus, Moisture Variation, and Soil Suction for Subgrade Soils,” *Transportation Research Record: Journal of Transportation Research Board*, No. 1874, pp. 99-107.

Khoury, N., Brooks, R., Boeni, S. Y., and Yada, D. (2012). “Variation of Resilient Modulus, Strength, and Modulus of Elasticity of Stabilized Soils with Postcompaction Moisture Contents.” *Journal of Materials in Civil Engineering*, 25(2), pp. 160–166.

Khot, L. R., Salokhe, V. M., Jayasuriya, H. P. W., and Nakashima, H. (2007). “Experimental validation of distinct element simulation for dynamic wheel–soil interaction.” *Journal of Terramechanics*, 44(6), 429–437.

Kim, K. (2010). “Numerical Simulation of Impact Rollers for Estimating the Influence Depth of Soil Compaction.” Texas A&M University.

Kim, S. H., Yang, J., and Jeong, J. H. (2014). “Prediction of Subgrade Resilient Modulus Using Artificial Neural Network.” *KSCE Journal of Civil Engineering*, 18(5), 1372-1379.

Kolymbas, D. (1978). *Ein nichtlineares viskoplastisches Stoffgesetz für Böden*. Inst. für Bodenmechanik und Felsmechanik.

Kopf, F., and Erdmann, P. (2005). “Numerische Untersuchungen der Flächendeckenden Dynamischen Verdichtungskontrolle FDVK (Numerical Analysis of Continuous Compaction Control).” *Osterreichische Ingenius und Architekten Zeitschrift (OIAZ)*, 150(4-5), 126–143.

Kröber, W. (1988). “Untersuchung der Dynamischen Vorgäge bei der Vibrationsverdichtung von Böden (Analysis of Dynamic Operation during the Vibrational Compaction of Soil).” Technischen Universität, Munchen.

Kröber, W., Floss, R., and Wallrath, W. (2001). “Dynamic Soil Stiffness as Quality Criterion for Soil Compaction.” *Geotechnics for Roads, Rail Tracks and Earth Structures*, A.A.Balkema Publishers, Tokyo, Japan, pp. 189–199.

Kung, J. H. S., Lin, H. D., Yang, S.-J., and Huang, W.-H. (2006). “Resilient Modulus and Plastic Strain of Unsaturated Cohesive Subgrade Soils.” *Unsaturated Soils*, 1247–1258.

Kuo, Y. L., Jaksa, M. B., Scott, B. T., Bradley, A. C., Power, C. N., Crisp, A. C., and Jiang, J. H. (2013). “Assessing the Effectiveness of Rolling Dynamic Compaction.” *18th International Conference on Soil Mechanics and Geotechnical Engineering*, Paris, France, 1309–1312.

Lanzo, G., Pagliaroli, A., and D’Elia, B. (2004). “Influence of Modeling Rayleigh Viscous Damping in the Analysis of Local Seismic Response (Influenza della modellazione di Rayleigh dello smorzamento viscoso nelle analisi di risposta sismica locale).” *XI Congresso Nazionale “L’Ingegneria Sismica in Italia,”* Associazione Nazionale Italiana di Ingegneria Sismica (ANIDIS), Genoa, Italy.

Ledesma, A., Gens, A., and Alonso, E. E. (1996). “Parameter and variance estimation in geotechnical backanalysis using prior information.” *International Journal for Numerical and Analytical Methods in Geomechanics*, 20(2), pp. 119-141.

Lee, W., Bohra, N. C., Altschaeffl, A. G., and White, T. D. (1977). “Resilient Modulus of Cohesive Soils.” *Journal of Geotechnical and Geoenvironmental Engineering*, ASCE, 123(2), pp. 131–136.

Lekarp, F., Isacsson, U., and Dawson, A. (2000). “State of the Art. I: Resilient Response of Unbound Aggregates.” *Journal of Transportation Engineering*, 126(1), pp. 68–75.

Levasseur, S., Malecot, Y., Boulon, M., and Flavigny, E. (2009). “Statistical Inverse Analysis based on Genetic Algorithm and Principal Component Analysis: Method and Developments using Synthetic Data.” *International Journal for Numerical and Analytical Methods in Geomechanics*, 33(12), pp. 1485-1511.

Li, S., and Su, Y. (2014). “Three Dimensional Finite Element Simulation of Vibratory Roller Impact on Subgrade Settlement.” *Electronic Journal of Geotechnical Engineering*, 19, 6193–6200.

Li, D., and Sun, Z. (2015). “The Effects of Moisture Content Fluctuation on a Dynamic Resilient Modulus of Compacted Clay.” *Advances in Civil Engineering and Building Materials IV*, Taylor & Francis Group, London, pp. 29-33.

Liang, J., and Xin, L. (2013). “Research on the Simulation of Vibrating System Based on LS-DYNA.” *Journal of Convergence Information Technology*, 8(3), 47–54.

Liang, R. Y., Al-Akhras, and K. Rabag'ah, S. (2006), "Field Monitoring of Moisture Variations Under Flexible Pavement," *Transportation Research Record: Journal of Transportation Research Board*, No. 1967, pp. 160-172.

Liang, R.Y., Rabag'ah, S., and Khasawneh, M. (2008), "Predicting Moisture-Dependent Resilient Modulus of Cohesive Soils Using Soil Suction Concept," *Journal of Transportation Engineering*, Vol. 134, No. 1, pp. 34-40.

Ling, J., Guo, R., and Yuan, J. (2006), "A Method to Monitor and Evaluate Seasonal Variation in Resilient Modulus of Pavement Subgrade," ASCE, *Pavement Mechanics and Performance 2006*, GSP 154.

Lundberg, G. (1939). "Elastische Berührung Zweier Halbräume (Elastic Contact between Two Half Spaces)." *Forschung auf dem Gebiete des Ingenieurwesens, Vereins Deutscher Ingenieure (VDI) -Zeitschrift*, 10(5), pp. 201–211.

Luong, M. P. (1982). "Mechanical Aspects and Thermal Effects of Cohesionless Soils under Cyclic and Transient Loading." In *Proc. IUTAM Conf. on Deformation and Failure of Granular Materials*, Delft, pp. 239-246.

Lytton R. L. (1989). "Backcalculation of Layer Moduli, State of the Art." NDT of Pavements and Backcalculation of Moduli, Vol. 3. *STP* 1026, A. J. Bush and G. Y. Baladi, eds., ASTM, pp. 7–38.

Machet, J. M. (1980). "Compactor-Mounted Control Devices." *International Conference on Compaction, Vol. II*, Paris, France, 577–581.

Maher, A., Bennert T., Gucunski, N., and Papp, W. J., (2000). "Resilient Modulus of New Jersey Subgrade Soils," FHWA Report No. 2000-01, Washington D.C.

Maina, J. W., Yokota, H., Mfinanga, D. A., and Masuda, S. (2000). "Prediction of Pavement Deterioration based on FWD Results." NDT of Pavements and Backcalculation of Moduli, Vol. 3, *STP* 1375, S. D. Tayabji, E. O. Lukanen, eds., ASTM , pp. 95–109.

Maina, J., Steyn, W. J., van Wyk, E. B., and le Roux, F. (2013). "Static and Dynamic Backcalculation Analyses of an Inverted Pavement Structure." *Advanced Materials Research*, Vol. 723, pp. 196-203.

Malla, R., and Joshi, S. (2007). "Resilient Modulus Prediction Models Based on Analysis of LTPP Data for Subgrade Soils and Experimental Verification." *Journal of Transportation Engineering*, Vol. 133, No. 9, 491–500.

Malla, R., and Joshi, S. (2008). "Subgrade resilient modulus prediction models for coarse and fine-grained soils based on long-term pavement performance data." *International Journal of Pavement Engineering*, Vol. 9(6): 431-444.

McAdams, M. L. (2014). "Dynamic finite element simulations of vibratory roller soil stiffness using iterative stress-dependent resilient moduli." Colorado School of Mines.

McCartney, J. and Khosravi, A. (2013). "Field-Monitoring System for Suction and Temperature Profiles under Pavements." *Journal of Performance of Constructed Facilities*, Vol. 27, Issue 6, pp. 818-825.

Meier, R. W. and Rix, G. J. (1994) "Backcalculation of Flexible Pavement Moduli using Artificial Neural Networks." *Transportation Research Record: Journal of the Transportation Research Board*, 1448, Transportation Research Board, National Research Council, Washington, DC, pp. 75–82.

Meier, R. W. and Rix, G. J. (1995) "Backcalculation of Flexible Pavement Moduli from Dynamic Deflection Basins using Artificial Neural Networks." *Transportation Research Record: Journal of the Transportation Research Board*, 1473, Transportation Research Board, National Research Council, Washington, DC, pp. 72–81.

Meißner, S., Quick, H., Arslan, U., and Zimmer, C. (2006). "Displacement Behavior of Shallow Foundations Under Cyclic Loading." *MAGLEV'2006: The 19th International Conference on Magnetically Levitated Systems and Linear Drives*, Dresden, Germany.

Melchor-Lucero, O., Abdallah, I., Nazarian, S., and Ferregut, C. (2002). "A Probabilistic Method for Estimating Pavement Performance Using Falling Weight Deflectometer Data." In *Proc. of the 6th International Conference on the Bearing Capacity of Roads and Airfields*, Lisbon, Portugal, 24-26 June, Vol 1., A. G. Correia and F. E. F. Branco, eds., pp. 475-485.

Micaelo, R., Ribeiro, J., Azevedo, M., and Azevedo, N. (2010). "HMA Compaction Study: Two Different Approaches." *11th ISAP – International Conference on Asphalt Pavements*, ISAP, Nagoya, Japan, 344–353.

Mohammad, L., Huang, B., Puppala, A., and Allen, A. (1999). "Regression Model for Resilient Modulus of Subgrade Soils. *Transportation Research Record: Journal of the Transportation Research Board*, (1687), 47-54.

Mohammad, L. N., Gaspard, K., Herath, A., and Nazzal, M. (2007). *Comparative Evaluation of Subgrade Resilient Modulus from Non-Destructive, In-Situ, and Laboratory Methods. Report FHWA/LA.06/417*, Baton Rouge, LA.

Mooney, M. A., and Adam, D. (2007). "Vibratory Roller Integrated Measurement of Earthwork Compaction: An Overview." In *Proc. 7th FMGM 2007 International Symposium on Field Measurements in Geomechanics*, American Society of Civil Engineering, pp. 1-12.

Mooney, M. A., and Facas, N. W. (2013). *Extraction of Layer Properties from Intelligent Compaction Data. Final Report for NCHRP Highway IDEA Project 145*, Transportation Research Board of the National Academies, Washington, DC.

Mooney, M. A., and Rinehart, R. V. (2007). "Field Monitoring of Roller Vibration during Compaction of Subgrade Soil," *Journal of Geotechnical and Geoenvironmental Engineering*, 133(3), ASCE, pp. 257-265.

Mooney, M. A., and Rinehart, R. V. (2009). "In Situ Soil Response to Vibratory Loading and Its Relationship to Roller-Measured Soil Stiffness." *Journal of Geotechnical and Geoenvironmental Engineering*, American Society of Civil Engineers, 135(8), 1022–1031.

Mooney, M. A., Gorman, P. B., Farouk, E., Gonzalez, J. N., and Akanda, A. S. (2003). "Exploring Vibration Based Intelligent Soil Compaction." Oklahoma Department of Transportation. Project No. 2146, Final Report, 250 pp.

Mooney, M.A., Gorman, P.B., and Gonzalez, J.N. (2005). "Vibration Based Health Monitoring During Earthwork Construction." *Journal of Structural Health Monitoring*, Vol. 2, No. 4, pp. 137–152.

Mooney, M. A., Rinehart, R. V., Facas, N. W., Musimbi, O. M., and White, D. J. (2010). *NCHRP Report 676: Intelligent Soil Compaction Systems*. National Cooperative Highway Research Program, Transportation Research Board, Washington, DC.

Mooney, M., Rinehart, R., and van Susante, P. J. (2006). "The Influence of Heterogeneity on Vibratory Roller Compactor Response." *GeoCongress 2006: Geotechnical Engineering in the Information Technology Age*, D. J. DeGroot, J.T. DeJong, D. Frost, and L.G. Baise, eds., American Society of Civil Engineers, Atlanta, GA, 1–6.

Moossazadeh J., and Witczak, M.W. (1981). "Prediction of Subgrade Moduli for Soil that Exhibits Nonlinear Behavior", *Transportation Research Record 810*, TRB, National Research Council, Washington, D.C., pp. 9-17.

Musimbi, O. M., Rinehart, R. V., and Mooney, M. A. (2010). "Comparison of Measured and BEM Computed Contact Area between Roller Drum and Layered Soil." *GeoFlorida 2010: Advances in Analysis, Modeling & Design (GSP 199)*, D. O. Fratta, A. J. Puppala, and B. Muhunthan, eds., ASCE, West Palm Beach, FL, 2444–2453.

Navarro, E., Garibay, J., Abdallah, I., and Nazarian, S. (2012). "Development of Models to Estimate Modulus and Permanent Deformation of Texas Bases," Technical Memorandum: 0-6622-4a. Subtask 4.1: MR and PD Model Developments for Granular Base Materials. Center for Transportation Infrastructure Systems, The University of Texas at El Paso, El Paso, TX.

Nazarian, S., Abdallah, I., and Yuan, D. (2004). "Neural Networks for Rapid Reduction Interpretation of Spectral Analysis of Surface Waves Results." *Transportation Research Record: Journal of the Transportation Research Board*, (1868), pp. 150-155.

Nazarian, S., Mazari, M., Abdallah, I., Puppala, A. J., Mohammad, L. N., and Abu-Farsakh, M. Y. (2014). *Modulus-Based Construction Specification for Compaction of Earthwork and Unbound Aggregate*. *NCHRP Project 10-84*, El Paso, TX.

Nazzal, M. (2014). *Non-nuclear methods for compaction control of unbound materials*, Research Project 20-05, Topic 44-10, NCHRP Synthesis of Highway Practice 456, Transportation Research Board, Washington, D.C.

Nazzal, M. D., and Mohammad, L. N. (2010). Estimation of Resilient Modulus of Subgrade Soils for Design of Pavement Structures. *Journal of Materials in Civil Engineering*, 22(7), 726-734.

Nazzal, M. D., and Tatari, O. (2013). "Evaluating the Use of Neural Networks and Genetic Algorithms for Prediction of Subgrade Resilient Modulus." *International Journal of Pavement Engineering*, Taylor & Francis Group, 14(4), 364–373.

Neff, A., Wang, J. and Mooney, M.A. (2015) "Analysis of Center of Gravity Roller Drum Vibration and Resultant Soil Stiffness on Layered Earthwork." Canadian Geotechnical Journal, 52(4), pp. 459-468.

Ng, C. W. W., Zhou, C., Yuan, Q., and Xu, J. (2013). "Resilient Modulus of Unsaturated Subgrade Soil: Experimental and Theoretical Investigations." *Canadian Geotechnical Journal*, 50(2), pp. 223-232.

Ni, B., Hopkins, T.C., Sun, L. and Beckham, T.L. (2002). "Modeling the Resilient Modulus of Soils." In *Proceedings of the Sixth International Conference Bearing Capacity of Roads, Railways and Airfields*, Lisbon, Portugal.

Niemunis, A. (2002). "Extended hypoplastic models for soils." Ruhr-Universität Bochum.

Niemunis, A., and Herle, I. (1997). "Hypoplastic model for cohesionless soils with elastic strain range." *Mechanics of Cohesive-frictional Materials*, 2(4), 279–299.

Nikas, G. K., and Sayles, R. S. (2008). "Finite-element analysis of layered rolling contacts." *Proceedings of the Institution of Mechanical Engineers, Part J: Journal of Engineering Tribology*, SAGE Publications, 222(7), 865–886.

Oh, J. H. and Fernando, E. G. (2011), *Development of Correction Factors between Lab and Field Modulus*, Report No. BDL76-1, Submitted to the Florida Department of Transportation, Texas Transportation Institute, College Station, TX.

Oloo, S. Y., and Fredlund, D. G. (1998), "The Application of Unsaturated Soil Mechanics Theory to the Design of Pavements," *Proceedings of the 5th International Conference on the Bearing Capacity of Roads and Airfields*, pp. 1419-1428, Trondheim, Norway.

Ooi, P. S. K., Archilla, A. R., and Sandefur, K. G. (2004), "Resilient Modulus Models for Compactive Cohesive Soils," *Transportation Research Record: Journal of the Transportation Research Board*, No. 1874, pp. 115-124.

Ooi, P. S., Sandefur, K. G., and Archilla, A. R. (2006). "Correlation of Resilient Modulus of Fine-Grained Soils with Common Soil Parameters for Use in Design of Flexible Pavements." Report No. HWY-L-2000-06, University of Hawaii, Manoa.

Pacheco, L.G., and Nazarian, S. (2011), "Impact of Moisture Content and Density on Stiffness-Based Acceptance of Geomaterials," *Transportation Research Record: Journal of Transportation Research Board*, No. 2212, pp. 1-13.

Park, S. W., Park, H. M., and Hwang, J. J. (2010). "Application of Genetic Algorithm and Finite Element Method for Backcalculating Layer Moduli of Flexible Pavements." *KSCE Journal of Civil Engineering*, 14(2), pp. 183-190.

Patrick, J., and Werkmeister, S. (2010). *Compaction of Thick Granular Layers, NZ Transport Agency Research Report No. 411*. New Zealand Transport Agency, Wellington, New Zealand.

Pekcan, O., Tutumluer, E., and Ghaboussi, J. (2010). "Soft Computing Methodology to Determine Pavement Thickness from Falling Weight Deflectometer Testing." *Proc. GeoFlorida 2010: Advances in Analysis, Modeling & Design*, GSP 199, D. O. Fratta, A. J. Puppala, and B. Muhunthan, eds., ASCE, Orlando, FL, pp. 2621-2630.

Petersen, D. L., and Peterson, R. (2006). "Intelligent Compaction and In-Situ Testing at MnDOT TH53." Minnesota Department of Transportation, MnDOT Report MN/RC-2006-13, CNA Consulting, Minneapolis, MN.

Petersen, J. S., Romanoschi, S. A., and Hossain, M. (2007). "Development of Stiffness-Based Specifications for In-Situ Embankment Compaction Quality Control." Report No. K-TRAN: KSU-04-6. Kansas State University, Manhattan, KS.

Pezo, R. F., Kim, D. S., Stokoe, I. I., Kenneth, H., and Hudson, W. R. (1991). A reliable resilient modulus testing system. *Transportation Research Record*, (1307).

Ping, W. V., Yang, Z., and Gao, Z. (2002). "Field and Laboratory Determination of Granular Subgrade Moduli." *Journal of Performance of Constructed Facilities*, 16(4), 149.

Pistrol, J., Falkner, F.-J., Adam, D., and Adam, C. (2012). "Comparison of Constitutive Soil Models for the Simulation of Dynamic Roller Compaction." *6th European Congress on Computational Methods in Applied Sciences and Engineering (ECCOMAS 2012)*, J. Eberhardsteiner, H. J. Böhm, and F. G. Rammerstorfer, eds., Vienna, Austria.

Puppala, A.J. (2008), *Estimating Stiffness of Subgrade and Unbound Materials for Pavement Design*, NCHRP Synthesis 382, National Cooperative Highway Research Program, Transportation Research Board, Washington, D.C.

Quibel, A. (1980). "Le comportement vibratoire: Trait d'union entre le choix des parameters et l'efficacite des rouleaux vibrants (The Vibratory Behavior: Interactions Between Vibration Parameters and the Effectiveness of Vibratory Rollers)." *Colloque International sur le Compactage (International Conference on Compaction, Session VII Compaction Equipment), ENPC, LCPC, Paris.*, 671–676.

Rabaiotti, C., Puzrin, A., Caprez, M., and Ozan, C. (2013). "Pavement Structural Health Evaluation based on Inverse Analysis of Three Dimensional Deflection Bowl." *International Journal of Pavement Engineering*, 14(4), pp. 374-387.

Rahman, F., Hossain, M., Hunt, M. M., and Romanoschi, S. A. (2007). "Intelligent Compaction Control of Highway Embankment Soil." *86th Annual Meeting of the Transportation Research Board*, Annual Meeting CD-ROM.

Rahman, F., Hossain, M., Romanoschi, S. A., and Brennan, J. (2012). "Kansas Experience with Stiffness-Based Quality Control/Quality Assurance Specifications for Compaction of Highway Embankments." *GeoCongress 2012*, American Society of Civil Engineers, pp. 1522-1561.

Reddy, M. A., Reddy, K. S., and Pandey, B. B. (2004). "Selection of Genetic Algorithm Parameters for Backcalculation of Pavement Moduli." *International Journal of Pavement Engineering*, 5(2), pp. 81-90.

Richter, C. (2006), *Seasonal Variations in the Moduli of Unbound Pavement Layers*, Publication No. FHWA-HRT-04-079, Turner-Fairbanks Highway Research Center, McLean, VA.

Rinehart, R., Berger, J., and Mooney, M. (2009). "Comparison of Stress States and Paths: Vibratory Roller-Measured Soil Stiffness and Resilient Modulus Testing." *Transportation Research Record: Journal of the Transportation Research Board*, Transportation Research Board of the National Academies, 2116, 8–15.

Rinehart, R. V., Mooney, M. A., and Berger, J. R. (2008). "In-Ground Stress-Strain Condition Beneath Center and Edge of Vibratory Roller Compactor." *1st International Conference Advances in Transportation Geotechnics*, E. Ellis, N. Thom, H.-S. Y. Yu, A. Dawson, and G. McDowell, eds., CRC Press (Taylor & Francis Group), Nottingham, UK, 737–741.

Rinehart, R., Mooney, M., Facas, N., and Musimbi, O. (2012). "Examination of Roller-Integrated Continuous Compaction Control on Colorado Test Site." *Transportation Research Record: Journal of the Transportation Research Board*, (2310), pp. 3-9.

Roesset, J. M. and Shao, K. Y. (1985). "Dynamic Interpretation of Dynaflect and Falling Weight Deflectometer Tests." *Transportation Research Record: Journal of the Transportation Research Board*, 1022, TRB, Washington, DC, pp. 7–16.

Roudgari, R. (2012). "Compaction of Soil by Repeated Loading." Concordia University.

Sabnis, A. K., Abdallah, I. N., Nazarian, S., and Puppala, A. J. (2009). "Development of Shrinkage Model Based on Index Properties for Clays." In *Proceedings of the 88th Annual Meeting of the Transportation Research Board* (No. 09-2153), Washington, DC.

Saltan, M. (2002). "Modeling Deflection Basin using Neurofuzzy in Backcalculating Flexible Pavement Layer Moduli." *Pakistan Journal of Information and Technology*, 1(2), pp. 180-187.

Saltan, M., and Terzi, S. (2005). "Comparative Analysis of using Artificial Neural Networks (ANN) and Gene Expression Programming (GEP) in Backcalculation of Pavement Layer Thickness." *Indian Journal of Engineering Materials Science*, 12(1), pp. 42-50.

Sangghaleh, A., Pan, E., Green, R., Wang, R., Liu, X. and Cai, Y. (2014). "Backcalculation of Pavement Layer Elastic Modulus and Thickness with Measurement Errors," *International Journal of Pavement Engineering*, 15(6), pp. 521-531.

Santha, B. L. (1994). "Resilient Modulus of Subgrade Soils: Comparison of Two Constitutive Equations." *Transportation Research Record*, (1462), 79–90.

Sawangsuriya, A., Edil, T. B., Benson, C. H. (2009), "Effect of Suction on Resilient Modulus of Compacted Fine-Grained Subgrade Soils," *Transportation Research Record: Journal of the Transportation Research Board*, No. 2101, pp. 82-87.

Seed H.B., Chan, C. K. and Lee, C. E. (1967). "Resilience Characteristics of Subgrade Soils and their Relation to Fatigue Failures in Asphalt Pavements", *Proceedings of the 1st International Conference on the Structural Design of Asphalt Pavements*, University of Michigan, Ann Arbor, Michigan, pp. 611-636.

Senseney, C., Krahenbuhl, R., and Mooney, M. (2013). "Genetic Algorithm to Optimize Layer Parameters in Light Weight Deflectometer Backcalculation." *International Journal of Geomechecanics*, 13(4), pp. 473–476.

Siddagangaiah, A. K., Aldouri, R., Nazarian, S., Chang, C. M., and Puppala, A. (2014), "Improvement of Base and Soil Construction Quality by Using Intelligent Compaction Technology." Report FHWA/TX-13/0-6740-1, Center for Transportation Infrastructure Systems, The University of Texas at El Paso, El Paso, TX.

Siekmeier, J. A. (2011), "Unsaturated Soil Mechanics Implementation during Pavement Construction Quality Assurance," *Proceedings of 59th Annual Geotechnical Engineering Conference*, St. Paul, MN.

Simpson, B., O'Riordan, N. J., and Croft, D. D. (1979). "A computer model for the analysis of ground movements in London Clay." *Géotechnique*, Thomas Telford, 29(2), 149–175.

Shackel, B. (1973). "Changes in Soil Suction in a Sand-Clay Subjected to Repeated Triaxial Loading." *Highway Research Record*, No. 429, Highway Research Board, pp 29-39.

Sharma, S. and Das, A. (2008). "Backcalculation of Pavement Layer Moduli from Falling Weight Deflectometer Data Using Artificial Neural Network." *Canadian Journal of Civil Engineering*, 35(1), pp. 57–66.

Smith, J. O., and Liu, C. K. (1953). "Stresses due to Tangential and Normal Loads on an Elastic Solid with Application to Some Contact Stress Problems." *Journal of Applied Mechanics*, 20, 157–166.

Stubbs, N., Torpunuri, V. S., Lytton, R. L., and Magnuson, A. H. (1994). "A Methodology to Identify Material Properties in Pavements Modeled as Layered Viscoelastic Half-Spaces." *NDT of Pavements and Backcalculation of Moduli*, Vol. 2, *STP* 1198, H. L. Von Quintus, A. J. Bush, and A. J. Baladi, eds., ASTM, pp. 159-169.

Taciroglu, E. (1998). "Constitutive Modeling of the Resilient Response of Granular Solids." University of Illinois at Urbana-Champaign.

Tang, X., and Yang, X. (2013). "Inverse Analysis of Pavement Structural Properties Based on Dynamic Finite Element Modeling and Genetic Algorithm." *International Journal of Transportation Science and Technology*, 2(1), pp. 15-30.

Tanyu, B. F., Kim, W. H., Edil, T. B., and Benson, C. H. (2003). Comparison of laboratory resilient modulus with back-calculated elastic moduli from large-scale model experiments and FWD tests on granular materials. *ASTM STP 1437*, 191-208.

Tarawneh, B., and Nazzal, M. D. (2014). "Optimization of Resilient Modulus Prediction from FWD Results using Artificial Neural Network." *Periodica Polytechnica Civil Engineering*, 58(2), pp. 143-154.

Thompson, M. R., and Robnett, Q. L. (1976). "Resilient Properties of Subgrade Soils", Transportation Engineering Series No. 14. Illinois Cooperative Highway and Transportation Series No. 160, University of Illinois at Urbana-Champaign.

Thompson, M., and White, D. (2007). "Field Calibration and Spatial Analysis of Compaction-Monitoring Technology Measurements." *Transportation Research Record: Journal of the Transportation Research Board*, No. 2004, pp. 69–79.

Thurner, H. F., and Forsblad, L. (1978). *Compaction Meter on Vibrating Rollers*. Research Bulletin Nr. 8022, Solna, Sweden.

Thurner, H. F., and Sandström, Å. (1980). "A New Device for Instant Compaction Control." *Proceedings of International Conference on Compaction*, Paris, France, pp. 611–614.

Titus-Glover, L., and Fernando, E. B. (1995). *Evaluation of Pavement Subgrade Material Properties and Test Procedures*. Report No. FHWA/TX-96/1335-2, Texas Transportation Institute, Texas A&M University, College Station, TX.

Tutumluer, E. (2013). *Practices for Unbound Aggregate Pavement Layers*. *NCHRP Synthesis 445*, National Cooperative Highway Research Program, Transportation Research Board, Washington, D.C.

Tutumluer, E., and Seyhan, U. (1998). "Neural Network Modeling of Anisotropic Aggregate Behavior from Repeated Load Triaxial Tests." *Transportation Research Record: Journal of the Transportation Research Board*, (1615), pp. 86-93.

Ullidtz P. (2000). "Will Nonlinear Backcalculation Help?" NDT of Pavements and Backcalculation of Moduli, Vol. 3. STP 1375, S. D. Tayabji, E. O. Lukanen, eds., ASTM, pp. 14–22.

Uzan J. "Advanced Backcalculation Techniques." *NDT of Pavements and Backcalculation of Moduli, Special Technical Publication STP* 1198, H. L. Von Quintus, A. J. Bush, and G. Y. Baladi, G. Y., eds., ASTM, pp. 3–37.

Van Susante, P. J., and Mooney, M. A. (2008). "Capturing Nonlinear Vibratory Roller Compactor Behavior through Lumped Parameter Modeling." *Journal of Engineering Mechanics*, 134(8), 684–693.

Velasquez, R., Hoegh, K., Yut, I., Funk, N., Cochran, G., Marasteanu, M., and Khazanovich, L. (2009). "Implementation of the MEPDG for New and Rehabilitated Pavement Structures for Design of Concrete and Asphalt Pavements in Minnesota," MnDOT Research Report MN/RC 2009-06, University of Minnesota, Minneapolis, MN.

Von Quintus, H. L., and Killingsworth, B. (1998), "Analyses Relating to Pavement Material Characterizations and Their Effects on Pavement Performance," FHWA-RD-97-085, Federal Highway Administration, McLean, VA.

Von Quintus, H. L., Rao, C., Minchin, R. E., Nazarian, S., Maser, K.R., and Prowell, B. (2009), *NDT Technology for Quality Assurance of HMA Pavement Construction*, NCHRP Report 626, National Cooperative Highway Research Program, Transportation Research Board, Washington, D.C.

Von Quintus, H. L., Rao, C., Bhattacharya, B., Titi, H., and English, R. (2010), "Evaluation of Intelligent compaction technology for Densification of Roadway Subgrades and Structural Layers," Submitted to the Wisconsin Highway Research Program (WHRP), Draft Final Report, WHRP Study No. 00092-08-07, Applied Research Associates, Inc., University of Wisconsin at Milwaukee.

Vosoughi, A. R., Banan, M. R., Banan, M. R., and Malekzadeh, P. (2014). "Hybrid FE–IDQ–CG method for dynamic parameters estimation of multilayered half-space." *Composites Part B: Engineering*, 56, pp. 74-82.

Wang W., Ishikawa H., Yuki H. (2001). "An Inverse Method for Determining Material Properties of a Multi-Layer Medium by Boundary Element Method." *International Journal of Solids and Structures*, 38, pp. 8907–8920.

Wang, L., Zhang, B., Wang, D., and Yue, Z. (2007). "Fundamental Mechanics of Asphalt Compaction through FEM and DEM Modeling." *Analysis of Asphalt Pavement Materials and Systems Analysis: Engineering Methods, GSP 176*, L. Wang and E. Masad, eds., American Society of Civil Engineers, Boulder, CO, 45–63.

Werkmeister, S., Numrich, R., Dawson, A., and Wellner, F. (2003). Design of granular pavement layers considering climatic conditions. *Transportation Research Record: Journal of the Transportation Research Board*, (1837), 61-70.

White, D. J., Jaselskis, E. J., Schaefer, V. R., and Cackler, E. T. (2005). "Real-Time Compaction Monitoring in Cohesive Soils from Machine Response," *Journal of the Transportation Research Board: Transportation Research Record*, 1936, pp. 173-180.

White, D. J., Vennapusa, P. K., and Thompson, M. J. (2007). "Field Validation of Intelligent Compaction Monitoring Technology for Unbound Materials." Center for Transportation Research and Education (CTRE), Iowa State University, Ames, IA.

White, D. J., and Thompson, M. J. (2008). "Relationships Between in Situ and Roller-Integrated Compaction Measurements for Granular Soils." *Journal of Geotechnical and Geoenvironmental Engineering*, American Society of Civil Engineers, 134(12), pp. 1763-1770.

White, D. J., Thompson, M. J., Vennapusa, P., and Siekmeier, J. (2008). "Implementing Intelligent Compaction Specification on Minnesota TH-64 Synopsis of Measurement Values, Data Management, and Geostatistical Analysis." *Transportation Research Record, Journal of the Transportation Research Board*, (2045), pp. 1–9.

White, D. J., Vennapusa, P. K., and Gieselman, H. H. (2011). "Field assessment and specification review for roller-integrated compaction monitoring technologies." Advances in Civil Engineering, Vol. 2011.

White, D., Becker, P., Vennapusa, P., Dunn, M., and White, C. (2013). "Assessing Soil Stiffness of Stabilized Pavement Foundations." *Transportation Research Record: Journal of the Transportation Research Board*, (2335), pp. 99-109.

White, D. J., and Vennapusa, P. K. R. (2015). *Report of the 3rd Workshop for Intelligent Compaction Consortium*. Intrans Project 10-395, Center for Transportation Research and Education (CTRE), Iowa State University, Ames, IA.

Witczak, M. W., and Uzan, J. (1988). *The Universal Airport Design System, Report I of IV: Granular Material Characterization*. College Park, MD.

Witzack, M. W., & Uzan, J. (2004). "Harmonized Test Method for Laboratory Determination of Resilient Modulus for Flexible Pavement Design." NCHRP Project 1-28A, TRB, National Research Council, Washington, D.C.

Wolfe, W., and Butalia, T. (2004). *Continued monitoring of SHRP pavement instrumentation including soil suction and relationship with resilient modulus*, Report No. FHWA/OH-2004/007.

Xia, K. (2011). "Finite element modeling of tire/terrain interaction: Application to predicting soil compaction and tire mobility." *Journal of Terramechanics*, ISTVS, 48(2), pp. 113–123.

Xia, K., and Pan, T. (2010). "Understanding Vibratory Asphalt Compaction by Numerical Simulation." *International Journal of Pavement Research and Technology*, 4(3), pp. 185–194.

Xu, Q., Chang, G. K., Gallivan, V. L., and Horan, R. D. (2012). "Influences of intelligent compaction uniformity on pavement performances of hot mix asphalt." *Construction and Building Materials*, Elsevier Ltd, 30, 746–752.

Xu, Q. (2014). Development of a Computational Method for Inverting Dynamic Moduli of Multilayer Systems with Applications to Flexible Pavements, PhD dissertation, The University of Texas at Austin, Austin, TX.

Yang, S. R., Huang, W. H., and Tai, Y. T. (2005). Variation of Resilient Modulus with Soil Suction for Compacted Subgrade Soils. *Transportation Research Record: Journal of the Transportation Research Board*, (1913), pp. 99-106.

Yau, A., and Von Quintus, H.L. (2002). "Study of LTPP laboratory resilient modulus test data and response characteristics." *Final Report FHWA-RD- 02-051*, U.S. Department of Transportation, FHWA, Washington, D.C.

Yuan, D., and Nazarian, S. (2003). "Variation in Moduli of Base and Subgrade with Moisture." *2003 Annual Meeting of the Transportation Research Board, Road/Pavement Design for Seasonal Effects Session*, Transportation Research Board of the National Academies, Washington, D.C., 15.

Yesuf, G. Y. (2014). "Influence of Subsoil Conditions on the Design and Performance of Flexible Pavements." Norges Teknisk-Naturvitenskapelige Universitet (NTNU) -i Trondheim, Trondheim, Norway.

Yoo, T.-S., and Selig, E. T. (1979). "Dynamics of Vibratory-Roller Compaction." *Journal of the Geotechnical Engineering Division*, ASCE, 105(10), pp. 1211–1231.

Zaman, M., and Khoury, N. (2007). *Effect of Soil Suction and Moisture on Resilient Modulus of Subgrade Soils in Oklahoma*. Norman, OK.

APPENDIX D

Numerical Modeling of Compaction of Geomaterials

Introduction

A summary of the latest studies involving the numerical modeling of compact rollers is provided in Appendix C. The experimental data collected with the instrumented roller compactors reveal complex nonlinear roller vibration behaviors, which include the loss of contact between the drum and the soil, as well as the drum and the frame rocking (Adam and Kopf 2004; Anderegg and Kaufmann 2004; Mooney et al. 2006). Different numerical modeling techniques have been used for estimating the response of the roller.

Finite element (FE) models are the most versatile tools for obtaining the responses of geomaterials under different rollers. Simple 2D linear elasto-static FE models are rapid to execute. But, the 2-D FE modeling approach considers a uniform distribution of responses along the length of the drum (Mooney and Facas 2013). Some FE models include contact models that can better address the stress field and contact width. The execution time can become rather excessive for routine use as the problem is extended to 3D with dynamic loading, and as the plastic and nonlinear geomaterial behaviors are included in the model.

Various researchers considered the unbound granular and subgrade materials as linear-elastic (Patrick and Werkmeister 2010; Xia and Pan 2010; Mooney and Facas 2013), while other have included the Drucker-Prager/cap model (Chiroux et al. 2005; Kim 2010). Hügel et al. (2008) and Wang et al. (2007) further modeled soils using viscoplastic models. The implementation of these models requires the incorporation of laboratory tests such as the direct shear, triaxial and consolidations tests into the specifications. Nonlinear (resilient modulus) models for unbound granular base and subgrade materials as recommended by the mechanistic-empirical pavement design guide (MEPDG) are more realistic than the linear-elastic model since the highest state of stress that most layers experience is during compaction.

In this report, the development of a numerical model consisting of a 3-D FE model simulating the roller compaction of one- and two-layer geosystems is presented. Different levels of complexity in the model are being considered including the use of both linear and nonlinear geomaterial models, and the simulation of the roller operation from a static load, to stationary vibratory, to moving vibratory loads. The responses from each model with different geomaterial properties have been numerically assessed. Correlations have established among the responses from different models to study whether the simplified models can account for the behavior of the pavement under compaction adequately, and whether these relationships can be used to simplify the modeling.

Finite Element Modeling of Roller Compaction

Since the numerical modeling of soil response due to roller compaction is rather complex, a dynamic FE technique is necessary to evaluate the interaction of the roller with the geosystem. LS-DYNA, which is a multi-purpose FE program that makes use of explicit and implicit time integration techniques, is used to address this need. A 3-D mesh was assembled to represent a roller imparting energy to the geomaterials at a given amplitude and vibrating frequency. Figure D-1 shows a 3-D view of the geosystem and the roller. The drum of the roller compactor was modeled with rigid shell elements with common dimensions of IC

rollers (i.e., 2 m [80 in.] wide and 0.75 m [30 in.] in radius). Due to the size of the drum, the geomaterial was modeled as 4 m (160 in.) wide, 4 m (160 in.) long, and 2.5 m (100 in.) deep with non-reflective boundaries. A mesh consisting of brick elements was used to represent the geosystem. About 64,000 elements were used to model the geomaterials. Smaller elements with 50×50×50 mm (2×2×2 in.) dimensions were used underneath the roller up to 0.5 m (20 in.) in depth, 0.6 m (24 in.) longitudinally and 1.2 m (48 in.) transversally from the center of the roller, after which the elements become larger. To establish better the contact of the drum nodes with the soil's mesh, about 75,000 shell elements were used to simulate the drum.

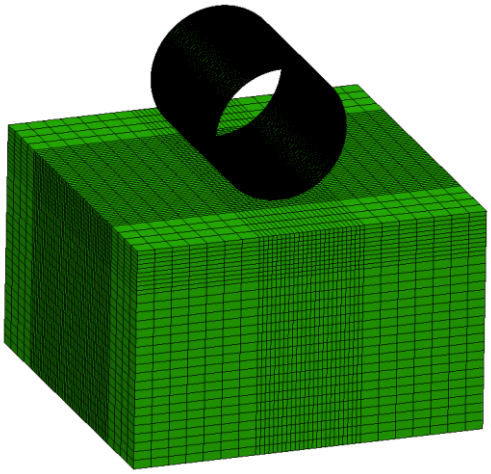

Figure D-1. FE modeling of roller and pavement structure.

Drum-Soil Contact Interaction

Figure D-2 shows the roller to surface contact model. The interaction between the roller and the geosystem was simulated using LS-DYNA's "Automatic Single-Surface" contact type. The single-surface contact types behave similarly to the surface-to-surface elements where a master surface and a slave surface are defined from a list of components. Unlike the Automatic Surface-to-Surface contact type, only one surface is defined and contact is considered between all the components that are in contact with the defined surface.

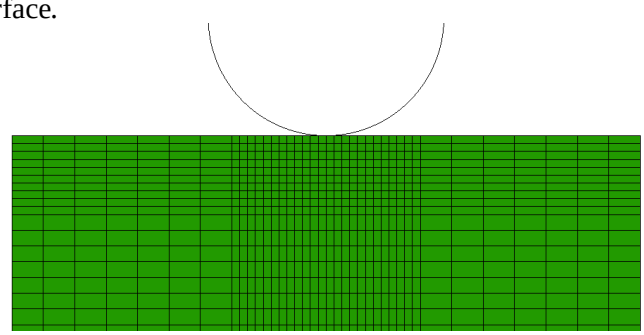

Figure D-2. Roller to soil contact.

A penalty method was implemented in single-surface contact type, where each slave node was checked for penetration through the master surface, as shown in Figure D-3. If the slave node penetrates, an interface force $\mathbf{f_s}$ is applied between the slave node and its contact point. The magnitude of this force is proportional to the amount of penetration that can be thought of as the addition of an interface spring. The interface force is a function of a stiffness factor k_i and penetration l of slave node n_s through master segment $\underline{s_i}$ given as

$$\mathbf{f_s} = -lk_i\mathbf{n_i} \quad \text{if } l < 0 \tag{D.1}$$

where $\boldsymbol{n_i}$ is the normal to master segment at the contact point. The stiffness factor k_i for the master segment s_i is given in terms of a bulk modulus K_i, the volume V_i, and the face area A_i of the element that contains s_i as:

$$k_i = \frac{f_{si}K_iA_i^2}{V_i} \quad \text{for brick elements, and} \tag{D.2}$$

$$k_i = \frac{f_{si}K_iA_i}{\max(\textit{shell diagonal})} \quad \text{for shell elements,} \tag{D.3}$$

where f_{si} is a scale factor for the interface stiffness and is normally defaulted to 0.10 (LSTC 2016).

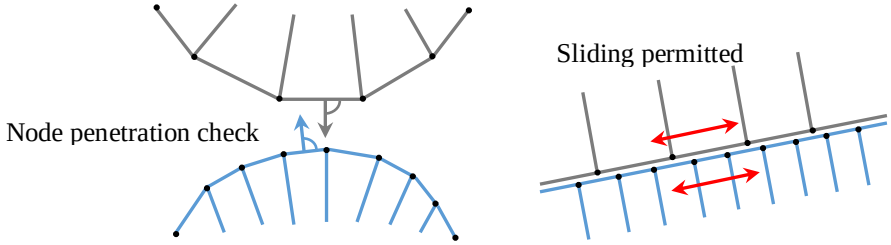

Figure D-3. Automatic single-surface contact to model drum-soil interface.

Constitutive Model

The ME design guides usually require the measurement or estimation of the resilient modulus (M_R) of each unbound layer as input for the calculation of the pavement response. The material model used in most ME guides is a variation of

$$M_R = k_1P_a\left(\frac{\theta}{P_a}\right)^{k_2}\left(\frac{\tau_{oct}}{P_a}+1\right)^{k_3} \tag{D.4}$$

where θ is the bulk stress, and τ_{oct} is the octahedral shear stress, P_a is the normalizing stress (atmospheric pressure) of 100 kPa (14.7 psi), k_1, k_2, and k_3 are model parameters (determined form fitting the laboratory data to the model). The bulk normal stress and the octahedral shear stress are defined as

$$\theta = \sigma_1 + \sigma_2 + \sigma_3 \tag{D.5}$$

$$\tau_{oct} = \frac{1}{3}\sqrt{(\sigma_1-\sigma_2)^2+(\sigma_2-\sigma_3)^2+(\sigma_1-\sigma_3)^2} \tag{D.6}$$

where σ_i is one of the principal stresses. The *k*-values capture the nonlinearity and stress sensitivity of the stiffness properties of the unbound granular materials. The model contains a hardening term and a softening term to capture the stiffening behavior due to the densification as well as the degradation of the modulus due to the shear softening in the unbound materials.

Pavement ME recommends the measurement of resilient modulus parameters from the laboratory testing (Level 1), the use of correlations with other material properties (Level 2) or estimating them based on their soil classifications (Level 3). The input level selected affects the procedure for determining the structural responses of the pavement system (Khazanovich et al. 2006).

The moduli required for design purposes must represent the state of stress due to vehicular loads and overburden pressure. Since the state of stress in pavements is a function of the selected moduli, a rigorous process for selecting the modulus has to be through an iterative process. To simplify this process, NCHRP 1-28A recommended the states of stress of θ = 210 kPa (31 psi) and τ_{oct} = 50 kPa (7.5 psi) for base and subbase materials, and θ = 85 kPa (12.4 psi) and τ_{oct} = 20 kPa (3 psi) for subgrade soils (Oh 2011).

Nazarian et al. (2014) found the resilient modulus constitutive model proposed by Ooi et al. (2004) using AASHTO T-307-93 loading sequences yields more representative responses of the modulus-based devices for estimating the nonlinear structural response of geomaterials as compared to the standard MEPDG equation. The constitutive model proposed by Ooi et al. (2004) is given by

$$M_R = k_1' P_a \left(\frac{\theta}{P_a} + 1 \right)^{k_2'} \left(\frac{\tau_{oct}}{P_a} + 1 \right)^{k_3'} \tag{D.7}$$

where k'_1, k'_2, and k'_3 are model parameters (determined from fitting the laboratory data to the model). Nazarian et al. (2014) also provided the following relationships between the regression parameters of the MEPDG and Ooi models:

$$k_1' = k_1 e^{-1.32 k_2}, \tag{D.8a}$$

$$k_2' = 1.88 k_2, \text{ and} \tag{D.8b}$$

$$k_3' = k_3 . \tag{D.8c}$$

To implement the modified MEPDG constitutive model, a user defined material (UMAT) FORTRAN subroutine was incorporated into LS-DYNA. The inclusion of the UMAT subroutines requires the use of implicit analysis. Considering a large number of elements in the model, the implicit time integration method required the use of an iterative solver using the Lanczos with Incomplete Choleski pre-conditioner method for solving the system of equations. This method was chosen as the symmetric multiprocessor (SMP) parallel multi-frontal sparse solver was unable to obtain the responses without incurring in the use of a very large amount of physical memory (RAM).

Vibratory Load and Damping

The centrifugal force caused by the rotation of the eccentric masses inside the drum induces an excitation force, F_e, defined as

$$F_e(t) = m_0 e_0 \Omega^2 \cos(\Omega t), \tag{D.9}$$

where Ω is the rotational frequency and e_0 is the eccentricity of the counter-rotating masses m_0. Typical values used for the simulated drum are shown in Table D-1. The vibratory motion of the roller was maintained for t = 200 msec, equivalent to six load cycles. The stress, strain, and displacement time histories were calculated for every time interval of one msec underneath the center of the roller.

Table D-1. Specifications for simulated drum.

Operating Parameter	Symbol	Value
Width of drum (compaction width)	L	2.0 m (80 in.)
Diameter of drum	d	1.5 m (60 in.)
Mass of drum	m_d	6000 kg (34.3 lb·s^2/in)
Weight of drum	$m_d g$	58,840 N (13,200 lb)
Mass-eccentricity	$m_0 e_0$	5.36 kg·m (1.20 lb·s^2)
Centrifugal force (Vertical excitation force)	F_{ev}	170 kN (38 kips)
Frequency	f	28 Hz (1680 vpm)
Frequency	Ω	176 rad/s
Operating speed	v	0.9 m/s (3.24 km/h, 2.0 mph)

The Rayleigh damping as defined by Equation D.10 was introduced to simulate the material damping in the soil:

$$[C] = \alpha [M] + \beta [K] \quad \text{(D.10)}$$

where $[M]$ is the mass matrix, $[K]$ is the stiffness matrix, and Rayleigh constants were defined as $\alpha = 25$ and $\beta = 0.0002$ as recommended by Mooney and Facas (2013) to minimize the dilatational and shear wave reflections.

Development of Comprehensive Database of Pavement Sections

A comprehensive database of linear and nonlinear 3D dynamic cases with different input parameters was assembled for single-layer and two-layer geosystems. The information stored in the database was used to evaluate the sensitivity of the geosystem response to different input parameters. The database contains the following general types of data:

- Roller operating parameters, including drum dimensions, mass of drum, frequency, vertical excitation force, and operating speed.
- Geosystem structure and geomaterials properties, including layer thickness, nonlinear k' parameters of layers, and the representative resilient modulus per layer.
- Level of sophistication of the FE model, including the type of analysis (static, quasi-static or dynamic), geomaterial constitutive model (linear-elastic or nonlinear), and contact type (roller load applied directly to the geosystem or by means of a contact model).
- Pavement responses obtained after simulation of roller compaction, including maximum surface vertical displacement, maximum stress observed under the load, and depth of influence.

Pavement Structure and Geomaterial Properties

Three groups of geosystems were simulated consisting of a single-layer (subgrade only) system and two-layer systems with top layer (base) thicknesses of 150 mm (6 in.) and 300 mm (12 in.) on top of the subgrade. Feasible ranges of k nonlinear parameters as proposed by Velasquez et al. (2009) for the coarse- and fine-grained geomaterials are shown in Table D-2.

Table D-2. Feasible range of layer properties (Velasquez et al. 2009).

Material Type	Nonlinear Parameters		
	k_1	k_2	k_3
Coarse-grained	400 – 3000	0.2 – 1.0	-0.9 – -0.1
Fine-grained	1000 – 4000	0.01 – 0.5	-6.0 – -1.5

For each geosystem, 200 randomly generated cases were selected considering a uniform distribution within the feasible range of values shown in Table D-2. This prototype database that contained information about the distributions of stress, strain, displacement, modulus (when applicable) was used to study the feasibility of different concepts. As soon as a concept deemed feasible, a more expanded strategic database relevant to that concept was developed.

The representative resilient modulus of the base was not allowed to exceed 700 MPa (100 ksi) nor less than 70 MPa (10 ksi), while the representative resilient moduli of subgrade were limited to 350 MPa (50 ksi) to 35 MPa (5 ksi).

Level of Sophistication of FE Model

Six levels of sophistication of the FE model were considered as represented in Table D-3. The main levels of sophistication consisted of the following items:

- **Linear vs. Nonlinear Behavior of Geomaterials:** The use of the nonlinear material models requires iterative procedures to update the state of stress during the simulation leading to longer execution times. For this reason, the linear-elastic material models are commonly used. The responses of the linear models were compared with their comparable nonlinear models to explore the possibility of establishing relationships that could estimate the nonlinear response knowing the linear response and the geomaterial k′ nonlinear parameters.
- **Static vs. Vibratory Drum:** The implications of considering the applied load as static instead of vibratory were also studied. For static loading conditions, a quasi-static analysis was implemented, where the load was applied in 1 msec as a ramp load until the peak excitation force was reached, and then the load was maintained at a constant magnitude for the following 19 msec. In that manner, the impact of inertia was reduced, allowing the contact elements accommodate the drum. The simulation of a vibratory load consisted of a sinusoidal load with peak vertical force of 170 kN (38 kips) and a frequency of 28 Hz, in addition to the weight of the drum. At that frequency, six load cycles were produced in 200 msec of simulation time.
- **Stationary vs. Moving/Rolling Drum:** To accommodate the rolling movement of the drum, a prescribed motion to the drum was included in the input, where velocity, angular velocity and direction of movement were specified. These assumptions lend to slower executions if the nonlinear behavior of the geomaterials was considered due to the iterative process required to update the state of the stress. Stationary drums were simulated at a unique location; thus, a prescribed motion input was not included. The vibrating load applied to the drum is still included in the models.

Table D-3. Characteristics of different levels of sophistication of FE model for parametric study.

FE Model Characteristics	Label	Load Type	Constitutive Model	Roller Velocity
Static Stationary Linear	SSL	Static	Linear-Elastic	-
Static Stationary Nonlinear	SSN	Static	Modified MEPDG	-
Vibratory Stationary Linear	VSL	Dynamic	Linear-Elastic	-
Vibratory Stationary Nonlinear	VSN	Dynamic	Modified MEPDG	-
Vibratory Moving Linear	VML	Dynamic	Linear-Elastic	0.9 m/s (3 mph)
Vibratory Moving Nonlinear	VMN	Dynamic	Modified MEPDG	0.9 m/s (3 mph)

Computation Time

The level of sophistication of the FE model affects the analysis time. The analysis time increases as the model becomes more sophisticated. The model becomes more sophisticated in the order listed in Table D-3. Typical analysis times for a higher end personal computer are shown in Table D-4. Simulation of six load cycles of the vibratory load took about ten times longer than analyses with a static load. The inclusion of the nonlinear soil model increased the computation time by 3 seconds per time step, or ~20% more time than the linear case. The moving/rolling motion of the drum increased the computational time by 1 second per time step as compared to the stationary vibratory case.

Table D-4. Typical computation time on a 3.30 GHz Intel i5-4590 and 8 GB RAM, 64-bit operating system for different levels of sophistication of the FE model.

FE Model Type	Total Computation Time, min	Computation Time per Time Step, sec
SSL	5	14
SSN	6	17
VSL	54	16
VSN	64	19
VML	57	17
VMN	68	20

Evaluation of Pavement Responses at Different Levels of Sophistication of FE Model

The goal of this task was to find an optimized model among the six models in Table D-4 to simulate the response of different geomaterials subjected to a vibratory roller. As indicated before, given the amount of information available, deciphering the mechanical properties of more than two layers is not feasible.

Effect of Nonlinear Behavior of Geomaterials on Geosystems' Responses

- **Static Loading.** The roller responses of one and two-layer geosystems were evaluated simulating the load imposed by the drum as static and geomaterials simulated as static stationary linear (SSL) or as nonlinear (SSN). By comparing these responses, the following observations were made:
  - ***Single-Layer System:*** As shown in Figure D-4, the displacements obtained with the nonlinear (SSN) and linear (SSL) models seemed to be correlated with some uncertainty as judged by the number of cases lying outside the ±20% uncertainty bounds.
  - ***Two-Layer System:*** As shown in Figure D-5, fewer cases fell outside the ±20% uncertainty lines and lower standard errors of estimate were observed as compared to single-layer geosystems. The stiffer top layer (base) tended to reduce the effects of the nonlinear behavior of the subgrade as the stresses attenuated more.

  The examples above imply that establishing relationships that account for the nonlinearity of geomaterials is viable.
- **Vibratory Stationary Loading.** Based on the comparison of the maximum displacements of one and two-layer geosystems using vibratory linear (VSL) and nonlinear (VSN) FE models, the following observations were made:
  - ***Single-Layer System:*** As shown in Figure D-6, a well-correlated relationship between the displacements of the linear (VSL) and nonlinear (VSN) cases exists. In comparison to the static stationary (SSL vs. SSN) cases for single-layer systems, the correlation exhibits higher R^2 and lower standard errors of estimate.
  - ***Two-Layer System:*** Figure D-7 shows that the uncertainty of the results decreases in comparison to the results for the single-layer subgrade. Fewer cases are outside of the ±20% error bounds. In other words, the nonlinear behavior of geomaterials is diminished when a stiffer top (base) layer is placed; therefore, deploying a stiffer top (base) layer over the subgrade results in higher R^2 and lower standard errors of estimate.

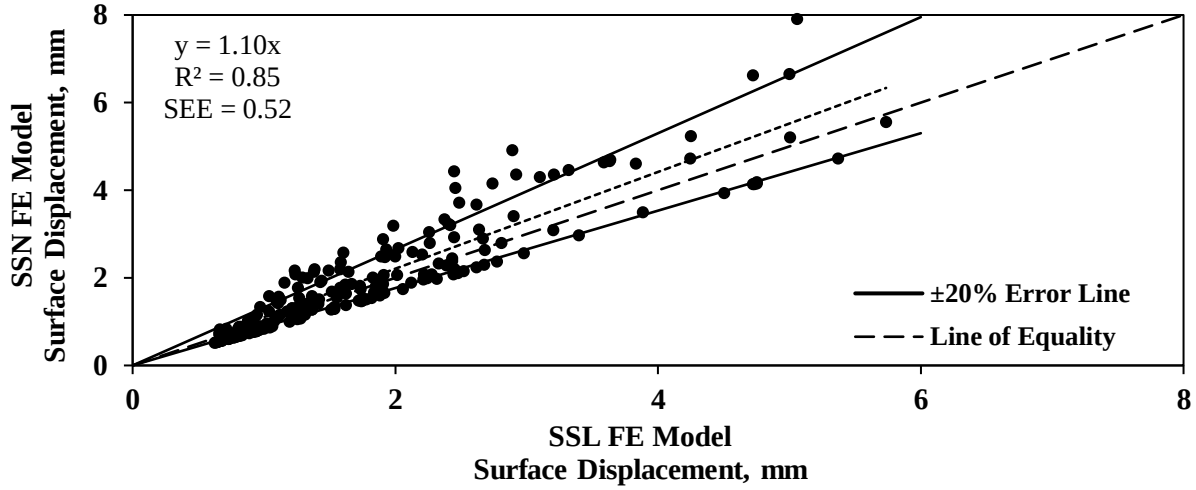

Figure D-4. Relationship of surface displacement under roller between linear (SSL) and nonlinear (SSN) static stationary FE models for a single-layer (subgrade) geosystem.

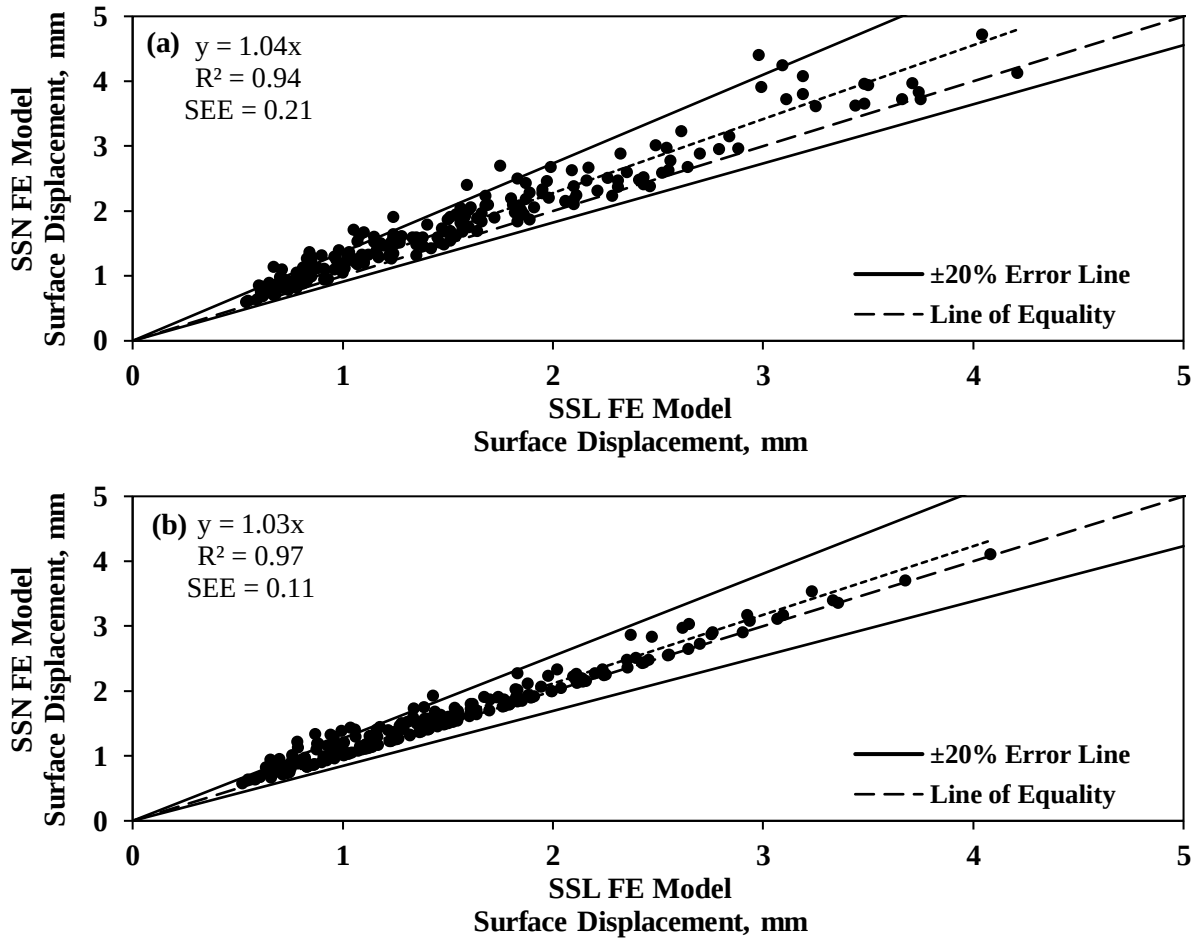

Figure D-5. Relationship of surface displacement under roller between linear (SSL) and nonlinear (SSN) static stationary FE models for two-layered geosystem with (a) 150 mm (6 in.) base layer and (b) 300 mm (12 in.) base layer on top of subgrade.

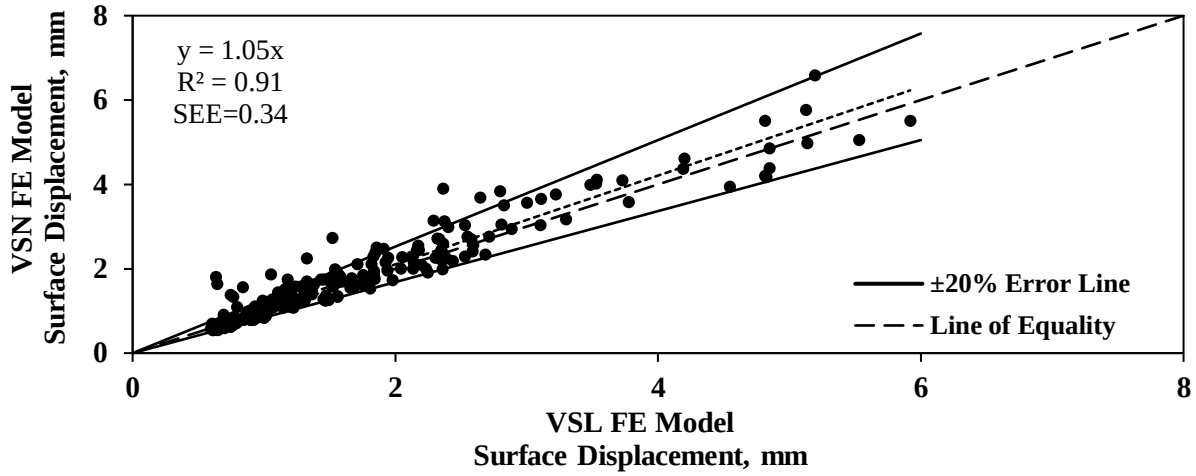

Figure D-6. Relationship of surface displacement under roller between linear (VSL) and nonlinear (VSN) vibratory stationary FE models for a single-layer (subgrade) geosystem.

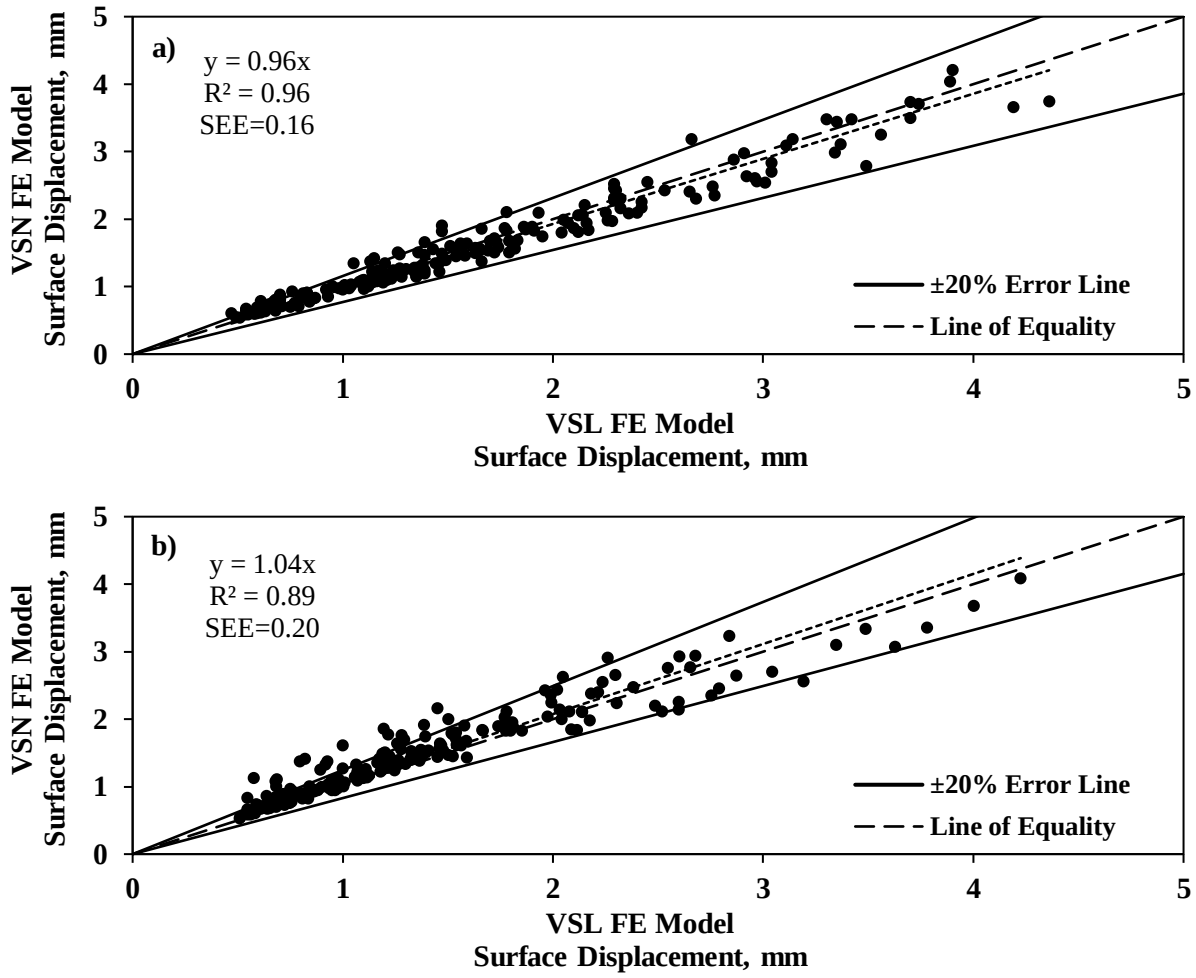

Figure D-7. Relationship of surface displacement under roller between linear (VSL) and nonlinear (VSN) vibratory stationary FE models for two-layer geosystem with (a) 150 mm (6 in.) base layer and (b) 300 mm (12 in.) base layer on top of subgrade.

- **Vibratory Moving Loading.** Considering the nonlinear behavior of geomaterials subjected to a vibratory, but moving, roller (VML vs. VMN) yielded the following observations:
  - ***Single-Layer System:*** Figure D-8 shows that the maximum displacements observed from the nonlinear (VMN) cases are correlated well with the corresponding results obtained from the linear (VML) cases. The stiffer the geomaterials are, the more scattered the results will be. Vibratory moving (VML vs. VMN) cases demonstrate lower R^2 and higher standard errors of estimate (SEE), compared to the correlations observed for vibratory stationary (VSL vs. VSN) cases.
  - ***Two-Layer System:*** Figure D-9 shows the relationships obtained from the two-layer geosystems. The slopes of the best-fit lines are similar to the ones observed for the single-layer geosystems, the relationships between the linear and nonlinear cases for the two-layer geosystems show an improvement in R^2 and SEE values compared to single-layer geosystems.

Effect of Vibratory Motion of Drum on Pavement Responses

The displacements under a vibratory stationary and a static stationary roller were compared to study the influence of the vibratory motion of the drum on the geomaterials' responses.

- **Linear-Elastic Geosystems.** For the cases when the geomaterials are considered linearly elastic, the outcome of this study can be summarized in the following manner:
  - ***Single-Layer System:*** The displacements observed from VSL and SSL FE models agree well. Figure D-10 confirms that the displacements of the linear-elastic geomaterials calculated from both scenarios are not sensitive to the vibratory motion of drum.
  - ***Two-Layer System***: The corresponding displacements for the two-layer linear-elastic geosystems obtained from the VSL and SSL FE analyses are compared in Figure D-11. A decrease in the soil stiffness leads to more variations in the results as more scatter is observed in those areas. The correlation between the static and vibratory FE models improves with a reduction in the base thickness.
- **Nonlinear Geosystems**. For the cases when the geomaterials are considered nonlinear, the outcome of this study can be summarized in the following manner:
  - ***Single-Layer System:*** As shown in Figure D-12, the displacements from the static and vibratory conditions are correlated well for the softer geosystems that experience greater displacements. However, for the stiffer geosystems, the relationship is less certain.
  - ***Two-Layer System:*** Figure D-13 shows that the trend observed for each of the two base thicknesses is similar to the trend explained for the single-layer geosystems. Once again, the standard errors of estimate (SEE) for the two-layer geosystems are less than those from the comparable single-layer geosystems.

Effect of Rolling and Translational Motion of Drum on Pavement Responses

The displacements from a vibratory stationary roller are compared to the comparable responses obtained from the vibratory rolling cases when the drum moved at a speed of 0.9 m/s (3 mph) and rotated with an angular velocity of 1.2 rad/s.

- **Linear-Elastic Geosystems.** For the case when the geomaterials are considered linearly elastic, the outcome of this study can be summarized in the following manner:
  - ***Single-Layer System:*** Figure D-14 indicates that the displacements from the moving and stationary rollers are correlated. The surface displacements imposed by a vibratory (VML) roller can be predicted using the responses under a stationary (VSL) roller.
  - ***Two-Layer System:*** The relationships between the displacements under the stationary and moving rollers for the two-layer geosystems are correlated well as shown in Figure D-15. As the thickness of the base layer increases, the dispersion in the results increases.

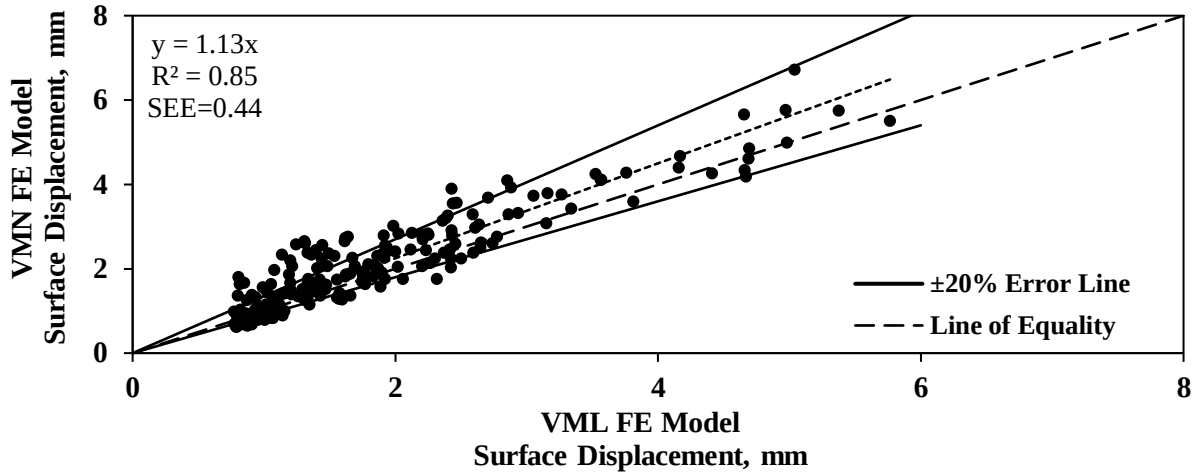

Figure D-8. Relationship of surface displacement under roller between linear (VML) and nonlinear (VMN) vibratory moving FE models for a single-layer (subgrade) geosystem.

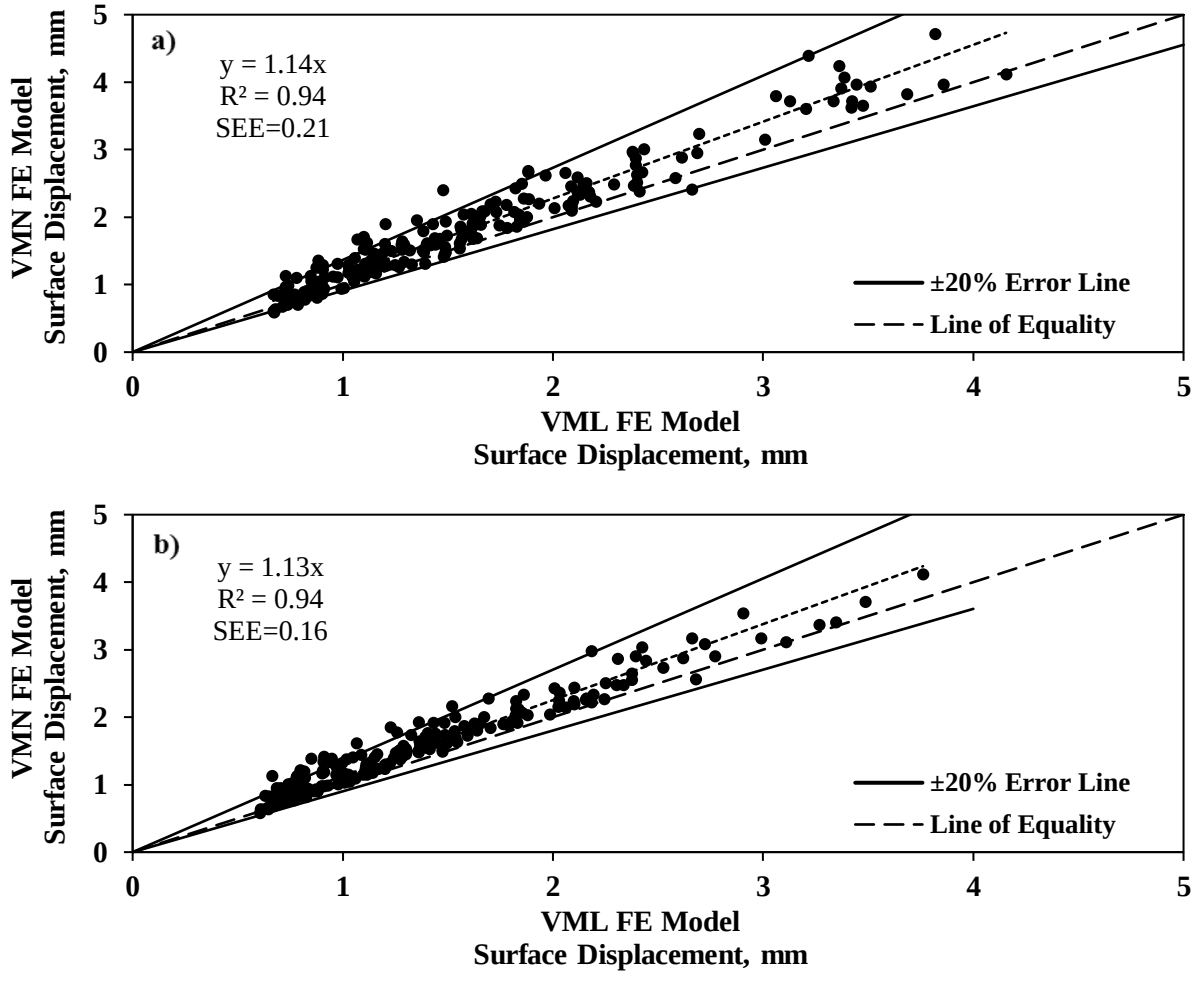

Figure D-9. Relationship of surface displacement under roller between linear (VML) and nonlinear (VMN) vibratory moving FE models for two-layer geosystem with (a) 150 mm (6 in.) base layer and (b) 300 mm (12 in.) base layer on top of subgrade.

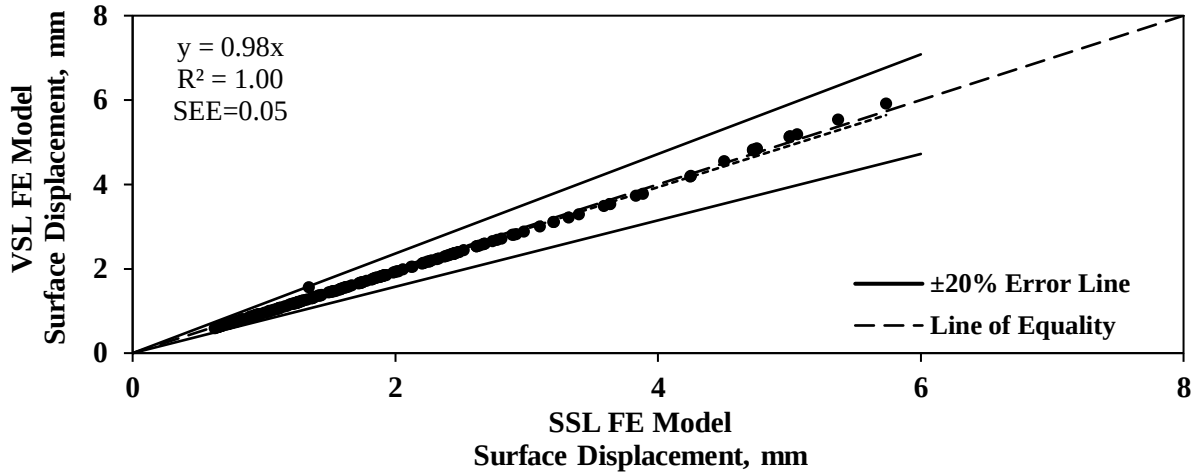

Figure D-10. Relationship of maximum surface displacement under roller between vibrating stationary (VSL) and static stationary (SSL) linear FE models for a single-layer system.

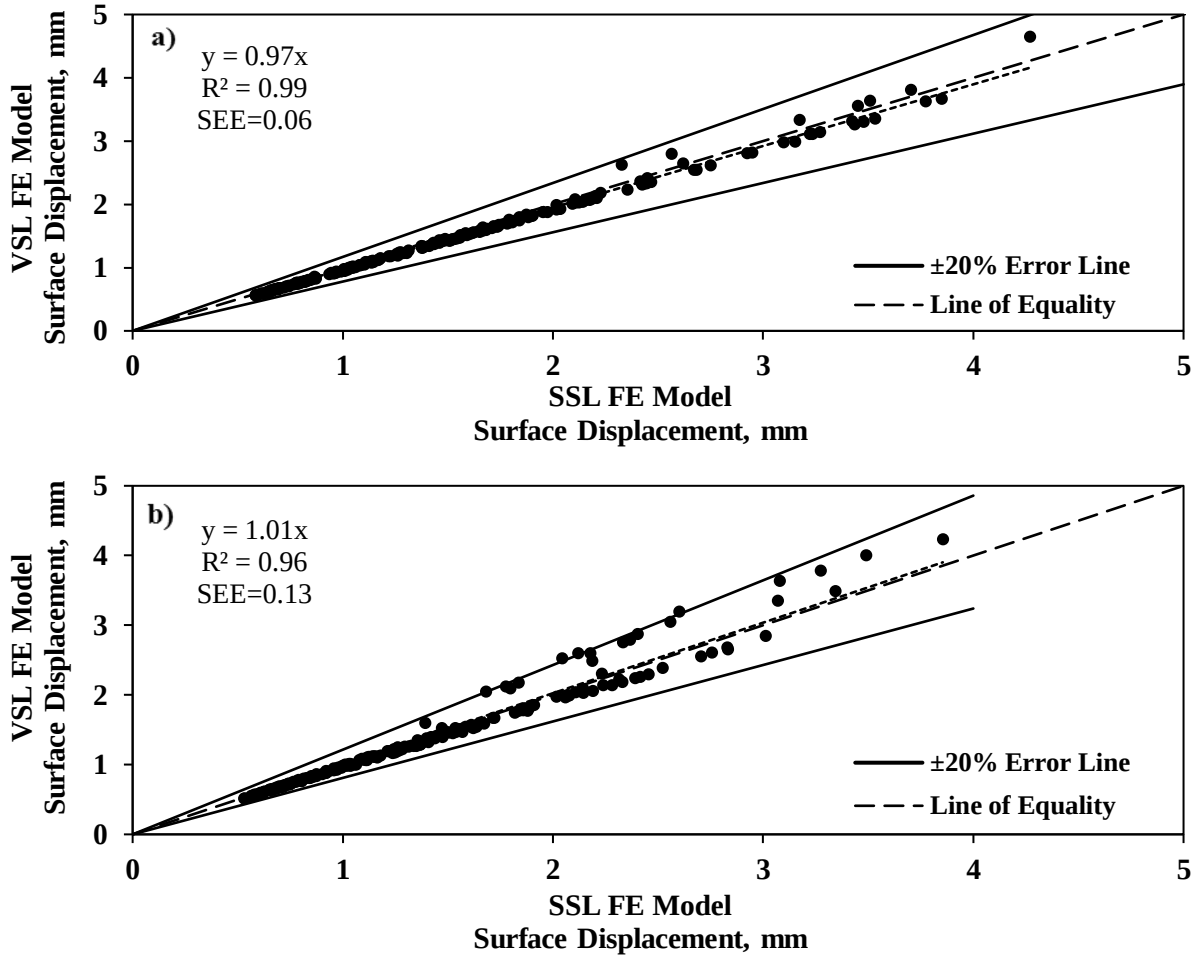

Figure D-11. Relationship of surface displacement under roller between vibratory stationary (VSL) and static stationary (SSL) linear FE models for two-layer systems consisting of (a) 150 mm (6 in.) base layer and (b) 300 mm (12 in.) base layer on top of subgrade.

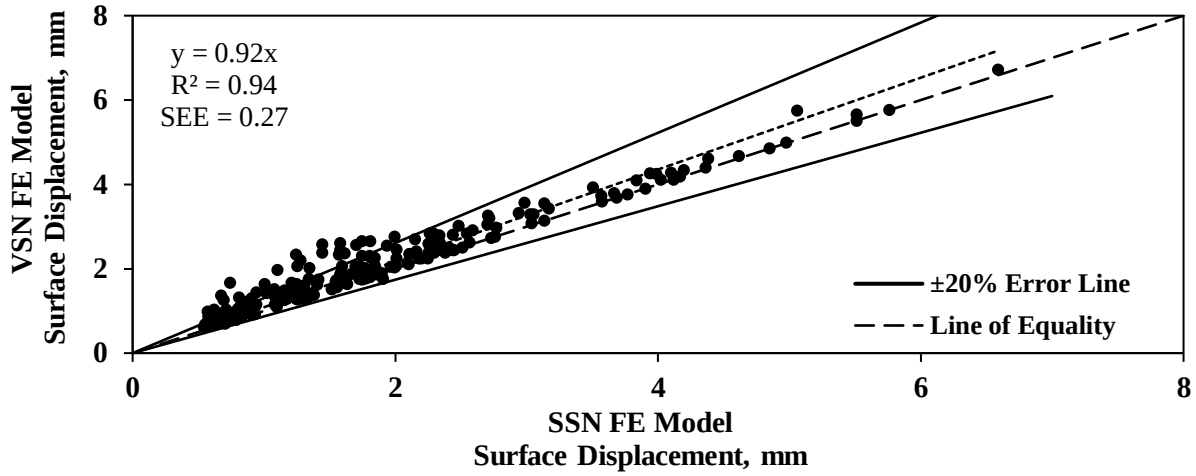

Figure D-12. Relationship of maximum surface displacement under roller between vibrating stationary (VSN) and static stationary (SSN) nonlinear FE models for a single-layer system.

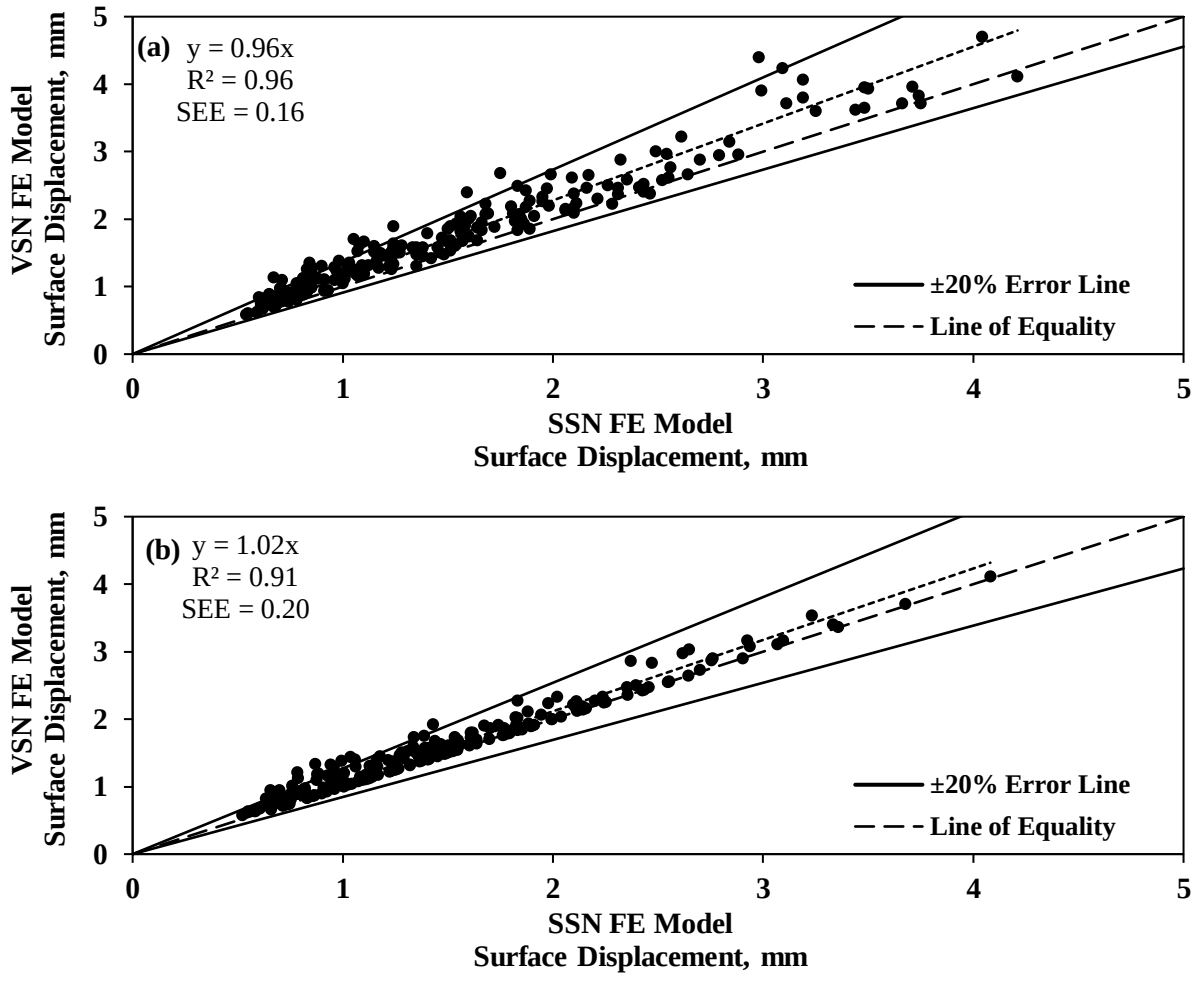

Figure D-13. Relationship of surface displacement under roller between vibratory stationary (VSN) and static stationary (SSN) nonlinear FE models for two-layer systems consisting of (a) 150 mm (6 in.) base layer and (b) 300 mm (12 in.) base layer on top of subgrade.

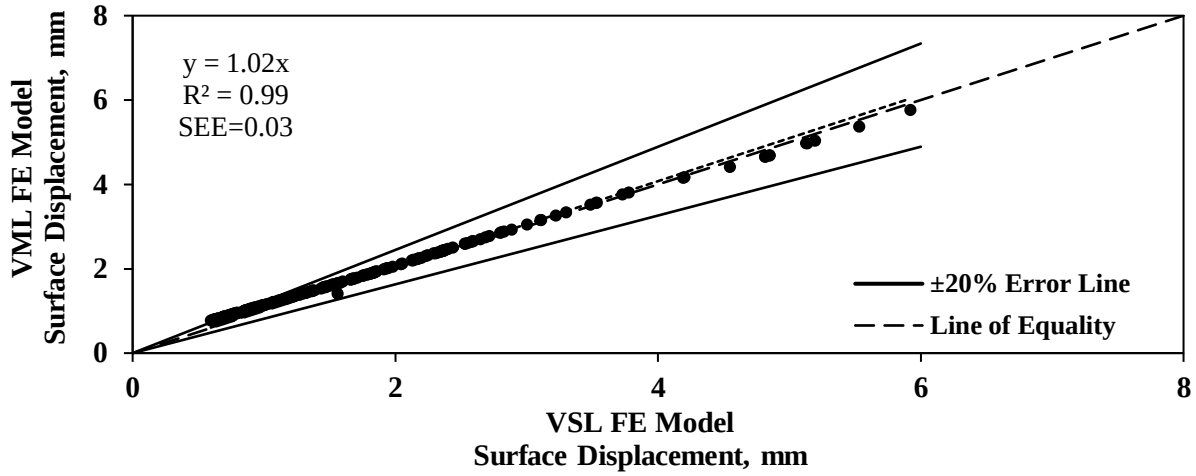

Figure D-14. Relationship of maximum surface displacement under roller between vibratory stationary (VSN) and vibratory moving (VMN) linear FE models for a single-layer system.

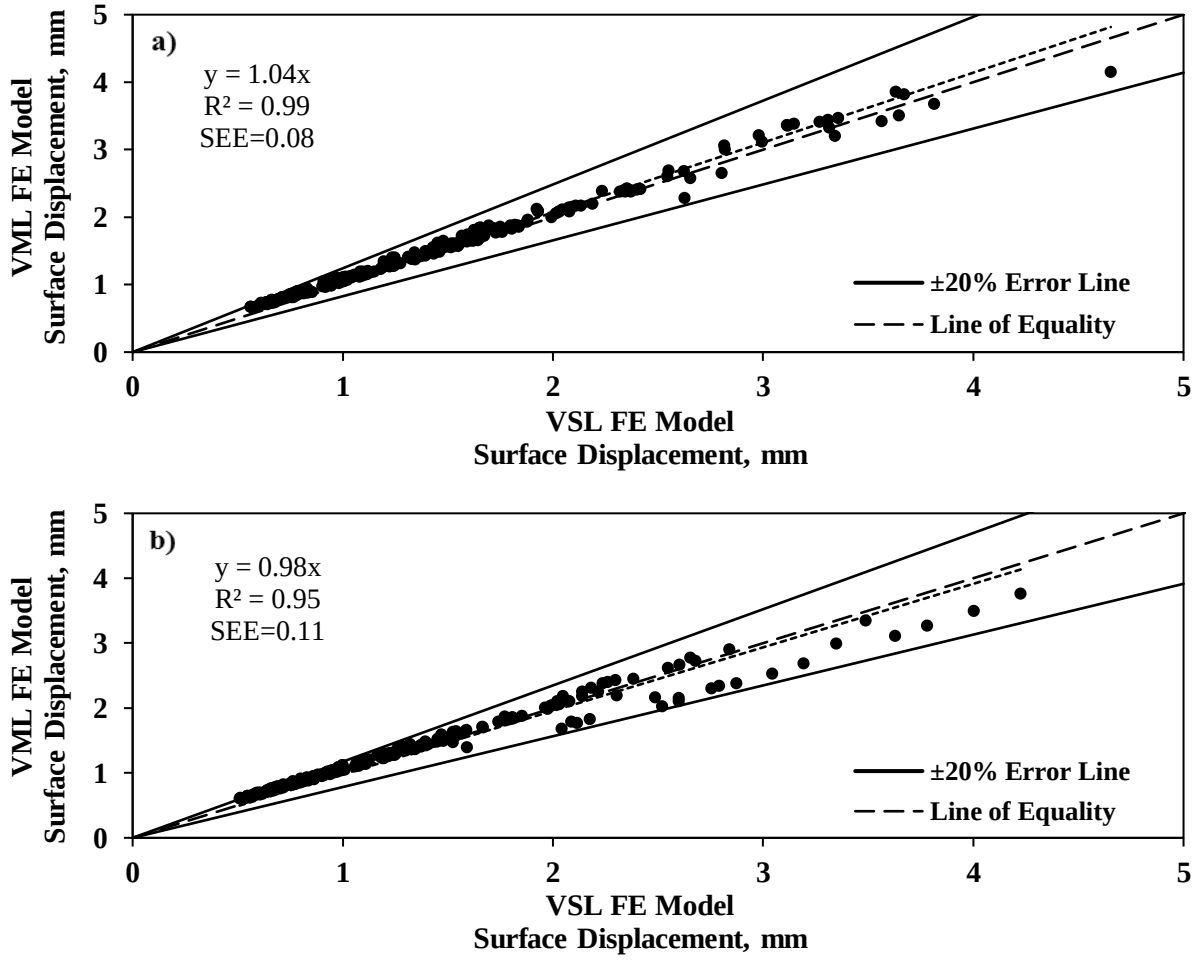

Figure D-15. Relationship of maximum surface displacement under roller between vibratory stationary (VSN) and vibratory moving (VMN) linear FE models for two-layer systems consisting of (a) 150 mm (6 in.) base layer and (b) 300 mm (12 in.) base layer on top of subgrade.

- **Nonlinear Geosystems.** For the case when the geomaterials are considered nonlinear, the outcome of this study can be summarized in the following manner:
  - ***Single-Layer System:*** Figure D-16 shows that the displacements from the rolling and stationary rollers demonstrate the same trends but with some uncertainty at the lower displacements (stiffer geosystems) as judged by the number of cases falling outside the ±20% uncertainty bounds.
  - ***Two-Layer System:*** Figure D-17 shows that the relationships between the stationary and moving rollers are similar to the trend observed for the single-layer geosystem, with the SEE being less for the two-layer geosystems.

Summary of Level of Sophistication of FE Model on the Pavement Responses

The slopes, coefficients of determination (R^2 values) and normalized SEE of the regression lines from all scenarios reported are summarized in Table D-5 for the single-layer system and Table D-6 for two-layer geosystems. The normalized standard error of the estimate, NSEE, is calculated from

$$NSEE = \sqrt{\frac{\sum_{i=1}^{n}(Y_i' - Y_i)^2}{\sum_{i=1}^{n}(Y_i')^2}} \tag{D.11}$$

where Y'_i is the estimated displacement obtained from the linear equation of the fitted trend and Y_i is the displacement from the FE simulation. Parameter n is the total number of points.

From Tables D-5 and D-6, almost all displacement pairs are correlated with the R^2 values of greater than 0.85 and typically greater than 0.90. The normalized errors of estimate that are typically less than 0.2, indicate that perhaps one can include other geomaterials-related parameters to improve the relationships. The descriptive statistics provide an indication that the surface deflection as obtained from the more sophisticated FE models may be estimated using relationships that adjust the responses of the less sophisticated, i.e. less computationally expensive, FE models.

Influence Depth of Roller

The penetration depth is worthy of attention as a measure of influence of compaction as well as a representative measurement of a composite ICMV during the backcalculation of the layers' mechanical properties. The depth of influence can be determined based on different criteria, such as the depth at which the geomaterial's response diminishes to 10% of the peak observed response. Different depths can be obtained based on the selection criterion being either the displacements or stresses or strains developed beneath the drum. The impact of geomaterials' properties, in terms of the nonlinear parameters, on the depth of influence was studied using the databases discussed above. In this section, the results obtained from different FE models with different levels of sophistication are discussed.

Influence Depth with Respect to Displacement

The study focused on the impact of the representative resilient moduli for the linear-elastic cases as well as the nonlinear parameters k'_1 through k'_3 for all cases. The analyzed cases were categorized into three different ranges of k'_1 values, corresponding to soft, intermediate and stiff geomaterials. Unless otherwise stated, the depths of influence are based on the displacement criterion. For consistency, the influence depths were normalized with respect to the roller contact width. The drum contact width was found to be about 300 mm (12 in.) for the simulated drum with operating features presented in Table D-1.

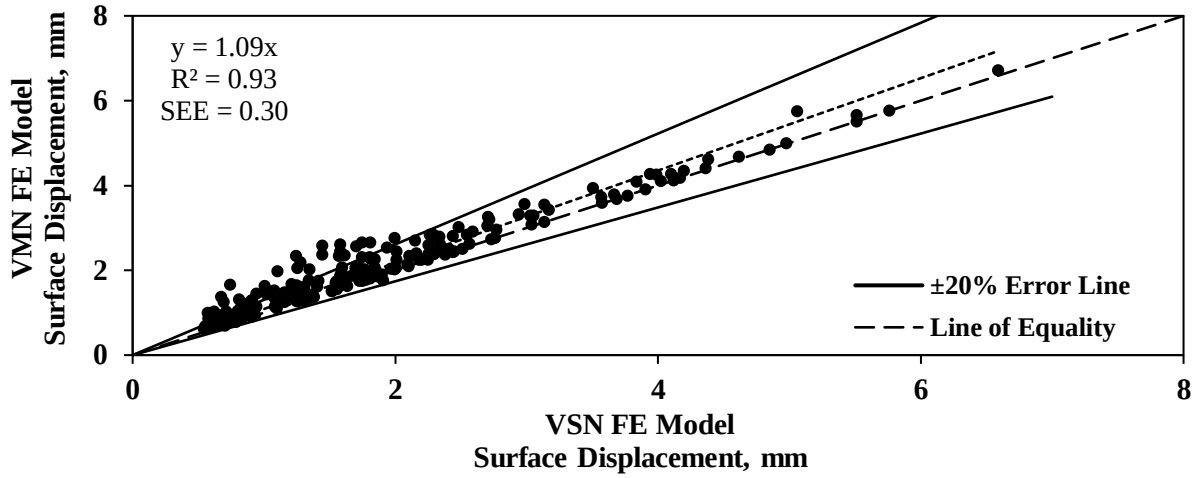

Figure D-16. Relationship of maximum surface displacement under roller between vibratory stationary (VSN) and vibratory moving (VMN) nonlinear FE models for a single-layer system.

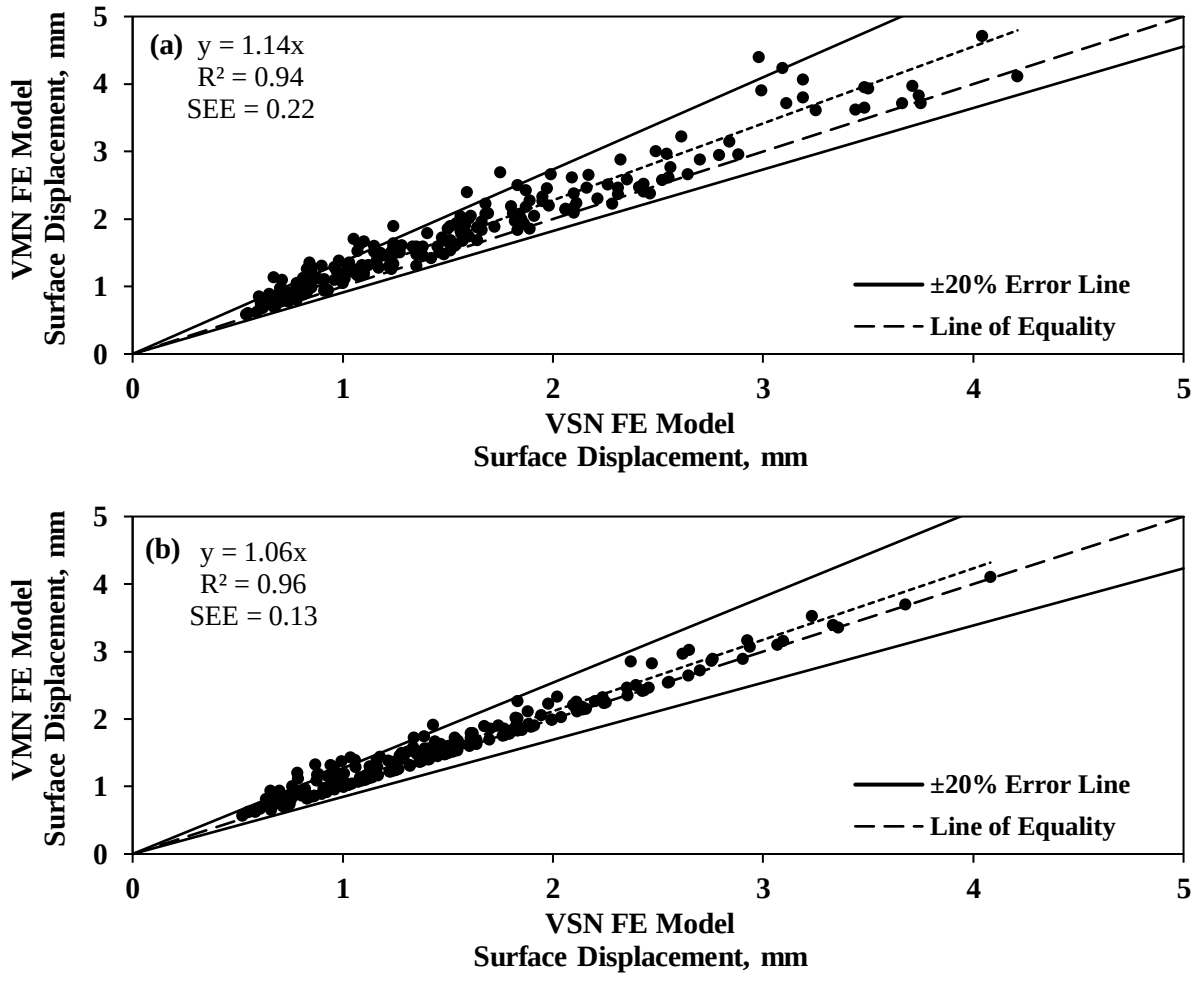

Figure D-17. Relationship of maximum surface displacement under roller between vibratory stationary (VSN) and vibratory moving (VMN) nonlinear FE models for two-layer systems consisting of (a) 150 mm (6 in.) base layer and (b) 300 mm (12 in.) base layer on top of subgrade.

Table D-5. Summary of descriptive statistics for various levels of sophistication of FE model of single-layer pavement system.

Model	Slope of Fitted Linear Relationship						Coefficient of Determination, R^2						Normalized Standard Error of Estimate, NSEE					
	SSL	SSN	VSL	VSN	VML	VMN	SSL	SSN	VSL	VSN	VML	VMN	SSL	SSN	VSL	VSN	VML	VMN
SSL	1	1.10	0.98	1.04	1.00	1.13	1	0.85	1.00	0.92	0.99	0.93	-	0.22	0.03	0.15	0.04	0.19
SSN		1	0.85	0.92	0.87	1.00		1	0.83	0.95	0.79	0.90		-	0.23	0.12	0.23	0.15
VSL			1	1.05	1.02	1.14			1	0.91	0.99	0.82			-	0.16	0.05	0.21
VSN				1	0.95	1.09				1	0.90	0.93				-	0.16	0.12
VML					1	1.13					1	0.85					-	0.19
VMN						1						1						-

Table D-6. Summary of descriptive statistics for various levels of sophistication of FE model of two-layered pavement system.

(a) 150 mm (6 in.) base on top of subgrade.

Model	Slope of Fitted Linear Relationship						Coefficient of Determination, R^2						Normalized Standard Error of Estimate, NSEE					
	SSL	SSN	VSL	VSN	VML	VMN	SSL	SSN	VSL	VSN	VML	VMN	SSL	SSN	VSL	VSN	VML	VMN
SSL	1	1.04	0.97	1.01	1.01	1.15	1	0.94	0.99	0.99	0.99	0.93	-	0.11	0.04	0.04	0.03	0.11
SSN		1	0.93	0.96	0.96	1.10		1	0.93	0.96	0.92	0.90		-	0.12	0.09	0.13	0.14
VSL			1	1.03	1.04	1.18			1	0.96	0.99	0.91			-	0.06	0.05	0.13
VSN				1	0.99	1.14				1	0.98	0.93				-	0.06	0.11
VML					1	1.14					1	0.94					-	0.10
VMN						1						1						-

(b) 300 mm (12 in.) base on top of subgrade.

Model	Slope of Fitted Linear Relationship						Coefficient of Determination, R^2						Normalized Standard Error of Estimate, NSEE					
	SSL	SSN	VSL	VSN	VML	VMN	SSL	SSN	VSL	VSN	VML	VMN	SSL	SSN	VSL	VSN	VML	VMN
SSL	1	1.03	1.01	1.06	1.00	1.13	1	0.97	0.96	0.95	0.99	0.93	-	0.07	0.09	0.09	0.03	0.10
SSN		1	0.98	1.02	0.96	1.08		1	0.96	0.92	0.96	0.88		-	0.09	0.12	0.08	0.14
VSL			1	1.04	0.98	1.10			1	0.89	0.95	0.84			-	0.14	0.09	0.16
VSN				1	0.93	1.06				1	0.95	0.96				-	0.09	0.08
VML					1	1.13					1	0.94					-	0.09
VMN						1						1						-

- Static Stationary Loading.
  - ***Single-Layer System:*** Figure D-18 shows the depth of influence for single-layer when a static stationary linear (SSL) model is used as *z*/*B* of approximately six, i.e. about 1.8 m (70 in.). The modulus of the geomaterial does not seem to affect the depth of influence in the linear models. However, when material nonlinearity is introduced, the depth of influence increases as k'_2 increases (i.e., geomaterial becomes more granular) and decreases as the absolute value of k'_3 increases (i.e., geomaterial becomes less cohesive). The normalized influence depth with respect to the drum contact width (z/B) varies between 4.5 and 6.9.
  - ***Two-Layer System:*** Figure D-19 shows the variation of the influence depth with nonlinear *k'* parameters of subgrade calculated from static stationary cases for a 150 mm (6 in.) thick top (base) layer. In comparison to the single-layer systems, the average influence depth increases slightly as the geosystem becomes stiffer. The nonlinear *k'* parameters of subgrade do not affect appreciably the depth of influence. Figure D-20 demonstrates that the influence depth is also essentially independent of the nonlinear parameters of the base as well when the base thickness is 150 mm (6 in.). Similar patterns are observed in Figures D-21 and D-22 for 300 mm (12 in.) thick base layer.

  A summary of the normalized depth of influence for stationary static models including both linear and nonlinear geosystems is provided in Table D-7. The influence depth from the single-layer SSL analyses is about 5.9 times the drum contact width. However, the influence depth varies between 4.5 and 6.8 of the drum contact width for the nonlinear (SSN) cases. The average *z*/*B* from the SSL models for the two-layer systems with 150 mm (6 in.) and 300 mm (12 in.) base thicknesses are between 5.8 and 6.8. For the SSN models, *z*/*B* varied between 5.1 and 6.8 for 150 mm (6 in.) base thickness, and between 5.4 and 6.5 for 300 mm (12 in.) base thickness.

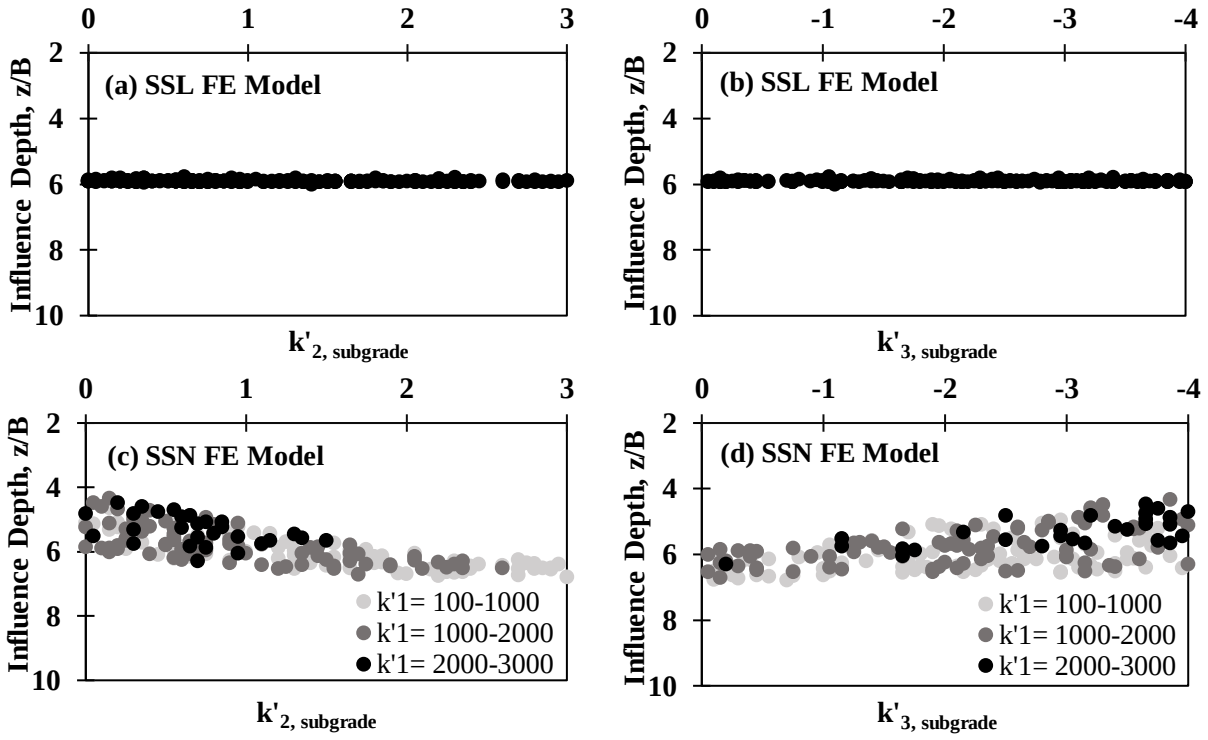

Figure D-18. Variation in influence depth with nonlinear k' parameters of subgrade for single-layer systems based on displacement criterion.

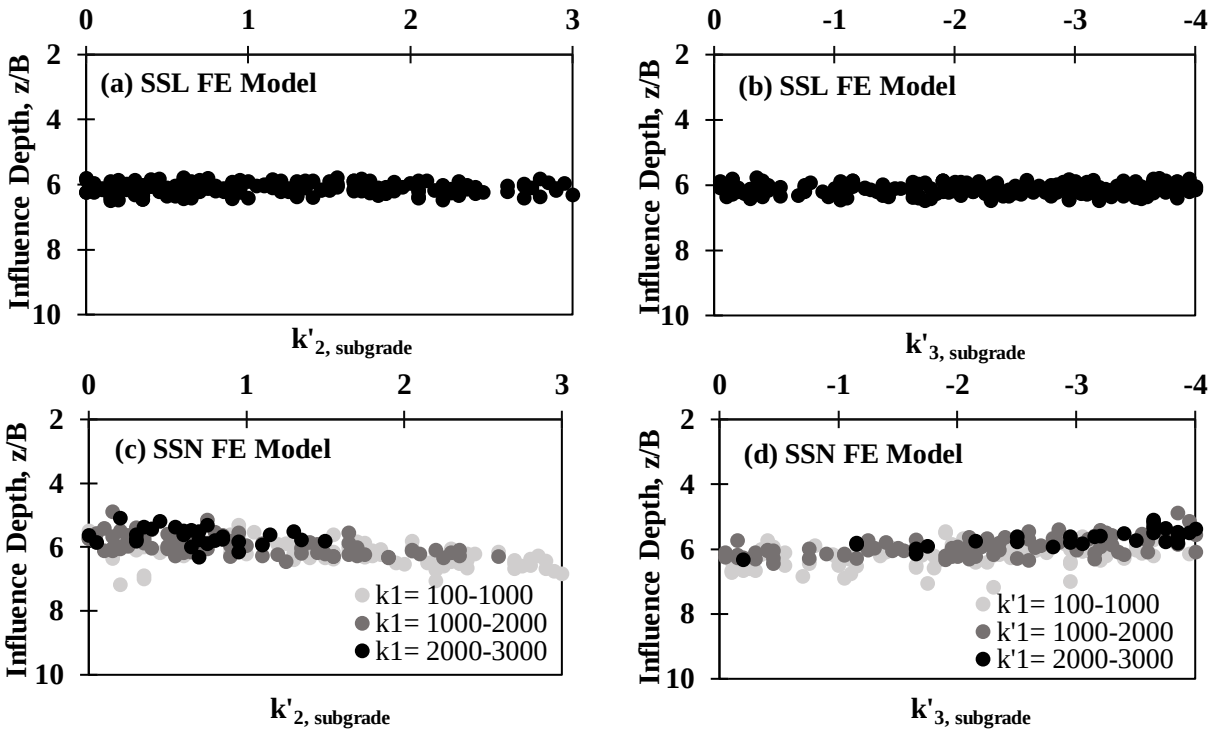

Figure D-19. Variation in influence depth with nonlinear k' parameters of subgrade for two-layer systems with 150 mm (6 in.) base thickness based on displacement criterion.

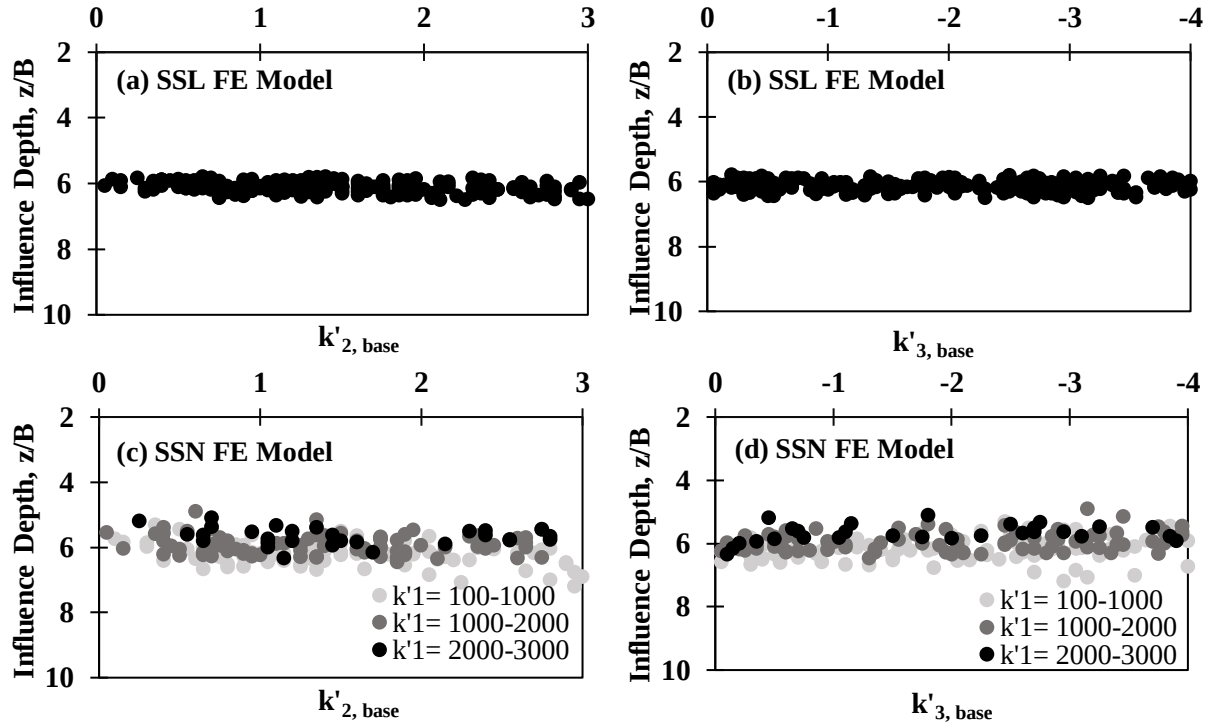

Figure D-20. Variation in influence depth with nonlinear k' parameters of base for two-layer systems with 150 mm (6 in.) base thickness based on displacement criterion.

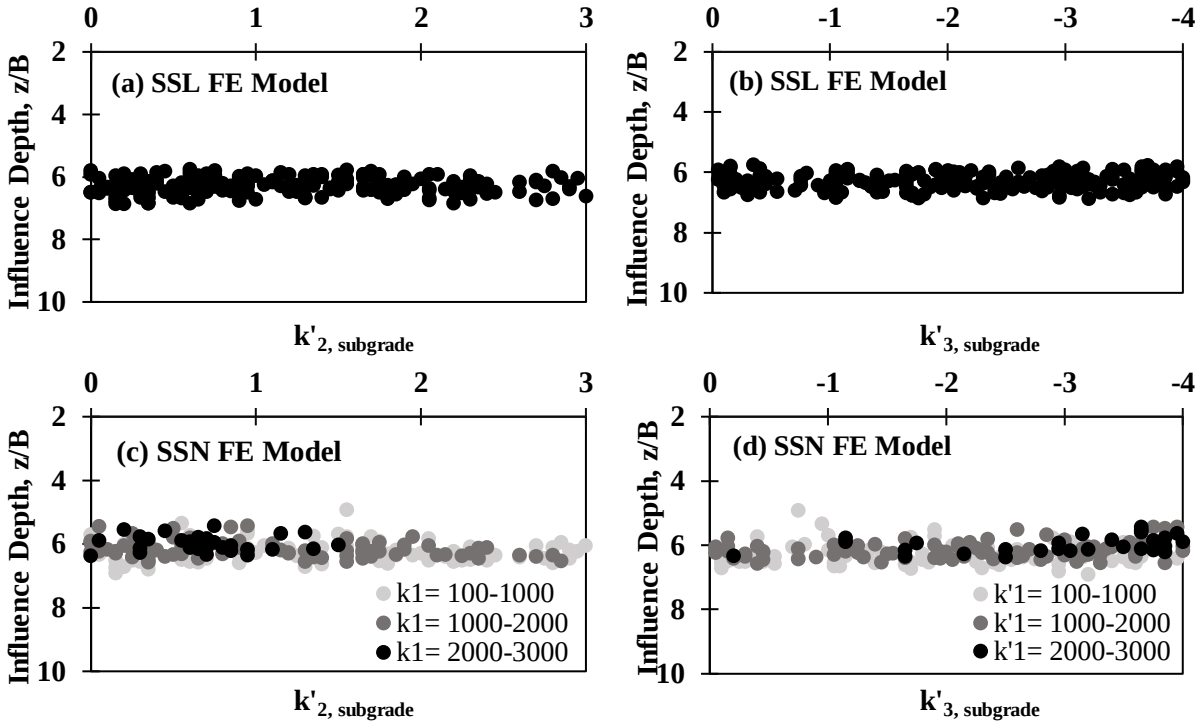

Figure D-21. Variation in influence depth with nonlinear k' parameters of subgrade for two-layer systems with 300 mm (12 in.) base thickness based on displacement criterion.

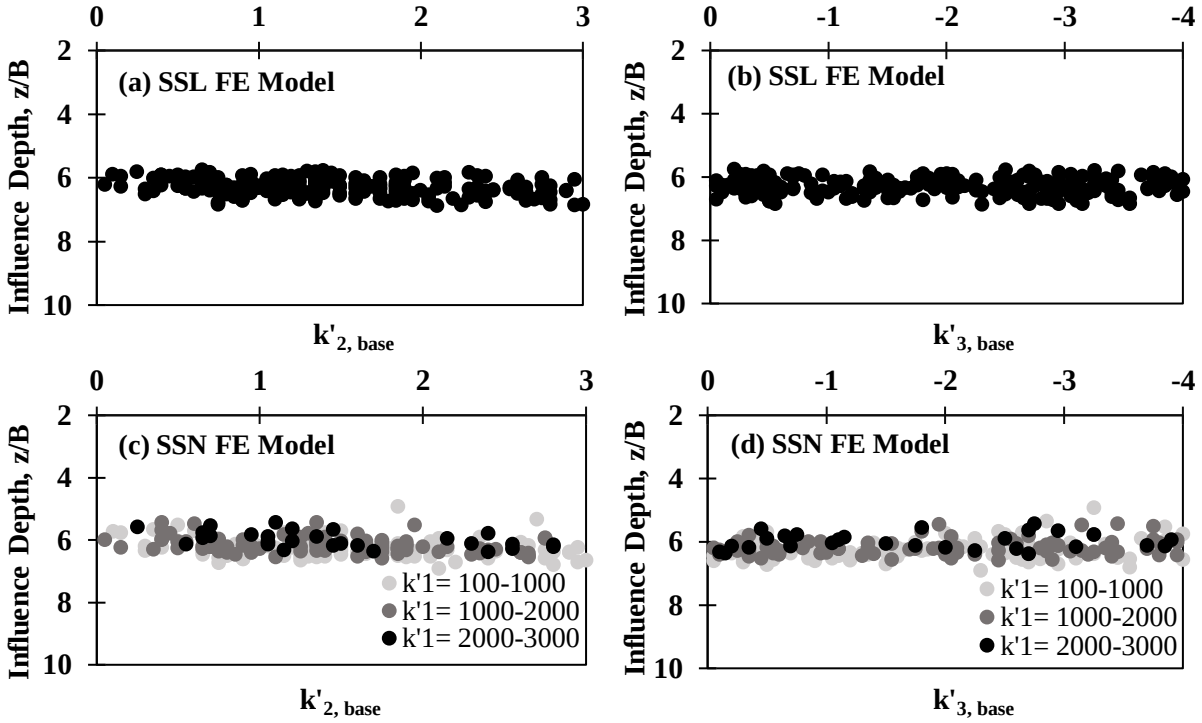

Figure D-22. Variation in influence depth with nonlinear k' parameters of base for two-layer systems with 300 mm (12 in.) base thickness based on displacement criterion.

Table D-7. Summary of descriptive statistics of normalized depth of influence with respect to displacement for SSL and SSN FE models.

Normalized Depth of Influence Based on Displacement Criterion	SSL FE Model			SSN FE Model		
	One Layer System	Two-Layer System		One Layer System	Two-Layer System	
		150 mm Base	300 mm Base		150 mm Base	300 mm Base
Mean	5.89	6.12	6.29	5.82	6.01	6.18
Median	5.90	6.13	6.30	5.91	6.03	6.03
Standard Deviation	0.03	0.17	0.26	0.58	0.37	0.37

- **Vibratory Stationary Loading.** To measure the influence depth from the vibratory stationary drum, six continuous cycles of loading with peak vertical force of 170 kN (38 kips) in addition to the weight of the drum at a frequency of 28 Hz were simulated. The influence depths extracted from different cycles were stable for the linear models, as shown in Table D-8. The first cycle was thus used to calculate the depth of influence for vibratory stationary (VSL and VSN) cases.
  - ***Single-Layer System:*** As demonstrated in Figure D-23, the influence depth does not change appreciably with the variation of the nonlinear *k'* parameters for the VSL cases where the moduli are defined as single representative values. Similar trends are observed for the VSN cases, with more scatter in the results as compared to the VSL cases. In other words, the difference in the influence depth among the granular geomaterials (i.e., geomaterials with higher values of k'_2 and lower absolute values of k'_3) and clayey geomaterials (i.e., geomaterials with lower values of k'_2 and higher absolute values of k'_3) is not discernable for the single-layer geosystems.
  - ***Two-Layer System:*** Figure D-24 demonstrates the effects of the nonlinear k' parameters of the subgrade on the influence depths obtained from the vibratory stationary cases (VSL and VSN) for a 150 mm (6 in.) thick top (base) layer. The influence depth does not vary with the changes in nonlinear k' parameters of subgrade for the VSL cases. The depth of influence obtained from the VSN model slightly increases with the decrease in parameters k'_1 and k'_3. The nonlinear parameter k'_2 of subgrade does not appreciably affect the penetration depth (see Figure D-24). The variation of the influence depth with the nonlinear k' parameters of the base for two-layer geosystems with 150 mm (6 in.) base thickness is depicted in Figure D-25. The depth of influence is not sensitive to the k' parameters of base for neither the VSL nor VSN cases. The same patterns were observed for 300 mm (12 in.) thick base (Figure D-26 and D-27). Table D-9 summaries these results.

Table D-8. Summary of descriptive statistics of depth of influence calculated for six different cycles of loading for two-layer VSL FE model with 300 mm (12 in.) base thickness based on displacement criterion.

Depth of Influence Based on Displacement Criterion (m)	1st Cycle	2nd Cycle	3rd Cycle	4th Cycle	5th Cycle	6th Cycle
Mean	2.02	2.02	2.02	2.02	2.00	2.00
Median	2.02	2.02	2.02	2.02	2.02	2.02
Standard Deviation	0.08	0.08	0.08	0.08	0.08	0.12

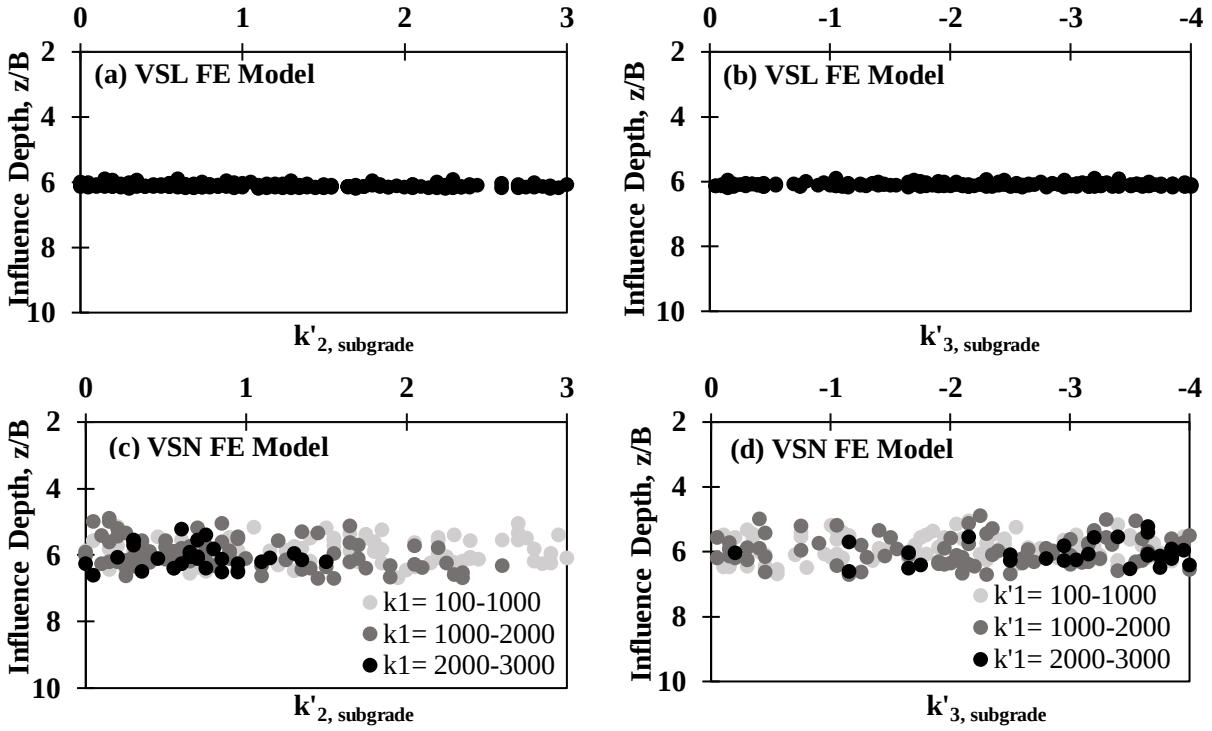

Figure D-23. Variation in influence depth with nonlinear k' parameters of subgrade for single-layer systems based on displacement criterion.

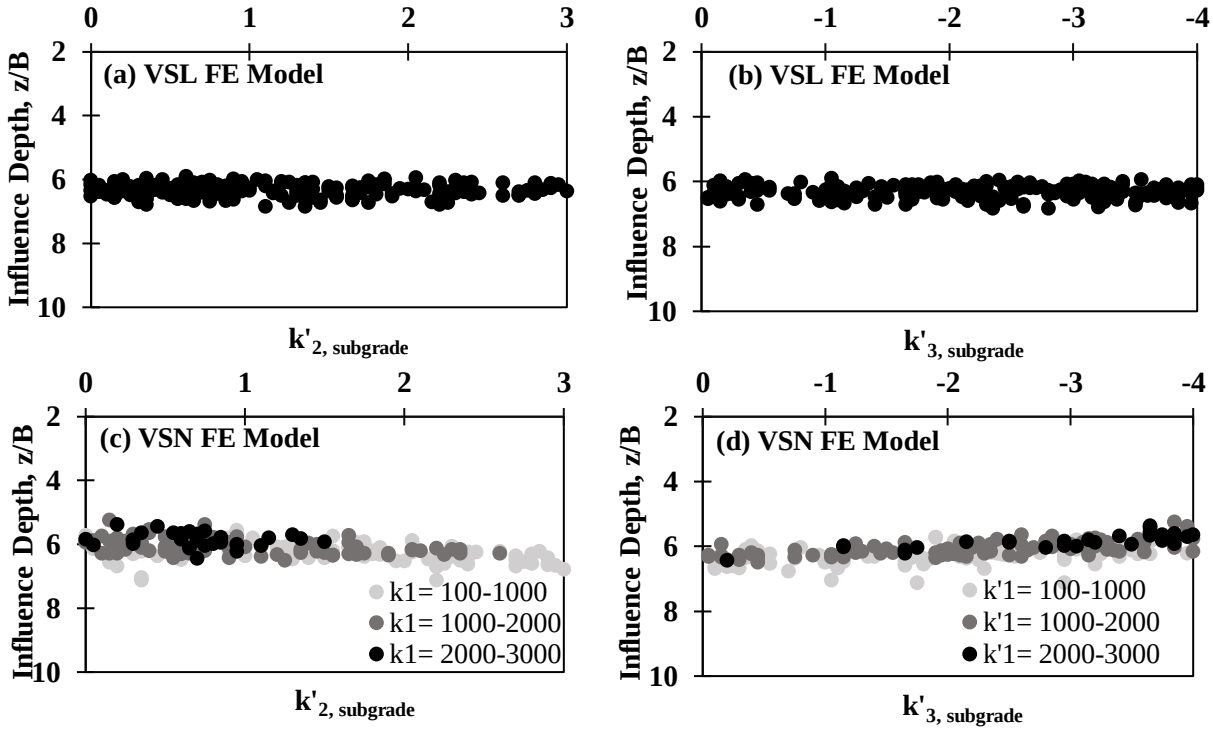

Figure D-24. Variation in influence depth with nonlinear k' parameters of subgrade for two-layered systems with 150 mm (6 in.) base thickness based on displacement criterion.

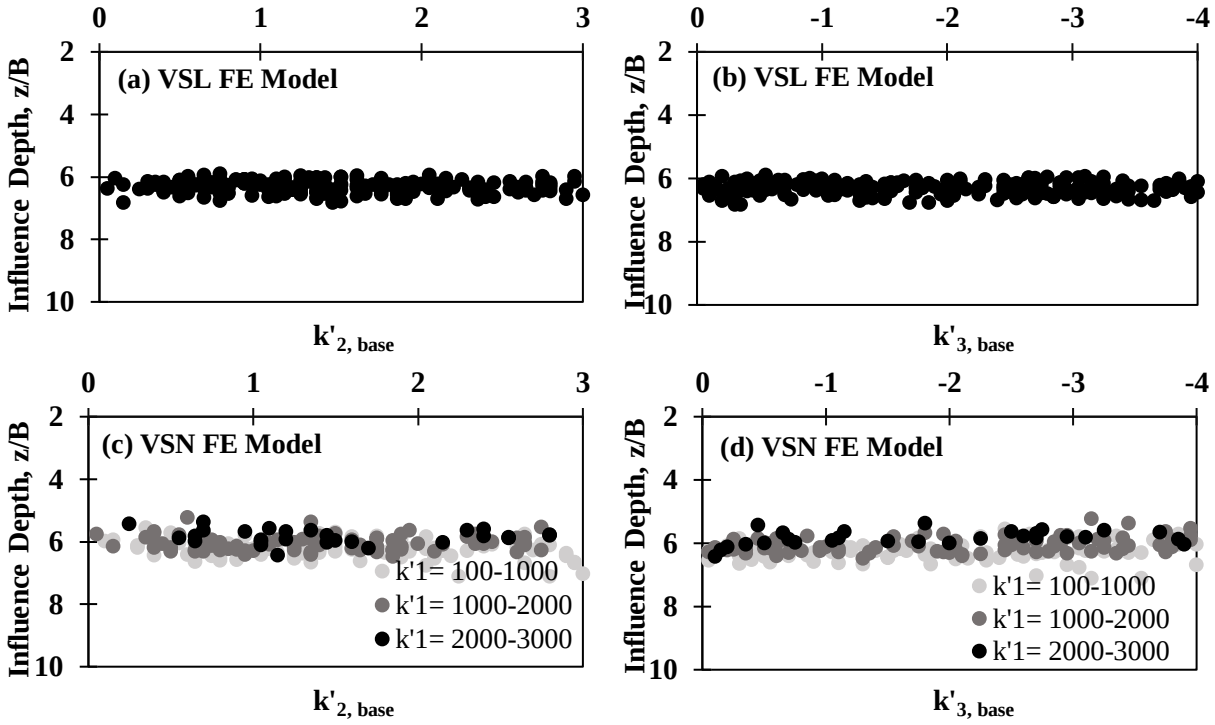

Figure D-25. Variation in influence depth with nonlinear k' parameters of base for two-layered systems with 150 mm (6 in.) base thickness based on displacement criterion.

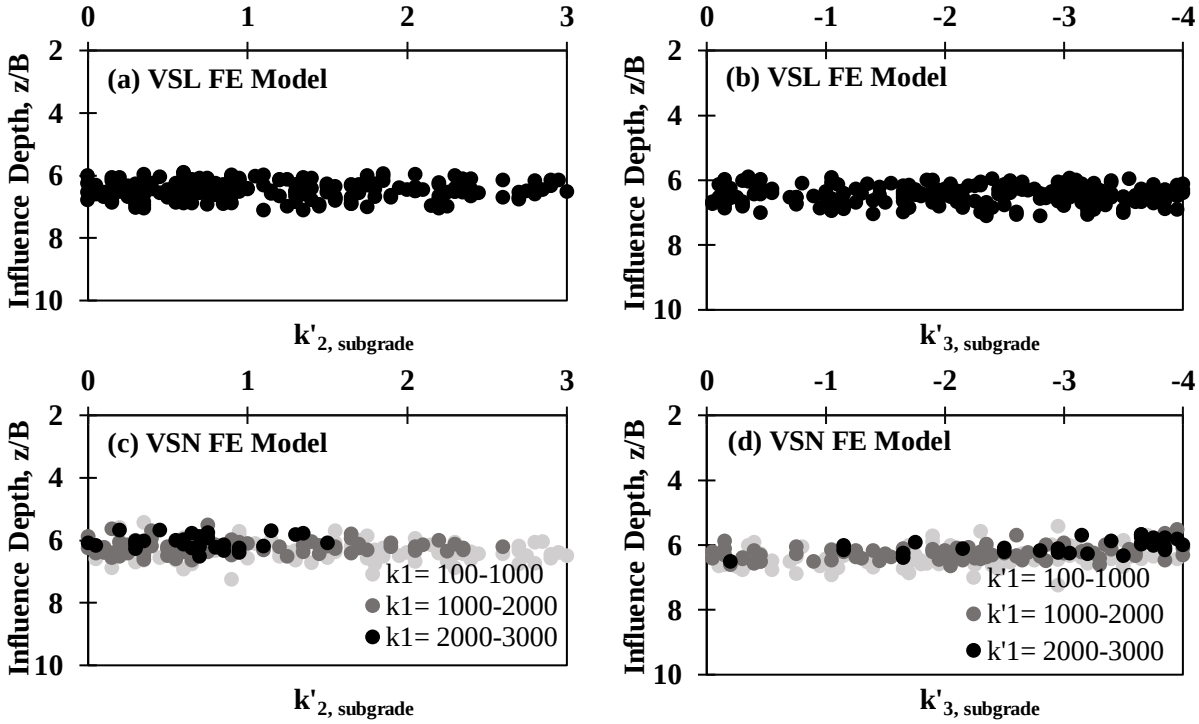

Figure D-26. Variation in influence depth with nonlinear k' parameters of subgrade for two-layered systems with 300 mm (12 in.) base thickness based on displacement criterion.

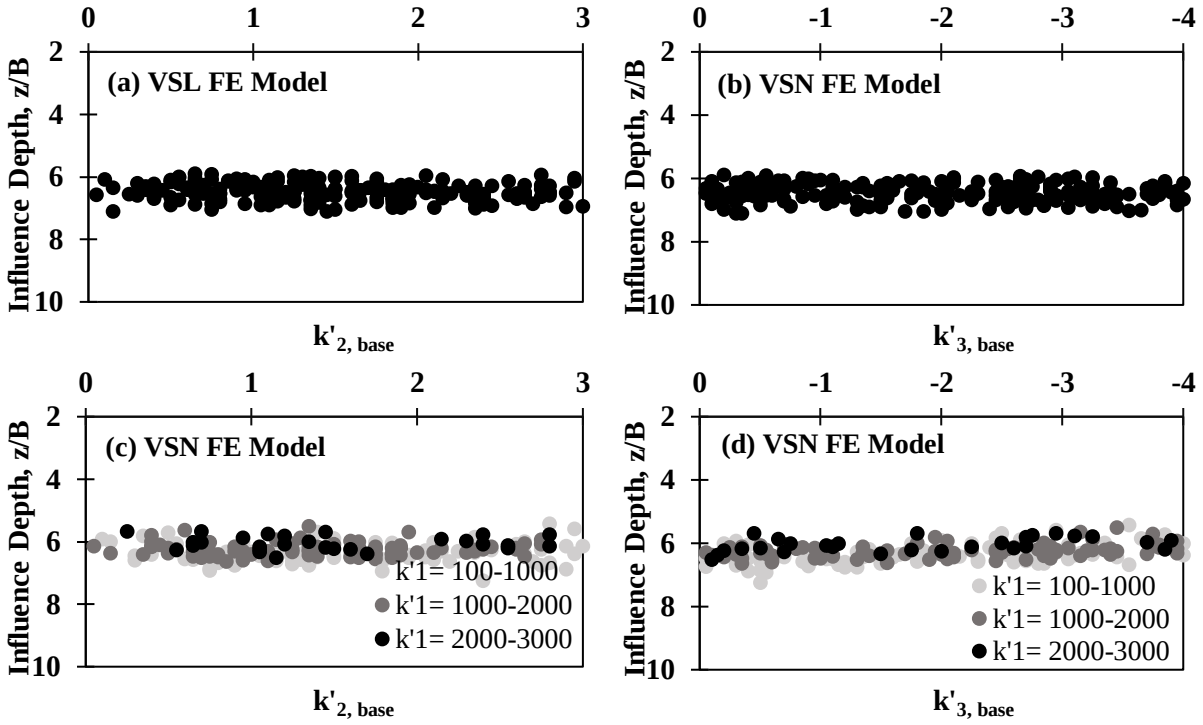

Figure D-27. Variation in influence depth with nonlinear k' parameters of base for two-layered systems with 300 mm (12 in.) base thickness based on displacement criterion.

Table D-9. Summary of descriptive statistics of normalized depth of influence with respect to displacement for VSL and VSN FE models.

Normalized Depth of Influence Based on Displacement Criterion	VSL FE Model			VSN FE Model		
	One Layer System	Two-Layer System		One Layer System	Two-Layer System	
		150 mm Base	300 mm Base		150 mm Base	300 mm Base
Mean	6.09	6.31	6.46	5.94	6.11	6.24
Median	6.11	6.30	6.46	5.99	6.13	6.30
Standard Deviation	0.06	0.19	0.28	0.40	0.30	0.28

- **Vibratory Moving Loading.** Similar to the results gathered from the vibratory stationary drum, the influence depth was estimated for a vibratory roller while the drum moved at a speed of 4.8 km/hr (3 mph) and rotated with an angular velocity of 1.2 rad/s. The results for the single- and two-layered geosystems subjected to the vibratory moving drum (VML and VMN) are summarized in Table D-10. The average *z*/*B* increases with an increase in the thickness of the base (top) layer, i.e. the stiffer the geomaterial is, the deeper the depth of influence will become. The depths of influence from VMN cases (i.e. the most complicated FE model) for single-layer and two-layer systems with 150 mm (6 in.) and 300 mm (12 in.) base thicknesses were about 5.9, 6.1 and 6.2 times the effective drum width, respectively. Comparing the results represented in Tables D-7 and D-9, the average *z*/*B* slightly increases for the vibratory drums as compared to the stationary and vibratory or static conditions. Nevertheless, the differences among the six different cases is less than 11%. Based on these case studies, one can approximate the depth of influence to about six times the effective width for practical purposes.

Table D-10. Summary of descriptive statistics of normalized depth of influence with respect to displacement for VML and VMN FE models.

Normalized Depth of Influence Based on Displacement Criterion	VML FE Model			VMN FE Model		
	One Layer System	Two-Layer System		One Layer System	Two-Layer System	
		150 mm Base	300 mm Base		150 mm Base	300 mm Base
Mean	6.12	6.33	6.49	5.91	6.08	6.24
Median	6.13	6.34	6.51	5.99	6.09	6.25
Standard Deviation	0.05	0.17	0.27	0.43	0.32	0.28

Influence Depth with Respect to Stress

The depth of influence with respect to stress is defined as the depth where the vertical stress dissipates to 10% of the maximum stress. The outcome of this study obtained from different FE analyses based on stress can be summarized in the following manner:

- Static Stationary Loading.
  - ***Single-Layer System:*** As shown in Figure D-28 and Table D-11, the depth of influence are about 4.1 times the roller contact width, i.e. 1.3 m (4 ft), for the SSL and SSN models. The influence depth under static stationary roller with respect to stress is not sensitive to the nonlinear k' parameters.
  - ***Two-Layer System:*** Figures D-29 through D-32 show the compiled results from the linear and nonlinear FE models for the two-layer geosystems. The influence depths obtained for the two-layer systems do not vary significantly with the nonlinear k′ parameters of subgrade or base layer. Similar to the single-layer systems, the nonlinearity of the soil does not significantly affect the penetration depth with respect to stress criterion.
- **Stationary or Moving Vibratory Drum**. The descriptive statistics of the normalized depth of influence with respect to stress criterion for different levels of sophistication of FE model are presented in Table D-11. The average *z*/*B* decreases with an increase in the base thickness, i.e. the stiffer the soil is, the shallower the penetration depth will be. The average *z*/*B* is 3.8 for the single-layer geosystems of VMN scenario. The normalized depth of influence for two-layer geosystems with 150 mm (6 in.) and 300 mm (12 in.) base thicknesses subjected to the vibratory moving drum are about 3.7 and 3.6, respectively, i.e. 1.1 m (3.7 ft).

Establishing Depth of Influence

This section summarizes an effort to establish a relationship between the influence depth and the representative resilient moduli for the base and subgrade layers determined from lab tests.

- Static Stationary Loading.
  - ***Based on Displacement Criterion:*** The variations in normalized influence depth, *z*/*B*, derived from the SSL cases on top of the two-layer geosystems are related to the ratio of the representative resilient moduli of the base and subgrade in Figure D-33. The greater the base-subgrade modulus ratio is, the deeper the depth of influence will become. The normalized influence depth can be predicted from:

$$\frac{z}{B} = a\ln\left(\frac{MR_{Base}}{MR_{Subgrade}}\right) + b \tag{D.12}$$

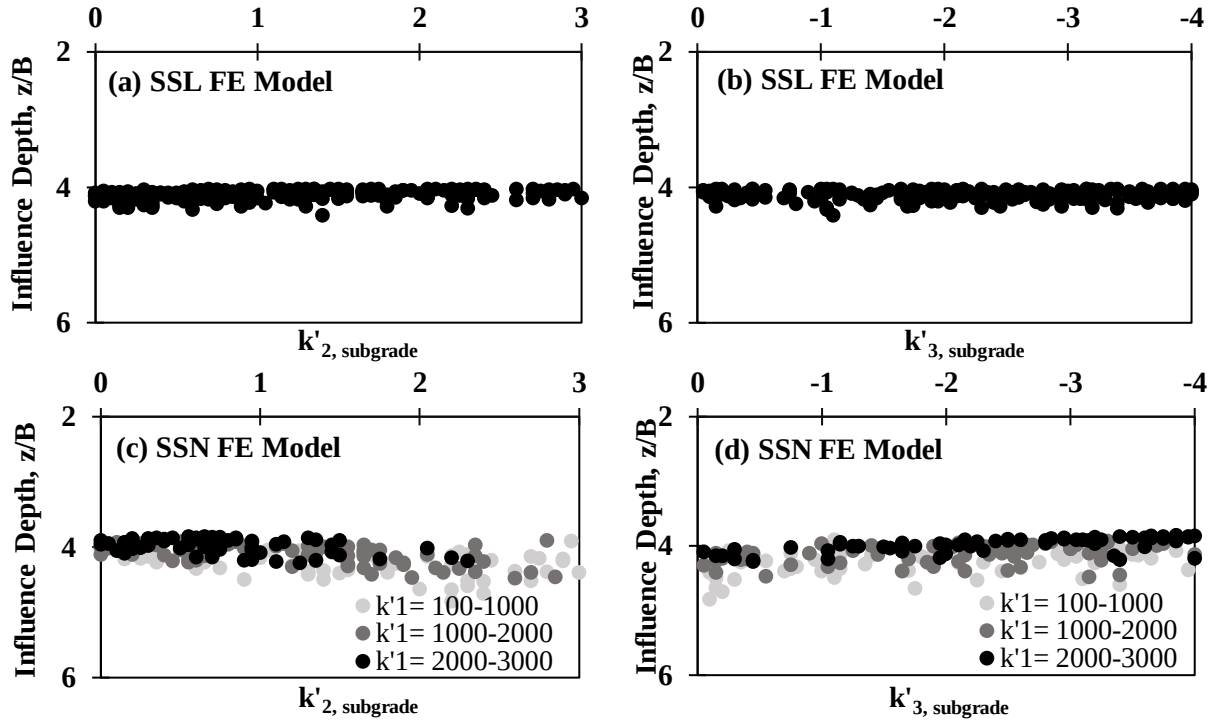

Figure D-28. Variation in influence depth with nonlinear k' parameters of subgrade for single-layer systems based on stress criterion.

Table D-11. Summary of descriptive statistics of normalized depth of influence with respect to stress for different levels of sophistication of FE model.

Normalized Depth of Influence (z/B)	Different Levels of Sophistication of FE Model					
	One Layer System	Two-Layer System		One-Layer System	Two-Layer System	
		150 mm Base	300 mm Base		150 mm Base	300 mm Base
Static Stationary	**Linear Geomaterial (SSL)**			**Nonlinear Geomaterial (SSN)**		
Mean	4.11	4.17	4.06	4.08	4.08	4.05
Median	4.10	4.16	4.06	4.05	4.07	4.03
Standard Deviation	0.07	0.07	0.13	0.23	0.30	0.26
Vibratory Stationary	**Linear Geomaterial (VSL)**			**Nonlinear Geomaterial (VSN)**		
Mean	4.22	4.19	4.02	4.40	4.20	4.01
Median	4.21	4.19	4.01	4.27	4.15	4.06
Standard Deviation	0.07	0.10	0.06	0.43	0.24	0.39
Vibratory Moving	**Linear Geomaterial (VML)**			**Nonlinear Geomaterial (VMN)**		
Mean	3.76	3.61	3.53	3.77	3.70	3.64
Median	3.79	3.64	3.58	3.80	3.67	3.64
Standard Deviation	0.22	0.21	0.28	0.26	0.28	0.29

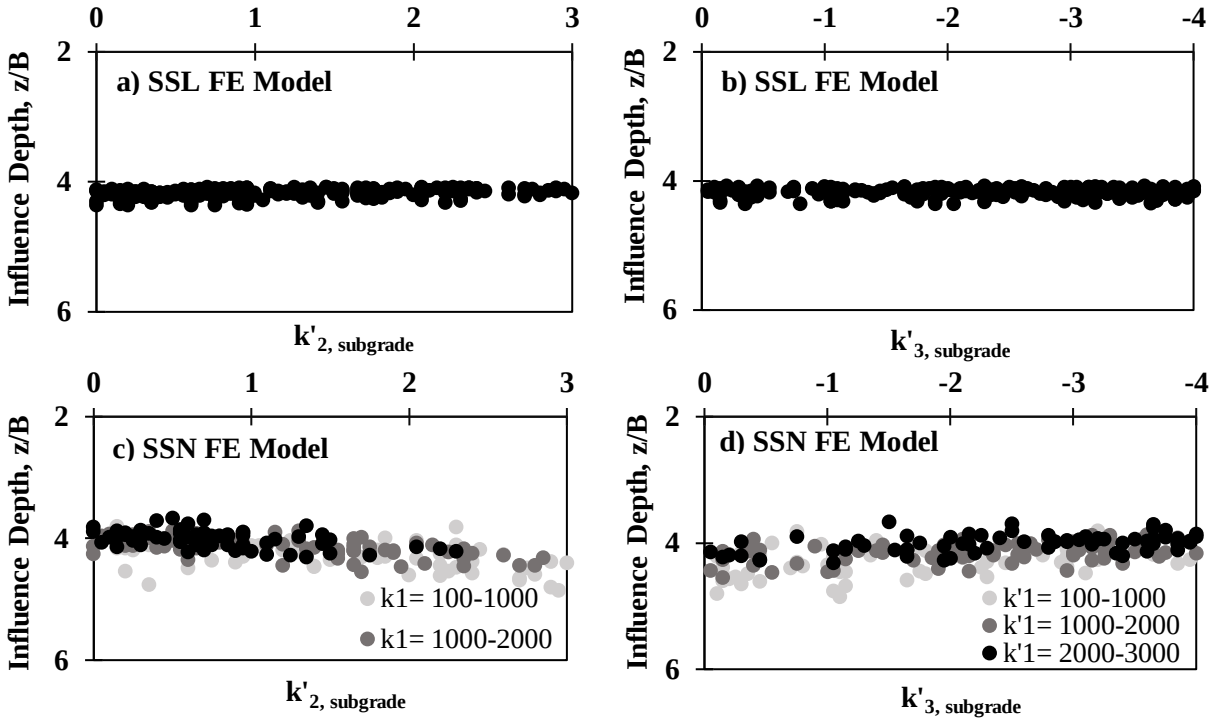

Figure D-29. Variation in influence depth with nonlinear k' parameters of subgrade for two-layered systems with 150 mm (6 in.) base thickness based on stress criterion.

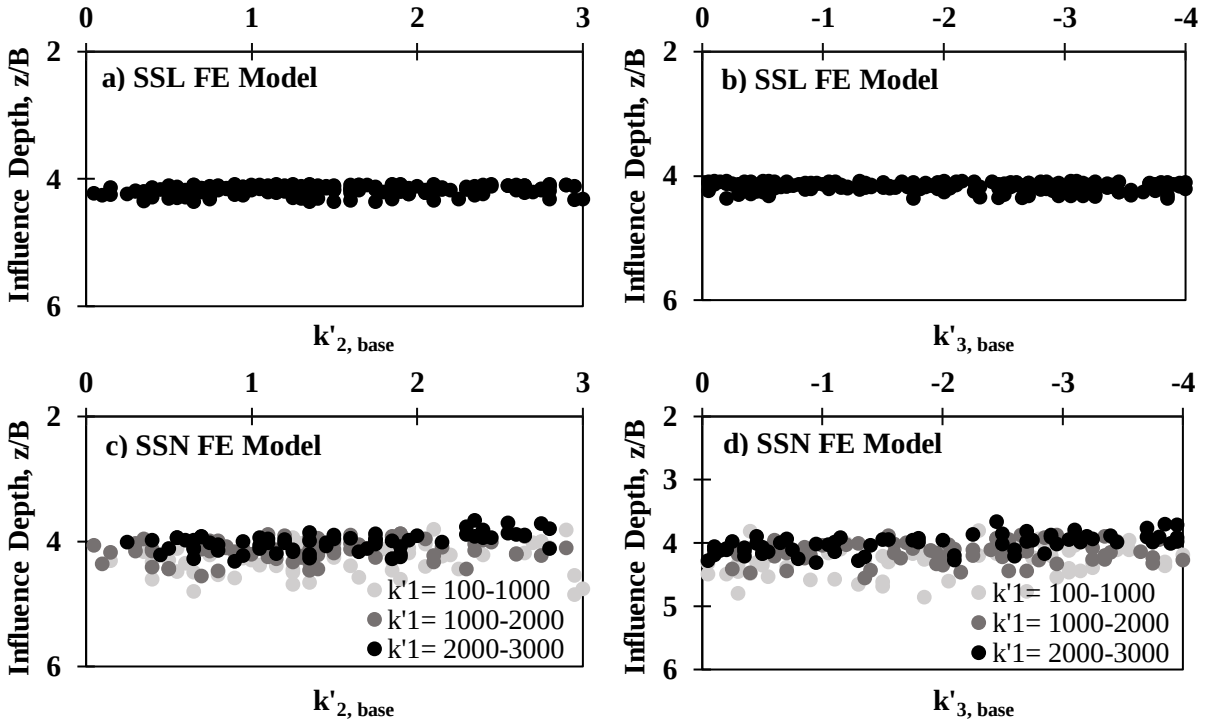

Figure D-30. Variation in influence depth with nonlinear k' parameters of base for two-layered systems with 150 mm (6 in.) base thickness based on stress criterion.

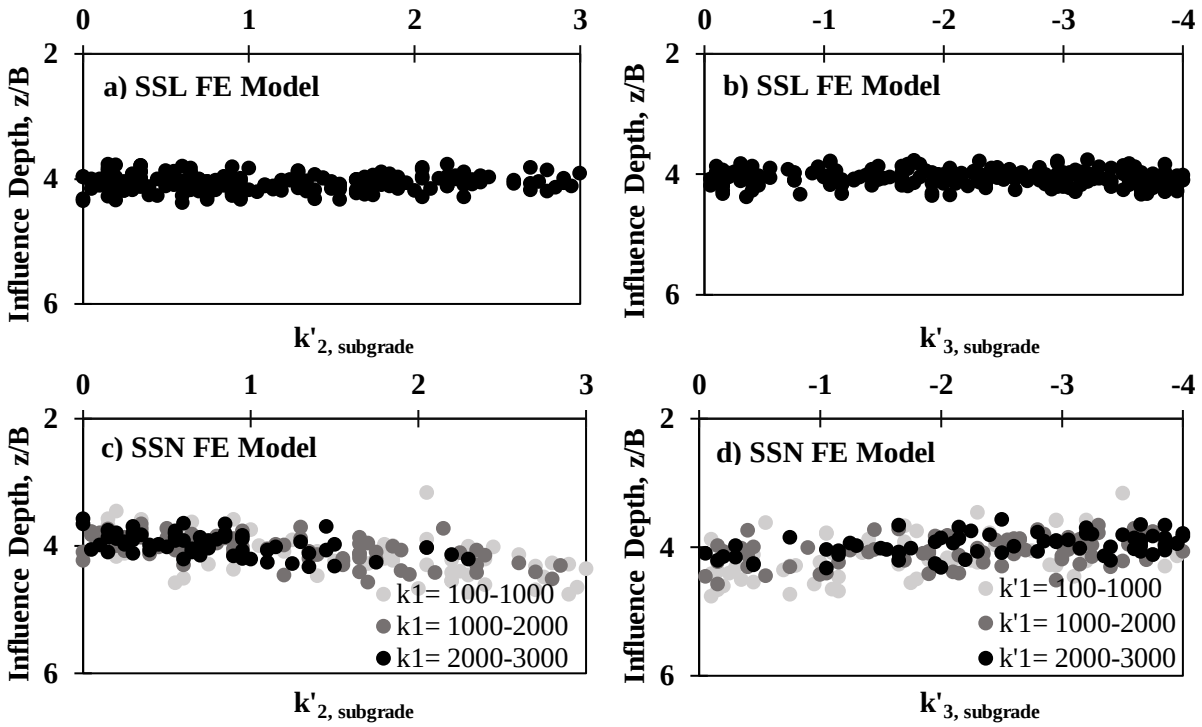

Figure D-31. Variation in influence depth with nonlinear k' parameters of subgrade for two-layered systems with 300 mm (12 in.) base thickness based on stress criterion.

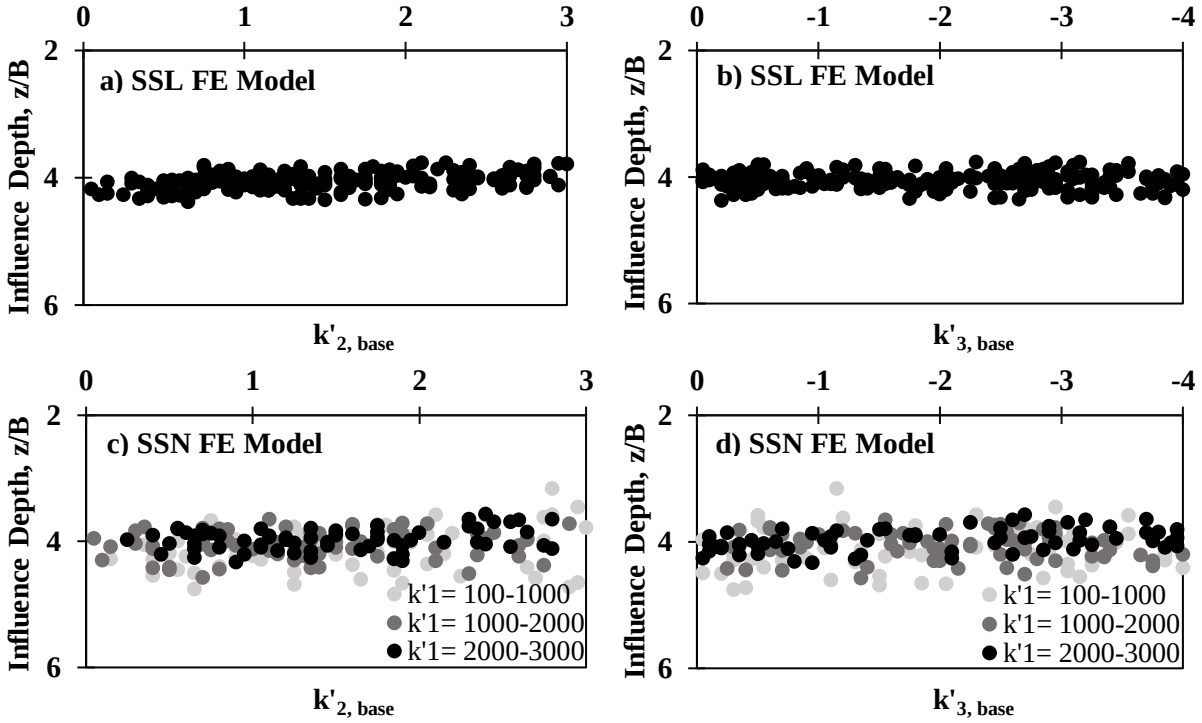

Figure D-32. Variation in influence depth with nonlinear k' parameters of base for two-layered systems with 300 mm (12 in.) base thickness based on stress criterion.

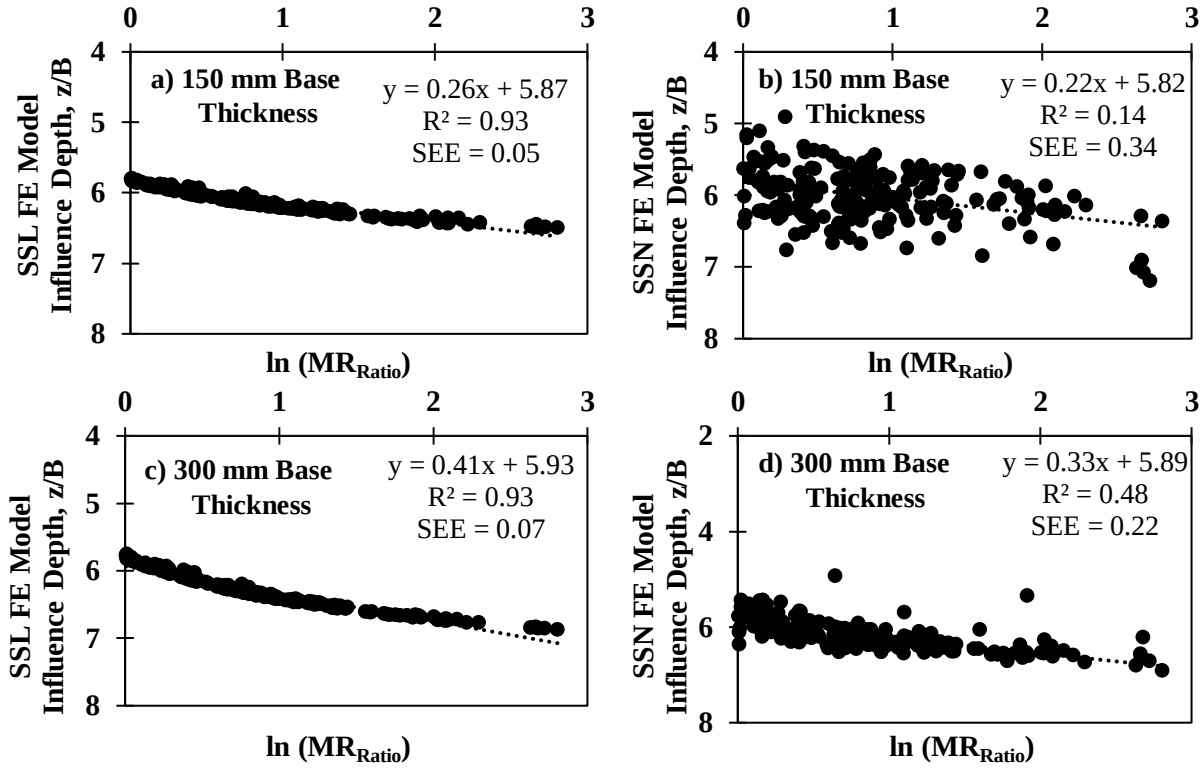

Note: $MR_{Ratio} = MR_{Base}/MR_{Subgrade}$.

Figure D-33. Variation in influence depth with representative resilient modulus ratio (MR_{Ratio}) for two-layer systems based on displacement criterion.

The slopes (parameter *a*), intercepts (parameter *b*), coefficients of determination (R^2 values), and SEE of the regression lines from static models are reported in Table D-12. More analyses are underway using different levels of sophistication of FE models in order to accomplish a certain level of confidence in the models.

- ***Based on Stress Criterion***: The descriptive statistics of the fitted lines passed through the results are summarized in Table D-13. From Figure D-34, the influence depths are nearly constant for the two-layer SSL and static stationary nonlinear (SSN) geosystems with 150 mm (6 in.) of base thickness. These results are more dispersed as compared to the results based on the displacement criterion. The normalized depth of influence slightly decreases with an increase in the resilient modulus ratio for the 300 mm (12 in.) thick base.

Table D-12. Summary of descriptive statistics for correlation of influence depth and resilient modulus ratio for two-layer SSL and SSN models based on displacement criterion.

Model	Descriptive Statistics of The Normalized Depth of Influence			
	a	***b***	***R^2***	***SEE***
150 mm (6 in.) Base Thickness				
SSL	0.26	5.87	0.93	0.05
SSN	0.22	5.82	0.14	0.34
300 mm (12 in.) Base Thickness				
SSL	0.41	5.93	0.93	0.07

SSN	0.33	5.89	0.48	0.22

Table D-13. Summary of descriptive statistics for correlation of influence depth and resilient modulus ratio for two-layer SSL and SSN models based on stress criterion.

Model	Descriptive Statistics of The Normalized Depth of Influence			
	a	***b***	***R²***	***SEE***
150 mm (6 in.) Base Thickness				
SSL	0.02	4.15	0.16	0.07
SSN	-0.02	4.09	NA	NA
300 mm (12 in.) Base Thickness				
SSL	-0.19	4.22	0.81	0.06
SSN	-0.19	4.22	NA	NA

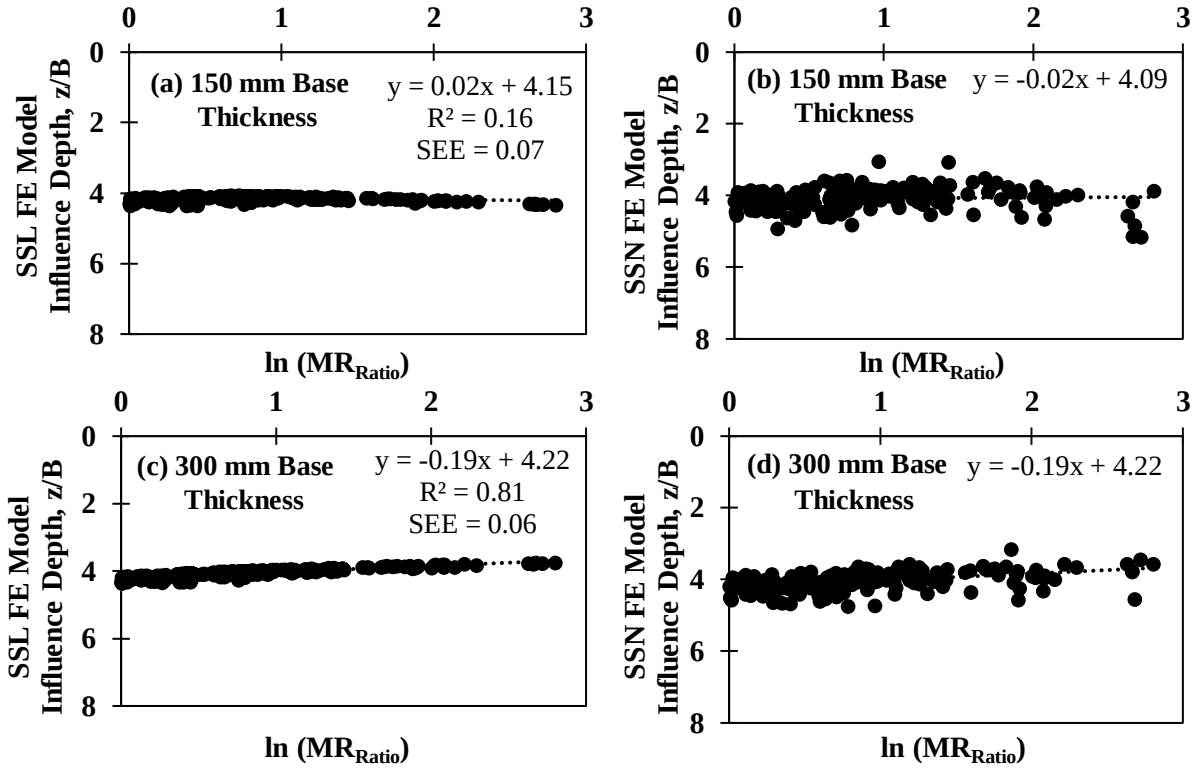

Figure D-34. Variation in influence depth with representative resilient modulus ratio (MR_{Ratio}) for two-layer systems based on stress criterion.

- Vibratory Loading (Stationary or Moving).
  - ***Based on Displacement Criterion:*** The results for vibratory stationary cases are summarized in Table D-14. The computed *z*/*B* is constant for linear geomaterials as the representative resilient moduli ratio changes. The results are more scattered for the VSL cases in comparison to SSL ones as reflected by the SEE values. The average *z*/*B* for the nonlinear cases is sensitive to the variation of resilient modulus ratio. Hence, the greater the resilient moduli ratio is, the deeper the depth of influence will become.

- ***Based on Stress Criterion***: From Table D-15, the influence depth is only marginally affected by the resilient modulus ratio.

Table D-14. Summary of descriptive statistics for correlation of influence depth and resilient modulus ratio for two-layer VSL and VSN models based on displacement criterion.

Model	Descriptive Statistics of The Normalized Depth of Influence			
	a	***b***	***R^2***	***SEE***
150 mm (6 in.) Base Thickness				
VSL	-0.02	6.33	NA	NA
VSN	0.22	5.92	0.21	0.27
300 mm (12 in.) Base Thickness				
VSL	0.00	6.39	NA	NA
VSN	0.26	6.03	0.35	0.23

Table D-15. Summary of descriptive statistics for correlation of influence depth and resilient modulus ratio for two-layer VSL and VSN models based on stress criterion.

Model	Descriptive Statistics of The Normalized Depth of Influence			
	a	***b***	***R^2***	***SEE***
150 mm (6 in.) Base Thickness				
VSL	0.00	4.17	NA	NA
VSN	0.01	4.16	NA	NA
300 mm (12 in.) Base Thickness				
VSL	0.00	4.02	NA	NA
VSN	0.02	4.01	NA	NA

Impact of Geomaterial Properties on IC Measurement Values and Responses

Given the results explained in the previous sections, and the desire to utilize ICMVs as an indicator for quality control (QC) of compacted geomaterials, it is imperative to quantify the effects of the nonlinear k'parameters on the roller responses.

Spearman Correlation

The influence of the nonlinear nature of the geomaterials on the pavement responses was studied using Spearman's correlation (McDonald 2014). The results of such activities are discussed for surface displacement and stress, as well as the depth of influence for one and two-layer geosystems. Different levels of sophistication of the FE models are also taken into consideration.

- Surface Displacement.
  - ***Single-Layer System:*** Table D-16 shows the nonlinear parameters k'_1 (related to stiffness) and k'_2 (granularity causing stress hardening) impact surface displacement.
  - ***Two-Layer System:*** As shown in Table D-17, nonlinear k'_1 parameter of subgrade affects the surface displacement the most, followed by k'_2 of the subgrade and k'_3 of the base. These results indicate both the stiffness and granularity of the subgrade affect the surface displacement.
- Surface Stress.

- ***Single-Layer System:*** Table D-18 shows the influence of the nonlinear k' parameters on the surface vertical stresses for the single-layer geosystems at the center and at the edge of the drum. Parameter k'_2 impacts the surface stresses the most for both static stationary (SSN) and vibratory stationary (VSN) scenarios. The parameter k'_1 affects the surface stresses the most for VMN cases.

Table D-16. Impact of nonlinear material parameters on surface displacement for single-layer pavement system.

Level of Sophistication of FE Model	Spearmann's Correlation Coefficients		
	Subgrade Parameters		
	k'_1	k'_2	k'_3
SSN	-0.37	-0.42	-0.18
VSN	-0.42	-0.35	-0.15
VMN	-0.32	-0.37	-0.30

Table D-17. Impact of nonlinear material parameters on surface displacement for two-layer pavement system.

Level of Sophistication of FE Model	Spearmann's Correlation Coefficients					
	Base Parameters			Subgrade Parameters		
	k'_1	k'_2	k'_3	k'_1	k'_2	k'_3
150 mm (6 in.) Base Thickness						
SSN	-0.08	-0.14	-0.19	-0.45	-0.36	-0.15
VSN	-0.12	-0.10	-0.18	-0.56	-0.24	-0.06
VMN	-0.17	0.07	-0.29	-0.49	-0.30	-0.13
300 mm (12 in.) Base Thickness						
SSN	-0.12	-0.19	-0.28	-0.49	-0.20	-0.08
VSN	-0.21	-0.06	-0.23	-0.55	-0.22	-0.03
VMN	-0.24	0.03	-0.31	-0.54	-0.23	-0.05

Table D-18. Impact of nonlinear material parameters on surface stress for single-layer system.

Level of Sophistication of FE Model	Spearmann's Correlation Coefficients					
	Subgrade Parameters Vertical Surface Stress (Center)			Subgrade Parameters Vertical Surface Stress (Edges)		
	k'_1	k'_2	k'_3	k'_1	k'_2	k'_3
SSN	0.09	-0.14	-0.12	-0.13	0.18	0.14
VSN	-0.29	0.31	0.26	-0.28	0.33	0.26
VMN	0.52	0.35	-0.02	0.62	0.14	-0.08

- ***Two-Layer System:*** From Tables D-19, the vertical surface stress at the center of the drum is impacted more by k'_2 of the subgrade than the other nonlinear parameters. On the other hand, parameter k'_2 of the base influences the edge stress more significantly. The nonlinear parameters of the subgrade tend to influence the surface stresses less significantly, especially as the base thickness increases.

- Depth of Influence.

- ***Single-Layer System:*** As shown in Table D-20, parameters k'_2 and k'_1 correlate the best with the depth of influence from the SSN models for both the displacement and stress criteria. The parameter k'_2 (granularity causing stress hardening) affects the influence depth the most from the VSN models based on both displacement and stress criteria. For VMN scenario, the parameters k'_3 (i.e. cohesiveness causing softening) and k'_1 (stiffness of geomaterial) impact the most on the depth of influence based on displacement and stress criteria, respectively.

Table D-19. Impact of nonlinear material parameters on surface stress for two-layer system.

Level of Sophistication of FE Model		Spearmann's Correlation Coefficients					
		Base Parameters			Subgrade Parameters		
		k'_1	k'_2	k'_3	k'_1	k'_2	k'_3
150 mm (6 in.) Base Thickness							
SSN	Center of the IC Roller	-0.07	0.16	0.07	0.20	0.37	0.16
VSN		-0.14	-0.08	-0.05	-0.14	0.33	0.18
VMN		0.22	0.30	0.08	0.15	0.31	0.15
SSN	Edges of the IC Roller	-0.10	0.25	-0.14	-0.17	-0.08	0.00
VSN		-0.06	0.24	0.03	-0.27	-0.04	-0.02
VMN		-0.02	0.40	0.13	0.15	-0.10	-0.05
300 mm (12 in.) Base Thickness							
SSN	Center of the IC Roller	-0.09	0.09	-0.02	-0.06	0.14	0.08
VSN		-0.17	0.01	-0.17	-0.14	0.38	0.18
VMN		0.10	-0.05	0.13	0.05	0.26	-0.09
SSN	Edges of the IC Roller	-0.07	0.23	0.04	0.09	-0.12	0.07
VSN		0.11	-0.18	0.11	-0.15	-0.10	0.10
VMN		0.09	-0.16	0.13	0.05	0.03	-0.11

Table D-20. Impact of nonlinear parameters on depth of influence for single-layer system.

Level of Sophistication of FE Model	Spearmann's Correlation Coefficients					
	Based on Displacement Criterion Subgrade Parameters			Based onStress Criterion Subgrade Parameters		
	k'_1	k'_2	k'_3	k'_1	k'_2	k'_3
SSN	-0.56	0.78	0.54	-0.54	0.26	0.32
VSN	0.02	0.08	-0.02	0.03	0.07	0.06
VMN	-0.58	0.63	0.70	-0.60	-0.28	0.03

- ***Two-Layer System:*** The nonlinear parameters of the subgrade affect the influence depth more, as shown in Table D-21. However, the influence depth does not vary significantly, as shown in the section discussing the depths of influence.

Assessing Pavement Responses under IC Roller and LWD

Several state highway agencies around the US are gradually transitioning from the density-based tests to modulus-based tests for earthwork quality control/quality acceptance (QC/QA) (Vennapusa 2008). Lightweight Deflectometers (LWDs) have been gaining popularity as a practical tool for this purpose. The LWD helps to estimate the surface modulus of a material by dropping a weight from a known height to transmit a pulse load to a circular metal plate resting on the soil surface, and by measuring the deflection

of either the plate or the soil. Considering the pros and cons of LWD and IC technology, it seems reasonable to conduct QC with the IC roller and QA with LWD. An attempt was made to relate the moduli obtained from the LWD and IC roller.

Table D-21. Impact of nonlinear parameters on depth of influence for two-layer systems.

Level of Sophistication of FE Model		Spearmann's Correlation Coefficients					
		Base Parameters			Subgrade Parameters		
		k'_1	k'_2	k'_3	k'_1	k'_2	k'_3
150 mm (6 in.) Base Thickness							
SSN	**Based on Displacement Criterion**	-0.09	0.30	0.18	-0.64	0.51	0.52
VSN		0.03	0.23	0.20	-0.62	0.29	0.58
VMN		0.01	0.14	0.24	-0.66	0.26	0.64
SSN	**Based on Stress Criterion**	0.04	-0.25	0.23	-0.66	0.55	0.44
VSN		0.04	-0.05	0.09	0.03	0.06	0.03
VMN		-0.08	-0.26	-0.08	-0.65	0.23	0.27
300 mm (12 in.) Base Thickness							
SSN	**Based on Displacement Criterion**	-0.06	0.35	0.15	-0.52	0.12	0.32
VSN		0.09	0.17	0.17	-0.51	0.03	0.34
VMN		0.09	0.11	0.23	-0.54	-0.03	0.36
SSN	**Based on Stress Criterion**	-0.17	-0.05	0.05	-0.51	0.53	0.39
VSN		-0.01	0.01	0.04	-0.17	0.08	0.02
VMN		-0.17	-0.31	0.02	-0.50	0.36	0.25

An axisymmetric dynamic nonlinear model was developed using LS-DYNA to simulate the plate impact of the LWD test on top of a geomaterial. About 75,000 elements were used to model a 2 m (80 in.) wide and 2.5 m (100 in.) deep soil section. The Zorn ZFG 2000 LWD was modeled, with steel considered as a linear-elastic material rather than a rigid material. Other LWD devices may produce different surface deflections, and consequently different LWD moduli, for the same load (Tirado et al. 2015).

The LWD impact was simulated using a half-sine pulse, with a 6.7 kN (1500 lb) peak force and a pulse duration of 17 msec applied as a pressure load on a 25 mm (1 in.) diameter area corresponding to the ball protruding from the top of the unit, as shown in Figure D-35. A 2D surface-to-surface contact model that allowed the plate decoupling from the soil was implemented to represent better the conditions observed during field testing. In contrast, for the static model, which made use of the same soil mesh, a 205 kPa (30 psi) pressure load was uniformly distributed at the soil surface, as shown on Figure D-35c. The time histories of the responses were obtained underneath the center of the plate and along the soil surface, with a 1 ms time interval for the dynamic FE analyses. With this information, the variations of the vertical deflection and stress with depth were calculated during the plate impact.

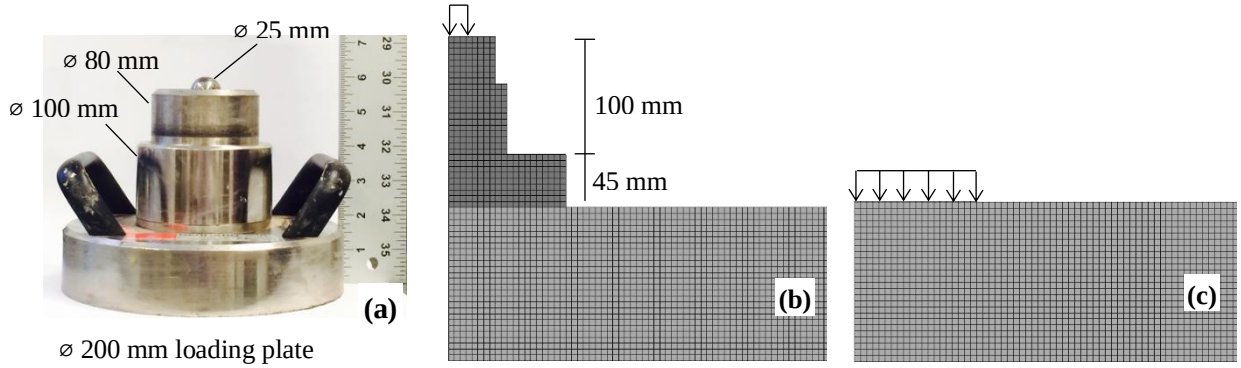

Figure D-35. Schematic and finite element (FE) models views from devices. (a) LWD device, (b) FE dynamic model and (c) FE static model.

Similar to the FE modeling of the IC roller, the nonlinear material model proposed by Ooi et al. (2006) was used for representing the behavior of the geomaterials. A parametric study was performed on a single-layer geosystem (representing a uniform subgrade) and on a two-layer geosystem (representing a subgrade and a base layer). The combinations of randomly selected nonlinear k' parameters comprising the 200 cases used for the IC roller were used for this parametric study as well. For each pavement case, the surface deflection was obtained from both the dynamic and static FE analyses.

Evaluation of Pavement Responses with Respect to Displacement

The displacements under different levels of sophistication of IC roller and LWD were compared in order to establish reliable relationships between the two devices.

- **Static LWD vs. Static Stationary IC Roller.** The descriptive statistics of the relationships between the deflections obtained under the IC roller and the LWD are summarized in Table D-22. The following conclusions can be drawn:
  - ***Single-Layer System:*** The displacements observed from static LWD and static stationary (SSN) IC roller agree well for single-layer geosystems as shown in Figure D-36. The average surface displacement under the static stationary IC roller with operating features mentioned in Table D-1 is about 6 times the corresponding results gathered from the static LWD. However, the average pressure exerted by the drum was found to be about 350 kPa (51 psi) which is 1.6 times the average pressure imposed by the LWD plate (i.e. 210 kPa).
  - ***Two-Layer System:*** The displacements for the two-layer geosystems obtained from the static stationary drum (SSN) and static LWD FE models are shown for both 150 mm (6 in.) and 300 mm (12 in.) base thickness in Figure D-37. Compared to single-layer systems, the slopes of the fitted lines increased for the two-layered geosystems to about 7.6. In addition, the data points representing the displacements for two-layer systems are more dispersed in comparison to the corresponding ones obtained for single-layer systems. In other words, the surface displacements for the two-layer systems seem to be correlated with some uncertainty as judged by the number of cases falling outside the ±20% error bounds.
- **Static LWD vs. Vibratory Stationary IC Roller.** The geomaterials' responses for one- and two-layer geosystems imposed by a vibratory stationary IC roller (VSN) and a uniformly distributed static load (S-LWD) are summarized below.
  - ***Single-Layer System:*** Similar to SSN cases, the maximum surface displacements determined for VSN cases are correlated well with the corresponding static LWD results on top of the subgrade (see Figure D-38).
  - ***Two-Layer System:*** As shown in Figure D-39, the average displacements for VSN models with 150 mm (6 in.) and 300 mm (12 in.) base thicknesses are about 7.5 and 7.8 times the corresponding results observed from S-LWD cases, respectively. The slope (S), R^2 values, and *SEE* of the regression lines from the comparison of VSN IC roller and S-LWD are presented in Table D-22. The dispersion in the results increases with an increase in the thickness of the base.

Table D-22. Descriptive statistics for correlation of maximum surface displacement obtained from static LWD and different levels of sophistication of IC roller for single- and two-layer systems.

Model	Slope of Fitted Linear Relationship, *S*			Coefficient of Determination, R^2			Standard Error of Estimate, SEE		
	SSN	VSN	VMN	SSN	VSN	VMN	SSN	VSN	VMN
Single-Layer System	5.93	5.50	6.00	0.92	0.93	0.87	0.27	0.20	0.27
150 mm (6 in.) Thick Base	7.61	7.45	8.40	0.69	0.75	0.58	0.49	0.41	0.56
300 mm (12 in.) Thick Base	7.59	7.82	8.28	0.64	0.56	0.48	0.42	0.42	0.44

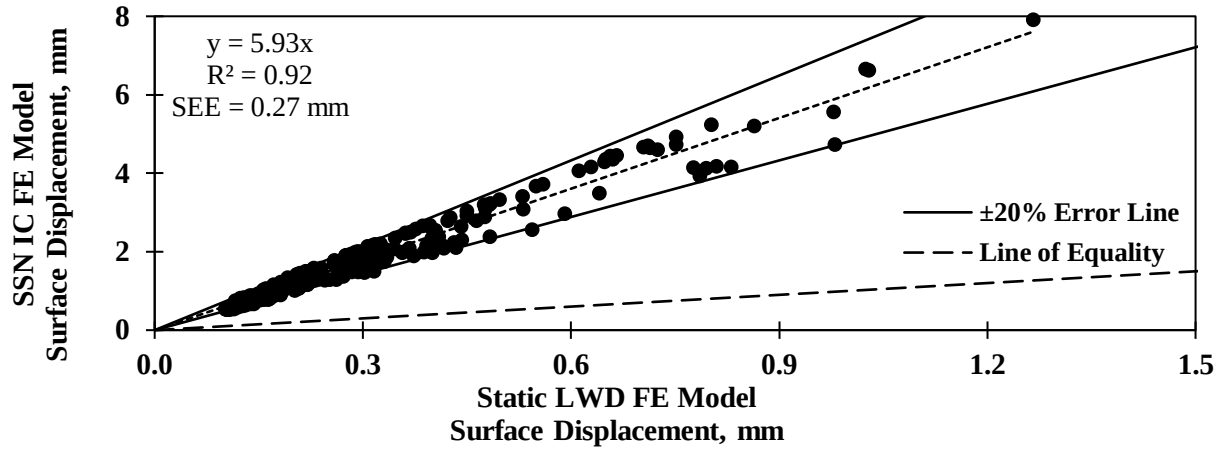

Figure D-36. Relationship of surface displacement between static LWD and static stationary nonlinear (SSN) IC roller for single-layer systems.

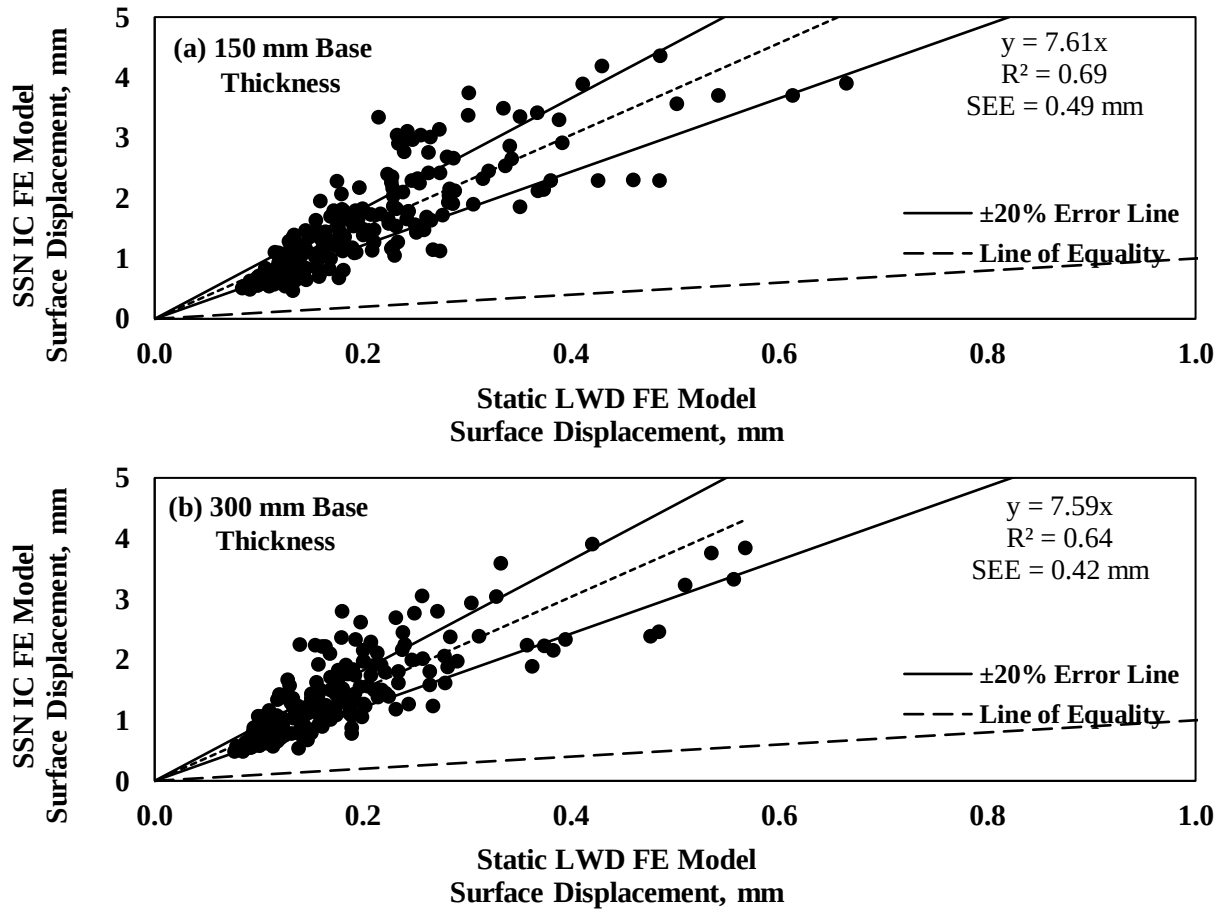

Figure D-37. Relationships of surface displacement between static LWD and static stationary nonlinear (SSN) IC roller for two-layer systems.

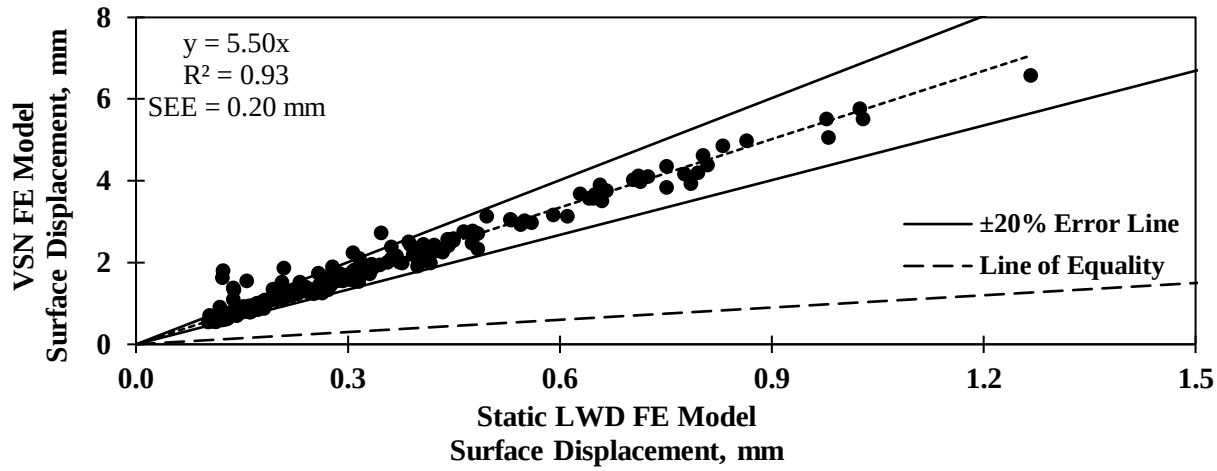

Figure D-38. Relationship of surface displacement between static LWD and vibratory stationary nonlinear (VSN) IC roller for single-layer systems.

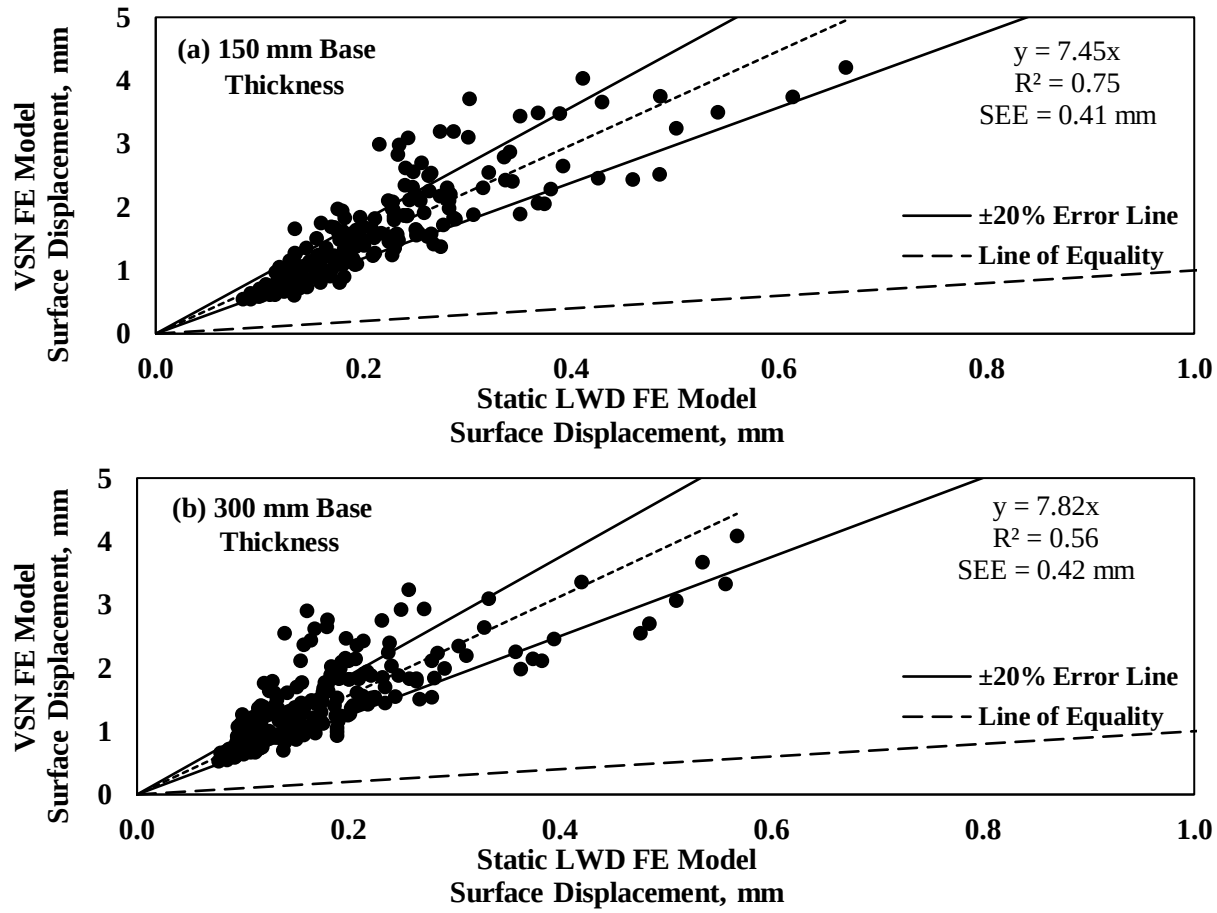

Figure D-39. Relationship of surface displacement between static LWD and vibratory stationary nonlinear (VSN) IC roller for two-layer systems with 300 mm (12 in.) base thickness.

- **Static LWD vs. Vibratory Moving IC Roller.** The maximum surface displacements recorded from a vibratory roller when the drum moves at a speed of 4.8 km/h (3 mph) and rotated with an angular velocity of 1.2 rad/s were compared with the results obtained from S-LWD cases.
  - ***Single-Layer System:*** Figure D-40 and Table D-22 show that the slope of the linear relationship between the maximum surface displacements of VMN IC roller and S-LWD models increases as the level of sophistication of the IC roller modeling increases.
  - ***Two-Layer System:*** As shown in Figure D-41, the displacements recorded for the two-layer systems under VMN IC roller and S-LWD are correlated with some uncertainties as judged by low coefficient of determination (R^2) and high *SEE* compared to SSN and VSN FE models.
- **Static LWD vs. Vibratory Moving IC Roller.** The maximum surface displacements recorded from a vibratory roller when the drum moves at a speed of 4.8 km/h (3 mph) and rotated with an angular velocity of 1.2 rad/s were compared with the results obtained from S-LWD cases.
  - ***Single-Layer System:*** Figure D-40 and Table D-22 show that the slope of the linear relationship between the maximum surface displacements of VMN IC roller and S-LWD models increases as the level of sophistication of the IC roller increases.
  - ***Two-Layer System:*** As shown in Figure D-41, the displacements recorded for the two-layer systems under VMN IC roller and S-LWD are correlated with some uncertainties as judged by low coefficient of determination (R^2) and high *SEE* compared to SSN and VSN FE models.
- **Dynamic LWD vs. IC Roller.** The maximum surface displacements recorded form dynamic LWD (D-LWD) and different levels of sophistication of IC roller FE models are compared in Table D-23.
  - ***Single-Layer System:*** The average surface displacements recorded from different scenarios of IC roller are about 4.5 times the comparable results obtained from D-LWD cases for single-layer geosystems. The corresponding SEE increased to 0.43 while R^2 decreased to 0.53.
  - ***Two-Layer System:*** The R^2 decreases with an increase in the thickness of the base (top) layer.

Bridging Relationship: IC Roller vs. LWD

The relationships between the responses of the two devices presented in the previous section are not robust. To improve those relationships, a comprehensive correlation analysis was carried out. This process was adopted to fit different nonlinear functions considering the transformation of all input parameters (e.g. $\sqrt{k_i'}$, $\ln\ k_i'$, $\exp k_i'$). The development of such relationships from the numerical data are explored here.

Relationships based on Displacement Criteria

- **Static Stationary Nonlinear IC Roller vs. Static LWD:** Based on the Spearman's correlation analysis of the IC drum displacement and the nonlinear material parameters described in the previous section, the surface displacements for the single- and two-layer systems were found to be more sensitive to the nonlinear parameters of the subgrade. To develop a robust relationship between the LWD surface displacement, d_{LWD}, and the surface displacement under the IC roller, the base thickness (h_b) and the nonlinear k' parameters of subgrade were taken into account in the general form of:

$$d_{IC-Roller} = f\left(k_i'^{S}, h_b, d_{LWD}\right) \quad \text{(D.13)}$$

Equation D.14 provides the best prediction of the surface displacement (d_{SSN}) under the regular static stationary roller (SSN) with the operating features discussed in Table D-1:

$$d_{SSN} = C_1 d_{S-LWD} + \frac{C_2 - C_3 h_b k_3'^{S}}{k_1'^{S}} - k_2'^{S} d_{S-LWD} \quad \text{(D.14)}$$

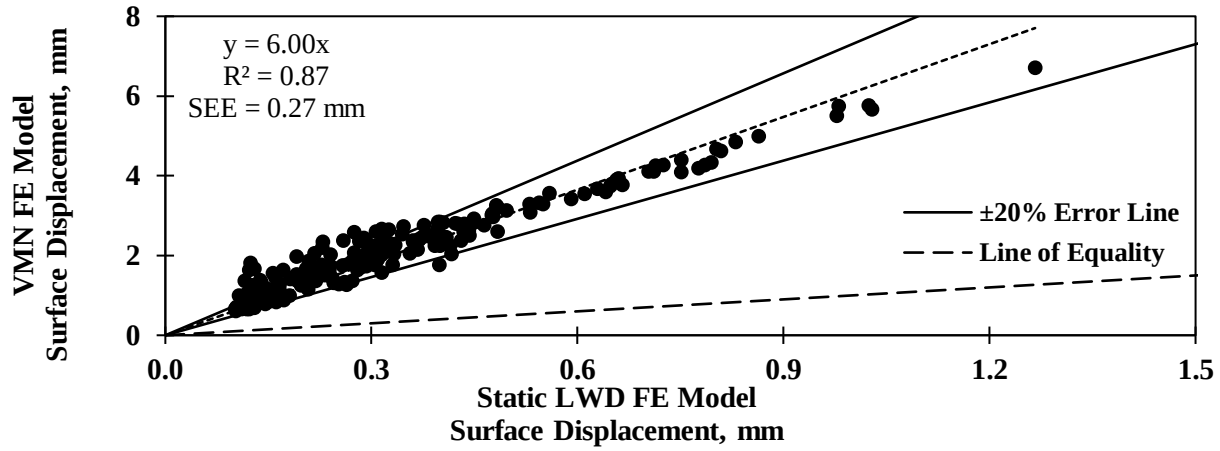

Figure D-40. Relationship of surface displacement between static LWD and vibratory moving nonlinear (VMN) IC roller for single-layer systems.

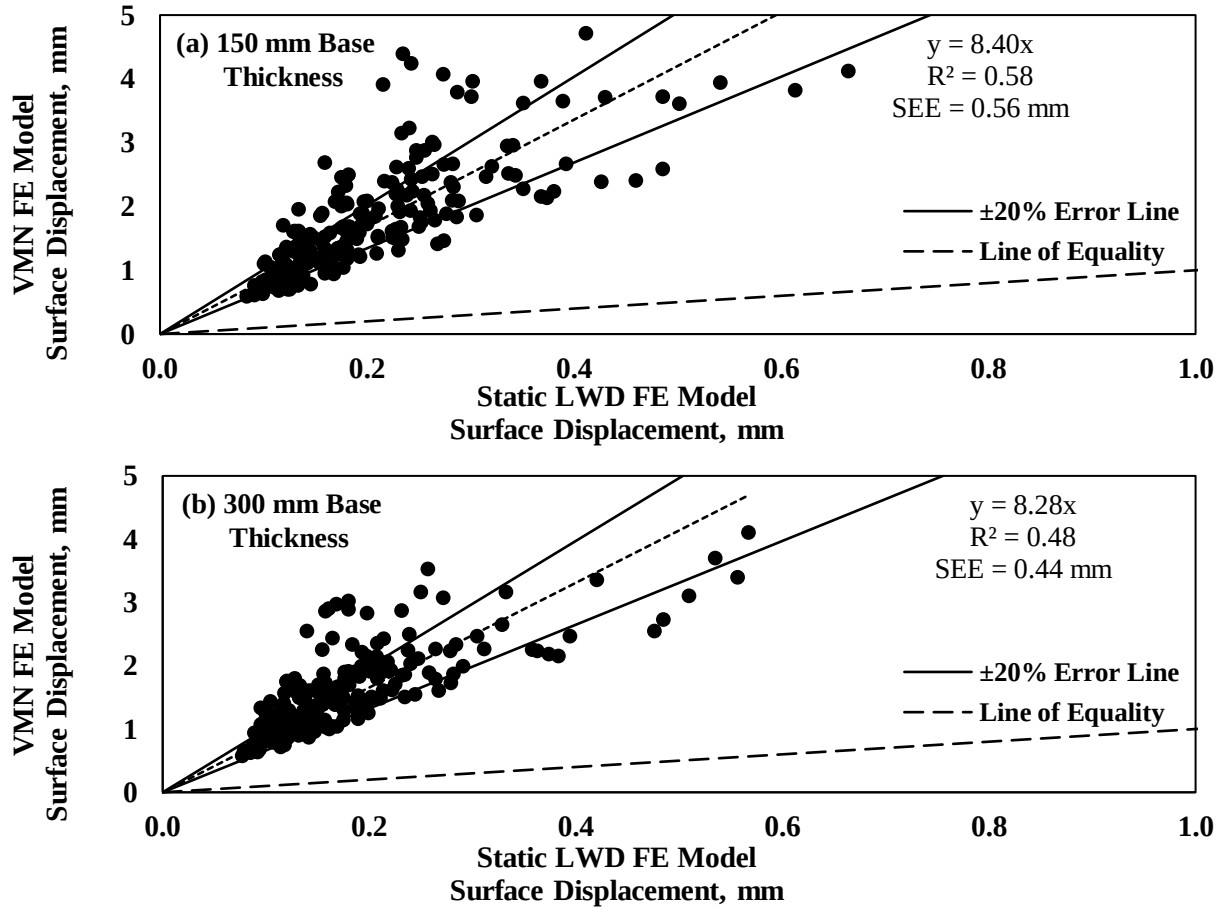

Figure D-41. Relationship of surface displacement between static LWD and vibratory moving nonlinear (VMN) IC roller for two-layer systems

Table D-23. Summary of descriptive statistics for correlation of maximum surface displacement obtained from dynamic LWD and different levels of sophistication of IC roller for single- and two-layer systems.

Model	Slope of Fitted Linear Relationship, *S*			Coefficient of Determination, R^2			Standard Error of Estimate, SEE		
	SSN	VSN	VMN	SSN	VSN	VMN	SSN	VSN	VMN
Single-Layer System	4.45	5.50	6.00	0.92	0.93	0.87	0.27	0.20	0.27
150 mm (6 in.) Thick Base	5.03	7.45	8.40	0.69	0.75	0.58	0.49	0.41	0.56
300 mm (12 in.) Thick Base	4.91	7.82	8.28	0.64	0.56	0.48	0.42	0.42	0.44

where C_1 = 6.85, C_2 = 50.7, C_3 = 0.432, $k_i'^s$ are the nonlinear parameters of subgrade, and $d_{D\text{-}LWD}$ is the surface displacement obtained from the application of static LWD. As shown in Figure D-42, the proposed equation provided a good estimate of the IC SSN responses, with an R^2 value of 0.91 and SEE of 0.17 mm. The proposed relationship adequately relates the two surface displacements.

- **Vibratory Stationary Nonlinear IC Roller vs. Dynamic LWD:** Similar to the static FE nonlinear models for both IC and LWD, a function to predict the surface deflection of IC roller as obtained from the VSN FE model using the dynamic FE model of the LWD was developed. The Spearman's correlation study for the VSN IC model concluded the nonlinear parameters k'_1 and k'_2 of subgrade had a significant effect on the surface displacement, as shown in Tables D-16 and D-17 for both single- and two-layered systems. The following equation was found to be as a good predictor for the surface displacement for a vibratory stationary roller (VSN):

$$d_{VSN} = C_1 d_{D-LWD} + \frac{C_2 - C_3 h_b k_3'^s}{k_1'^s} - k_2'^s d_{D-LWD}, \quad \text{(D.15)}$$

where d_{VSN} is VSN IC roller surface displacement, C_1 = 4.83, C_2 = 134.29, C_3 = 0.372, $k_i'^s$ are the nonlinear parameters of subgrade, and $d_{D\text{-}LWD}$ is the surface displacement obtained from the application of dynamic LWD.

The backcalculated top-layer displacements under the vibratory stationary drum agree well with the results gathered from the VSN forward model (shown in Figure D-13). The proposed relationship predicts VSN IC surface displacements with an R^2 of 0.91 and SEE of 0.27 mm.

- **Vibratory Moving Nonlinear IC Roller vs. Dynamic LWD:** In this case, the surface displacements were found to be most sensitive to parameters k'_1 and k'_2 of subgrade, respectively (Tables D-16 and D-17). Other parameters had relatively low impact on the surface displacements recorded from VSN and D-LWD FE models. The following equation is suggested to predict surface displacement (d_{VMN}) under a vibratory moving roller (VMN):

$$d_{VMN} = C_1 - \ln(k_1'^s) - C_2 k_2'^s + C_3 k_3'^s (C_4 h_b - 1) + C_5 {d_{D-LWD}}^2 \quad \text{(D.18)}$$

where C_1 = 8.59, C_2 = 0.725, C_3 = 0.389, C_4 = 0.0012, C_5 = 1.62, $k_i'^s$ are the nonlinear parameters of subgrade, and $d_{D\text{-}LWD}$ is the surface displacement under dynamic LWD. Figure D-44 shows that the predicted surface displacements are in a good agreement with the results obtained from VMN forward model.

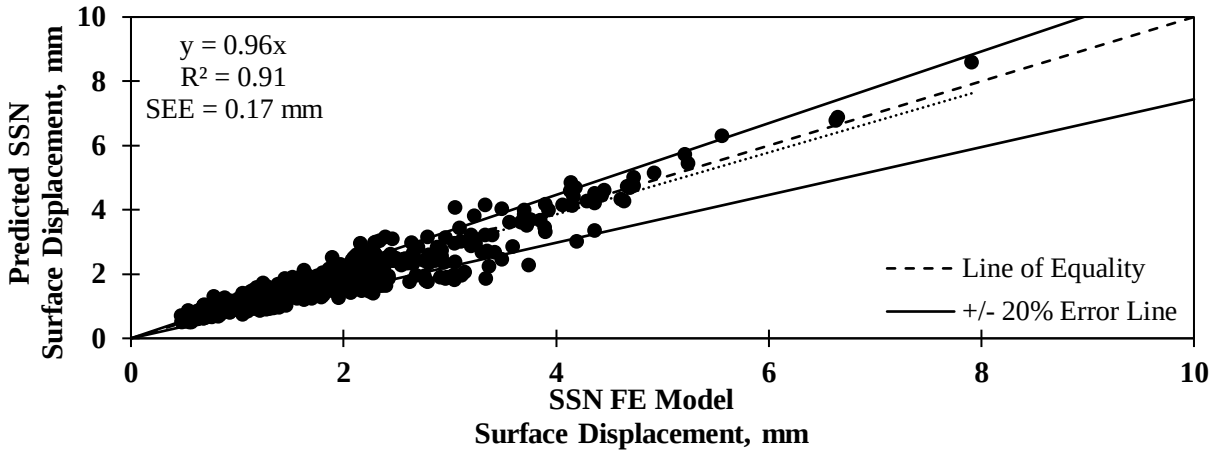

Figure D-42. Comparison of SSN surface displacement as predicted from LWD surface displacements using Equation D.14 vs. surface displacement from SSN FE model.

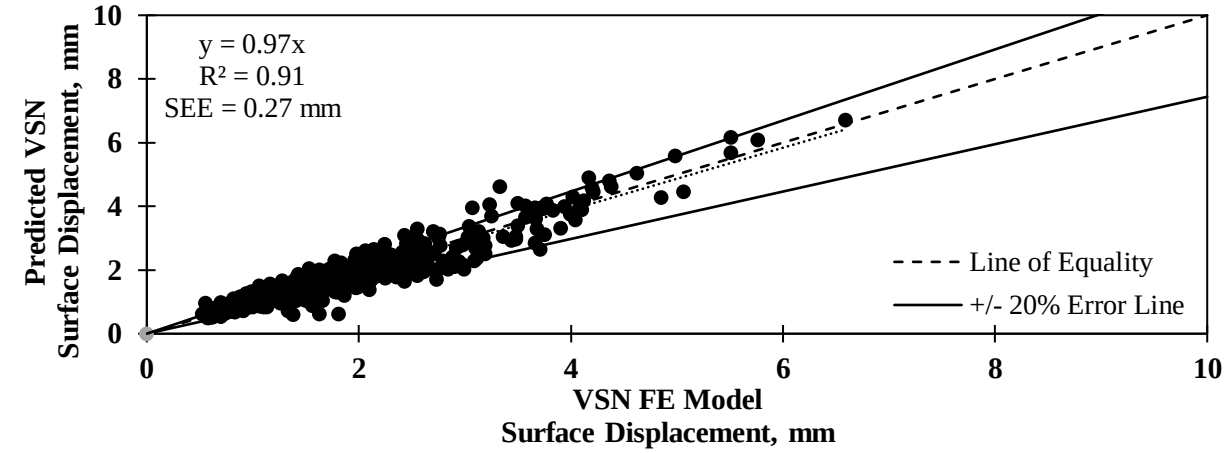

Figure D-43. Predicted VSN surface displacement vs. surface displacement from VSN FE model.

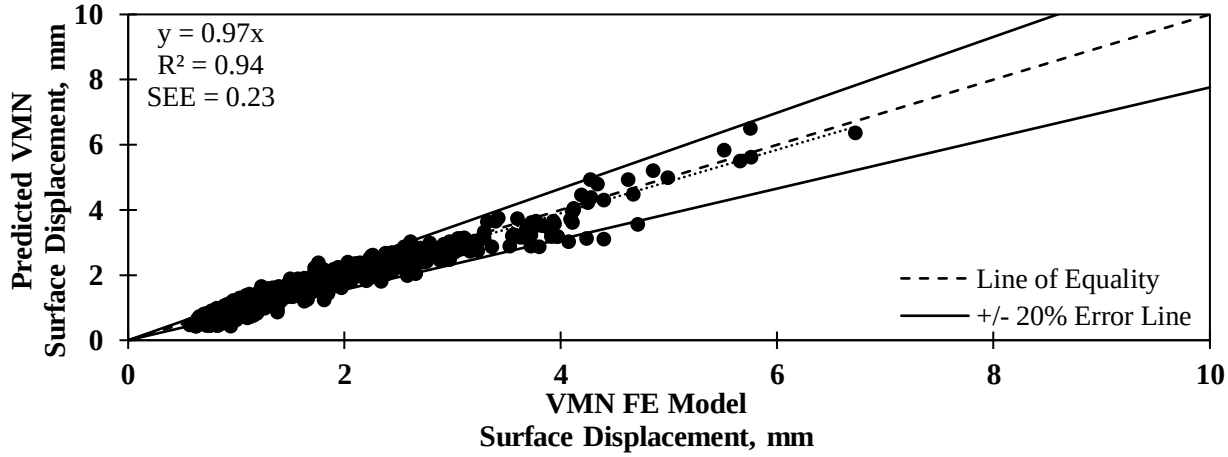

Figure D-44. Predicted VMN surface displacement vs. surface displacement from VMN FE model.

Pavement Responses under Rollers with Different Operating Features

Roller parameters significantly affect both the roller measurements and the geomaterials' responses during the mapping process. Aside from the pavement structure and mechanical properties of geomaterials (e.g., modulus, and nonlinear k' parameters), the impact of the roller's operating features (e.g., operating weight and dimensions of the drum and frame, vibratory system's centrifugal force, nominal vibration frequency and amplitude) on the pavement responses should be taken into consideration. Thirteen rollers with different operating features listed in Table D-24 were simulated. The rollers are identified using a code that summarizes the imparted force plus drum weight, length and diameter of the drum. The soil responses determined under a static load exerted by a stationary drum were evaluated on a set of 200 nonlinear geomaterials systems comprised of single- and two-layer pavement systems (i.e., 600 SSN FE models in total).

Table D-24. Characteristics of studied rollers with different operating features.

Model Code*	Drum Weight (kN)	Centrifugal Force (kN)	Length (m)	Diameter (m)	No. of SSN Cases
22.6W_1.00L_0.60D	7.45	15.12	1.00	0.60	600
45.1W_1.00L_0.60D	14.90	30.24	1.00	0.60	600
38.5W_1.20L_0.70D	23.93	14.60	1.20	0.70	600
77.1W_1.20L_0.70D	47.86	29.20	1.20	0.70	600
118.7W_1.50L_1.10D	88.55	30.20	1.50	1.10	600
118.7W_1.50L_0.55D	88.55	30.20	1.50	0.55	600
166.8W_1.50L_1.10D	88.55	78.30	1.50	1.10	600
166.8W_1.50L_0.55D	88.55	78.30	1.50	0.55	600
113.9W_2.00L_1.50D	29.42	84.50	2.00	1.50	600
227.8W_2.00L_1.50D	58.84	169.00	2.00	1.50	600
227.8W_2.00L_0.75D	58.84	169.00	2.00	0.75	600
227.8W_1.00L_1.50D	58.84	169.00	1.00	1.50	600
* W – operating weight + eccentric force, L – length of drum, D – diameter of drum				**Total No.**	7200

Impact of Weight on Soil Responses

To evaluate objectively the impact of the weight on the pavement responses, three rollers with different drum dimensions were considered, listed in Table D-25. To evaluate its impact on pavement responses for single- and two-layered geosystems, the weight imposed by the drum was doubled in magnitude while the drum length and diameter were maintained constant.

Table D-25. Rollers selected for evaluating effect of drum weight on pavement responses.

Case	Model Code	Drum Weight + Centrifugal Force (kN)	Length (m)	Diameter (m)
1	22.6W_1.00L_0.60D	22.6	1.00	0.60
2	38.5W_1.20L_0.70D	38.5	1.20	0.70
3	113.9W_2.00L_1.50D	113.9	2.00	1.50

The following conclusions can be drawn from these simulations:

- ***Surface Displacement***. Figure D-45 compares the surface displacements directly under the drum from the three selected rollers. Increasing the weight by a factor of two led to an increase in the surface displacement with a factor of 2.17 and 2.00 for single- and two-layer geosystems, respectively. The descriptive statistics of the surface displacements for each roller are summarized in Table D-26a. The means, medians and standard deviations of the surface displacements increased by a factor of about two, when the imposed weights were doubled.

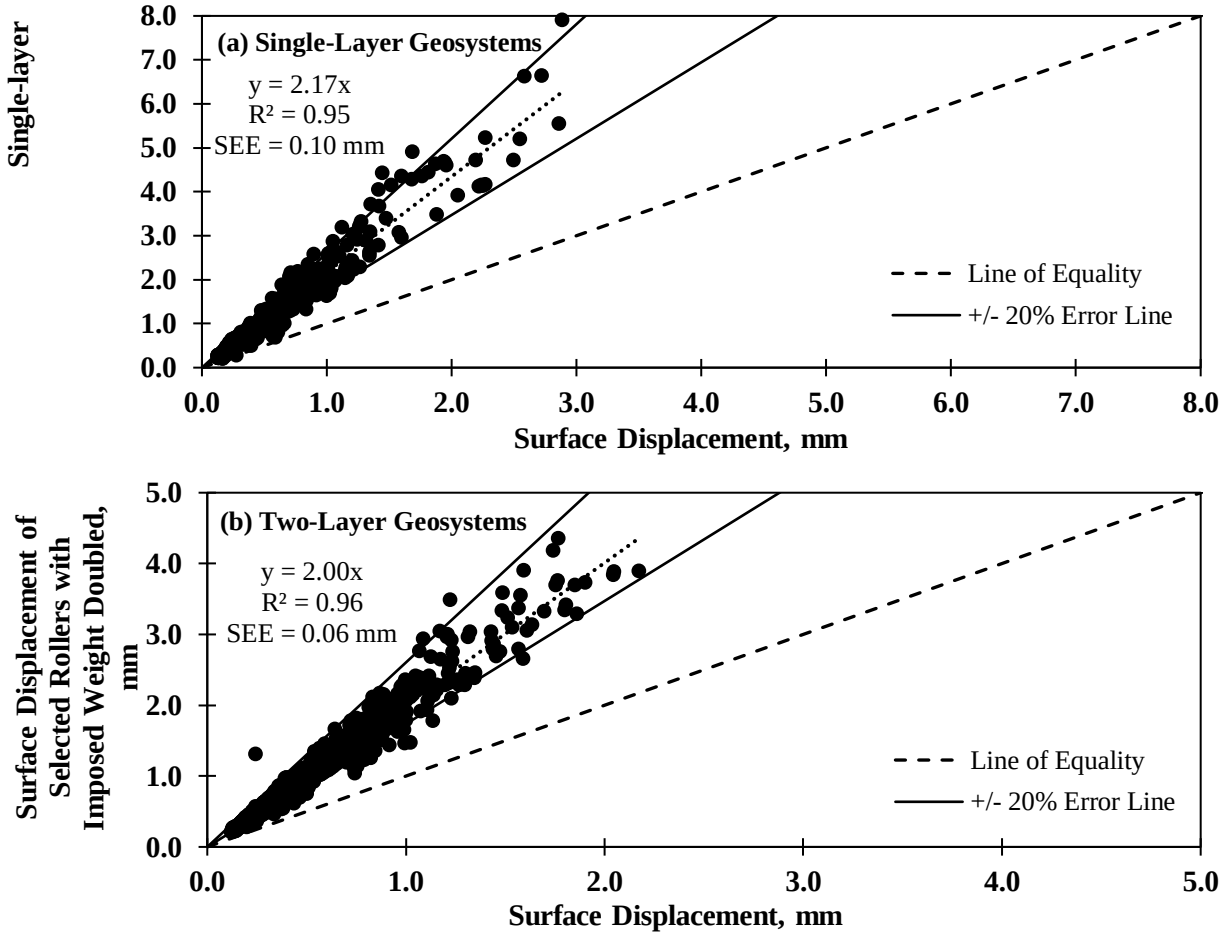

Figure D-45. Evaluation of weight impact on surface displacement for single- and two-layer geosystems.

- ***Surface Vertical Stress.*** Table D-26b summarizes the descriptive statistics of the surface vertical stresses obtained directly underneath the drum. Similar to the surface displacements, the surface vertical stresses directly under the drum increased by about a factor of two, when the magnitude of the imposed weight increased by a factor of two. However, the standard deviations point to more variability in the surface stresses as compared to the surface displacements, which may be attributed to the effects of the nonlinear parameters of the top layer geomaterial have on the contact area.
- ***Depth of Influence***. Tables D-26c and D-26d compare the depths of influence using the displacement and stress criteria, respectively. The influence depth did not increase as the force imposed by the drum increased in magnitude. However, the influence depth varied among the rollers, which happen to have different drum lengths and diameters. This is the subject of the analysis in the following subsection.

Table D-26. Evaluation of weight impact on pavement responses for single- and two-layer geosystems.

(a) Surface Displacement

Case	Weight (kN)	Length (m)	Diameter (m)	Surface Displacement (mm)					
				Single-Layer System			Two-Layer System		
				Mean	Median	Standard Deviation	Mean	Median	Standard Deviation
1	**22.6**	1.0	0.60	0.37	0.31	0.23	0.29	0.25	0.13
	Weight Doubled			0.75	0.64	0.48	0.55	0.48	0.27
2	**38.5**	1.2	0.70	0.38	0.31	0.23	0.30	0.26	0.14
	Weight Doubled			0.75	0.65	0.48	0.58	0.50	0.28
3	**113.9**	2.0	1.50	0.90	0.76	0.57	0.75	0.66	0.37
	Weight Doubled			1.99	1.66	1.34	1.50	1.29	0.81

(b) Surface Vertical Stress

Case	Weight (kN)	Length (m)	Diameter (m)	Surface Vertical Stress (kPa)					
				Single-Layer System			Two-Layer System		
				Mean	Median	Standard Deviation	Mean	Median	Standard Deviation
1	**22.6**	1.0	0.60	160	160	1.80	159	160	1.80
	Weight Doubled			315	316	5.69	316	317	6.09
2	**38.5**	1.2	0.70	135	136	1.06	136	136	1.12
	Weight Doubled			303	305	7.96	305	307	1.60
3	**113.9**	2.0	1.50	251	252	4.67	251	252	5.33
	Weight Doubled			472	480	9.02	478	483	13.76

(c) Depth of Influence Based on Displacement Criterion

Case	Weight (kN)	Length (m)	Diameter (m)	Depth of Influence (m)					
				Single-Layer System			Two-Layer System		
				Mean	Median	Standard Deviation	Mean	Median	Standard Deviation
1	**22.6**	1.0	0.60	1.45	1.46	0.06	1.60	1.57	0.15
	Weight Doubled			1.46	1.49	0.16	1.63	1.62	0.14
2	**38.5**	1.2	0.70	1.57	1.57	0.05	1.69	1.67	0.13
	Weight Doubled			1.57	1.60	0.14	1.72	1.72	0.13
3	**113.9**	2.0	1.50	1.88	1.89	0.08	1.92	1.95	0.07
	Weight Doubled			1.83	1.85	0.18	1.93	1.94	0.09

(d) Depth of Influence Based on Stress Criterion

Case	Weight (kN)	Length (m)	Diameter (m)	Depth of Influence (m)					
				Single-Layer System			Two-Layer System		
				Mean	Median	Standard Deviation	Mean	Median	Standard Deviation
1	**22.6**	1.0	0.60	0.71	0.71	0.02	0.69	0.70	0.05
	Weight Doubled			0.72	0.71	0.02	0.69	0.70	0.06
2	**38.5**	1.2	0.70	0.78	0.77	0.02	0.77	0.78	0.05
	Weight Doubled			0.79	0.78	0.03	0.77	0.77	0.10
3	**113.9**	2.0	1.50	1.28	1.27	0.06	1.28	1.28	0.06
	Weight Doubled			1.28	1.28	0.07	1.29	1.28	0.08

Impact of Drum Length on Soil Responses

The 227.8W_1.00L_1.50D roller with a drum weight plus peak centrifugal force of 227.8 kN, a drum length of 2.0 m, and a drum diameter of 1.50 m was compared with the same characteristics except that the drum length was shortened to 1.0 m, i.e. half the original drum length. The results are discussed next.

- **Surface Displacement.** As shown in Figure D-46 and Table D-27, shortening the drum by half its original length led to an increase in the surface displacement by a factor of 2.13 for single-layer systems, and 1.84 for two-layered systems.
- **Surface Vertical Stress.** As summarized in Table D-27, the surface stresses increased by about 100% as the drum length was shortened by 50%. The increase in the contact area with an increase in the drum length results in a reduction in the surface vertical stress.
- **Depth of Influence.** As observed in Table D-27, the shortening of the drum by 50% resulted in a decrease of about 84% to 90% in the depth of influence, if the displacement criterion was used, and a decrease of about 70% to 75% in influence depth, if the stress criterion was used. An increase in the ratio of the length-to-width (*L/B*) will typically cause an increase in the depth of influence for classical problems associated with shallow foundations (Das 2015). The ratio of the length-to-contact width may play a key role on the influence depth of the IC rollers.

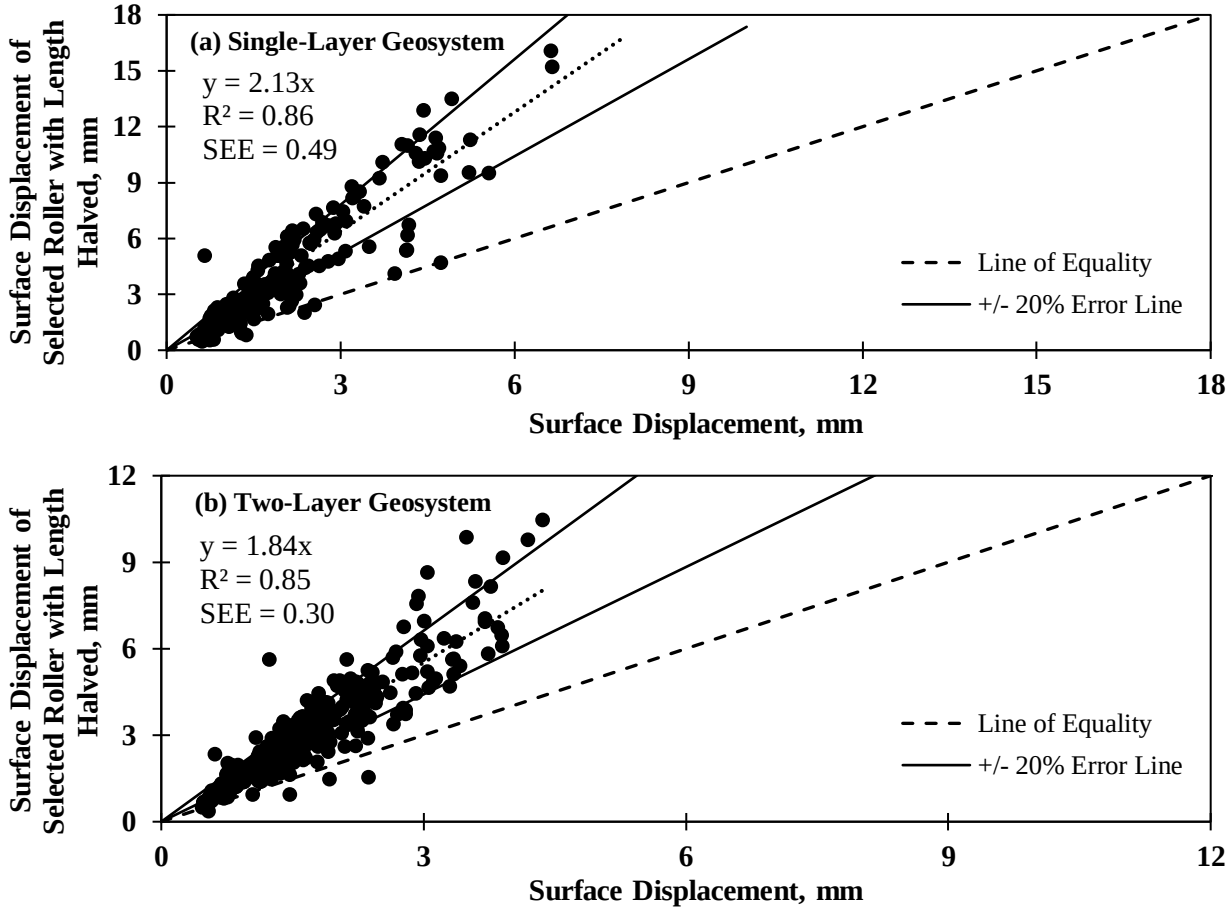

Figure D-46. Evaluation of length impact on displacement for single- and two-layer geosystems.

Table D-27. Evaluation of length impact on pavement responses for single- and two-layer geosystems.

Case	Weight (kN)	Length (m)	Diameter (m)	Surface Displacement (mm)					
				Single-Layer System			Two-Layer System		
				Mean	Median	Standard Deviation	Mean	Median	Standard Deviation
1	227.8	2.0	0.60	1.99	1.66	1.34	1.50	1.29	0.81
		1.0		4.08	4.09	3.34	2.69	2.23	1.73
				Surface Vertical Stress (kPa)					
1	227.8	2.0	0.60	472	480	9.02	478	483	13.76
		1.0		945	990	23.07	1018	1024	34.23
				Depth of Influence Based on Displacement Criterion (m)					
1	227.8	2.0	0.60	1.83	1.85	0.18	1.93	1.94	0.09
		1.0		1.53	1.56	0.33	1.73	1.76	0.23
				Depth of Influence Based on Stress Criterion (m)					
1	227.8	2.0	0.60	1.28	1.28	0.07	1.29	1.28	0.08
		1.0		0.97	0.96	0.12	0.91	0.93	0.13

Impact of Drum Diameter on Soil Responses

Three rollers, with characteristics listed in Table D-28, were selected to assess the effect of the drum diameter on soil responses. The drum diameter was halved for each roller while the imposed weight and drum length were kept constant. The results from this study can be summarized as follows.

Table D-28. Rollers selected for evaluating effect of drum diameter on pavement responses.

Case	Model Code*	Drum Weight + Centrifugal Force (kN)	Length (m)	Diameter (m)
1	118.8W_1.5L_1.1D	118.8	1.5	1.1
2	166.9W_1.5L_1.1D	166.9	1.5	1.1
3	227.8W_2.0L_1.5D	227.8	2.0	1.5

- **Surface Displacement**. Figure D-47 shows the comparison of the surface displacements under the selected rollers prior and after the drum diameters were halved while the imposed drum weights and lengths were kept constant. As shown in Figure D-47, the surface displacements did not change noticeably for the single- and two-layer geosystems. The summary of descriptive statistics of the analyzed rollers in terms of surface displacement are reported in Table D-29a.
- **Surface Vertical Stress.** As reported in Table D-29b, the surface vertical stress increased when the diameter was halved, ranging from 6% for the smaller and lighter roller (Case 1) to 34% for the heavier and larger roller (Case 3). This increase in the surface stress can be attributed to the shorter contact width occurring due to the shortening of the drum diameter, which becomes more significant when large loads are applied to the soil.
- **Depth of Influence**. Tables D-29c and D-29d summarize the influence depths with the displacement and stress criteria, respectively, prior and after the diameters were shortened. The depth of influence did not seem to be sensitive to a change in the drum diameter.

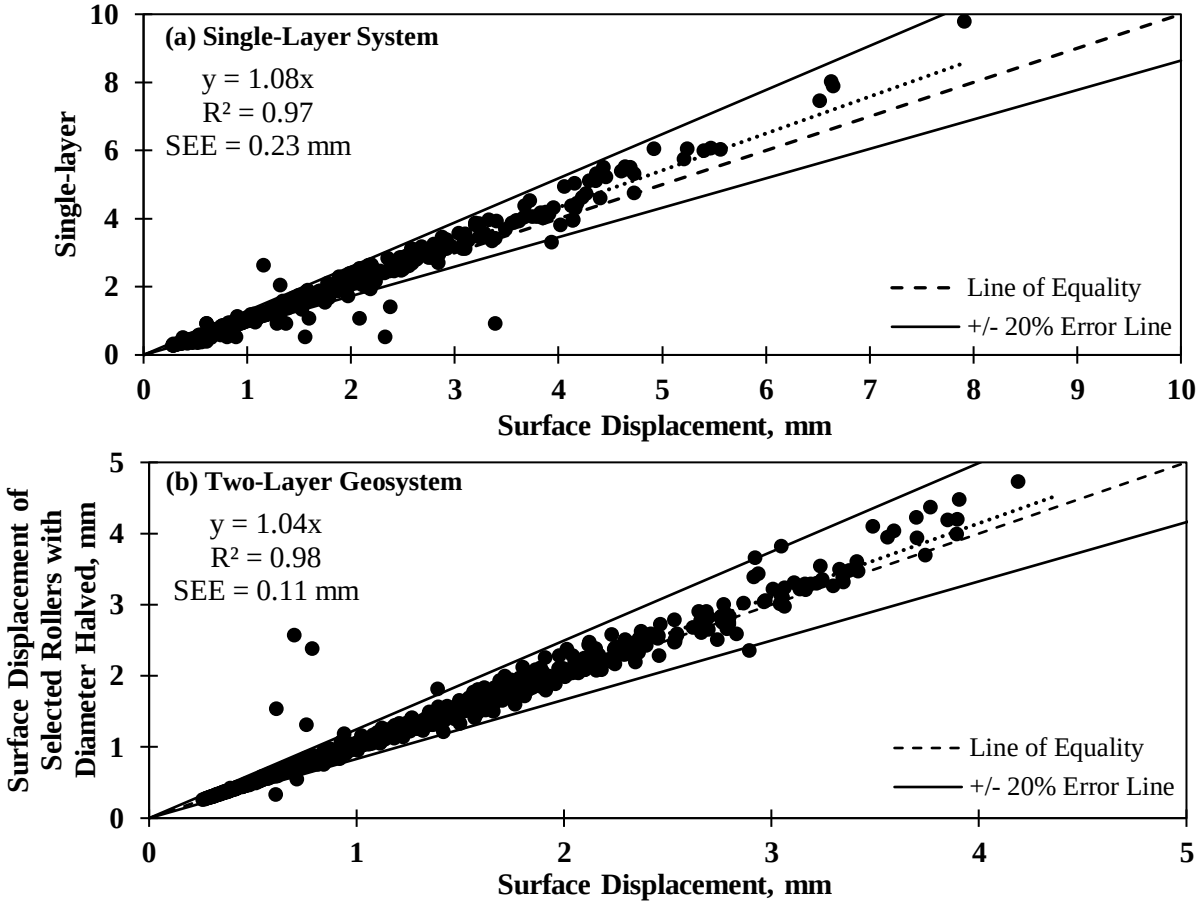

Figure D-47. Evaluation of drum diameter impact on surface displacement for single- and two-layer geosystems.

Prediction of Pavement Responses Using Soft Computing Techniques

The focus of this study is to develop simplified models with minimum computational efforts and reasonable accuracy to predict pavement responses (being displacement, stress and depth of influence) for single- and two-layer geosystems consisting of a base layer and subgrade. For this purpose, a database was generated consisting of 7200 cases of stationary static drum models with different operating features, listed in Table D-24, and geosystems with different base thicknesses and material properties using the feasible ranges of nonlinear *k'* parameters shown in Table D-2.

A combination of genetic programming (GP) and artificial neural network (ANN) was deployed to predict pavement responses. The following sections explain the process of developing predictive models for different types of responses.

Maximum Surface Displacement Underneath Center of Drum.

The general form of the mathematical model proposed using genetic algorithm for prediction of surface displacement consists of multiple functions as follows:

$$d_{SSN} = f\left(k_1'^b, k_2'^b, k_3'^b, k_1'^s, k_2'^s, k_3'^s, h, L, D, W\right) \quad \text{(D.19)}$$

Table D-29. Evaluation of length impact on pavement responses for single- and two-layer geosystems.

(a) Surface Displacement

Case	Weight (kN)	Length (m)	Diameter (m)	Surface Displacement (mm)					
				Single-Layer System			Two-Layer System		
				Mean	Median	Standard Deviation	Mean	Median	Standard Deviation
1	118.8	1.5	1.1	0.95	0.81	0.60	0.72	0.64	0.36
			Diameter Halved	0.97	0.82	0.63	0.72	0.64	0.36
2	166.9	1.5	1.1	1.65	1.35	1.13	1.18	1.04	0.63
			Diameter Halved	1.70	1.35	1.23	1.19	1.05	0.64
3	227.8	2.0	1.5	1.99	1.66	1.34	1.50	1.29	0.81
			Diameter Halved	2.18	1.75	1.62	1.57	1.35	0.88

(b) Surface Vertical Stress

Case	Weight (kN)	Length (m)	Diameter (m)	Surface Vertical Stress (kPa)					
				Single-Layer System			Two-Layer System		
				Mean	Median	Standard Deviation	Mean	Median	Standard Deviation
1	118.8	1.5	1.1	345	337	20.2	341	343	19. 4
			Diameter Halved	367	369	7.7	369	371	8.0
2	166.9	1.5	1.1	518	515	50.8	535	528	59.9
			Diameter Halved	581	585	19.4	591	591	29.5
3	227.8	2.0	1.5	472	480	9.0	478	483	13.8
			Diameter Halved	625	640	37.6	642	648	29.2

(c) Depth of Influence Based on Displacement Criterion

Case	Weight (kN)	Length (m)	Diameter (m)	Depth of Influence (m)					
				Single-Layer System			Two-Layer System		
				Mean	Median	Standard Deviation	Mean	Median	Standard Deviation
1	118.8	1.5	1.1	1.64	1.68	0.17	1.80	1.80	0.11
			Diameter Halved	1.63	1.67	0.17	1.79	1.80	0.12
2	166.9	1.5	1.1	1.62	1.68	0.24	1.80	1.81	0.14
			Diameter Halved	1.61	1.67	0.25	1.79	1.81	0.14
3	227.8	2.0	1.5	1.83	1.85	0.18	1.93	1.94	0.09
			Diameter Halved	1.81	1.85	0.21	1.95	1.97	0.12

(d) Depth of Influence Based on Stress Criterion

Case	Weight (kN)	Length (m)	Diameter (m)	Depth of Influence (m)					
				Single-Layer System			Two-Layer System		
				Mean	Median	Standard Deviation	Mean	Median	Standard Deviation
1	118.8	1.5	1.1	0.79	0.78	0.04	0.79	0.79	0.06
			Diameter Halved	0.79	0.78	0.04	0.79	0.79	0.06
2	166.9	1.5	1.1	0.81	0.79	0.08	0.79	0.79	0.11
			Diameter Halved	0.81	0.79	0.08	0.79	0.79	0.11
3	227.8	2.0	1.5	1.03	1.02	0.10	1.02	1.02	0.11
			Diameter Halved	1.03	1.02	0.10	1.02	1.02	0.11

where W is the weight that includes the operating weight and the eccentric force, L is the drum length, D is the drum diameter, h is the thickness of the base, and $k_i'^b$ and $k_i'^s$ are the nonlinear parameters of the base and subgrade, respectively. The following equation can predict the maximum surface displacement under stationary static (SSN) drums with different operating features:

$$d_{SSN} = C_1 + C_2 W + \frac{C_3}{k_1'^s} + C_4 \cos(W) + C_5 W(k_1'^s + k_2'^s + k_3'^s) + C_6 \psi \cdot k_1'^s (W + k_1'^s) + \frac{C_7 W}{\cos\left(\frac{223L}{D}\right)} + \frac{C_8 h.\psi}{k_1'^b \cdot k_2'^b \cdot k_3'^b} \quad \text{(D.20)}$$

where C_1 = 0.00425, C_2 = 0.0139, C_3 = 205, C_4 = 0.075, C_5 = 5.58×10^{-6}, C_6 = 2.98×10^{-10}, C_7 = 0.0004, C_8 = 4.65×10^{-5}, and ψ = an operating index defined as:

$$\psi = \frac{L}{D} \cdot W \quad \text{(D.21)}$$

Figure D-48 indicates that GP can provide a promising estimate of the peak surface displacement under rollers with different operating features, as most of the cases fall within the ± 20% uncertainty bounds, with an R^2 value of 0.73 and standard error of the estimate of 0.39 mm. An artificial neural network (ANN) was considered to improve further the estimation of the surface displacements. Table D-32 summarizes the ANN characteristics used in this activity. As shown in Figure D-49, the ANN model has the ability to predict the surface displacement with better accuracy than the GP model. The errors of estimate with ANN were less than 15% in 85% of the cases The ANN predicts surface displacements with an R^2 of 0.99 and SEE of 0.10 as observed in Figure D-50. The ANN models are well suited for predicting surface displacements from the layer properties and roller operating features.

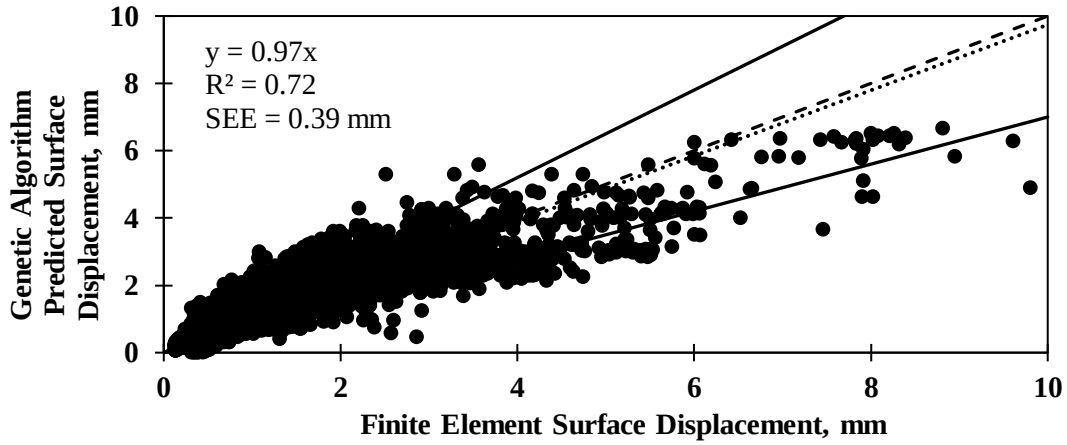

Figure D-48. Comparison of genetic algorithm predicted surface displacement to finite element (FE) surface displacement obtained from stationary drums with different operating features.

Contact Width

The FE model used included a contact model to simulate the interaction between the drum and the geosystem. The inclusion of the nonlinear behavior of the geomaterial allows more realistic conditions than the simplifying Hertzian contact theories that consider homogeneous and linear-elastic behavior of the surfaces. Figure D-51 shows different views of the contact area and the stresses in the geosystem due to drum loading. One of the limitations encountered by the use of the automatic single-surface contact model was that the nodes along the drum (master surface) that are in contact with the geosystem (slave surface) are not explicitly defined. For this reason, the contact width of the drum has to be estimated based on the stress distribution at the soil-drum interface.

Table D-30. Characteristics of the neural network used in the study.

No. All Cases	7200
Training Ratio	70%
Validation Ratio	15%
Testing Ratio	15%
Number of Input Parameters	10
Number of Output Parameters	1
Number of Neurons	20
Network training algorithm	Levenberg–Marquardt
Number of epochs (maximum number of training iterations before training is stopped)	321

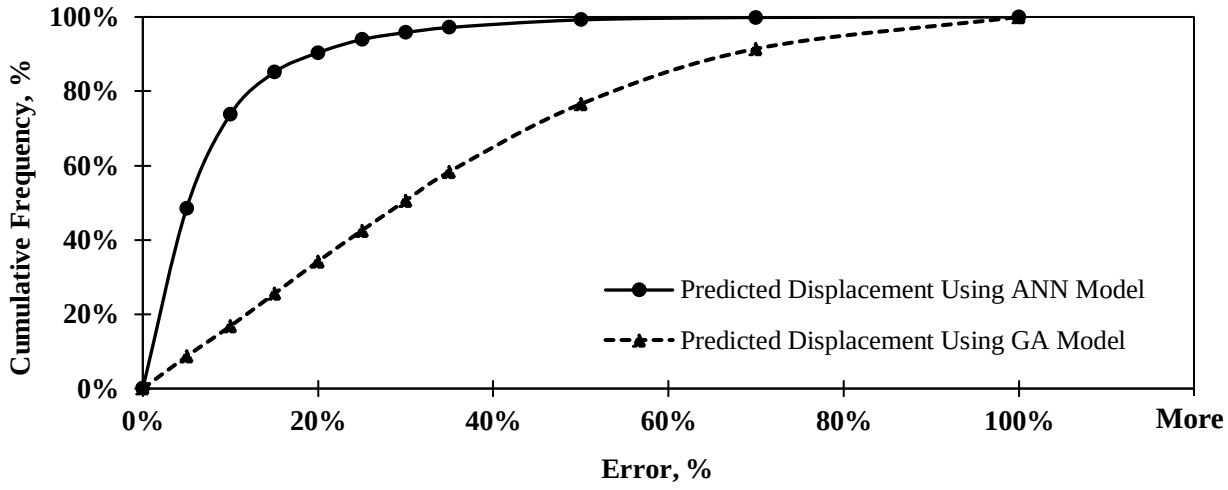

Figure D-49. Cumulative distribution of estimation error for the predicted surface displacement using GP and ANN models.

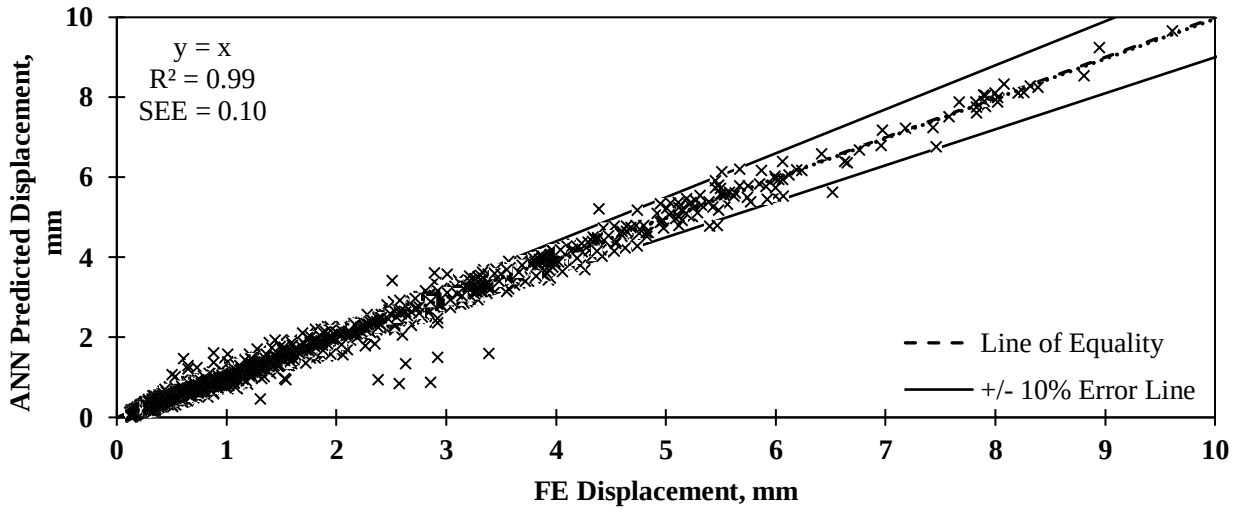

Figure D-50. Predicted surface displacement vs. surface displacement obtained from FE model.

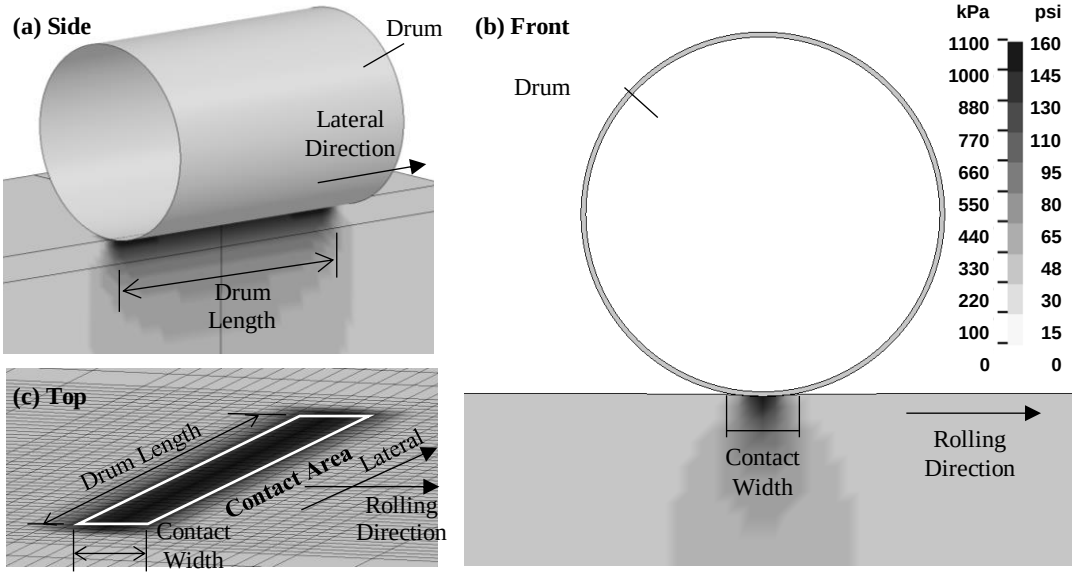

Figure D-51. Cross-sectional views of pavement and drum for the visualization of contact area at drum-soil contact.

The contact area, A_c, can be estimated from:

$$A_c = \frac{F_c}{\sigma_{ave}}, \tag{D.22}$$

where F_c is contact force, and σ_{ave} is average vertical stress within the contact area of the drum. The stress distribution along the drum length at two different distances from the centerline of the drum are shown in Figure D-52. The stress increases along the soil surface underneath the drum when closer to the edges of the drum. Likewise, a drop in stress occurs of about 90 kPa (13 psi) from a distance of 25 mm (1 in.) to 75 mm (3 in.) from the centerline of the drum cylinder in contact with the soil. Due to the mesh size, these two locations represent the centroid of the soil elements along the length of the drum.

The stress distribution of geomaterial in the rolling direction is illustrated in Figure D-53. The vertical stress decreases with respect to distance. Even though at 200 mm (8 in.) away from the centerline the stress is close to zero, this distance cannot be defined as the extent of the contact width. A criterion for defining the contact width is necessary, due to the cylindrical curvature of the drum and the size of elements along the pavement surface (50 mm-sided cubic elements). As a simplifying assumption, the contact width is assumed to be constant along the length of the drum. The contact width was set at the distance where the magnitude of the averaged stress is 85% of the peak observed stress. This arbitrary criterion was then compared with field measurements performed at different sites with distinct types of geomaterials.

The contact width under a static drum load was estimated for four different drums shown in Table D-31, on top of single- and two-layer geosystems. The drums become larger and heavier in the order listed. A set of 200 cases were simulated per drum, for each group of geosystems, consisting of a single-layer (subgrade only) and two-layer systems with top layer (base) thicknesses of 150 mm (6 in.) and 300 mm (12 in.) on top of the subgrade and the feasible ranges of nonlinear *k* parameters described in Table D-2.

The descriptive statistics of the contact width for these drums are summarized in Table D-32. The contact width for these drums are summarized in Table D-32. The contact width increases as the drum becomes larger. Figure D-54 shows as increase of the average contact width as the operating index, ψ, increases.

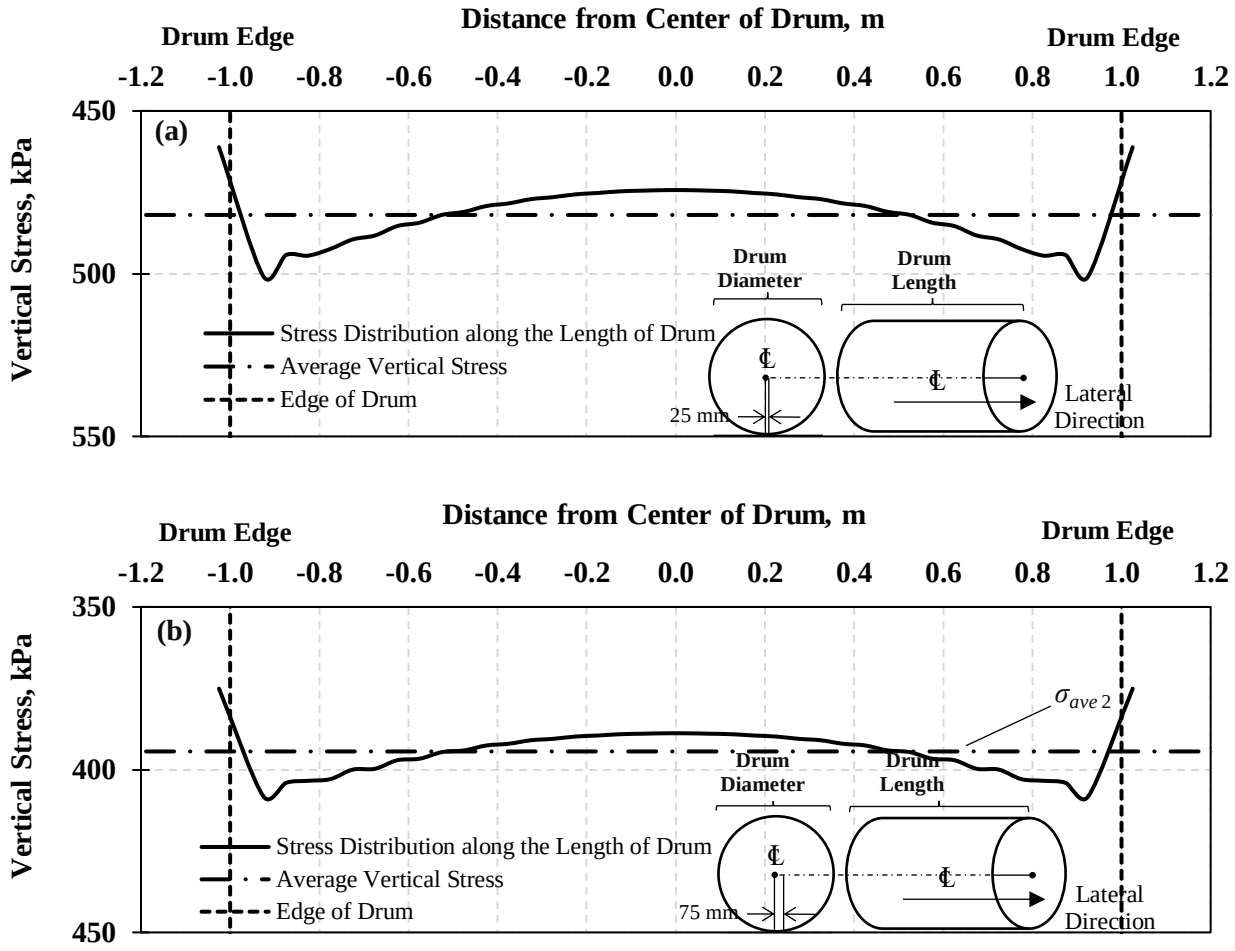

Figure D-52. Stress distribution of surface soil elements along the length of drum at (a) 25 mm away from the center line of drum, (b) 75 mm away from the center line of drum.

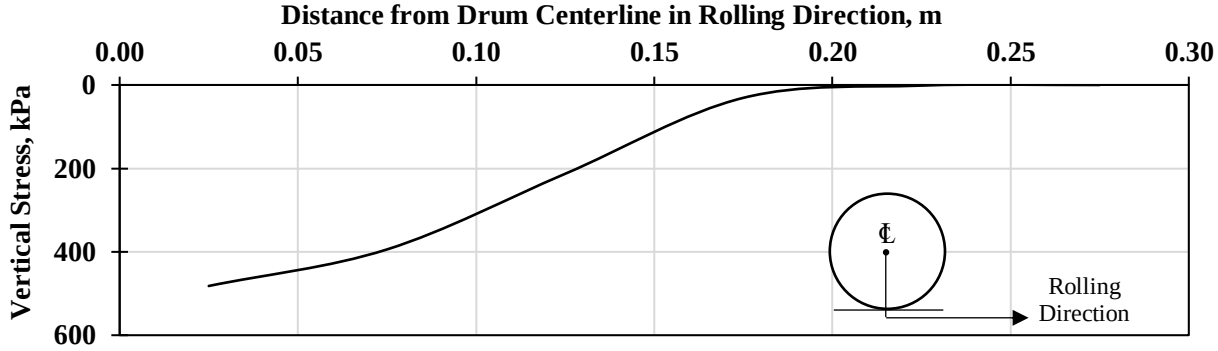

Figure D-53. Stress distribution from drum centerline in rolling direction.

Table D-31. Rollers selected for assessing contact width.

Drum	Model Code*	Operating Index, ψ** (kN)	Drum Weight (kN)	Centrifugal Force (kN)	Length (m)	Diameter (m)	No. of SSN Cases
Ⅰ	22.6W_1.00L_0.60D	37.7	7.45	15.1	1.00	0.60	600
Ⅱ	118.7W_1.50L_1.10D	161.9	88.55	30.2	1.50	1.10	600
Ⅲ	166.8W_1.50L_1.10D	227.5	88.55	78.3	1.50	1.10	600
Ⅳ	227.8W_2.00L_1.50D	303.7	58.84	169.0	2.00	1.50	600

* W = operating weight + eccentric force, L = length of drum, D = diameter of drum.

** ψ is defined in Equation D.21

Table D-32. Descriptive statistics of contact width for different-sized drums.

Drum	Model Code	Operating Index, ψ (kN)	Contact Width (mm)		
			Mean	Median	Standard Deviation
Ⅰ	22.6W_1.00L_0.60D	37.7	143.1	142.8	2.8
Ⅱ	118.7W_1.50L_1.10D	161.9	210.5	208.6	4.5
Ⅲ	166.8W_1.50L_1.10D	227.5	212.4	211.4	5.2
Ⅳ	227.8W_2.00L_1.50D	303.7	264.0	262.2	6.4

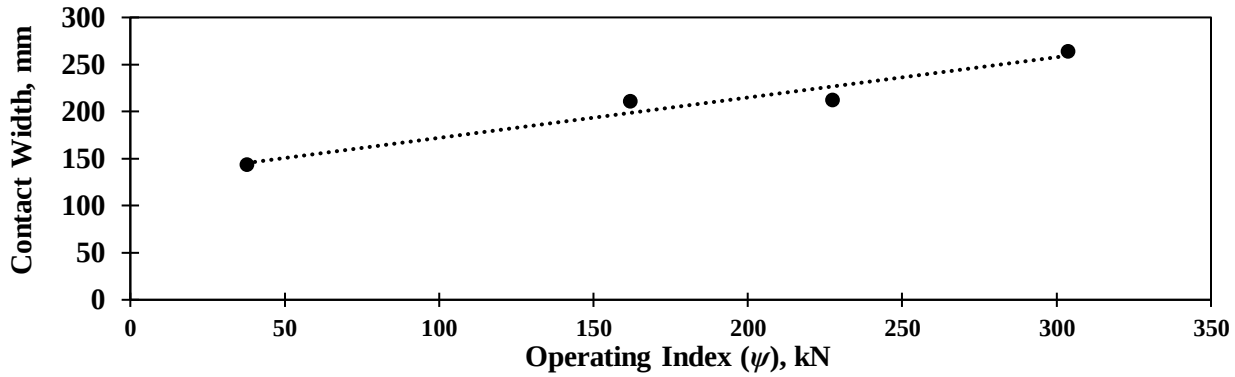

Figure D-54. Variation of contact width with operating index.

Figure D-55 shows the variation in the contact width with resilient modulus (M_R) as obtained from the simulation of a commercially available large-sized roller drum (IV) with operating features listed in Table D-31. For a typical range of resilient modulus for subgrade of 35 – 100 MPa (5 – 15 ksi), the contact width slightly decreases as the M_R increases (see Figure D-62a). The contact width does not seem to be sensitive to the resilient modulus for base materials with typical moduli of 200 – 550 MPa (30 – 80 ksi) on two-layered geosystems, as shown in Figure D-62b.

The contact widths of a Type IV roller drum, described in Table D-31, were measured while static at two subgrade sections and four base course materials. The subgrade sites consisted of a sandy subgrade and a clayey subgrade sections, while two distinct base layers were laid on top of each subgrade type (see Appendix D for the description of the sites). The contact width of the drum was measured by spray-painting the pavement structure underneath, in front of and behind, and along the length of the drum, as shown in Figure D-56. Figure D-57 shows the contact width measurements at the six locations.

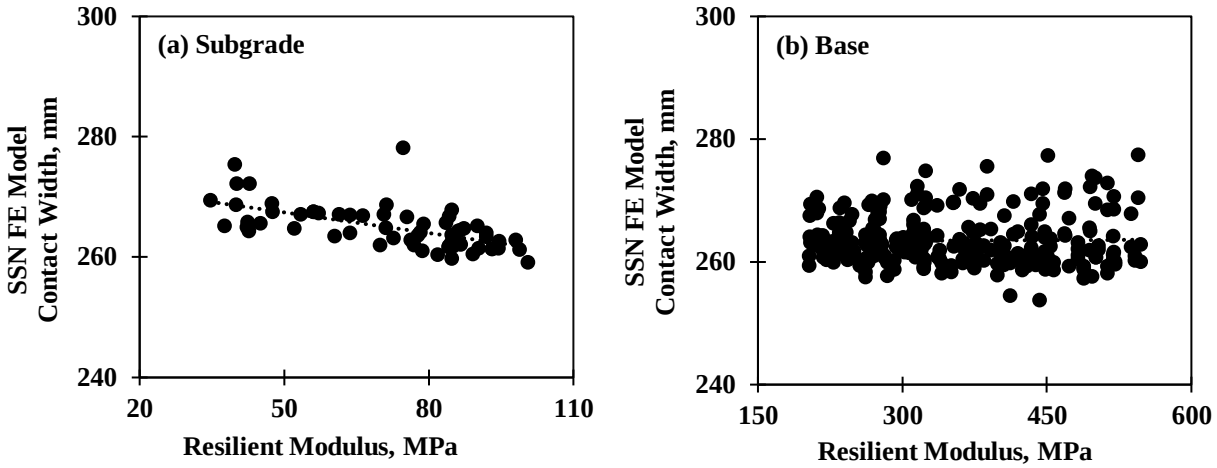

Figure D-55. Variation of contact width with resilient modulus for (a) subgrade and (b) base materials as obtained from finite element (FE) simulation.

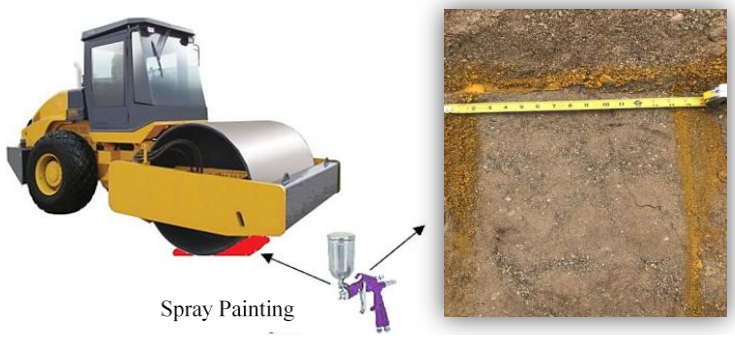

Figure D-56. Schematic view of contact width measurement at field.

Table D-33 lists the selected FE models with representative resilient moduli similar to LWD field surface moduli, and their respective contact widths. Figure D-58 compares the field contact width measurements with the corresponding results obtained from FE analyses. The FE results are in agreement with the measured field contact width.

Impact of Base Thickness on Pavement Responses

An extensive parametric and sensitivity analysis was carried out to understand which input parameters affect the geomaterial's responses using a comprehensive database assembled from different studies as discussed in the previous sections. The database was further expanded to include thirteen different base thicknesses ranging from 125 mm (5 in.) to 425 mm (17 in.) under a static stationary roller with the operating settings described in Table D-1. The following observations were made from the analyses of the data in the database.

Figure D-59 shows that the measured contact width decreases with an increase in the LWD modulus. In other words, the less stiff the geomaterial is, the wider the contact width will become.

Figure D-57. The measured contact width for subgrade and base materials at different MnROAD sections.

Table D-33. Contact width measurements obtained from field sections and similar representative resilient moduli FE models.

Case	Field Measurement		FE Analysis	
	LWD Modulus, MPa	Contact Width, mm	Resilient Modulus, MPa	Contact Width, mm
Clayey Subgrade	59.3	260	59.2	244
Sandy Subgrade	48.3	208	48.8	248
Sandy Subgrade	28.3	297	34.6	260
Base	64.1	203	62.1	229
Base	53.1	269	53.7	241
Base	63.4	264	63.8	238
Base	61.4	241	61.1	231
Base	59.9	234	59.4	241
Base	73.0	226	73.2	227

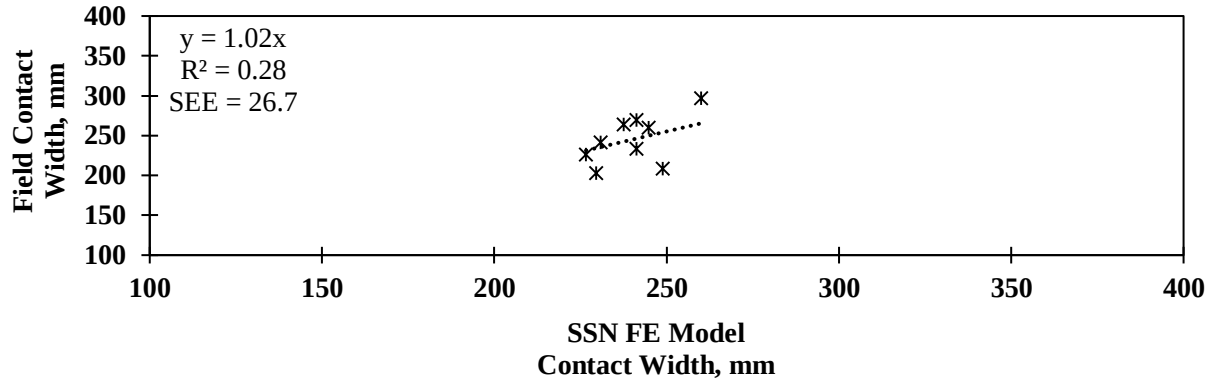

Figure D-58. Comparison of contact width measured from field and FE analysis.

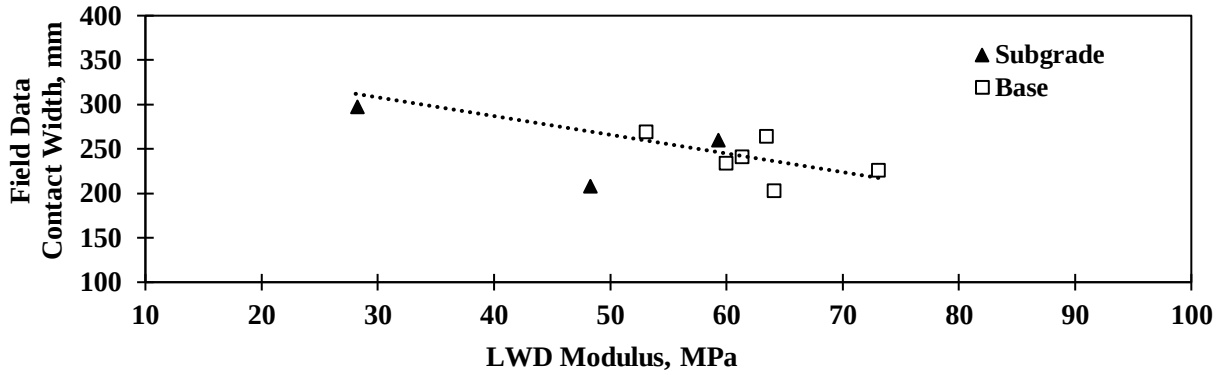

Figure D-59. Measured field contact width vs. LWD modulus for base and subgrade materials.

Surface Displacement

Figure D-60 shows the boxplots of the maximum surface displacements for different base thicknesses. The boxes indicate the first, median and third quantiles and the whiskers the range of values of displacements from the 200 cases per base thickness. The descriptive statistics of maximum displacements on top of different base layers are reported in Table D-3. The median surface displacement slightly decreases with an increase in the base thickness.

Contact Width

The distributions of the contact widths using the stress distribution method are presented in Figure D-61 and Table D-35. Thickening the base does not seem to affect the contact width significantly. The average contact width is about 260 mm (10.2 in.).

Depth of Influence

The influence depths with respect to displacement are demonstrated in Figure D-62 and Table D-36. The depth of influence increases marginally with the increase in the base thickness. Figure D-63 and Table D-37 show the depths of influence based on stress criterion. The mean depth of influence with respect to stress is not sensitive to the base thickness.

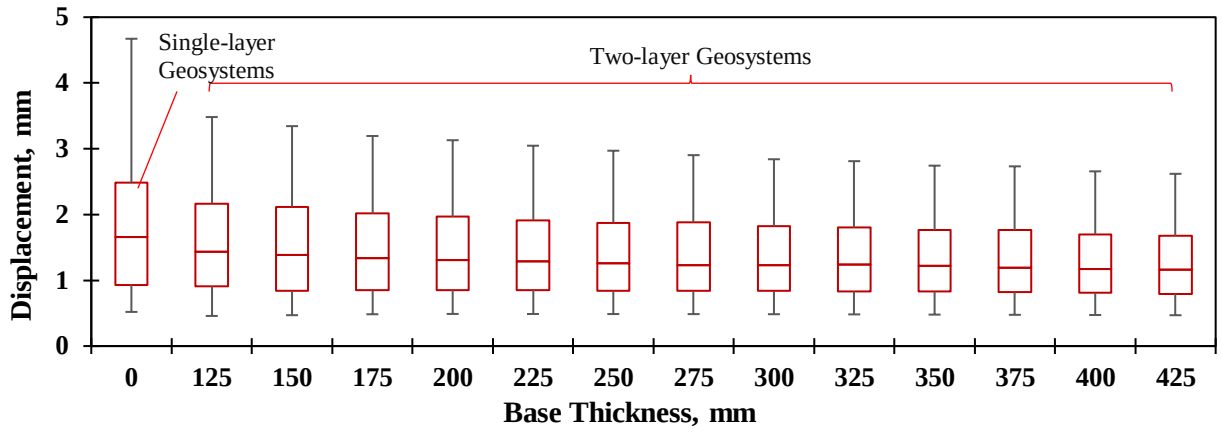

Figure D-60. Comparison of maximum displacement under a static stationary IC roller for different base thicknesses.

Table D-34. Descriptive statistics of maximum displacement for different base thicknesses.

Displacement (mm)	Base Thickness (mm)													
	0	125	150	175	200	225	250	275	300	325	350	375	400	425
Mean	1.99	1.65	1.59	1.54	1.51	1.49	1.46	1.43	1.40	1.39	1.37	1.36	1.32	1.31
Median	1.66	1.44	1.39	1.34	1.31	1.29	1.26	1.23	1.23	1.24	1.22	1.19	1.17	1.16
Standard Deviation	1.34	0.91	0.88	0.83	0.81	0.78	0.76	0.74	0.72	0.71	0.69	0.69	0.67	0.65

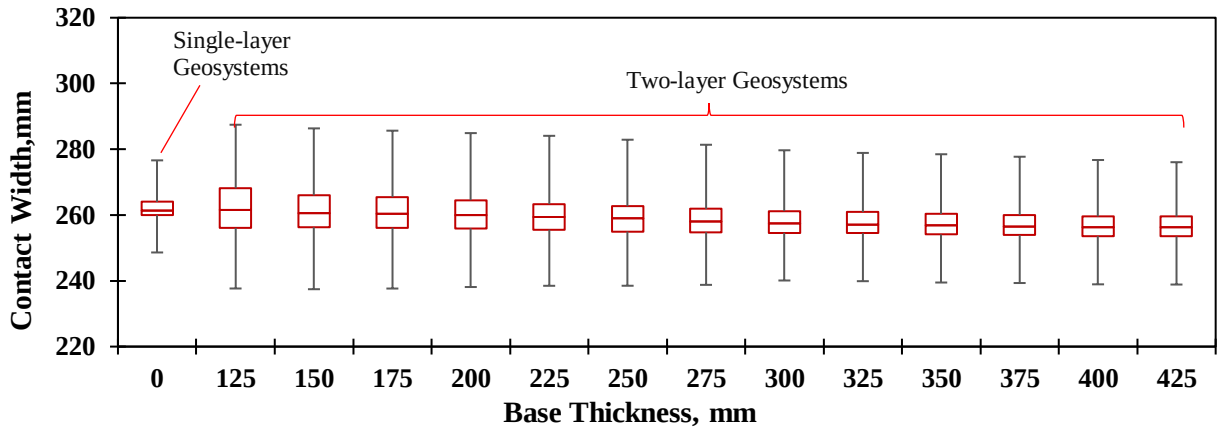

Figure D-61. Comparison of drum contact width for different base thicknesses.

Table D-35. Descriptive statistics of drum contact width for different base thicknesses.

Contact Width (mm)	Base Thickness (mm)													
	0	125	150	175	200	225	250	275	300	325	350	375	400	425
Mean	263	263	262	262	262	261	261	260	260	259	259	259	258	257
Median	261	262	261	260	260	259	259	258	258	257	257	256	256	256
Standard Deviation	4.67	8.30	8.15	8.00	7.80	7.60	7.40	7.10	6.60	6.50	6.50	6.40	6.30	6.20

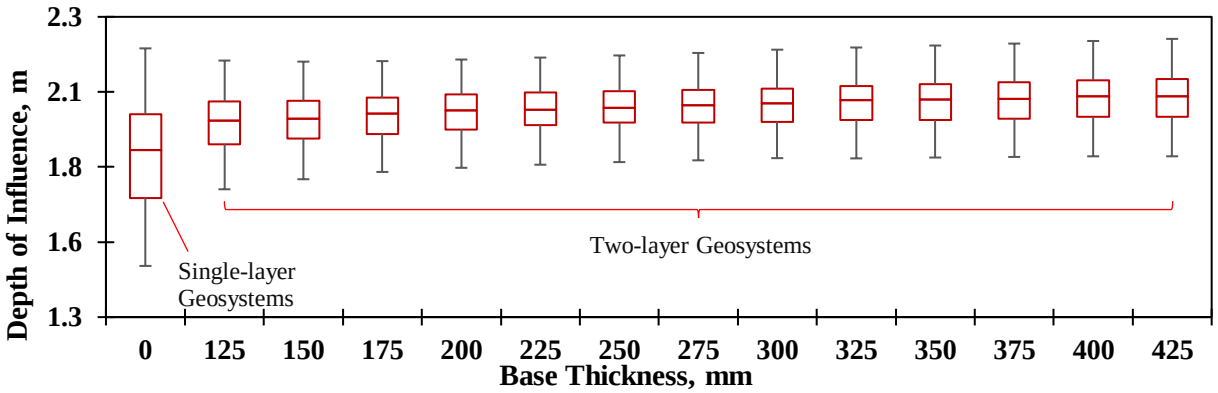

Figure D-62. Comparison of depth of influence with respect to displacement criterion for different base thicknesses.

Table D-36. Descriptive statistics of depth of influence with respect to displacement criterion for different base thicknesses.

Depth of Influence (m)	Base Thickness (mm)													
	0	125	150	175	200	225	250	275	300	325	350	375	400	425
Mean	1.83	1.94	1.96	1.97	1.98	1.99	1.99	2.00	2.01	2.01	2.02	2.02	2.03	2.03
Median	1.86	1.95	1.96	1.98	1.99	1.99	2.00	2.01	2.01	2.02	2.03	2.03	2.04	2.04
Standard Deviation	0.18	0.11	0.10	0.09	0.09	0.09	0.09	0.09	0.09	0.09	0.09	0.09	0.10	0.10

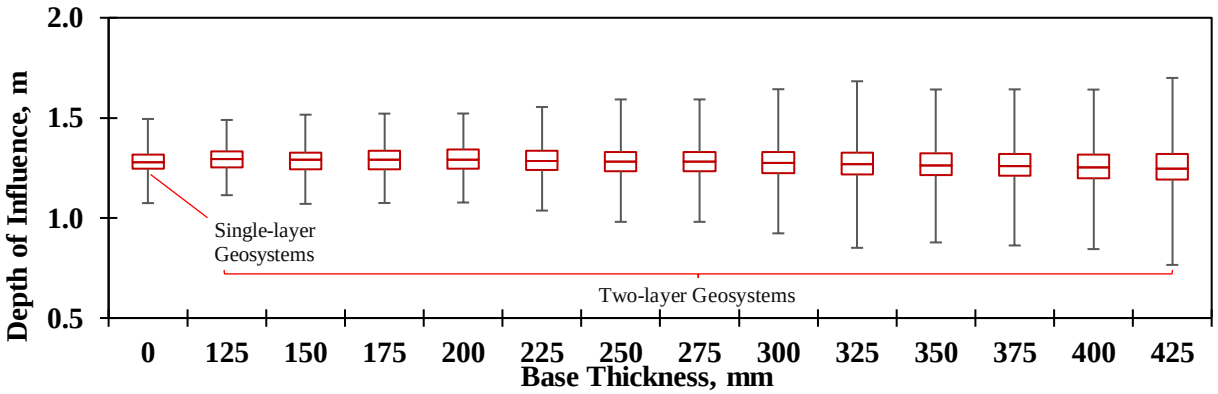

Figure D-63. Comparison of depth of influence with respect to stress criterion for different base thicknesses.

Table D-37. Descriptive statistics of depth of influence with respect to stress criterion for different base thicknesses.

Depth of Influence (m)	Base Thickness (mm)													
	0	125	150	175	200	225	250	275	300	325	350	375	400	425
Mean	1.28	1.30	1.29	1.30	1.30	1.30	1.29	1.29	1.28	1.27	1.26	1.25	1.24	1.23
Median	1.28	1.29	1.29	1.29	1.29	1.28	1.28	1.28	1.27	1.27	1.26	1.26	1.25	1.25
Standard Deviation	0.07	0.06	0.07	0.07	0.07	0.09	0.10	0.10	0.12	0.14	0.13	0.13	0.13	0.16

References

Adam, D., and Kopf, F. (2004). "Operational Devices for Compaction Optimization and Quality Control (Continuous Compaction Control & Light Falling Weight Device)." *International Seminar on Geotechnic Pavement and Railway Design and Construction*, Millpress, Rotterdam, The Netherlands, Athens, Greece, 97–106.

Anderegg, R., and Kaufmann, K. (2004). "Intelligent Compaction with Vibratory Rollers: Feedback Control Systems in Automatic Compaction and Compaction Control." *Transportation Research Record: Journal of the Transportation Research Board*, Transportation Research Board of the National Academies, 1868, 124–134.

Chiroux, R. C., Foster, W. A., Johnson, C. E., Shoop, S. A., and Raper, R. L. (2005). "Three-Dimensional Finite Element Analysis of Soil Interaction with a Rigid Wheel." *Applied Mathematics and Computation*, 162(2), 707–722.

Das, B. M. (2015). "Principles of Foundation Engineering." CL Engineering; 8 edition, Boston, MA, USA.

Hertz, H. R. (1882). "Ueber die Berührung fester elastischer Körper (On the Contact between Elastic Bodies)." *Journal für die reine und angewandte Mathematik*, 1882(92), pp. 156–171.

Hügel, H. M., Henke, S., and Kinzler, S. (2008). "High-Performance ABAQUS Simulations in Soil Mechanics." *2008 ABAQUS Users' Conference*, Newport, RI, 1–15.

Khazanovich, L., Celauro, C., Chadbourn, B., Zollars, J., and Dai, S. (2006). "Evaluation of Subgrade Resilient Modulus Predictive Model for Use in Mechanistic-Empirical Pavement Design Guide." *Transportation Research Record: Journal of the Transportation Research Board*, National Research Council, Washington, D.C., 1947, 155–166.

Kim, K. (2010). "Numerical Simulation of Impact Rollers for Estimating the Influence Depth of Soil Compaction." Texas A&M University.

Koza, J.R., Keane, M.A., Streeter, M.J. (2003). "Evolving inventions." *Scientific American*, 288(2), 52–59.

LSTC. (2016). *LS-DYNA Theory Manual*. Livermore Software Technology Corporation, Livermore, CA.

McDonald, J. H. (2014). "Handbook of Biological Statistics." Third Edition, Sparky House Publishing, Baltimore, Maryland, 209–212.

Mooney, M. A., and Facas, N. W. (2013). *Extraction of Layer Properties from Intelligent Compaction Data*. *Final Report for NCHRP Highway IDEA Project 145*, Transportation Research Board of the National Academies, Washington, DC.

Mooney, M. A., Rinehart, R. V., and van Susante, P. J. (2006). "The Influence of Heterogeneity on Vibratory Roller Compactor Response." *GeoCongress 2006: Geotechnical Engineering in the Information Technology Age*, D. J. DeGroot, J. T. DeJong, D. Frost, and L. G. Baise, eds., American Society of Civil Engineers, Atlanta, GA, 1–6.

Nazarian, S., Mazari, M., Abdallah, I., Puppala, A. J., Mohammad, L. N., and Abu-Farsakh, M. Y. (2014). *Modulus-Based Construction Specification for Compaction of Earthwork and Unbound Aggregate, National Cooperative Highway Research Program, NCHRP Project 10-84, Draft Final Report*. Washington, D.C.

Oh, J. H. (2011). *Comparison of Resilient Modulus Values Used in Pavement Design*. *Final Report BDL76-1*, College Station, TX.

Ooi, P. S. K., Archilla, R., and Sandefur, K. G. (2004). "Resilient modulus models for compacted cohesive soils." *Transportation Research Record: Journal of the Transportation Research Board*, (1874), 115–124.

Ooi, P. S., Sanderfur, K. G., and Archilla, A. R. (2006). *Correlation of Resilient Modulus of Fine-Grained Soils with Common Soil Parameters for Use in Design of Flexible Pavement*. Report No. HWY-L-2000-06. Hawaii Department of Transportation, Honolulu, Hawaii.

Patrick, J., and Werkmeister, S. (2010). *Compaction of Thick Granular Layers, NZ Transport Agency Research Report No. 411*. NZ Transport Agency Research Report 411, New Zealand Transport Agency, Wellington, NZ.

Simpson, B., O'Riordan, N. J., and Croft, D. D. (1979). "A computer model for the analysis of ground movements in London Clay." *Géotechnique*, Thomas Telford, 29(2), 149–175.

Tirado, C., Mazari, M., Carrasco, C., and Nazarian, S. (2015). "Simulating Response of Different Light Weight Deflectometer Testing Using Finite Element Modeling." *Transportation Research Board 94th Annual Meeting* (No. 15-2228).

Van Susante, P. J., and Mooney, M. A. (2008). "Capturing Nonlinear Vibratory Roller Compactor Behavior through Lumped Parameter Modeling." *Journal of Engineering Mechanics*, 134(8), 684–693.

Vennapusa, P. K. R. (2008). "Investigation of Roller-Integrated Compaction Monitoring and In-Situ Testing Technologies for Characterization of Pavement Foundation Layers." Doctoral Dissertation. Iowa State University, Ames, Iowa.

Wang, L., Zhang, B., Wang, D., and Yue, Z. (2007). "Fundamental Mechanics of Asphalt Compaction Through FEM and DEM Modeling." *Analysis of Asphalt Pavement Materials and Systems Analysis: Engineering Methods, GSP 176*, L. Wang and E. Masad, eds., American Society of Civil Engineers, Boulder, CO, 45–63.

Xia, K., and Pan, T. (2010). "Understanding Vibratory Asphalt Compaction by Numerical Simulation." *International Journal of Pavement Research and Technology*, 4(3), 185–194.

Yoo, T.-S., and Selig, E. T. (1979). "Dynamics of Vibratory-Roller Compaction." *Journal of the Geotechnical Engineering Division*, ASCE, 105(10), pp. 1211–1231.

APPENDIX E

Extracting Mechanical Properties from IC Data

Introduction

In this appendix, the efforts to develop an inverse algorithm to extract modulus of one- and two-layer geosystems are presented. Different levels of complexity in the methodology such as considering the nonlinearity of geomaterials as well as the moving and vibratory roller loads were incorporated in a more refined algorithm. The measurement errors and other sources of uncertainty associated with the modulus estimation were also considered as they can affect the backcalculation algorithm output.

Mechanistic pavement design algorithms can be based on one of many layer theory or finite element programs. The materials can be modeled as linear or nonlinear and elastic or viscoelastic. The applied load can be considered as dynamic or static. No matter how sophisticated or simple the process is made, the material properties should be measured in a manner that is compatible with the algorithm used. If a balance between the material properties and analytical algorithm is not achieved, the results may be unreliable. Ke et al. (2001) and Meshkani et al. (2002), amongst others, extensively discuss the implication of selecting different structural models. Different structural models require different input parameters that may yield different moduli under the same loading scenarios. For the linear elastic model, a representative modulus has to be calculated through a relationship similar to Equation D.4.

An inverse methodology has been developed to estimate the representative modulus of the base, M_2, based on the deflection values for the subgrade, d_1, and the base layer, d_2. The results from this exercise are included in the following sections.

Selecting Backcalculation Process

The backcalculation (a.k.a., system identification or inversion) is an optimization process performed to map inversely a known relation established by discrete or continuous data points. The most common backcalculation process in pavement engineering is related to the interpretation of the results from the Falling Weight Deflectometer (FWD). In FWD backcalculation, the measured deflections are "matched" with the calculated deflections from a numerical algorithm. Usually, the matching process between the measured and calculated responses is performed by an iterative process, in which the responses are calculated using different set of assumed mechanical properties.

A forward model and an inverse algorithm are utilized in the backcalculation process. In the forward modeling process, the responses are computed based on the loading and pavement structure. Different optimization processes such as nonlinear least squares, database search algorithms (DSA), and genetic algorithms (GA) can be used in the inverse process. The latter is an artificial intelligence (AI)-based model-free optimization technique, which mimics the theory of evolution. In the inverse process, the calculated responses are compared with the measured responses so that the new mechanical properties are determined by a parameter identification routine. The error minimization (optimization) is achieved based on an iterative process until the differences between the calculated and measured deflections stay under a certain error criterion.

Göktepe et al. (2006) provided a thorough comparison of the different backcalculation techniques in terms of modeling precision, computational expense, calculation details, and data requirements. Their overview of the different backcalculation methods is illustrated in Figure E-1. The implementation of more advanced processes has become possible due to the tremendous advances in computational power that significantly minimizes the computation time of the backcalculation processes.

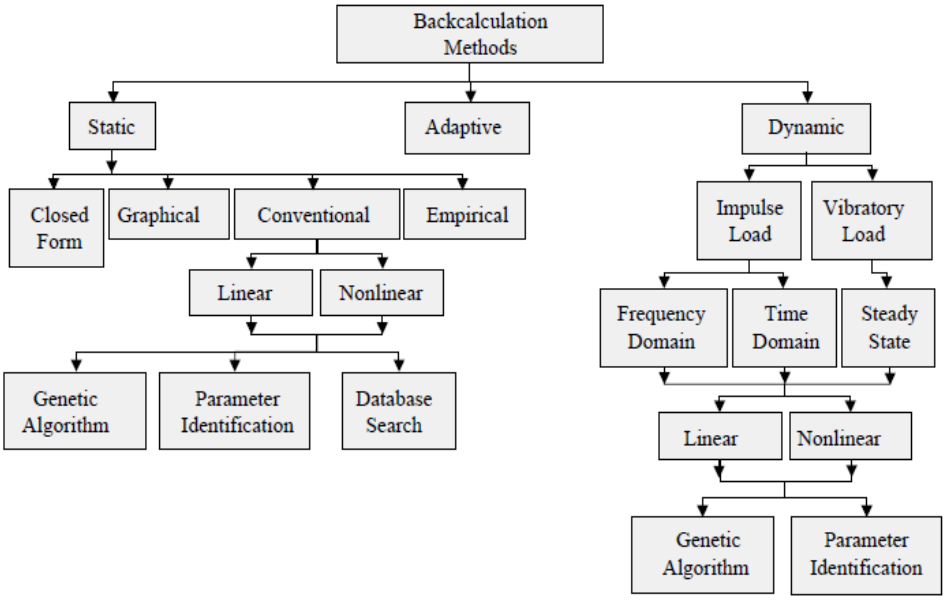

Figure E-1. Overview of backcalculation methods (Göktepe et al. 2006).

In the context of this study, the backcalculation methods can be categorized generally into static, dynamic and adaptive (Göktepe et al., 2006). Static and dynamic methods, which are classified by their loading types, utilize the conventional pavement response models. Adaptive methods, such as the neural networks and neuro-fuzzy systems, do not directly use a response model; instead, they simulate the inverse mapping by learning the target behavior via known input-output data patterns.

Traditional Backcalculation Methods. In the static approaches, the forward response is calculated using either layered elastic theory or finite element method for linear or nonlinear elastic material behaviors. In the backcalculation process, only the peak loads are utilized due to the linear elastic material assumption.

In the dynamic approaches, the loading is considered as either impulsive or vibratory. The relevant responses are obtained in the time domain for the impulse loads, and in the frequency domain for the steady state vibratory loads. The elasto-dynamic analysis, such as Green's function solution, and dynamic FEMs are usually performed to calculate the responses (Roesset and Shao, 1985; Kang, 1998; Stubbs et al, 1994; Maina et al, 2000; Ulliditz, 2000). Fourier analyses are usually conducted for the transformation of the domains.

Database Search Algorithms. The database search algorithms make use of the pattern searching algorithms through optimization routines. This approach utilizes a predetermined database instead of calculating deflections by means of response systems in each step of the optimization (Lytton, 1989; Uzan, 1994). Thus, deflections are computed from regression equations formulated to determine the layer moduli or interpolation techniques by making use of the database, thus avoiding the use of a forward calculation scheme in the iterative process (Uzan et al. 1989).

Genetic Algorithm (GA). GA is a robust and randomized search algorithm that can be employed to optimize the search domain for the backcalculation in the pavement engineering. The merits of this method

are the capability to overcome partially the issue of having many local optima (nonuniqueness) in the backcalculation procedure and the elimination of the dependency of the solution on the input seed values.

Adaptive Backcalculation Methods. In the adaptive backcalculation, supervised learning algorithms are used to combine the forward and inverse processes of traditional backcalculation approaches into one-step. An adaptive system is taught by known input-output patterns by simulating the nonlinear mapping between the input and output spaces. Meier and Rix (1994) first implemented them by applying the artificial neural networks (ANN) for the SASW test data inversion and backcalculation of flexible pavement layer properties. Similar to ANN, the adaptive neuro-fuzzy inference (ANFIS) has also been used for backcalculation of pavement moduli with previously determined input-output data patterns (Göktepe et al., 2005), though their large computational expense does not make it optimal for large training data. Soft computing techniques (in general) and artificial neural networks (ANN, in particular) have been proven as effective tools in solving complex nonlinear inverse problems in engineering.

Backcalculation of Modulus for Static Stationary Linear Model

The initial step in solving the inverse problem is to test different simulations of the forward problem for the single-layer as well as two-layer geosystems for different combinations of parameters describing the mechanical properties of the layers. The expectation is that some of these simplified models will be accurate enough to describe the behavior of the pavement reasonably well. Due to the nonlinearity of the actual pavement unbound layers, the modulus has different values at different depths. To gauge the quality of the pavement, it is therefore desirable to use a representative modulus that reflects the stiffness of the layer as a whole. In this study, the modulus at half-depth of the base is considered as this representative property.

For the single-layer geosystem (subgrade), the layer stiffness can be extracted directly from the "pre-mapping," where the stiffness of the layer at each spatial location can be determined by dividing the known force of the roller by the corresponding deflection at any particular location. In contrast to a single-layer geosystem, the stiffness of the base in a two-layer geosystem cannot be directly determined from the roller measurements. For each spatial location, the base stiffness has to be evaluated from the deflections measured before placing the base (pre-mapping), d_1, and measured after the compaction of base (mapping), d_2.

The linear elastic model is rather simple since the modulus at a given time is considered as a constant value independent of the state of stress applied to the geosystem. The advantage of the linear elastic models is that they can rapidly yield results. Their main limitation is that the results are rather approximate if the loads are large enough for the material to exhibit a nonlinear behavior. The Mechanistic Empirical Pavement Design Guide (MEPDG) requires the measurement or estimation of the representative resilient modulus of each unbound layer as input for the calculation of the pavement response. Equation D.4 represents the most common form of the material model in ME pavement design methods. This model is employed to calculate the representative modulus for the static stationary linear single-layer geosystem. The input parameters for the static stationary linear elastic response algorithm include:

- Thickness of the base,
- Maximum displacement of the geosystem before placing the base, and
- Maximum displacement of the base after it is compacted.

The output of this response algorithm includes the representative modulus of the base.

Solving Inverse Problem for Static Linear Case

Single Layer System: The soil response determined under a static load (exerted by a stationary drum) was evaluated on a set of 200 single layer cases. It is assumed that the modulus M has the same value for all spatial locations and for all depths. Suppose that u_i is a solution corresponding to this modulus M. One can show that for a different modulus value M', the following formula holds:

$$u_i' = \frac{M}{M'} u_i \tag{E.1}$$

General relationship between strain and displacement is given by:

$$\varepsilon_{ij} = \frac{1}{2} (u_{i,j} + u_{j,i}) \tag{E.2}$$

where ε_{ij} is the strain and $u_{i,j}$ and $u_{j,i}$ are denoted as derivatives of displacements with respect to the spatial Cartesian axes, respectively. An immediate result of Equations E.1 and E.2 is:

$$\varepsilon_{ij}' = \frac{M}{M'} \varepsilon_{ij} \tag{E.3a}$$

$$M' \varepsilon_{ij}' = M \varepsilon_{ij} \tag{E.3b}$$

where ε'_{ij} is the corresponding strain to the given modulus M'. Strains and stresses can be related through the following equation:

$$M \cdot \varepsilon_{ij} = (1 + \nu) \cdot \sigma_{ij} - \nu \cdot \delta_{ij} \cdot \sigma_{kk} \tag{E.4}$$

where ν is the Poisson's ratio and δ_{ij} is the Kronecker delta function. In the single-layer case, the product of the displacement and the modulus should be the same for all layer moduli. For different values of M_1, the product of the deflection and the modulus remains roughly the same.

$$M_1 = \frac{c}{d_1} \tag{E.5}$$

The constant c, which is represented by the product $d_1 \cdot M_1$, ranges from 204 to 212 in our database. The less than 4% variation in c is due to the finite-element numerical approximations in solving the elasticity equations. An average value of $c \approx 209$ N/m is reasonable.

Two Layer System: In the two-layer case, the product $d_2 \cdot M_2$ is no longer a constant and it is therefore assumed to be dependent on the deflections corresponding to the single layer and the two layer geosystem (d_1 and d_2), i.e.:

$$d_2 \cdot M_2 = f(d_1, d_2) \tag{E.6}$$

The representative moduli of the two-layer geosystems, M_1 and M_2, multiplied by a constant n is equivalent to the deflection of the two-layer system, d_2, divided by the same constant:

$$M_1' = nM_1 \tag{E.7a}$$

$$M_2' = nM_2 \tag{E.7b}$$

$$d_2' = \frac{1}{n} d_2 \tag{E.7c}$$

The product $d_2 \cdot M_2$ maintains the same value (i.e., $d'_2 \cdot M'_2 = d_2 \cdot M_2$). Thus, we can conclude that for all deflection values of the two-layer geosystem d_1, d_2, and the constant n, the following equation holds.

$$f(d_1, d_2) = (d_1', d_2') = f\left(\frac{d_1}{n}, \frac{d_2}{n}\right) \tag{E.8}$$

In particular, for the case of $n = d_2$, we conclude that

$$f(d_1, d_2) = f\left(\frac{d_1}{d_2}, 1\right) \tag{E.9}$$

when $M_1 = M_2$, the system reduces to a single-layer geosystem. In this case $d_1 = d_2$, and $d_2 \cdot M_2 = c$, hence $f(d_1, d_1) = c$. Hence, Equation E.9 can be rewritten as:

$$d_2 M_2 = f(d_1, d_2) = g(r), \tag{E.10}$$

where r is denoted as $r = \frac{d_1}{d_2}$ and $g(r) = f(r,1)$. An immediate advantage of this equivalent form is that for $d_1 = d_2$, or $r = 1$, the product $d_2 \cdot M_2 = c$ and thus, $g(1) = E$.

To get a general idea of how the product $d_2.M_2$ depends on r, three cases with $d_2 \cdot M_2$ of approximately 400, 800, and 1600 with corresponding $r \approx 1.3$, $r \approx 1.7$, and $r \approx 2.1$ are selected. An increase in the product

$d_2 \cdot M_2$ by double the amount, increments r by a constant that is a characteristic property of the logarithm function.

Since the logarithm of a product is equal to the sum of the logarithms, doubling the input value to the logarithm is equivalent to an increase in the result by a constant value of ln(2). A similar property holds for any linear function of the logarithm of the form:

$$F(x) = c_1 + c_2 \ln(x) \tag{E.11a}$$

$$F(2x) = c_1 + c_2\, ln(2x) = F(x) + c_2\, ln(2) \tag{E.11b}$$

$$F(2x) = F(x) + c_2\, ln(2) \tag{E.11c}$$

Therefore, doubling x results in an increase of the value of $F(x)$ by an additive constant $C_2 \ln(2)$. It is therefore conjectured that r is a linear function of the logarithm $\ln(d_2 \cdot M_2)$, or, equivalently, that the logarithm $\ln(d_2 \cdot M_2)$ should linearly depend on r for some values a and b.

$$ln(d_2 \cdot M_2) = a + b \cdot r = a + b\frac{d_1}{d_2} \tag{E.12}$$

Since for $d_1 = d_2$ Equation E.12 indicates that $\ln(c) = a + b$, it can be stated that $b = \ln(c) - a$, and as a result:

$$ln(d_2 \cdot M_2) = a + (ln(c) - a)\frac{d_1}{d_2}. \tag{E.13}$$

Figure E-2 demonstrates the verification of the relationship between the natural logarithm of the product $d_2 \cdot M_2$ and the ratio $r = d_1/d_2$ for two-layer geosystems subjected to a static stationary drum for three base thicknesses of 6 in., 12 in., and 18 in.

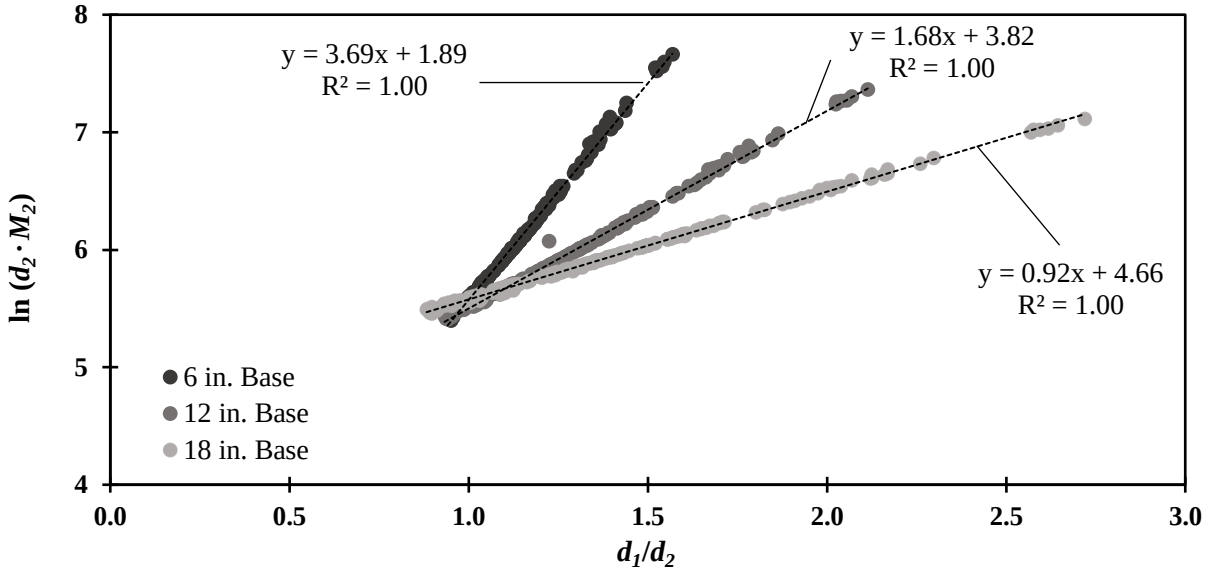

Figure E-2. Relationship for predicting representative modulus (M_2) of base layer using deflections of two-layer system (d_2) and single layer system (d_1) as obtained from Static Stationary Linear (SSL) finite element responses.

The modulus M_2 of the base can be calculated through the following equation based on the predetermined parameters d_1, d_2, and thickness h.

$$M_2 = \frac{1}{d_2}\exp\left(a(h) + \left(\ln(c) - a(h)\right)\frac{d_1}{d_2}\right) \tag{E.14}$$

In this formula, $c \approx 209$, and the coefficient $a(h)$ depends on the thickness h of the base:

- For h = 6 in., $a(h) = 1.89$;

- For h = 12 in., $a(h)$ = 1.68;
- For h = 18 in., $a(h)$ = 0.92.

Backcalculation of Modulus for Static Stationary Nonlinear Model

It is desirable to find the representative modulus of the base in terms of the known parameters d_1 and d_2 (the deflections recorded on the subgrade and the base, respectively) and the nonlinear parameters k'_2 and k'_3 corresponding to the base layer. These values are denoted by k'^{b}_2 and k'^{b}_3 and the corresponding k-values for the subgrade layer that are denoted by k'^{s}_2 and k'^{s}_3. Two different approaches have been deployed as discussed next.

Linear Regression Approach (LRA)

Single Layer System: According to the results for the static stationary linear case, the modulus M_1 is related to the corresponding deflection d_1 through the following equation:

$$\ln(d_1 \cdot M_1) = Const. \tag{E.15}$$

Substituting the modulus M_1 from the Equation D.7 into the Equation E.18 leads to the following equation:

$$\ln\left(d_1 \cdot k'_1 \cdot \left(\frac{\theta}{p_0}+1\right)^{k'_2} \cdot \left(\frac{\tau_{oct}}{p_0}+1\right)^{k'_3}\right) = Const. \tag{E.16}$$

Taking into account that the logarithm of the product is equal to the sum of the logarithms, Equation E.16 can be organized as:

$$\ln(d_1 \cdot k'_1) = Const. - a_2 \cdot k'_2 - a_3 \cdot k'_3, \tag{E.17a}$$

where

$$a_2 \stackrel{\text{def}}{=} \ln\left(\frac{\theta}{p_0}+1\right) \tag{E.17b}$$

and

$$a_3 \stackrel{\text{def}}{=} \ln\left(\frac{\tau_{oct}}{p_0}+1\right) \tag{E.17c}$$

In the static linear case, the Equation E.17a denotes the expression $ln(d_1 \cdot k'_1)$ as a linear function of the parameters k'_2, k'_3.

In many cases, i.e. when the subgrade is sufficiently stiff, the linear model is a good approximation. It is therefore reasonable to look for models in which there is a little need for expansion to the linear terms. A natural class of such models are polynomial models, in which the expansion takes place by adding higher-order terms. General expansion of Equation E.17a to quadratic terms is as follows:

$$ln(d_1 \cdot k'_1) = c_0 + c_2 \cdot k'_2 + c_3 \cdot k'_3 + c_{22}(k'_2)^2 + c_{23} \cdot k'_2 \cdot k'_3 + c_{33}(k'_3)^2 \tag{E.18}$$

For the case of single-layer under static stationary nonlinear (SSN) model included in our database, Equation E.18 has the following form:

$$ln(d_1 \cdot k'_1) = 7.611 - 0.855 \cdot k'_2 - 0.316 \cdot k'_3 + 0.083(k'_2)^2 + 0.083 \cdot k'_2 \cdot k'_3 + 0.018(k'_3)^2 \tag{E.19}$$

This approximation is carried out with R^2 of 0.99 and the mean squared error of 0.02%.

Two Layer System: In this case, k-values of both subgrade and base contribute to the overall regression analysis results. Taking into account d_1/d_2 and all possible variables in terms of k'_2 and k'_3 of the base and the subgrade leads to the following general formula:

$$\ln(d_2 \cdot M) = c_0 + c_2^b \cdot k_2^b + c_3^b \cdot k_3^b + c_2^s \cdot k_2^s + c_3^s \cdot k_3^s + c_{22}^b \cdot (k_2^b)^2 + c_{23}^b \cdot k_2^b \cdot k_3^b + c_{33}^b \cdot (k_3^b)^2 + c_{22}^s \cdot (k_2^s)^2 + c_{23}^s \cdot k_2^s \cdot k_3^s + c_{33}^s \cdot (k_3^s)^2 + c_{22}^{bs} \cdot k_2^b \cdot k_2^s + \tag{E.20}$$

$$c_{23}^{bs} \cdot k_2^b \cdot k_3^s + c_{32}^{bs} \cdot k_3^b \cdot k_2^s + c_{33}^{bs} \cdot k_3^b \cdot k_3^s + c_1^d \cdot \frac{d_1}{d_2}$$

where c_i values are regression coefficients that provide the best fit for the observed values $(d_2.M_2)$.

Equation E.20 has the following form for 150 mm (6 in.) base thickness:

$$\begin{aligned}\ln(d_2 \cdot M_2) = {} & 2.098 + 0.361 \cdot k_2^b + 0.336 \cdot k_3^b + 0.467 \cdot k_2^s + 0.093 \cdot k_2^b \cdot k_3^b + \\ & 0.053 \cdot (k_3^b)^2 - 0.305 \cdot (k_2^s)^2 - 0.264 \cdot k_2^s \cdot k_3^s - 0.079 \cdot (k_3^s)^2 + \\ & 0.242 \cdot k_2^b \cdot k_2^s + 0.091 \cdot k_2^b \cdot k_3^s + 0.053 \cdot k_3^b \cdot k_2^s + \\ & 3.509 \cdot \frac{d_1}{d_2} - 0.955 \cdot (\frac{d_1}{d_2} - 1)^2\end{aligned} \quad \text{(E. 21)}$$

The regression analysis resulted in R^2 of 0.95 and the mean squared error of 16%.

A similar analysis was implemented for 300 mm (12 in.) base thickness and the results are as follows

$$\begin{aligned}\ln(d_2 \cdot M) = {} & 3.870 + 0.380 \cdot k_2^b + 0.348 \cdot k_3^b + 0.408 \cdot k_2^s + 0.196 \cdot k_3^s + c_{22}^b \cdot (k_2^b)^2 + \\ & 0.078 \cdot k_2^b \cdot k_3^b + 0.037 \cdot (k_3^b)^2 + 0.177 \cdot (k_2^s)^2 - 0.160 \cdot k_2^s \cdot k_3^s - \\ & 0.029 \cdot (k_3^s)^2 + 0.138 \cdot k_2^b \cdot k_2^s + 0.065 \cdot k_2^b \cdot k_3^s + 0.069 \cdot k_3^b \cdot k_2^s + \\ & 0.041 \cdot k_3^b \cdot k_3^s + 1.656 \cdot \frac{d_1}{d_2} - 0.294 \cdot (\frac{d_1}{d_2} - 1)^2\end{aligned} \quad \text{(E. 22)}$$

This analysis provided a higher R^2 of 0.96 and the mean standard error of 11%. For both cases of 150 mm (6 in.) and 300 mm (12 in.) base thickness, the only significant quadratic term turned out to be $(\frac{d_1}{d_2} - 1)^2$. All other terms from the Equation E.22 proved to be insignificant.

Soft Computing Techniques

A combination of genetic algorithm (GA) and artificial neural network (ANN) was employed to improve further the relationships between the modulus of the base layer for the two layer geosystems. As the first step, the data for the two-layer geosystems were expanded from 200 cases to over 4400. The expanded data for the two layer geosystems including 150 mm (6 in.) and 300 mm (12 in.) base thicknesses were then combined to allow for thickness *h* to be incorporated as an independent variable into the prediction process.

To reach the best predictive function for the modulus of the base layer, genetic programming (GP) was utilized. The cases for the two-layer geosystems were divided into three groups. In this respect, 70% of the database (i.e., 3100 cases) was used for training the prediction algorithm. This group formed the initial population for the evolutionary algorithm. The standard error of estimate (SEE) was used to evaluate the evolution of the program towards the best fit using the following equation:

$$SEE = \sqrt{\frac{\sum_{i=1}^{n}(Y_i' - Y_i)^2}{n}} \quad \text{(E.23)}$$

where Y'_i is the estimated modulus of the base obtained from the predictive function of the fitted trend and Y_i is the actual values for the modulus of the base from the FE simulation. Parameter *n* is the total number of points. The second group of randomly chosen population, which included 15% of the database (i.e., 660 cases), was used to evaluate the predictive accuracy of the fitted model. The remaining 15% of the database was deployed to test the validity of the predicted model.

To develop the predictive function, the nonlinear k' parameters of base $k_i'^s$ and subgrade $k_i'^b$, base thickness (h) and the surface displacements (d_1) and (d_2) recorded on top of subgrade and base layer respectively were taken into consideration as shown in the following equation.

$$Mr_b = f\left(k_i'^s, k_i'^b, h, , d_1, d_2\right) \quad \text{(E.24)}$$

where Mr_b is the modulus of the base. The best prediction of the modulus of the middle at the base layer (Mr_{b-SSN}) under the static stationary roller (SSN) with the operating features discussed in Table E-1 is provided by Equation E.25:

$$Mr_{b-SSN} = C_1 k_1'^b + \frac{(C_2 - h)k_1'^b k_2'^b + C_3 k_1'^b k_3'^b}{d_2(h + k_1'^b + k_1'^s - k_1'^b k_3'^b) + C_4 h k_1'^b} \quad \text{(E.25)}$$

where $C_1 = 0.108$, $C_2 = 2.97 * 10^3$, $C_3 = 1.42 * 10^3$, $C_4 = 0.0098$, $k_i'^s$ are the nonlinear parameters of subgrade, $k_i'^b$ are the nonlinear parameters of base and Mr_{b-SSN} is the predicted modulus at the middle of base layer. The modulus of the base was found to be less sensitive to $k_2'^s$ and $k_3'^s$ and also the surface displacement recorded on top of subgrade for the single-layer system (d_1). Hence, these parameters are eliminated from Equation E.25.

As shown in Figure E-3, the proposed equation provides a reasonable estimate of the responses generated by SSN FE model, with an R^2 value of 0.94 and standard error of estimate of 64 MPa for training and 68 MPa from the validation data. It is noteworthy that in Equation E.25 h is an independent variable.

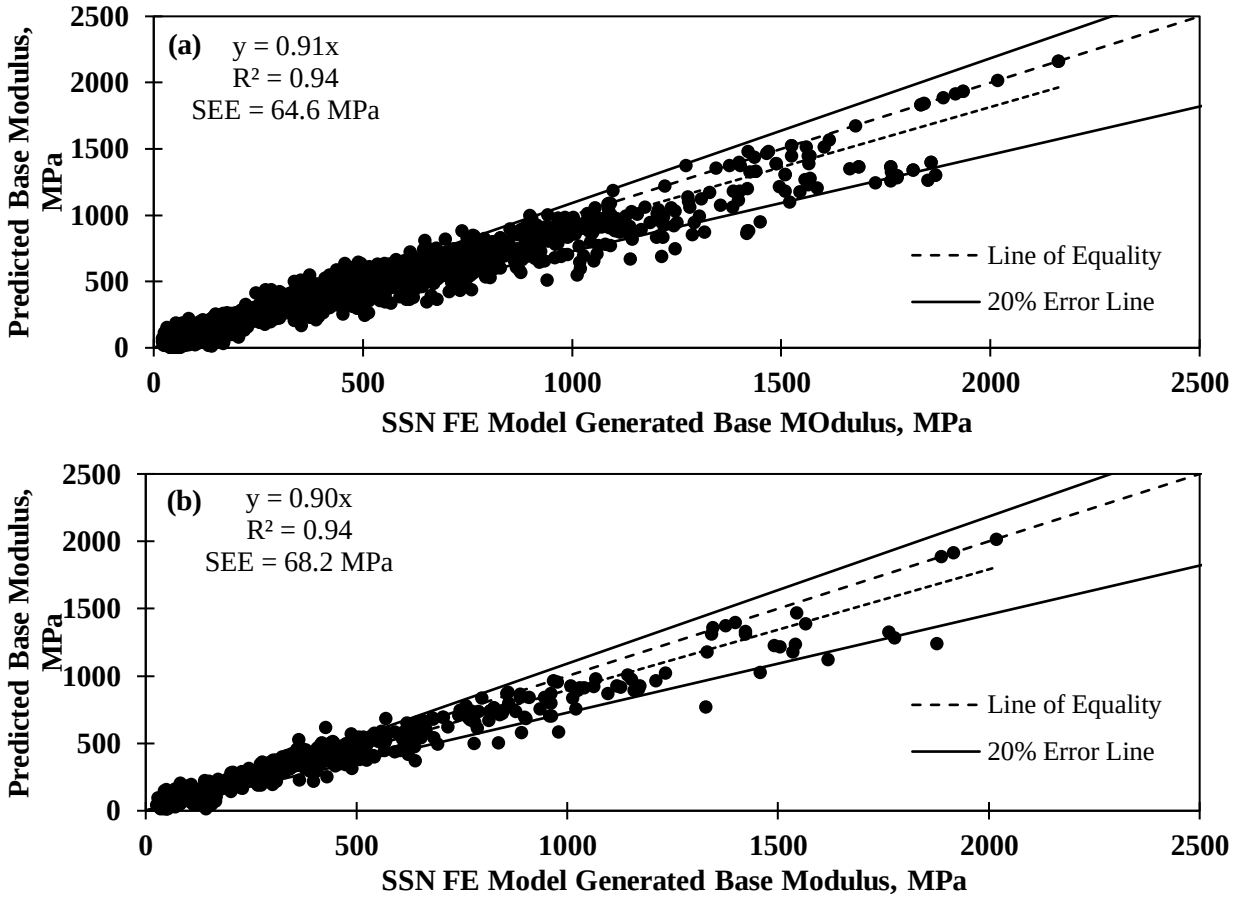

Figure E-3. Predicted and measured modulus values for training and validation data generated by genetic programming (GP): (a) GP-generated model performance for training data; (b) GP-generated model performance for validation data.

The GA results shown in Figure E-3 are further supported by the results obtained by an ANN algorithm. A multi-layer perceptron (MLP) feed-forward neural network model with Levenberg-Marquardt algorithm was deployed for that purpose. The ANN model used comprised of an input layer, including nine predictor independent variables i.e., the nonlinear k' parameters of base and subgrade, base thickness (h) and surface displacement (d_1) and (d_2) recorded on top of the subgrade and base layer respectively, and a hidden layer with ten neurons and an output layer which includes the proposed predicted values by the network. As for

the GA algorithm, the data were divided into three groups of 70% for training, 15% for evaluation and 15% for the validation of the proposed model.

As shown in Figure E-4, the ANN values also provide a reasonable estimate of the responses generated by SSN FE model, with R^2 values of 0.97 for both training and validation sets of data and standard error of estimate of 75 MPa for training and 56 MPa for the validation data.

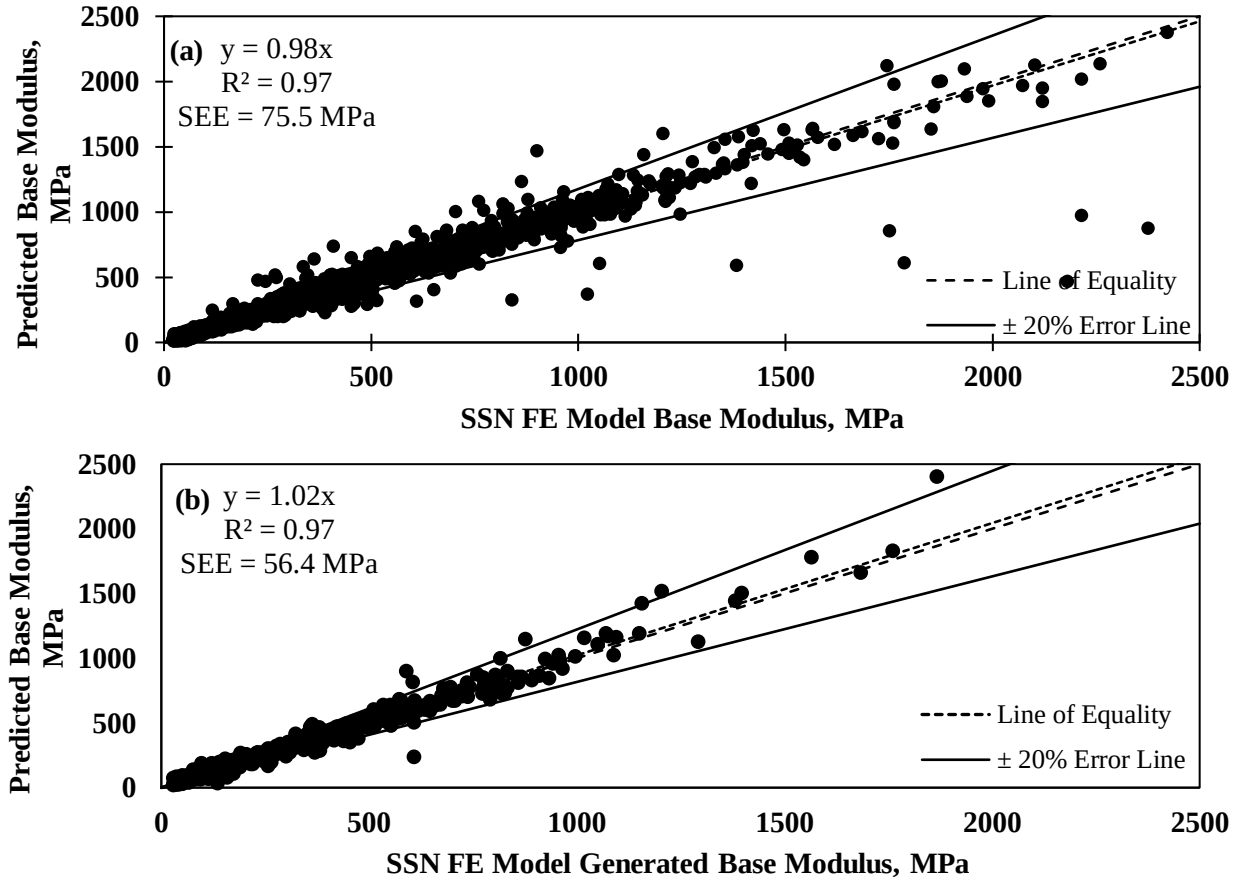

Figure E-4. Performance of (a) artificial neural network (ANN) model for training data and (b) ANN model for validation data.

Neural Network Optimization

Further validation of the ANN prediction models requires a thorough optimization of the network architecture. Towards this end, the database used for training the ANN prediction models for the two-layer geosystems were further expanded to include base thicknesses ranging between 150 mm (6 in.) and 300 mm (12 in.) at 25 mm (1 in.) increments. The expanded database for the two layer geosystems allows for base layer thickness h to be an independent variable in the prediction process. Data was categorized into two separate sets corresponding to the range of moduli for different types of base layer. The first set of data captured the modulus of the base layer $Mr_{b\text{-}SSN} < 1500$ MPa (~220 ksi corresponding to the stabilized and unbound base layer moduli) and the second set included the data for the modulus of the base layer $Mr_{b\text{-}SSN} < 500$ MPa (~70 ksi corresponding to unbound base layer).

Based on the available input parameters from IC field operation and laboratory test results, three backcalculation scenarios for the determination of the modulus of the base layer $Mr_{b\text{-}SSN}$ were proposed. These scenarios and their corresponding input parameters are listed in Table E-1.

The ANN backcalculation algorithms for each of the above-mentioned scenarios include an input layer, including five predictor independent variables i.e., thickness of the base layer (h), surface displacement (d_1), (d_2) obtained on top of the subgrade and base layer respectively, nonlinear k'_{2b}, k'_{3b} parameters, where b denotes the base layer and an output layer which includes the predicted values for the modulus of the base layer estimated by the network.

Table E-1. Feasible backcalculation scenarios based on available IC field/lab data.

Scenarios	Input Parameters	Target
1	h, k'_{2b}, k'_{3b}, d_2, d_1	Base Modulus
2	h, k'_{2b}, k'_{3b}, d_2, $M_{r\text{-}sub}$	Base Modulus
3	h, k'_{2b}, k'_{3b}, d_2, $M_{r\text{-}sub}$ *(Representative)*	Base Modulus
4	h, k'_{1b}, k'_{2b}, k'_{3b}, d_2, d_1	Base Modulus
5	h, k'_{1s}, k'_{2s}, k'_{3s}, k'_{1b}, k'_{2b}, k'_{3b}, d_2, d_1	Base Modulus

For the first scenario, nonlinear k'_{2b}, k'_{3b} parameters would be obtained from laboratory tests prior to or simultaneous to the compaction operation. Parameters d_1 and d_2, could be acquired during pre-mapping of the subgrade and mapping after the base layer is laid, respectively. Modulus of the subgrade for the single-layer system in the second scenario could be obtained through Equation E.5 for static stationary linear (SSL) and Equations E.19 and D.7 for the static stationary nonlinear (SSN) case. The representative resilient modulus of the subgrade in the third scenario could be directly calculated through Equation D.7 from the laboratory results.

Training Algorithm Optimization

As the first step to improve the performance and optimize the predictive power of the ANN models, two training algorithms, namely Levenberg-Marquardt (LM) and Bayesian Regularization (BR), were chosen. For a fixed network architecture, the training process for the LM method is often faster than BR. Moreover, even though the LM method requires more computational resources to execute, it provides less accurate predictions. The BR algorithm on the other hand, minimizes a linear combination of squared errors and weights and then determines the correct combination to produce a network that provides the most accurate generalization. The accuracy of BR algorithm is more pronounced for the scenarios with higher number of input parameters. In both algorithms, the time required for training and the number of training iterations (number of epochs) is determined by the change in mean squared error (MSE). Training process automatically stops improving as the mean squared error of the validation dataset increases.

The performance of the two training algorithms are compared in Figure E-5 using the data for all two-layered pavements with $Mr_{b\text{-}SSN}$ values less than 1500 MPa. The input parameters to the ANN training algorithms were chosen from the third scenario shown in Table E-1. Figures E-5(a) and E-5(b) show that the BR algorithm provides a slightly higher R^2 and lower standard error of estimate (SEE) than the LM algorithm. The difference in accuracy of the models proposed by these two algorithms becomes more pronounced when the number of input parameters is increased. Figure E-5(c) illustrates the cumulative distribution of the errors (SEEs) for the predicted moduli of the base layer employing the same set of input parameters from the third scenario and fixed network architecture. The cumulative distribution of SEE values for the network using BR algorithm provides a better error distribution.

Determination of Optimum Number of Neurons

The next step as part of the improvement of the performance and the predictive power of the ANN models consists of determining the optimum number of neurons in the fitting network's hidden layer. In that respect, the predictive performance of the ANN models was examined for a wide range of neurons varying

from 1 to 50. A larger number of neurons in the hidden layer allows the network to be more flexible as the network has more parameters for optimization. Mean squared error (MSE) and standard error of estimate (SEE) values were computed for each of the training, validation and test datasets for each case. After thorough analyses of the training algorithm performance on several different scenarios with different set of inputs and network architectures, Bayesian Regularization was employed as the network-training algorithm to determine the optimum number of neurons for each of the aforementioned scenarios.

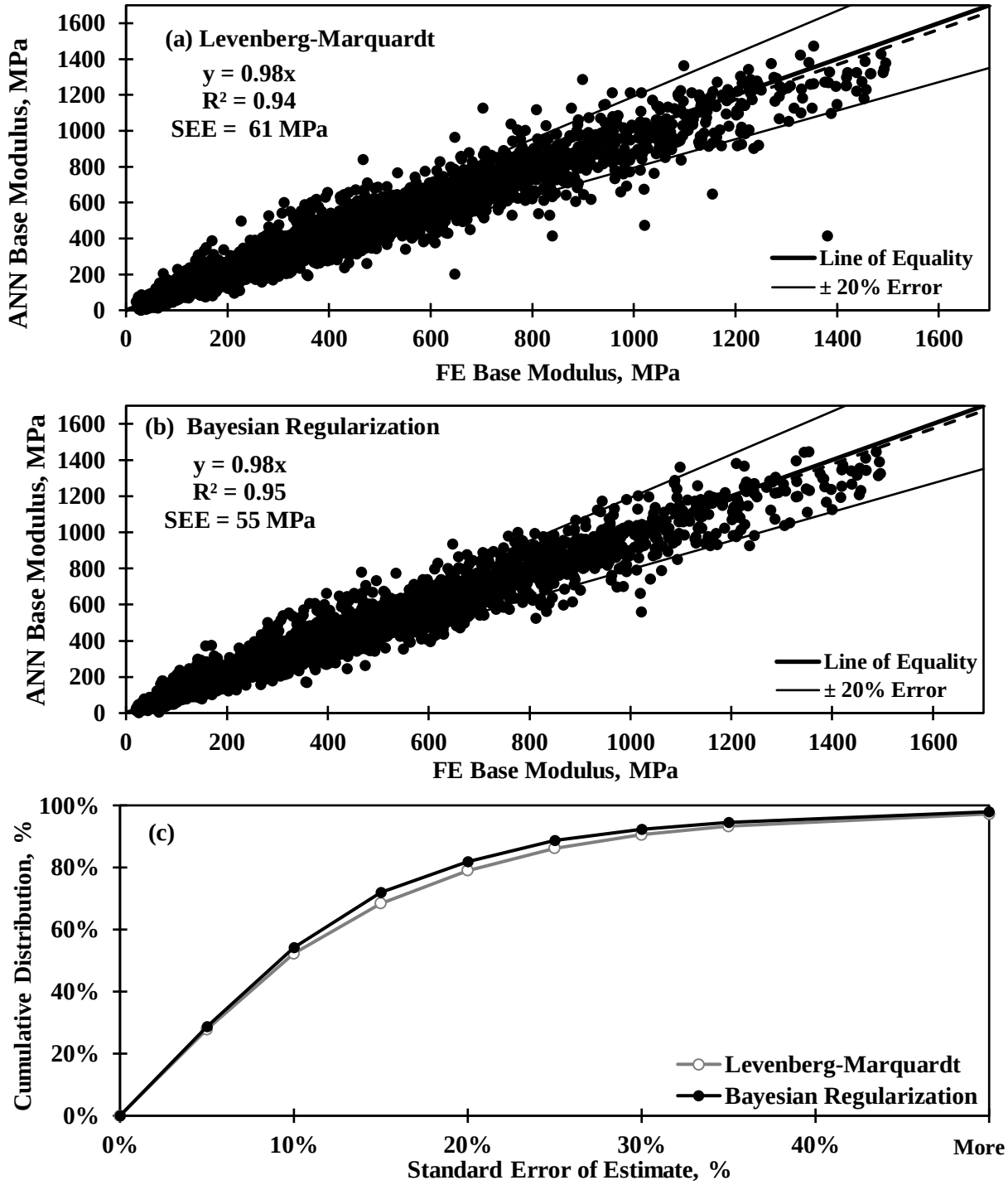

Figure E-5. Artificial neural network (ANN) performance comparison.

Figure E-6 illustrates the evolution of coefficient of determination (R^2) and standard error of estimate (SEE) with respect to the number of neurons in the hidden layer for base moduli less than 1500 MPa and less than 500 MPa. As shown in Figures E-5a and E-5b, the SEE values continue to decrease by increasing the number of neurons in the hidden layer for both datasets however the SEEs demonstrate a nearly asymptotic behavior after about twenty neurons for both datasets. Further consideration of the SEE and R^2 values for these datasets recognized twenty neurons as the optimum number for the scenarios mentioned in Table E-1. Larger number of neurons should be avoided to prevent overfitting which would influence the generalization power of the network adversely. The summary of the optimized neural network properties is included in Table E-2.

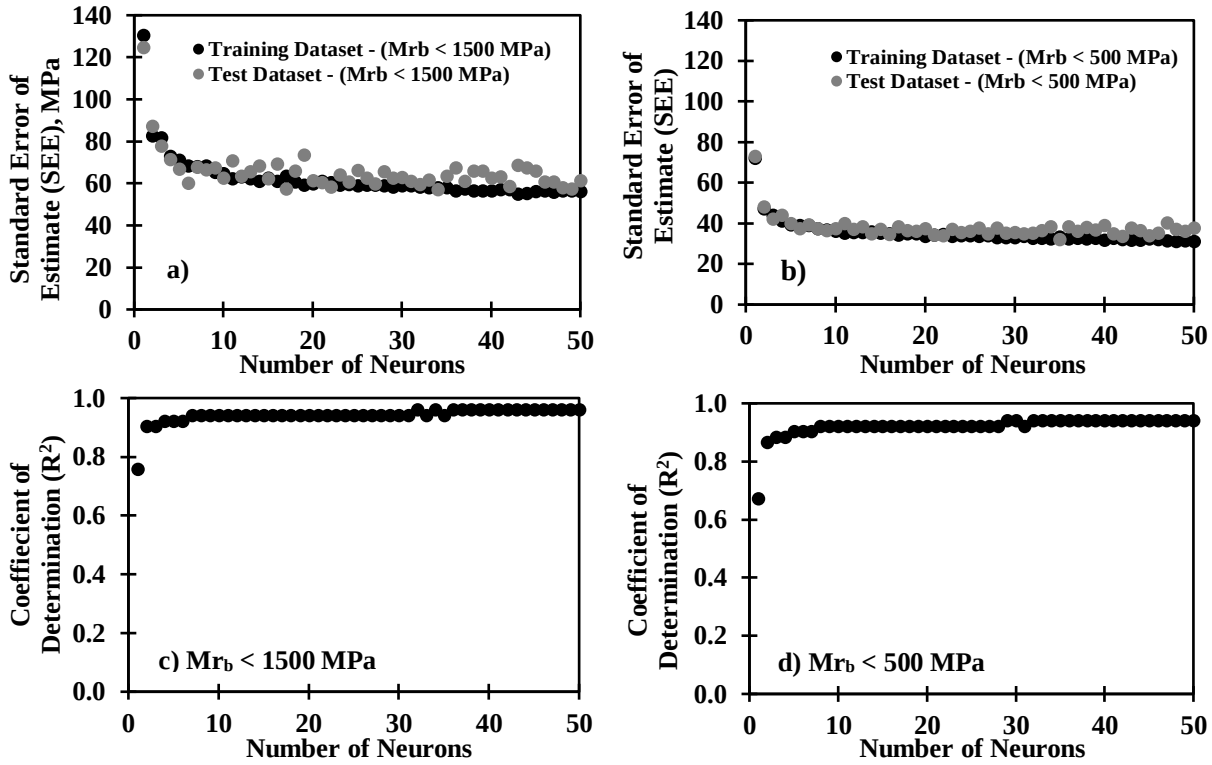

Figure E-6. Architecture of neural networks.

Table E-2. Summary of the optimized neural network properties.

Number of input parameters	5
Number of hidden layers	1
Number of neurons in hidden layer	20
Inputs pre-processing function	Sigmoid function
Outputs post-processing function	Linear function
Neural network type	Feed-forward
Network training algorithm	Bayesian Regularization Backpropagation
Number of epochs (maximum number of training iterations before training is stopped)	1000
Training ratio	70%
Validation ratio	15%
Testing ratio	15%

The optimized architecture for multi-layer perceptron (MLP) feed-forward neural network with Bayesian-Regularization algorithm is illustrated schematically in Figure E-7. Five independent input parameters as described earlier in this section, twenty neurons as the optimum number of neurons along with a tan-sigmoid and linear transfer functions and the output network estimate of the modulus of the base $M_{rb\text{-}SSN}$ are the main constituents of the optimized back-propagation neural network architecture. Multiple layers of neurons with nonlinear transfer functions allow the network to learn nonlinear relationships between input parameters and output vector.

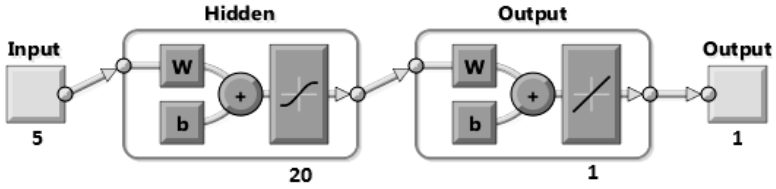

Figure E-7. Artificial neural network (ANN) architecture implemented for prediction of modulus of base layer.

For further analyses, the optimized network was employed to approximate the modulus of the base layer for the five scenarios mentioned earlier in this section. The corresponding results and cumulative errors of estimate for $Mr_{\text{b-SSN}} < 500$ MPa and $Mr_{\text{b-SSN}} < 1500$ MPa datasets are illustrated in Figure E-8. The third scenario with h, k'_{2b}, k'_{3b}, d_2, $M_{r\text{-}sub}$ (Representative) provides a better approximation of the modulus of the base layer with a considerably better cumulative distribution of standard error of estimates (SEE) as compared to the first two scenarios for both datasets.

Machine Learning Approach

To further improve the performance of the inverse algorithm, we have developed a Machine Learning (ML) process to evaluate the synthetic data and to predict the output of FE model using the input parameters. The input parameters for the ML algorithm are those summarized in Table E-1. Five different scenarios were considered to evaluate the performance of prediction model using different combination of input parameters. These scenarios are summarized in Table E-1.The first step in developing the ML algorithm was to perform a correlation analysis to find the input parameters that show higher impact on the targeted output (which is the modulus of base layer in this phase of analysis). The Pearson Correlation coefficients were calculated between pairs of input parameters as listed in Table E-1 and the target value ($Mr_{b\text{-}SSN}$). A radar chart was generated to better represent the most influential input parameters. Figure E-9 represents the output of correlation analysis and the radar chart which shows the most impacting input parameter for prediction of $Mr_{b\text{-}SSN}$. $M_{r\text{-}sub}$ (Representative) followed by d_2, k'_{3b} and k'_{2b} are the most impacting factors.

The next step was to develop an ML algorithm that can predict the $Mr_{b\text{-}SSN}$ using the input parameters. The model was then evaluated using five combinations of input parameters as represented by Scenarios 1 through 5 in Table E-1. A backpropagation feedforward neural network was developed to pre-process the input parameters and predict the target values for $Mr_{b\text{-}SSN}$. Figure E-10 shows the constructed architecture for the most complex inverse solver, scenario 5. Eighty percent of the synthetic database was used to train the neural network and the other twenty percent was used to verify and validate the developed model. Since the selection of data records to be included in the training and testing datasets are completely random, a cross-validation process was employed to select different combination of random training and testing data to ensure a uniform prediction power.

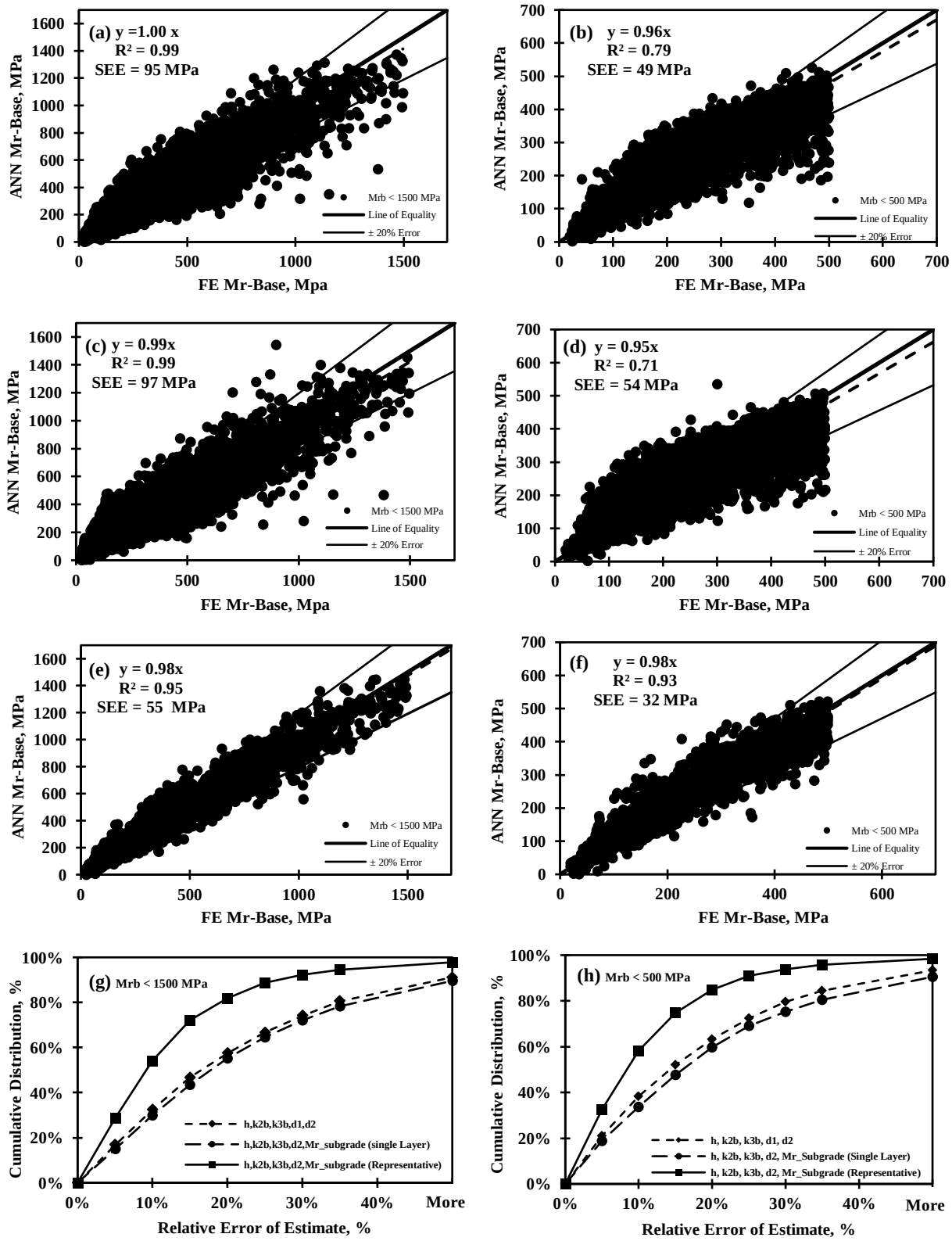

Figure E-8. Optimized Artificial Neural Network (ANN) results for $M_{rb\text{-}SSN}$ < 1500 MPa and $M_{rb\text{-}SSN}$ < 500 MPa datasets: (a) and (b) 1st scenario, (c) and (d) 2nd scenario, (e) and (f) 3rd scenario, (g) and (h) corresponding cumulative error of estimates for all three scenarios.

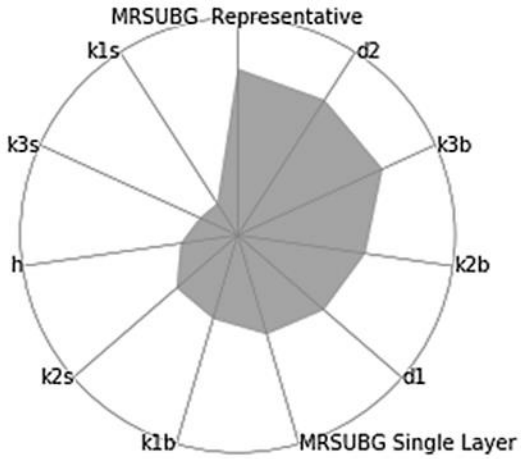

Figure E-9. Results of correlation analysis showing the most impacting input parameters.

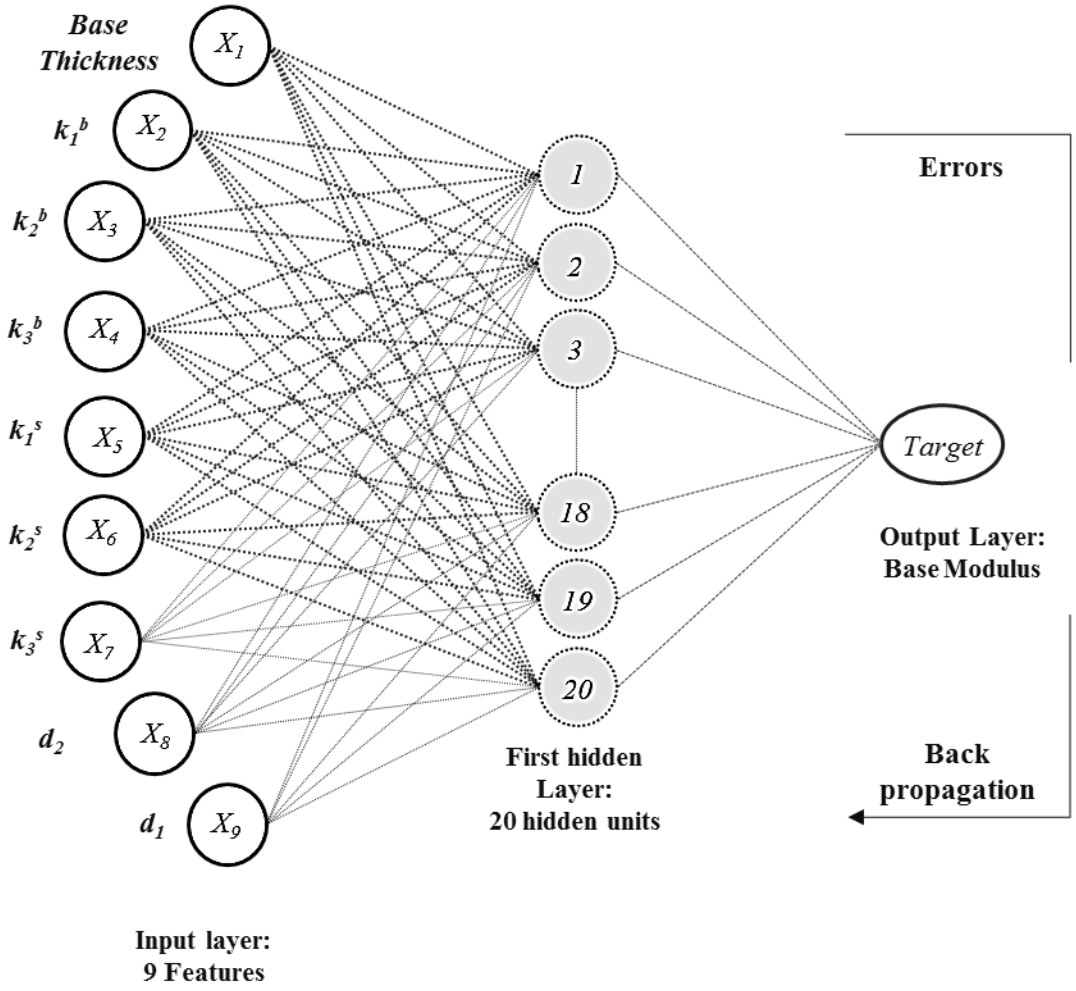

Figure E-10. Architecture of a multi-layer perceptron ANN model used for backcalculation of base modulus.

The results of the trained algorithms using the five scenarios that was summarized in Table E-1, are illustrated in Figures E-11 through E-15. To evaluate the performance of each scenario, its root mean squared error (RMSE) is represented in its corresponding figure. Although the overall prediction power of all five scenarios are better compared to the previous prediction models, it seems that scenario 5 (using h, k'_{1s}, k'_{2s}, k'_{3s}, k'_{1b}, k'_{2b}, k'_{3b}, d_2, d_1 in Table E-1) followed by scenarios 4, 1, 3, and 2 are the most promising combinations. The boundaries of $Mr_{b\text{-}SSN}$ in the synthetic FE database was limited to 300 MPa to represent realistic field conditions.

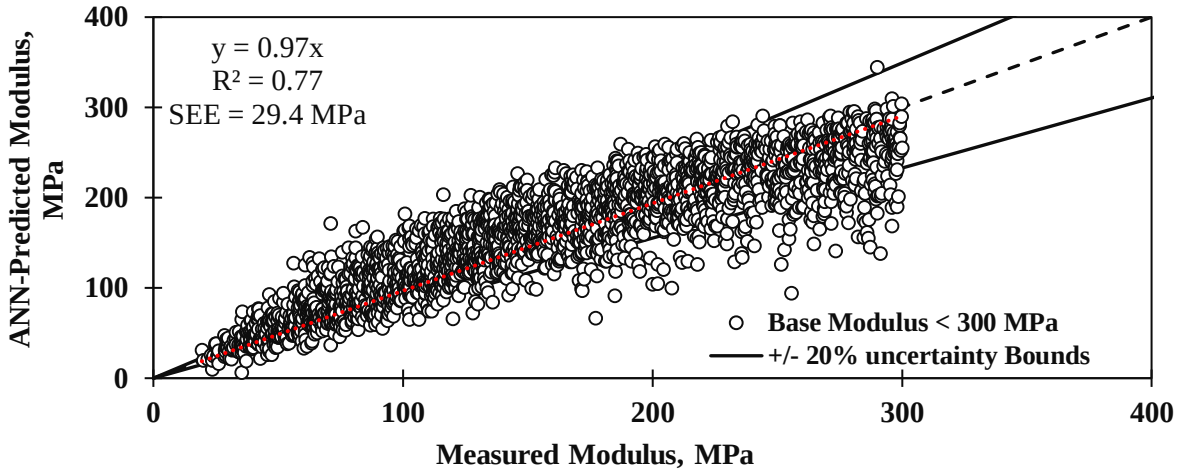

Figure E-11. ANN-predicted vs. FE-measured $Mr_{b\text{-}SSN}$ (MPa) using Scenario 1 input combination [RMSE = 29.4 MPa].

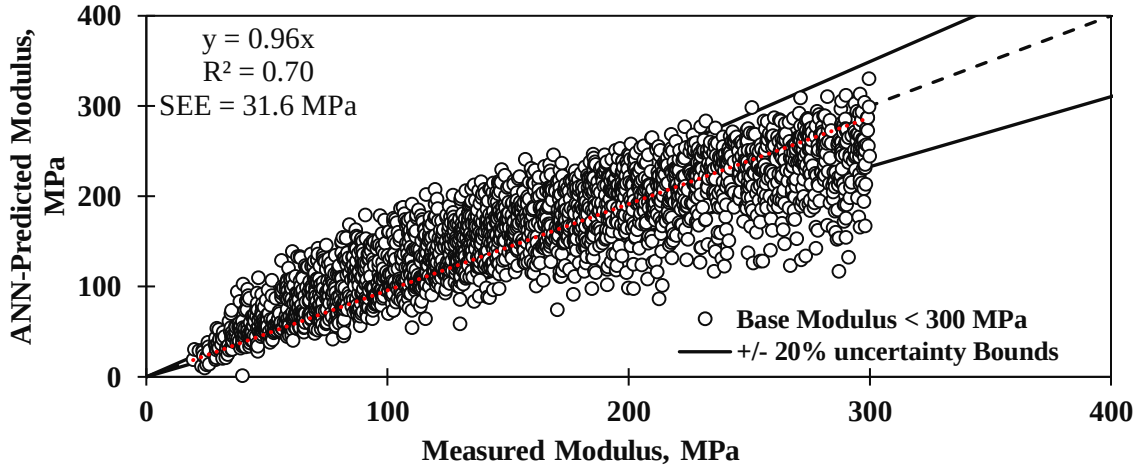

Figure E-12. ANN-predicted vs. FE-measured $Mr_{b\text{-}SSN}$ (MPa) using Scenario 2 input combination [RMSE = 31.6 MPa].

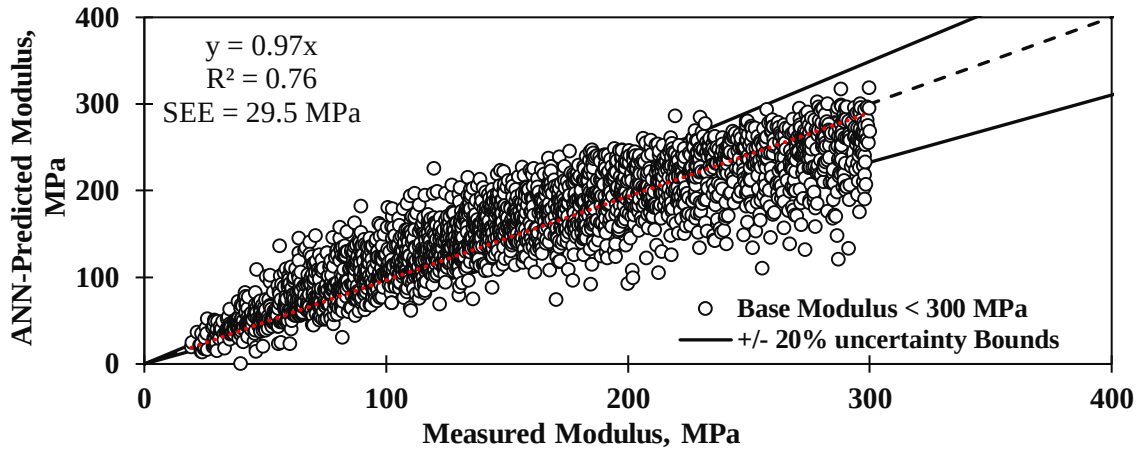

Figure E-13. ANN-predicted vs. FE-measured $Mr_{b\text{-}SSN}$ (MPa) using Scenario 3 input combination [RMSE = 29.5 MPa].

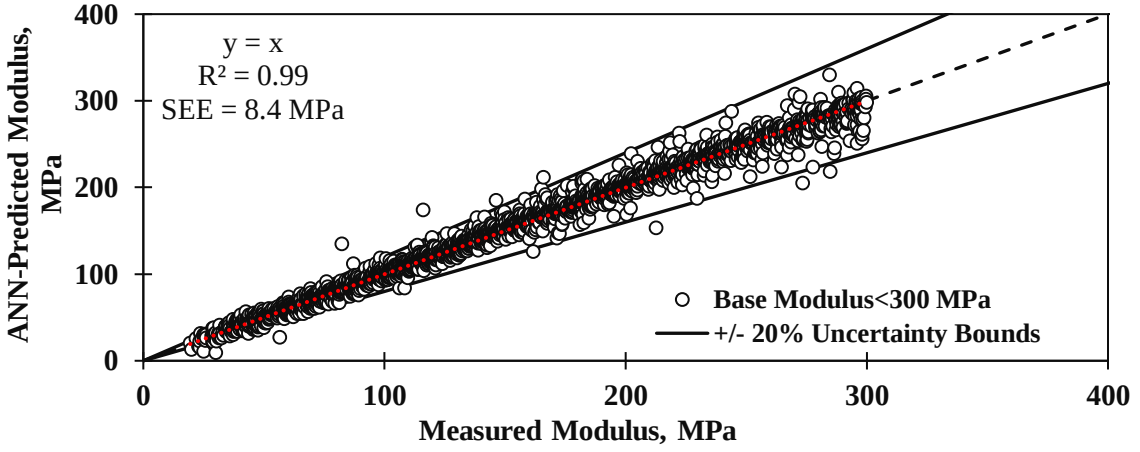

Figure E-14. ANN-predicted vs. FE-measured $Mr_{b\text{-}SSN}$ (MPa) using Scenario 4 input combination [RMSE = 8.41 MPa].

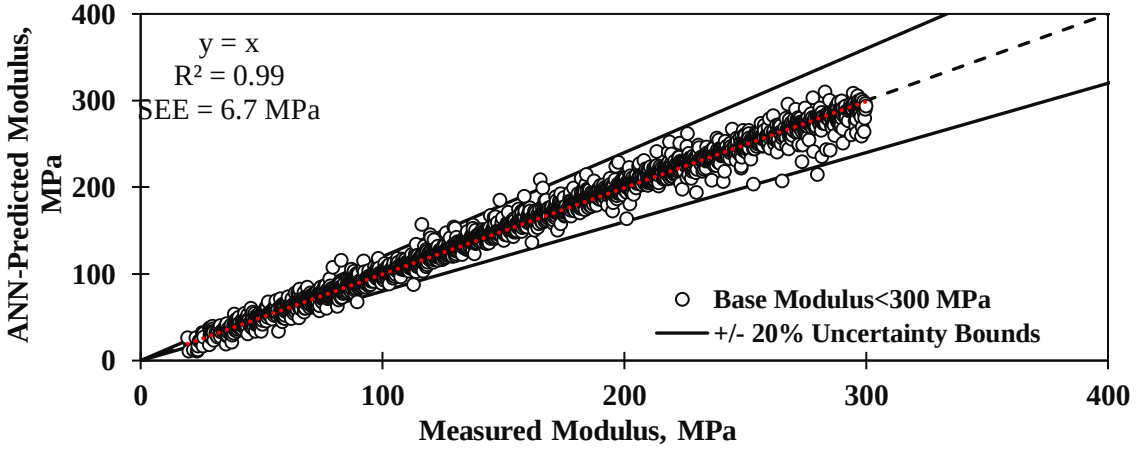

Figure E-15. ANN-predicted vs. FE-measured $Mr_{b\text{-}SSN}$ (MPa) using Scenario 5 input combination [RMSE = 6.7 MPa].

Backcalculation of Modulus for Vibratory Stationary Nonlinear Model

For practical reasons, a simplified model is preferred over a more realistic yet computationally intensive and inefficient model if the error of estimation from these two models are within an acceptable range. An investigation has been initiated to understand whether the vibratory stationary nonlinear (VSN) and static stationary nonlinear (SSN) models can be avoided in the backcalculation process. The results are discussed below.

Single Layer System: In the static case, M_1 was calculated through the expression $\ln(d_1 \cdot M_1)$ under the assumption that the displacement on the subgrade d_1 was known. It may be reasonable to express the parameter k'_1 through a similar expression (i.e. $\ln(d_1 \cdot k_1)$. It is desirable to reconstruct $ln(d_1^{VSN} \cdot k_1')$ as a linear function of $ln\left(d_1^{SSN} \cdot k_1'\right)$ with an acceptable accuracy. The general form of this function can be:

$$\ln\left(d_1^{VSN} \cdot k_1'\right) = a_0 + a_1 \cdot \ln(d_1^{SSN} \cdot k_1'), \quad \text{(E.26)}$$

where d_1^{VSN} denotes the displacement recorded on the subgrade for the vibratory stationary nonlinear model and d_1^{SSN} denotes the displacement recorded on the subgrade for the static stationary nonlinear model.

Based on linear regression analysis, the dependence between VSN and SSN models can be expressed with the following linear equation with a mean square error of 14%:

$$\ln\left(d_1^{VSN} \cdot k_1'\right) = 0.67 + 0.91 \cdot \ln(d_1^{SSN} \cdot k_1') \quad \text{(E.27)}$$

The regression coefficients for all possible higher order terms (i.e., linear and quadratic terms with respect to k'_2 and k'_3) turned out to be insignificant. Thus, for the case of single layer VSN model, the results of the dynamic simulations can be reconstructed with and acceptable accuracy using the outputs for the corresponding SSN model.

Two Layer System: Representing the mean modulus of base by $M_{2\_average}^{VSN}$, , it is desirable to check whether the expression $\ln(d_2^{VSN} \cdot M_{2\_average}^{VSN})$ can be described in terms of the similar static expression $\ln(d_2^{SSN} \cdot M_2^{SSN})$ considering the parameters k'_2 and k'_3 of the base and the subgrade.

For the case of 150 mm (6 in.) thick base, the following formula provided a reasonable estimation with the R^2 value of 79% standard error of 17% (see Figure E-16[a]).

$$\ln\left(d_2^{VSN} \cdot M_{2\_average}^{VSN}\right) = 0.96 + 0.81 \cdot \ln(d_2^{SSN} \cdot M_2^{SSN}) \quad \text{(E.28)}$$

For the 300 mm (12 in.) thick base, a similar formula provided an approximation with an R^2 value of 75% and the standard error of 16% (see Figure E-16[b]).

$$\ln\left(d_2^{VSN} \cdot M_{2\_average}^{VSN}\right) = 1.68 + 0.69 \cdot \ln(d_2^{SSN} \cdot M_2^{SSN}) \quad \text{(E.29)}$$

Based on this study, it is reasonable to conclude that the results of the dynamic simulations can be approximated from the results of the corresponding static simulations to avoid time-consuming dynamic simulations.

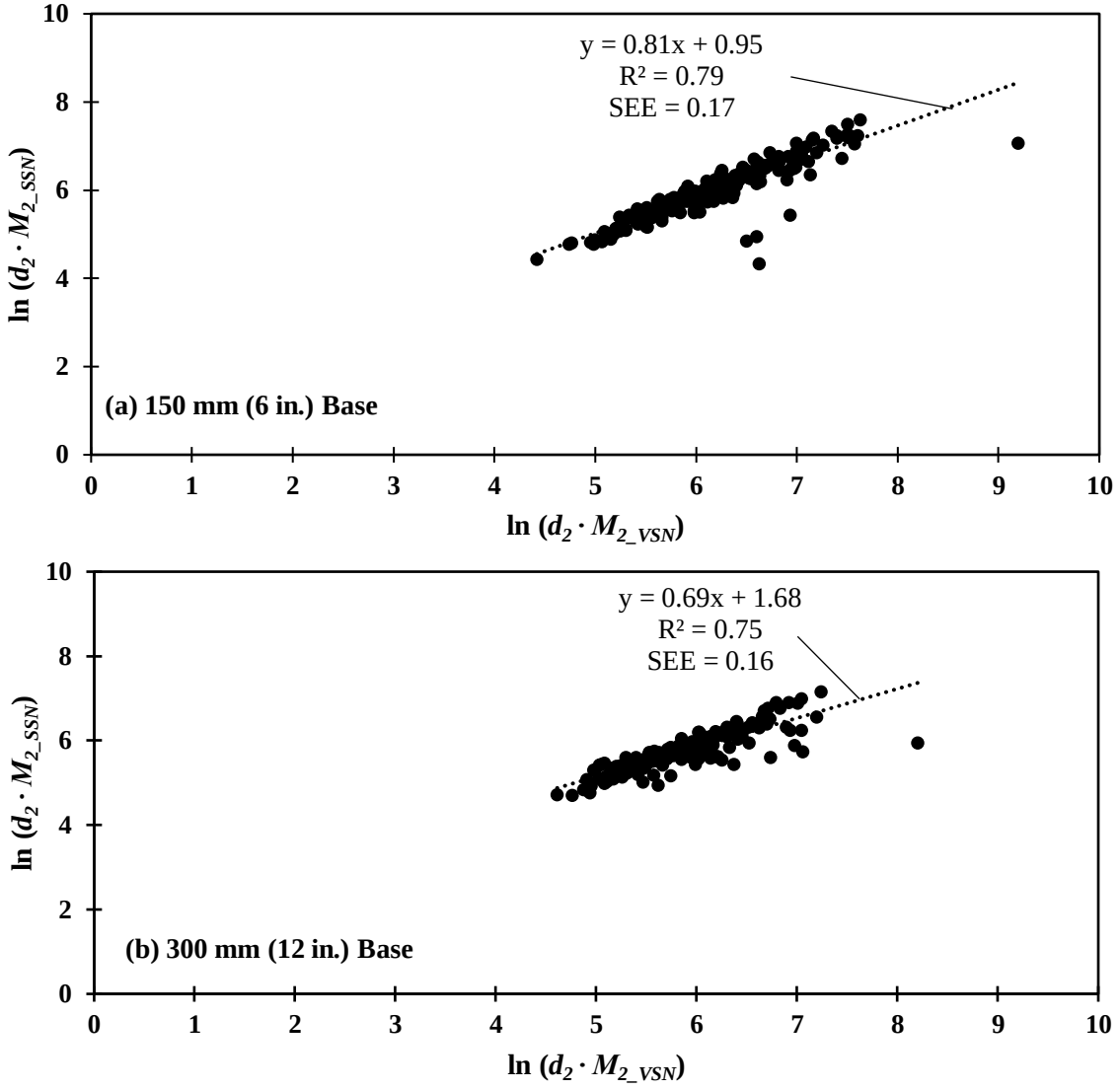

Figure E-16. Relationship between modulus of base for a two-layer geosystem obtained from vibratory stationary nonlinear (VSN) and static stationary nonlinear (SSN) finite element responses at a depth of (a) 150 mm (6 in.) and (b) 300 mm (12 in.).

References

Göktepe, A. B., Ağar, E., and Lav, A. H. (2005). "Comparison of Multilayer Perceptron and Adaptive Neuro-Fuzzy System on Backcalculating the Mechanical Properties of Flexible Pavements." ARI The Bulletin of the Istanbul Technical University, 54(3), pp. 65-67.

Göktepe, A. B., Ağar, E., and Lav, A. H. (2006). "Advances in Backcalculating the Mechanical Properties of Flexible Pavements." Advances in Engineering Software, 37(7), pp. 421-431.

Kang Y. V. (1998). "Multi-Frequency Backcalculation of Pavement Layer Moduli." Journal of Transportation Engineering, 124(1), pp. 73–81.

Kargah-Ostadi, N., and S. Stoffels, M. (2013). "Backcalculation of flexible pavement structural properties using a restart covariance matrix adaptation evolution strategy", Journal of Computing in Civil Engineering, Paper 04014035.

Ke, L., Nazarian, S., Abdallah, I., and Yuan, D., (2001), "A Sensitivity Study of Parameters Involved in Design with Seismic Moduli," Research Report 1780-2, Center for Highway Materials Research, the University of Texas at El Paso.

Maina, J. W., Yokota, H., Mfinanga, D. A., and Masuda, S. (2000). "Prediction of Pavement Deterioration based on FWD Results." NDT of Pavements and Backcalculation of Moduli, Vol. 3, STP 1375, S. D. Tayabji, E. O. Lukanen, eds., ASTM, pp. 95–109.

Mazari M., Tirado, C., Abdallah, I., and Nazarian, S. (2016). "Mechanical estimation of lightweight deflectometer target field modulus for construction quality control", Geotechnical Testing Journal, doi:10.1520/GTJ20150266.

Meier, R. W. and Rix, G. J. (1994) "Backcalculation of Flexible Pavement Moduli using Artificial Neural Networks." Transportation Research Record: Journal of the Transportation Research Board, 1448, Transportation Research Board, National Research Council, Washington, DC, pp. 75–82.

Meshkani, A., Abdallah, I., and Nazarian, S. (2002), "Determination of Nonlinear Parameters of Flexible Pavement Layers from Nondestructive Testing," Research Report 1780-3, Center for Highway Materials Research, the University of Texas at El Paso, TX, p. 97.

Mooney, M. A., and Facas, N. W. (2013). "Extraction of Layer Properties from Intelligent Compaction Data", Final Report for NCHRP Highway IDEA Project 145, Transportation Research Board of the National Academies, Washington, DC.

Ooi, P. S. K., Archilla, R., and Sandefur, K. G. (2004). "Resilient modulus models for compacted cohesive soils." Transportation Research Record: Journal of the Transportation Research Board, (1874), 115–124.

Roesset, J. M. and Shao, K. Y. (1985). "Dynamic Interpretation of Dynaflect and Falling Weight Deflectometer Tests." Transportation Research Record: Journal of the Transportation Research Board, 1022, TRB, Washington, DC, pp. 7–16.

Ullidtz P. (2000). "Will Nonlinear Backcalculation Help?" NDT of Pavements and Backcalculation of Moduli, Vol. 3. STP 1375, S. D. Tayabji, E. O. Lukanen, eds., ASTM, pp. 14–22.

Uzan J. (1994). "Advanced Backcalculation Techniques." NDT of Pavements and Backcalculation of Moduli, Special Technical Publication STP 1198, H. L. Von Quintus, A. J. Bush, and G. Y. Baladi, G. Y., eds., ASTM, pp. 3–37.

APPENDIX F

Field Study for Implementation and Evaluation of Nondestructive Tests and Intelligent Compaction for Quality Acceptance and Design Modulus Verification

Process of Instrumenting Four Cells at MnROAD

This section presents a brief explanation of field protocols used for the implementation of rapid nondestructive tests (NDT) for quality acceptance and design modulus verification at the MnROAD facility. The MnROAD facility, shown in Figure F-1, is a 6-mile test pavement facility located 40 miles northwest of Minneapolis/St. Paul, between Albertville and Monticello, MN.

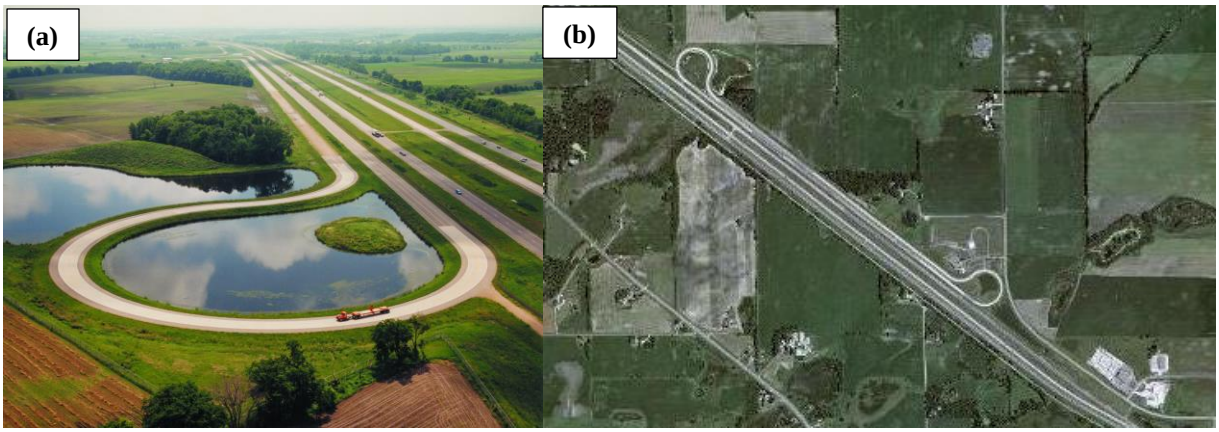

Figure F-1. MnROAD test track: (a) aerial view of MnROAD low-volume road and (b) satellite view of low-volume road, mainline and bypass I-94.

Field Testing: The field testing performed to achieve the objective is summarized in the following steps:

1. Instrumenting the subgrade using 3-D geophones and pressure cells, as discussed below.
2. Proof mapping the completed subgrade with an intelligent compaction (IC) roller after compaction.
3. Conducting field tests with nuclear density gauge (NDG), lightweight deflectometer (LWD) and dynamic cone penetrometer (DCP) on prepared subgrade after proof mapping.
4. Preparing and compacting the unbound aggregate base (UAB).
5. Installing instrumentation in the base as discussed below.
6. Mapping the completed base with an IC roller after compaction.

7. Conducting field tests with NDG, LWD, DCP and falling weight deflectometer (FWD) on prepared base after proof mapping.

Lab Testing: To support the goals of this project, samples of geomaterials were collected at the site to determine the variations in moisture content in the laboratory and to conduct laboratory resilient modulus tests at several moisture contents, as well as index tests (gradation and Atterberg limits) and moisture-density.

Instrumentation: A data acquisition system (DAQ) developed at UTEP was used to collect vibration data and ground response generated by the roller during IC operations. A schematic of the system is depicted in Figure F-2. The system consists of two accelerometers that were mounted on the roller (drum), a data acquisition box, a GPS antenna and receiver, a power supply and a laptop computer.

A similar data acquisition system was also used to monitor the propagation of roller vibration within the geomaterials by embedding geophones and pressure cells at different depths in the subsurface. The components of that system are shown in Figure F-3. The GPS unit on the second DAQ system was used to synchronize the geophone data with the accelerometers mounted on the rollers. The geophones were embedded in the existing ground layer (before placement of the new test layers) to monitor the soil layer responses during the IC operation. The geophones recorded the vertical, transversal and/or longitudinal amplitudes of vibration, with the longitudinal response being in the same direction as the roller movement and the transversal response being perpendicular to the moving direction.

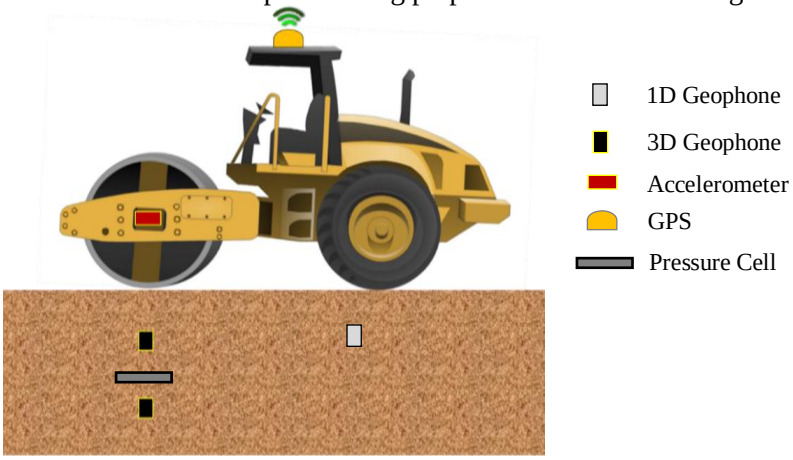

Figure F-2. Schematic of the IC calibration system.

Figure F-3. Components of the data acquisition system developed for this research.

Summary of Activities at MnROAD

Table F-1 contains a summary of the activities at each site. Each activity is briefly explained below.

1. **Identification of test strip:** Tests were carried out in cells 185–189.[1] These cells are located on the south side of MnROAD low-volume road loop, as shown in Figure F-4. The pavement structures of the four test sections are shown in Figure F-5. All sections consist of a 300 mm (12 in.) base over a 90 mm (3.5 in.) intermediate layer of granular material on top of subgrade. Coarse and fine recycled concrete aggregates (RCAs) were used for the base layer in cells 185 and 186, respectively. Limestone and recycled aggregate Class 6 were used for the base layers in cells 188 and 189, respectively. The existing subgrade was tens of feet of an imported sandy material for Cells 185 and 186, while a natural clayey subgrade was used for Cells 188 and 189. Geophones were installed at 150 mm (6 in.) and 600 mm (24 in.) into the subgrade, and at 150 mm (6 in.) within the base layer, and pressure cells were placed 300 mm (12 in.) into the base and subgrade, as shown in Figure F-5. Actual identification of a test strip and preparations for ground instrumentation are shown in Figure F-6. Instrumentation of the test strip is shown in Figure F-7.
2. **Setup of GPS:** MnDOT base station was used. Data acquisition of the UTEP system was synchronized with the roller's Controller Area Network (CAN) system.
3. **Setup of IC roller:** UTEP, in cooperation with Caterpillar personnel, prepared the setup of the IC roller. A smooth-drum IC vibratory soil compactor with an operating weight of 157 kN (35.2 kip), shown in Figure F-8, was used for mapping the test sections after compaction. Specifications of the IC roller are shown in Table F-2. Sensors were mounted on the IC roller to collect vibration data. The IC roller was checked for proper data collection and operating settings including roller speed, and vibration frequency and amplitude. Instrumentation of roller at the test site is shown in Figure F-9.
4. **Carry out construction as normally done:** UTEP team observed the construction processes but was not involved in or interfered with the operation.
5. **Perform proof mapping:** MnDOT and UTEP personnel coordinated to perform proof mapping of test sections after compaction of the section was finished. Four forward passes were performed to cover the test section width. Embedded ground sensor measurements were monitored and recorded by UTEP personnel as the roller passed along the line passing over the embedded sensors. UTEP researchers monitored the adequate accelerometer's measurements during each of the roller passes, as evidenced in Figure F-10.
6. **Carry out tests on cells:** Figure F-11 illustrates the nominal schematics of the test layout in each cell. After the completion of proof mapping. UTEP and MnDOT personnel carried out spot tests at 36 points for correlation testing, separated at a spacing of 7.5 m (25 ft) longitudinally, and 2.1 m (7 ft) in the transverse direction, as schematically shown in Figure F-11. The spacing of spot test measurements was modified for Cells 185 and 186 to accommodate enough representative measurements. The NDT devices used for those tests include:
   - Nuclear Density Gauge (NDG) by MnDOT,
   - Dynamic Cone Penetrometer (DCP) by UTEP/MnDOT,
   - Light Weight Deflectometer (LWD) by UTEP/MnDOT,
   - Falling Weight Deflectometer (FWD) by MnDOT, and
   - Moisture sampling for validation of NDG by UTEP. Low-frequency and low-amplitude.

Figure F-12 shows a satellite view of the four cells, showing the location of the spot tests and embedded ground sensors. Collected data from all NDT spot tests used in the field and from roller and ground instrumentation were analyzed to meet the goal of this study.

[1] Cell 187 was not available and was not included as part of this study.

Table F-1. Test activity and schedule.

Time	Tasks	Activities
July 17–19, 2017	Coordination and Initial Set up	• Construction and compaction of subgrade layer • Sample representative subgrade (MnDOT) • Coordinate with IC roller operator on how to collect, record, save, download and transfer data for this project (CAT and UTEP)
July 20–25, 2017	Subgrade	• Mark the test section and test spots in each cell (UTEP) • Arrange for field instrumentation (MnROAD, UTEP) • Obtain GPS coordinates for spot test locations (UTEP) • Install geophones at a depth of 150 mm (6 in.) and 600 mm (24 in.) from the top of subgrade, and pressure cells at a depth of 300 mm (12 in.) from the top of subgrade (UTEP, MnROAD) • Map subgrade with IC roller (CAT and UTEP) • Carry out in-situ testing with modulus-based devices and NDG to establish moduli (UTEP, MnDOT)
August 1–2, 2017	Unbounded Aggregate Base (UAB)	• Construction and compaction of base prior to testing • Sample representative prior to testing (MnDOT) • Install geophone at a depth of 150 mm (6 in.) within the base, and pressure cell at a depth of 300 mm (24 in.) from the top of base (UTEP, MnROAD) • Map Aggregate Base with IC roller (CAT and UTEP) • Carry out in-situ testing with modulus-based devices and NDG to establish moduli (UTEP, MnDOT)

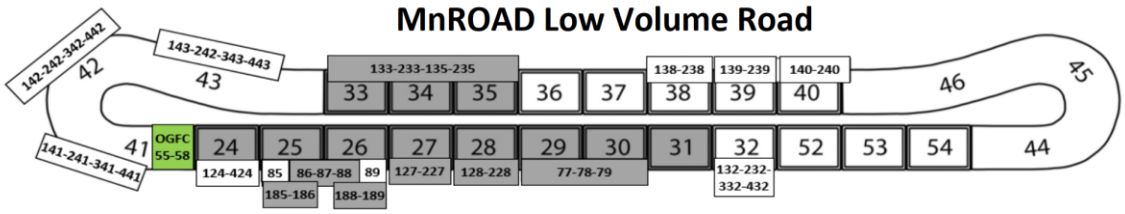

Figure F-4. Location of Cells 185–189, test sections within MnROAD low-volume road.

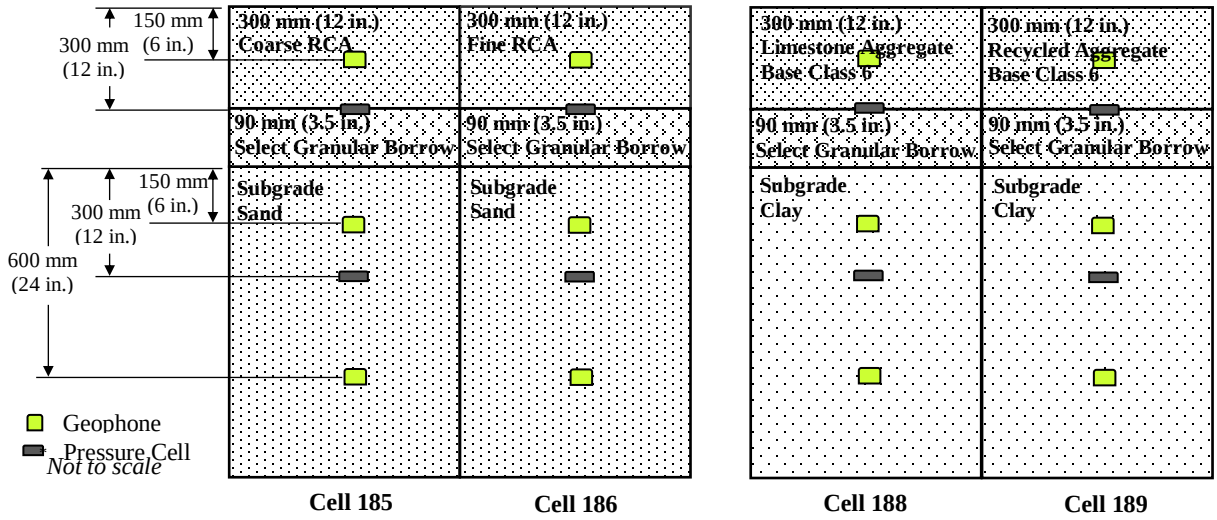

Figure F-5. Pavement structure of Cells 185–189 and installation of ground sensors.

Figure F-6. (a) Test strip; (b) and (c), UTEP and MnROAD personnel making preparations for embedding ground instrumentation.

Figure F-7. Installation of ground sensors: (a) preparation of ground sensors; (b) wiring of sensors by UTEP and MnROAD personnel; (c) embedment of geophone; (d) and (e) geophone within geomaterial; and (f) pressure cell within geomaterial.

Figure F-8. IC roller used for mapping purposes.

Table F-2. Specifications of IC roller used in test sections.

Mass/Weights		
Operating Weight	157 KN	35,260 lb
Drum and Frame Weight	116 KN	26,110 lb
Mass of Drum	5153 Kg	353.1 lb·s^2/ft
Eccentric Mass, m_0e_0	5.06 kg·m	1.137 lb·s^2
Operating Specifications		
Compaction Width	2.1 m	84 in.
Static Linear Load	48.8 KN/m	278.7 lb/in.
Dimensions		
Drum Diameter	1.5 m	60.4 in.
Drum Width	2.1 m	84 in.
Vibratory System		
Centrifugal Force – Maximum	332 KN	74,600 lb
Centrifugal Force – Minimum	166 KN	37,300 lb
Nominal Amplitude – High	2.1 mm	0.083 in.
Nominal Amplitude – Low	1.0 mm	0.039 in.
Centrifugal Force – Maximum	332 KN	74,600 lb

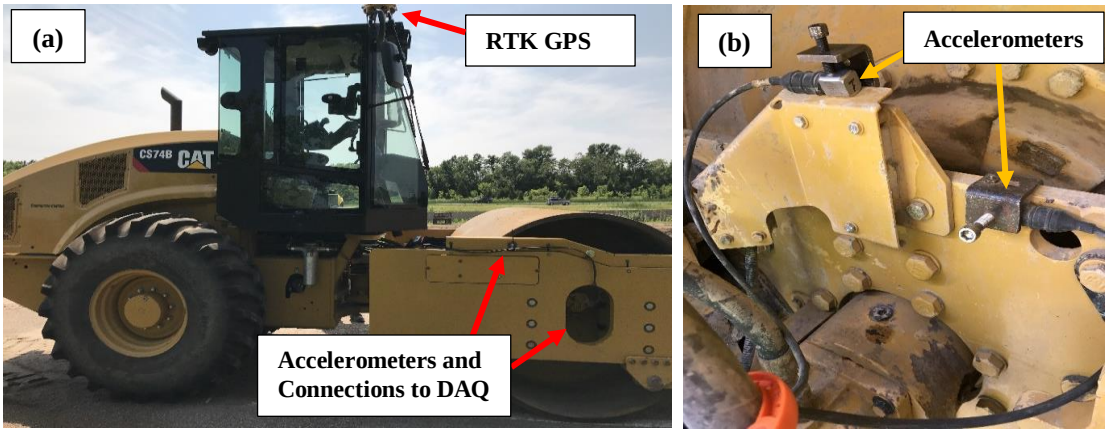

Figure F-9. Field site instrumentation of roller compactor: (a) RTK GPS and wiring of accelerometers to data acquisition system and (b) installation of both accelerometers to measure vertical and horizontal vibration on roller compactor drum frame.

Figure F-10. UTEP personnel monitors proof mapping process.

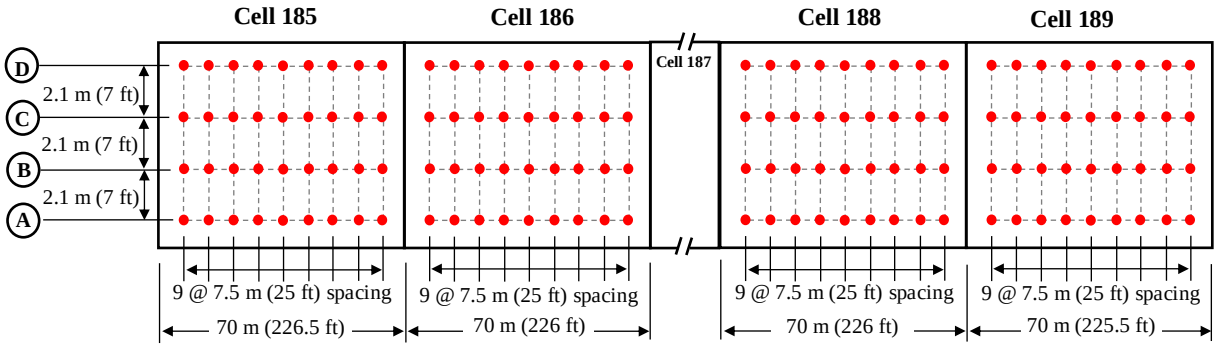

Figure F-11. Schematic of the proposed test layout.

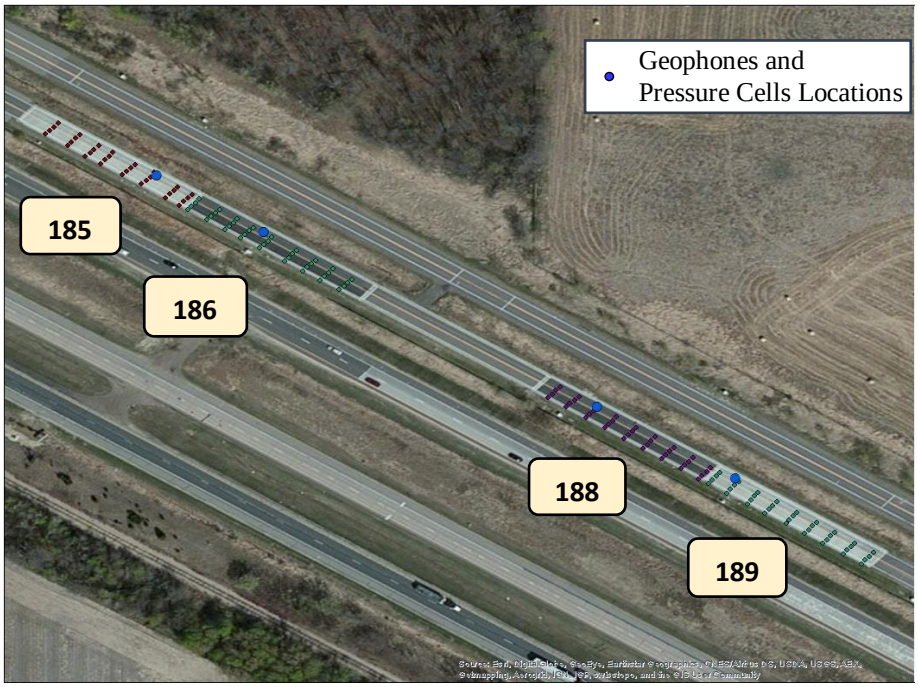

Figure F-12. Spot-test layout and location of geophones and pressure cells.

Laboratory Evaluation

The purpose of laboratory evaluation is to determine the correlation between extracted mechanical properties of compacted geomaterials under field conditions with those estimated under laboratory conditions. All necessary index and moisture-density tests were carried out as per AASHTO test methods. The resilient modulus tests were carried out as per AASHTO T-307 in duplicate at OMC, OMC±1% or OMC±10%OMC (if OMC<10%), and OMC±2% or OMC±20%OMC (if OMC>10%).

Log of Activities and Data Records

Proof mapping of the four cell sections was performed using a CAT CS74B IC roller. The operating vibrating settings of the roller are provided in Table F-3.

Table F-3. Vibration settings of CAT CS74B IC roller.

Settings	Low	High
Nominal Amplitude	1.0 mm (0.039 in.)	2.1 mm (0.083 in.)
Centrifugal Force	166 kN (37,600 lb)	332 kN (74,600 lb)
Vibration Range	23.3 – 28 Hz (1400 – 1680 vpm)	
Vibration Frequency - Standard	28 Hz (1680 vpm)	

In the following sections, the testing activities conducted at MnROAD are described for each of the days of the study.

Thursday, July 20, 2017

The construction of the subgrade for Cells 185 and 186 reached the plan elevation. The construction of the subgrade involved the use of a compactor (not instrumented with IC technology) to compact the subgrade and a grader to prepare a smooth surface. Simultaneously, the research team instrumented the IC roller with the UTEP-developed data acquisition system (DAQ) for mapping. A virtual reference system (VRS) from MnROAD was used to improve the precision of the IC roller's GPS measurements. After final grading, the research team proceeded to mark the spots for NDT testing for Cells 185 and 186, as shown in Figure F-13. Four rows of spots, separated by a distance of 2.1 m (7 ft) along the IC roller passes, were marked. Spots along each row were marked with a spacing of 15 m (50 ft). Using a hand-held GPS rover and ground-base station, the research team captured the coordinates of the marked spots.

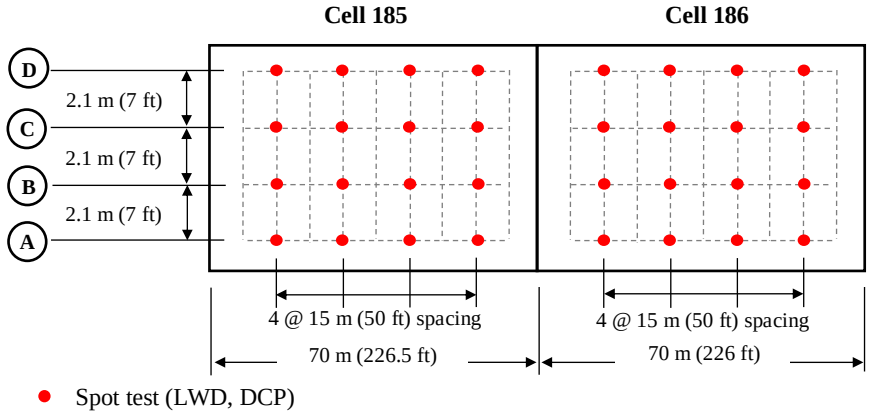

Figure F-13. Schematic of the test layout on subgrade of Cells 185 and 186.

Using an auger, MnROAD personnel along with the UTEP research team installed ground sensors into the subgrade of Cells 185 and 186 at different depths, as schematically shown in Figure F-5, along Line A. Trenches were excavated to securely transfer the cables from the pressure cells and vibration transducers through a PVC pipe to the shoulder for connection to the DAQ, as shown in Figure F-14.

Figure F-14. Excavation for installation of ground sensors into subgrade in cells 185 and cells 186 by MnROAD personnel and UTEP researchers.

The instrumented CAT CS74B smooth-drum roller was then used to map the compacted subgrade. After the mapping process, the UTEP research team conducted NDT testing using a lightweight deflectometer (LWD) and a dynamic cone penetrometer (DCP). Simultaneously, MnROAD personnel conducted in-situ determination of density and moisture content using a nuclear density gauge (NDG).

The research team then proceeded to retrieve samples of subgrade material from points adjacent to the marked spots for further moisture content determination in the laboratory using the oven-dry method. Finally, the contact width of the IC roller drum in stationary static condition was measured on top of the subgrade. Table F-4 summarizes the activities for July 20, 2017.

Friday, July 21, 2017

The research team repeated the mapping of Cells 185 and 186 to acquire pressure cell measurements, in addition to the geophones'. The CAT CS74B smooth-drum roller was again used to map the subgrade. After mapping, the UTEP research team conducted NDT testing. Four rows of spots, separated by a distance of 2.1 m (7 ft) along the IC roller passes, were marked. Spots along each row were marked with a spacing of 7.5 m (25 ft), as illustrated in Figure F-11. Using a hand-held GPS rover and ground-base station, the research team captured the coordinates of the marked spots. Due to unanticipated rain, fewer spot tests were carried out. Table F-5 summarizes the mapping and nondestructive testing activities for July 21, 2017.

Tuesday, July 25, 2017

Construction of the subgrade for Cells 188 and 189 reached the plan elevation. The research team marked the spots for NDT testing for Cells 188 and 189, as shown in Figure F-11. Four rows of spots, separated by a distance of 2.1 m (7 ft) along the IC roller passes, were marked. Spots along each row were marked with a spacing of 7.5 m (25 ft), as illustrated in Figure F-11. With help from MnROAD personnel, the research team installed ground sensors into the subgrade in cells 188 and 189 at different depths, as per Figure F-5. 1-ft wide trenches were excavated to securely transfer sensor cables and the pressure cell's pressure transducer through a PVC pipe to the shoulder for connection to the DAQ. The research team in

Table F-4. Summary of activities for July 20, 2017.

Test Sections			
Cell	**Layer**	**Material**	
185	Subgrade	Sand	
186	Subgrade	Sand	
Compaction			
Activities	• Compaction of subgrade • Grader to prepare smooth surface		
Installation of Ground Sensors in Cells 185 and 186			
	Installation into subgrade*	**Sensors Location**	**Observations**
Geophones	• 600 mm (24 in.) deep • 150 mm (6 in.) deep	Line A	Data collected during mapping
Pressure Cell	• 300 mm (12 in.)	Line A	Installed but not recorded
Mapping			
Activities	• Compaction of subgrade • Grader to prepare smooth surface • Mapping using CAT CS74B IC roller - IC data recorded by Trimble DAQ and UTEP DAQ; Controller Area Network (CAN) data and roller pulse data also collected with UTEP DAQ • Ground sensor measurements for all line passes (pressure cell data not collected)		
NDT Performed			
Activities	• LWD • DCP • NDG (by MnROAD personnel)		
Additional Activities			
Activities	• Sampling of material for moisture content • Sampling of material for further laboratory testing • Measurement of CAT CS74B drum's contact width on top of subgrade.		

* Refer to Figure F-5.

conjunction with MnROAD personnel then proceeded to perform mapping and NDT testing of the subgrade. Table F-6 summarizes the mapping and nondestructive testing activities for July 25, 2017.

Tuesday, August 1, 2017

Construction of the base layer for Cells 185 and 186 reached the plan elevation. The research team marked the spots for NDT testing for Cells 185 and 186, as shown in Figure F-11. Four rows of spots, separated by a distance of 2.1 m (7 ft) along the IC roller passes, were marked. Spots along each row were marked with a spacing of 7.5 m (25 ft), as illustrated in Figure F-11. With help from MnROAD personnel, the research team installed into the base layer ground sensors in both Cells 185 and 186 at different depths, as per Figure F-5. 1-ft wide trenches were excavated to securely transfer the geophones and pressure cell cables through a PVC pipe to the shoulder. The research team in conjunction with MnROAD personnel then proceeded to perform mapping and NDT testing of the base layer. Table F-7 summarizes the mapping and nondestructive testing activities for August 1, 2017 on the base layer of Cells 185 and 186.

Table F-5. Summary of activities for July 21, 2017.

Test Sections			
Cell	**Layer**	**Material**	
185	Subgrade	Sand	
186	Subgrade	Sand	
Previously Installed Ground Sensors Data Collection during Mapping			
	Installation into subgrade*	**Sensors Location**	**Observations**
Geophones	• 600 mm (24 in.) deep • 150 mm (6 in.) deep	Line A	Data collected during mapping
Pressure Cell	• 300 mm (12 in.)	Line A	Data collected during mapping
Mapping			
Activities	• Mapping using CAT CS74B IC roller - IC data recorded by CAT DAQ and UTEP DAQ; Controller Area Network (CAN) data and roller pulse data also collected with UTEP DAQ • Ground sensor measurements for all line passes		
NDT Performed			
Activities	• LWD (fewer spot measurements collected than planned due to imminent rain) • DCP (interrupted by rain in Cell 185, not collected on Cell 186) • NDG (by MnROAD personnel) • FWD (by MnROAD personnel)		
Additional Activities			
Activities	• Sampling of material for moisture content • Sampling of material for further laboratory testing • Measurement of CAT CS74B drum's contact width on top of subgrade.		

* Refer to Figure F-5.

Wednesday, August 2, 2017

Construction of the base layer for Cells 188 and 189 reached the plan elevation. The research team marked the spots for NDT testing for Cells 188 and 189, as shown in Figure F-11. Four rows of spots, separated by a distance of 2.1 m (7 ft) along the IC roller passes, were marked. Spots along each row were marked with a spacing of 7.5 m (25 ft), as illustrated in Figure F-11. With help from MnROAD personnel, the research team installed ground sensors into the base layer in both Cells 188 and 189 at different depths, as per Figure F-5. 1-ft wide trenches were excavated to securely transfer the geophones and pressure cell cables through a PVC pipe to the shoulder. The research team in conjunction with MnROAD personnel then proceeded to perform mapping and NDT testing of the base layer. Table F-8 summarizes the mapping and nondestructive testing activities for August 1, 2017 on the base layer of Cells 188 and 189.

Table F-6. Summary of activities for July 25, 2017.

Test Sections			
Cell	**Layer**	**Material**	
188	Subgrade	Clay	
189	Subgrade	Clay	
Compaction			
Activities	Compaction of subgrade Grader to prepare smooth surface		
Installation of Ground Sensors in Cells 185 and 186			
	Installation into subgrade*	**Sensors Location**	**Observations**
Geophones	• 600 mm (24 in.) deep • 150 mm (6 in.) deep	Line A	Data collected during mapping
Pressure Cell	• 300 mm (12 in.)	Line A	Data collected during mapping
Mapping			
Activities	• Mapping using CAT CS74B IC roller - IC data recorded by CAT DAQ and UTEP DAQ; Controller Area Network (CAN) data and roller pulse data also collected with UTEP DAQ • Ground sensor measurements for all line passes		
NDT Performed			
Activities	• LWD • DCP • NDG (by MnROAD personnel) • FWD (by MnROAD personnel)		
Additional Activities			
Activities	• Sampling of material for moisture content • Sampling of material for further laboratory testing • Measurement of CAT CS74B drum's contact width on top of subgrade.		

* Refer to Figure F-5.

Table F-7. Summary of activities for August 1, 2017.

Test Sections			
Cell	**Layer**	**Material**	
185	Base	Coarse Recycled Course Aggregate	
186	Base	Fine Recycled Course Aggregate	
Compaction			
Activities	• Compaction of base layer • Grader to prepare smooth surface		
Installation of Ground Sensors in Base			
	• **Installation into base***	**Sensors Location**	**Observations**
Geophones	• 150 mm (6 in.) deep	Line A	Data collected during mapping
Pressure Cell	• 300 mm (12 in.)	Line A	Data collected during mapping
Previously Installed Ground Sensors in Subgrade			
	Installation into subgrade*	**Sensors Location**	**Observations**
Geophones	• 900 mm (36 in.) • 450 mm (18 in.)	Line A	Data collected during mapping
Pressure Cell	• 600 mm (24 in.)	Line A	Data collected during mapping
Mapping			
Activities	• Mapping using CAT CS74B IC roller - IC data recorded by Trimble DAQ and UTEP DAQ; Controller Area Network (CAN) data and roller pulse data also collected with UTEP DAQ • Ground sensor measurements for all line passes		
NDT Performed			
Activities	• LWD • NDG (by MnROAD personnel) • FWD (by MnROAD personnel)		
Additional Activities			
Activities	• Sampling of material for moisture content • Sampling of material for further laboratory testing • Measurement of CAT CS74B drum's contact width on top of base.		

* Refer to Figure F-5.

Table F-8. Summary of activities for August 2, 2017.

Test Sections			
Cell	**Layer**	**Material**	
188	Base	Limestone Aggregate Base Class 6	
189	Base	Recycled Aggregate Base Class 6	
Compaction			
Activities	Compaction of base layer Grader to prepare smooth surface		
Installation of Ground Sensors in Base			
	Installation into base*	**Sensors Location**	**Observations**
Geophones	• 150 mm (6 in.) deep	Line A	Data collected during mapping
Pressure Cell	• 300 mm (12 in.)	Line A	Data collected during mapping
Previously Installed Ground Sensors in Subgrade			
	Installation into subgrade*	**Sensors Location**	**Observations**
Geophones	• 900 mm (36 in.) • 450 mm (18 in.)	Line A	Data collected during mapping
Pressure Cell	• 600 mm (24 in.)	Line A	Data collected during mapping
Mapping			
Activities	• Mapping using CAT CS74B IC roller - IC data recorded by CAT DAQ and UTEP DAQ; Controller Area Network (CAN) data and roller pulse data also collected with UTEP DAQ • Ground sensor measurements for all line passes		
NDT Performed			
Activities	• LWD • NDG (by MnROAD personnel) • FWD (by MnROAD personnel)		
Additional Activities			
Activities	• Sampling of material for moisture content • Sampling of material for further laboratory testing • Measurement of CAT CS74B drum's contact width on top of base.		

Summary of Collected Data

A summary of the data collected by the UTEP DAQ mounted on the IC roller and ground sensors is provided in Tables F-9 through F-13, for each of the days that testing was performed.

Table F-9. Data collected by the UTEP DAQ for July 20, 2017.

Section:	**Cell 185**
Material:	**Subgrade - Sand**
IC Roller:	**CAT CS74B**

				UTEP DAQ Data Files	
Computer Time	**Line Pass**	**Vibration Amplitude Mode**	**Observation**	**Accelerometer Folder: iX104**	**Geophone Folder: CF19**
3:33 PM	A	LOW – 28 Hz		333PM.dat	329PM.dat
3:36 PM	B	LOW – 28 Hz	IC roller stopped early	336PM.dat	331PM.dat
3:37 PM	B	LOW – 28 Hz		337PM.dat	332PM.dat
3:39 PM	C	LOW – 28 Hz		339PM.dat	335PM.dat
3:41 PM	D	LOW – 28 Hz		341PM.dat	337PM.dat
3:45 PM	A	LOW – 28 Hz		345PM.dat	340PM.dat

NOTES:

- CMV calculated from CAN and UTEP's DAQ system.
- Trimble data provided by Caterpillar.
- Vibration mode determined as a function of the annotations, amplitude and frequency values showed on accelerometers records.
- Data from GEOKON pressure cells not collected.

Section:	**Cell 186**
Material:	**Subgrade - Sand**
IC Roller:	**CAT CS74B**

				UTEP DAQ Data Files	
Computer Time	**Line Pass**	**Vibration Amplitude Mode**	**Observation**	**Accelerometer Folder: iX104**	**Geophone Folder: CF19**
2:49 PM	A	LOW – 28 Hz	Operator did not drive on line A No pulses recorded on roller DAQ	249PM.dat	245PM.dat
2:51 PM	A	LOW – 28 Hz	Full coverage of line A No pulses recorded on roller DAQ	251PM.dat	247PM.dat
2:58 PM	B	LOW – 28 Hz	No pulses recorded on roller DAQ	258PM.dat	254PM.dat
3:04 PM	A	LOW – 28 Hz		304PM.dat	259PM.dat
3:08 PM	B	LOW – 28 Hz		308PM.dat	303PM.dat
3:10 PM	C	LOW – 28 Hz		310PM.dat	305PM.dat
3:14 PM	A	LOW – 28 Hz		314PM.dat	310PM.dat

NOTES:

- CMV calculated from CAN and UTEP's DAQ system.
- Trimble data provided by Caterpillar.
- Vibration mode determined as a function of the annotations, amplitude and frequency values showed on accelerometers records.
- Data from GEOKON pressure cells not collected.

Table F-10. Data collected by the UTEP DAQ for July 21, 2017.

Section:	**Cell 185**
Material:	**Subgrade - Sand**
IC Roller:	**CAT CS74B**

				UTEP DAQ Data Files	
Computer Time	**Line Pass**	**Vibration Amplitude Mode**	**Observation**	**Accelerometer Folder: iX104**	**Geophone Folder: CF19**
9:05 AM	A	LOW – 28 Hz		905AM.dat	905AM.dat
9:08 AM	B	LOW – 28 Hz		908AM.dat	908AM.dat
9:11 AM	C	LOW – 28 Hz		911AM.dat	911AM.dat
9:13 AM	D	LOW – 28 Hz		913AM.dat	914AM.dat
9:16 AM	A	LOW – 28 Hz		916AM.dat	916PM.dat

NOTES:

- CMV calculated from CAN and UTEP's DAQ system.
- Trimble data provided by Caterpillar.
- Vibration mode determined as a function of the annotations, amplitude and frequency values showed on accelerometers records.

Section:	**Cell 186**
Material:	**Subgrade - Sand**
IC Roller:	**CAT CS74B**

				UTEP DAQ Data Files	
Computer Time	**Line Pass**	**Vibration Amplitude Mode**	**Observation**	**Accelerometer Folder: iX104**	**Geophone Folder: CF19**
8:28 AM	A	LOW – 28 Hz		828AM.dat	829AM.dat
8:32 AM	B	LOW – 28 Hz		832AM.dat	833AM.dat
8:35 AM	C	LOW – 28 Hz		835AM.dat	835AM.dat
8:37 AM	D	LOW – 28 Hz		837AM.dat	837AM.dat
8:40 AM	A	LOW – 28 Hz		840AM.dat	840AM.dat

NOTES:

- CMV calculated from CAN and UTEP's DAQ system.
- Trimble data provided by Caterpillar.
- Vibration mode determined as a function of the annotations, amplitude and frequency values showed on accelerometers records.

Table F-11. Data collected by the UTEP DAQ for July 25, 2017.

Section:	**Cell 188 (*Data collected will not be used for analysis, see observations*)**
Material:	**Subgrade – Clay**
IC Roller:	**CAT CS74B**

Computer Time	Line Pass	Vibration Amplitude Mode	Observation	UTEP DAQ Data Files: Accelerometer Folder: iX104	UTEP DAQ Data Files: Geophone Folder: CF19
2:30 PM	A	LOW – 28 Hz	Data collected using UTEP's 90W inverter for pressure cells.	230PM.dat	230PM.dat
2:32 PM	B	LOW – 28 Hz		232PM.dat	232PM.dat
2:34 PM	C	LOW – 28 Hz		234PM.dat	234PM.dat
2:36 PM	D	LOW – 28 Hz		236PM.dat	236PM.dat
2:38 PM	A	LOW – 28 Hz		238PM.dat	238PM.dat

NOTES:
- Power inverter was too noisy, data will not be used for analysis.
- Trimble data provided by Caterpillar.
- Vibration mode determined as a function of the annotations, amplitude and frequency values showed on accelerometers records.

Section:	**Cell 188 (*Data collected appropriately*)**
Material:	**Subgrade - Clay**
IC Roller:	**CAT CS74B**

Computer Time	Line Pass	Vibration Amplitude Mode	Observation	UTEP DAQ Data Files: Accelerometer Folder: iX104	UTEP DAQ Data Files: Geophone Folder: CF19
5:09 PM	A	LOW – 28 Hz	Data collected using MnROAD's van power inverter for pressure cells.	509PM.dat	509PM.dat
5:11 PM	B	LOW – 28 Hz		511PM.dat	511PM.dat
5:13 PM	C	LOW – 28 Hz		513PM.dat	513PM.dat
5:14 PM	D	LOW – 28 Hz		514PM.dat	515PM.dat
5:16 PM	A	LOW – 28 Hz		516PM.dat	516PM.dat

NOTES:
- CMV calculated from CAN and UTEP's DAQ system.
- Trimble data provided by Caterpillar.
- Vibration mode determined as a function of the annotations, amplitude and frequency values showed on accelerometers records.

Section:	**Cell 189**
Material:	**Subgrade - Clay**
IC Roller:	**CAT CS74B**

Computer Time	Line Pass	Vibration Amplitude Mode	Observation	UTEP DAQ Data Files: Accelerometer Folder: iX104	UTEP DAQ Data Files: Geophone Folder: CF19
4:26 PM	A	LOW – 28 Hz	Roller operator stopped vibration before end of section	426PM.dat	426PM.dat
4:28 PM	A	LOW – 28 Hz		428PM.dat	428PM.dat
4:30 PM	B	LOW – 28 Hz		430PM.dat	430PM.dat
4:33 PM	C	LOW – 28 Hz		433PM.dat	433PM.dat
4:35 PM	D	LOW – 28 Hz		435PM.dat	435PM.dat
4:37 PM	A	LOW – 28 Hz		437PM.dat	438PM.dat

NOTES:
- CMV calculated from CAN and UTEP's DAQ system.
- Trimble data provided by Caterpillar.
- Vibration mode determined as a function of the annotations, amplitude and frequency values showed on accelerometers records.

Table F-12. Data collected by the UTEP DAQ for August 1, 2017.

Section:	**Cell 185**
Material:	**300 mm (12 in.) Coarse RCA Base and 90 mm (3.5 in.) Select Granular Borrow on top of Sandy Subgrade**
IC Roller:	**CAT CS74B**

				UTEP DAQ Data Files	
Computer Time	**Line Pass**	**Vibration Amplitude Mode**	**Observation**	**Accelerometer Folder: iX104**	**Geophone Folder: CF19**
2:54 PM	A	LOW – 28 Hz		254PM.dat	254PM.dat
2:55 PM	B	LOW – 28 Hz		255PM.dat	255PM.dat
2:56 PM	C	LOW – 28 Hz		256PM.dat	256PM.dat
2:58 PM	D	LOW – 28 Hz		258PM.dat	258PM.dat
2:59 PM	A	LOW – 28 Hz		259PM.dat	259PM.dat

NOTES:

- CMV calculated from CAN and UTEP's DAQ system.
- Trimble data provided by Caterpillar.
- Vibration mode determined as a function of the annotations, amplitude and frequency values showed on accelerometers records.

Section:	**Cell 186**
Material:	**300 mm (12 in.) Fine RCA Base and 90 mm (3.5 in.) Select Granular Borrow on top of Sandy Subgrade**
IC Roller:	**CAT CS74B**

				UTEP DAQ Data Files	
Computer Time	**Line Pass**	**Vibration Amplitude Mode**	**Observation**	**Accelerometer Folder: iX104**	**Geophone Folder: CF19**
3:34 PM	A	LOW – 28 Hz	The power supply to the pressure cells was initially disconnected	334PM.dat	334PM.dat
3:35 PM	B	LOW – 28 Hz		335PM.dat	335PM.dat
3:37 PM	C	LOW – 28 Hz		337PM.dat	337PM.dat
3:38 PM	D	LOW – 28 Hz		338PM.dat	338PM.dat
3:40 PM	A	LOW – 28 Hz		340PM.dat	340PM.dat

NOTES:

- CMV calculated from CAN and UTEP's DAQ system.
- Trimble data provided by Caterpillar.
- Vibration mode determined as a function of the annotations, amplitude and frequency values showed on accelerometers records.

Table F-13. Data collected by the UTEP DAQ for August 2, 2017.

Section:	**Cell 188**				
Material:	**300 mm (12 in.) Limestone Aggregate Base Class 6 and 90 mm (3.5 in.) Select Granular Borrow on top of Clayey Subgrade**				
IC Roller:	**CAT CS74B**				
				UTEP DAQ Data Files	
Computer Time	**Line Pass**	**Vibration Amplitude Mode**	**Observation**	**Accelerometer Folder: iX104**	**Geophone Folder: CF19**
1:15 PM	A	LOW – 28 Hz		115PM.dat	115PM.dat
1:17 PM	B	LOW – 28 Hz		117PM.dat	117PM.dat
1:18 PM	C	LOW – 28 Hz		118PM.dat	118PM.dat
1:20 PM	D	LOW – 28 Hz		120PM.dat	120PM.dat
1:21 PM	A	LOW – 28 Hz		121PM.dat	121PM.dat
Section:	**Cell 189**				
Material:	**300 mm (12 in.) Recycled Aggregate Base Class 6 and 90 mm (3.5 in.) Select Granular Borrow on top of Clayey Subgrade**				
IC Roller:	**CAT CS74B**				
				UTEP DAQ Data Files	
Computer Time	**Line Pass**	**Vibration Amplitude Mode**	**Observation**	**Accelerometer Folder: iX104**	**Geophone Folder: CF19**
1:53 PM	A	LOW – 28 Hz		153PM.dat	153PM.dat
1:55 PM	B	LOW – 28 Hz		155PM.dat	155PM.dat
1:57 PM	C	LOW – 28 Hz		157PM.dat	157PM.dat
1:58 PM	D	LOW – 28 Hz		158PM.dat	158PM.dat
2:00 PM	A	LOW – 28 Hz		200PM.dat	200PM.dat

NOTES (for both Cells 188 and 189):

- CMV calculated from CAN and UTEP's DAQ system.
- Trimble data provided by Caterpillar.
- Vibration mode determined as a function of the annotations, amplitude and frequency values showed on accelerometers records.

Data Collected at MnROAD Construction Sites from July 20 through August 2, 2017

The following section presents the collected ICMV data and nondestructive spot tests at the MnROAD facility. Data reduction process for obtaining CMV from the accelerometer measurements are documented extensively as part of Appendix I of Phase I report and will be omitted here.

Comparison of Data Acquisition Systems ICMV

Figures F-15 and F-16 show the raw CMV data as collected by the Controller Area Network (CAN) for the communication between the roller's data acquisition components and the UTEP data acquisition system for both sandy and clayey subgrades. The CMV data are shown per line pass, all of them covering a distance of at least 65 m (210 ft). The CMV as collected by the CAN and the UTEP data acquisition system are almost identical. However, it must be pointed out that the amplitude of the UTEP calculated CMV data was adjusted by using a coefficient c = 400, instead of typical value of 300, in the calculation of CMV, shown in Equation F.1, to match the CAN's CMV magnitudes. CMV is defined as

$$CMV = c\frac{A_{2\Omega}}{A_{\Omega}}, \tag{F.1}$$

where A_{Ω} is the operating frequency and $A_{2\Omega}$ is the second harmonic of the operating frequency.

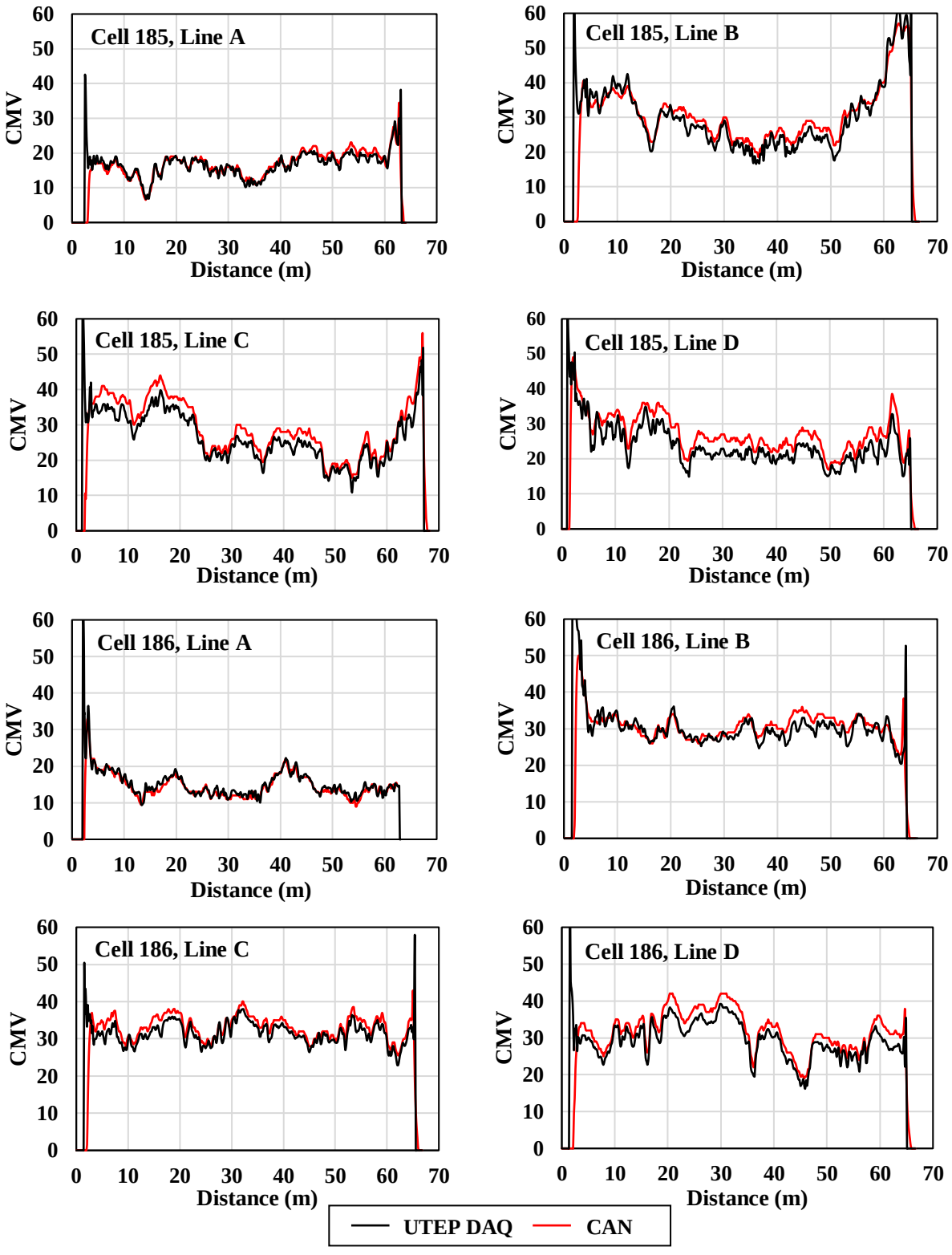

Figure F-15. CMVs as collected by the CAN and the UTEP DAQ system while proof mapping on sandy subgrade of Cells 185 and 186 along lines A through D.

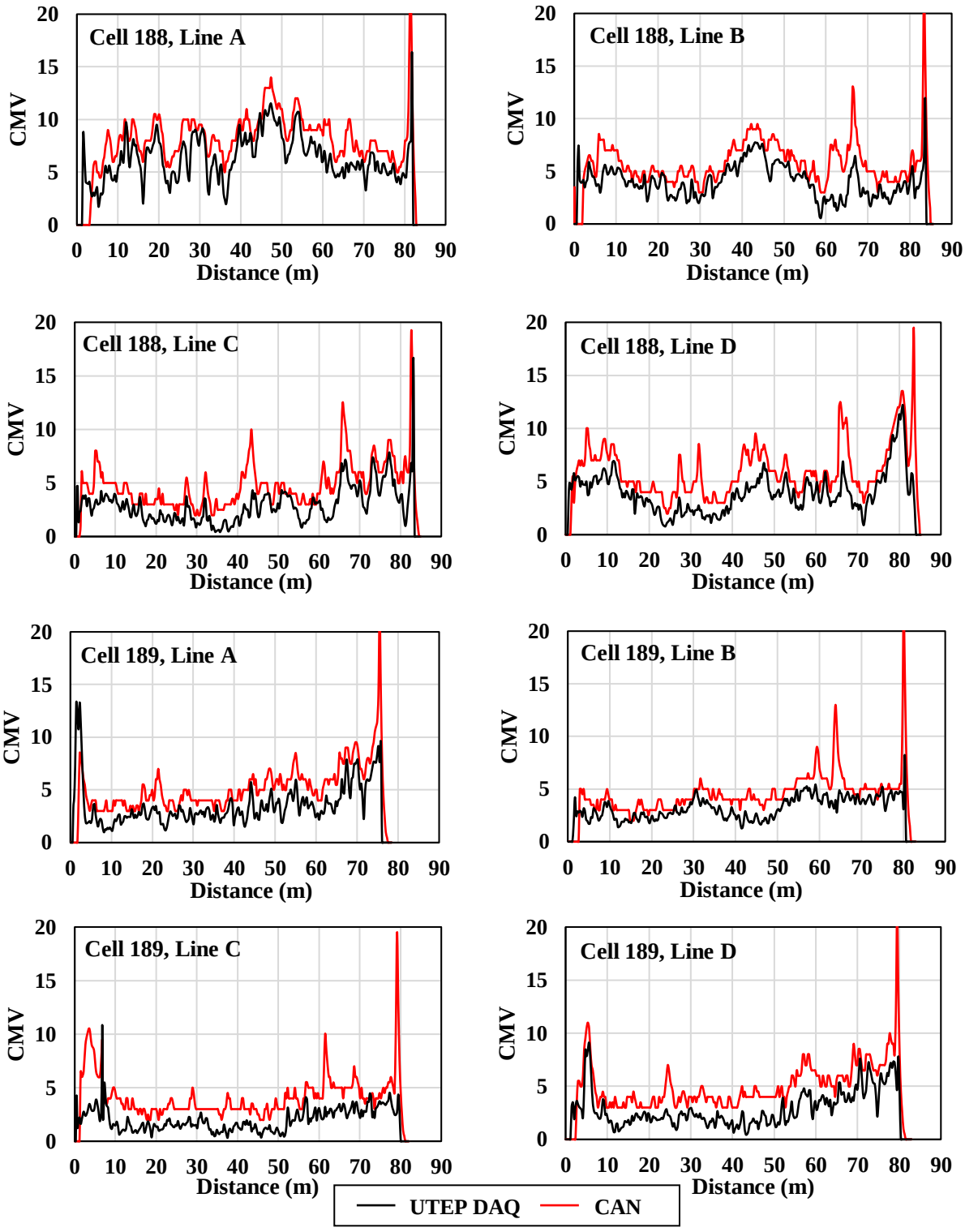

Figure F-16. CMVs as collected by the CAN and the UTEP DAQ system while proof mapping clayey subgrade of Cells 188 and 189 along Lines A through D.

Sandy subgrades exhibited higher CMVs than clayey subgrades. Moreover, higher CMVs are observed at the beginning and ending of the operation of the roller that is attributed to the roller's proof mapping at speeds and/or frequencies other than its required operating speed and frequency for a brief period.

Figures F-17 and F-18 show the raw CMV data as collected by the CAN and the UTEP DAQ for the flexible base on top of sandy and clayey subgrades, respectively. CMVs obtained on top of the flexible base were larger in magnitude than those obtained on their respective subgrades.

Mapping of ICMV

For mapping ICMV measurements, rectangular buffer areas around feature points defined by the geo-referenced spot test locations were established following the proposed test layout illustrated in Figure F-11. Figure F-19 shows the roller line passes through the rectangular buffer areas, as well as the number of ICMV measurement points per rectangular buffer area for each of the four cells in subgrade. ICMVs found within these buffered areas were averaged to obtain a representative ICMV for that block. This approach for discretizing the continuous collected CMV data allows a better comparison with the spot test measurements.

Figures F-20 through F-23 show the rectangular buffered areas averaged CMVs in a color-coded map, for the data acquired by the UTEP DAQ system on top of the subgrade and flexible base of the four cells. The descriptive statistics of the averaged CMVs and the coefficient of variation of CMVs within each rectangular buffer are also provided. The average operating frequency of the roller compactor and its speed for each block were also mapped and are provided next to the CMV map. Color-coded maps were created using the criteria shown in Table F-14 to compare the values obtained in each block for the IC data and the spot test measurements. Empty blocks are attributed to lack of or erroneous measurements.

Similar to what is shown in Figures F-15 through F-18, the sandy subgrade yielded higher CMVs than those obtained on clayey subgrade, as seen in Figures F-20 and F-21, respectively. Likewise, higher CMVs occurred on flexible bases laid on top of a sandy subgrade than on flexible bases on top of clayey subgrade, as shown in Figures F-22 and F-23, respectively. This can be attributed to the roller proof mapping compaction penetrating well into the subgrade.

The mapping of the frequency of vibration and the speed of the roller allows to better understand the CMV measurements and their variability. For instance, proof mapping on the subgrade was mostly performed uniformly with an operating frequency of 28 Hz; however, operating frequencies below 28 Hz were observed along some line passes during the proof mapping of the base material. This led to an increase in the variability of the measurements, as seen on the higher coefficient of variation of the CMV measurements in cells 185 and 186, in Figure F-22, and Cell 188, in Figure F-22. To reduce variability in the roller measurements, operating conditions must be adhere at the roller's recommended settings, i.e. operating frequency of 28 Hz and speed of about 5 km/h (3 mph).

Table F-14. Criterion for color-coded maps.

Color	Criterion for CMV, Frequency, Speed and LWD Modulus.	Criterion for the Mapping of Coefficient of Variation
Red	< 75% Mean	> 35%
Yellow	75% Mean – Mean	25% - 35%
Green	> Mean	> 25%

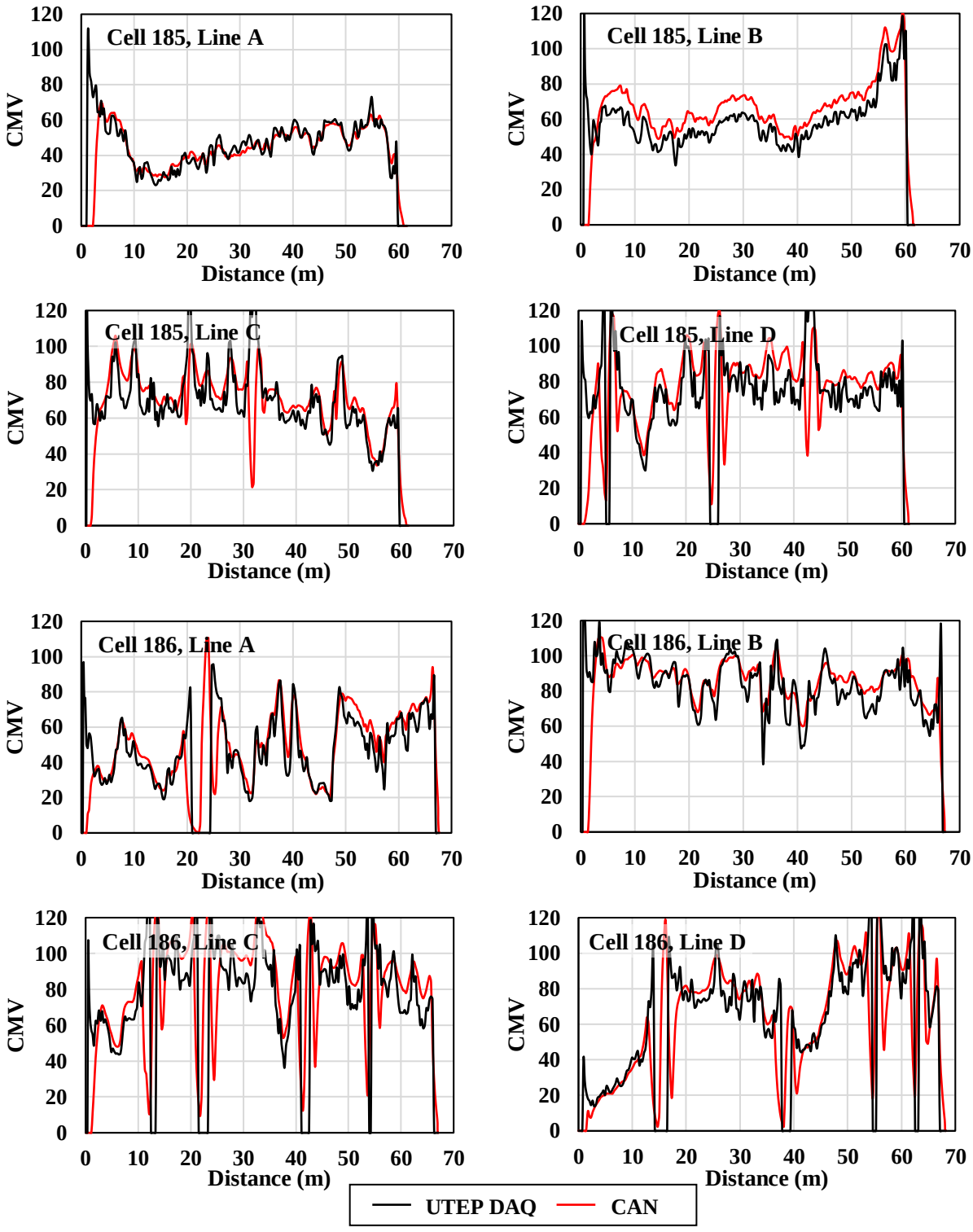

Figure F-17. CMVs as collected by the CAN and the UTEP DAQ system while proof mapping base layer on top of sandy subgrade of Cells 185 and 186 along lines A through D.

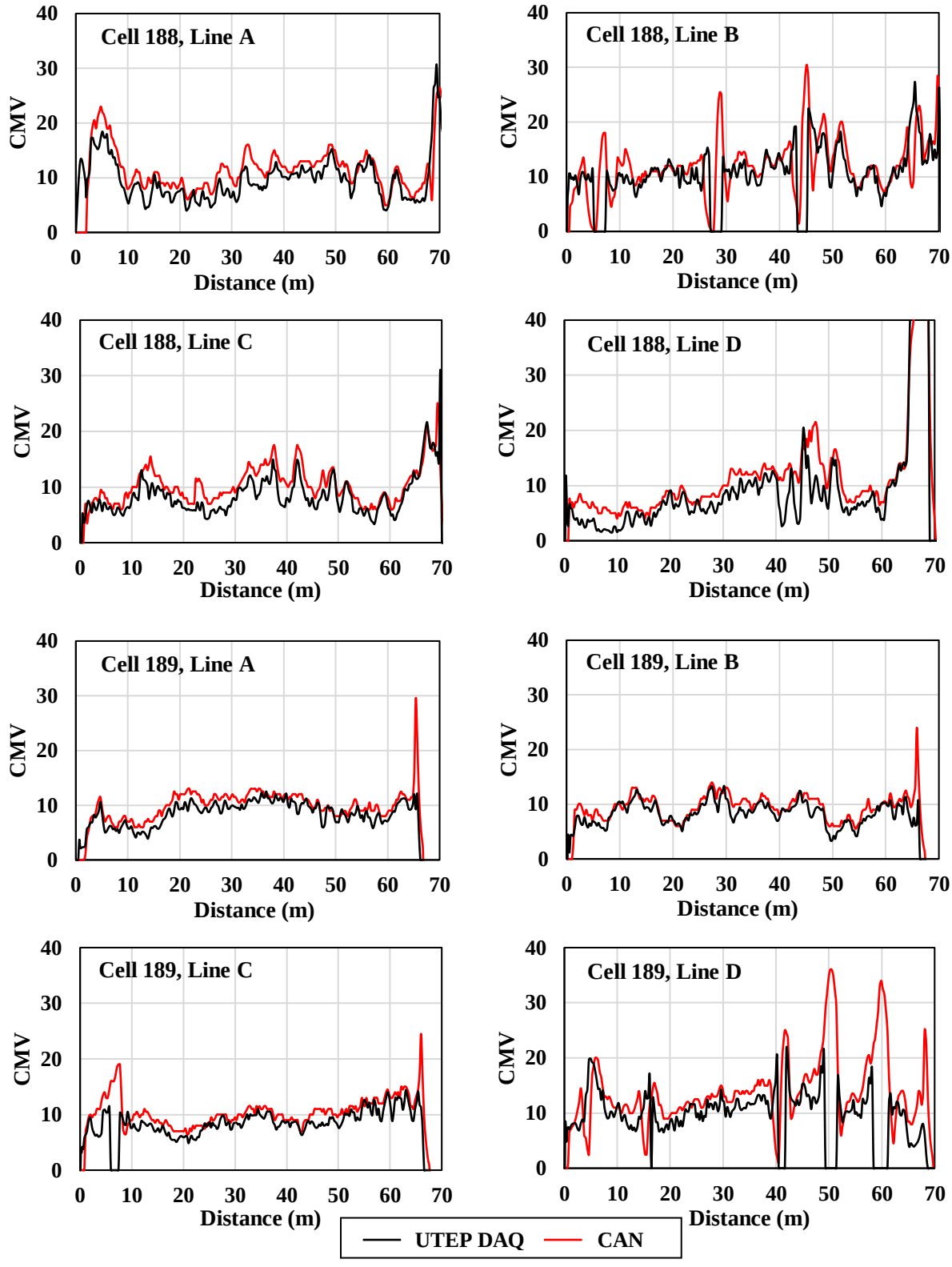

Figure F-18. CMVs as collected by the CAN and the UTEP DAQ system while proof mapping base layer on top of clayey subgrade of Cells 188 and 189 along lines A through D.

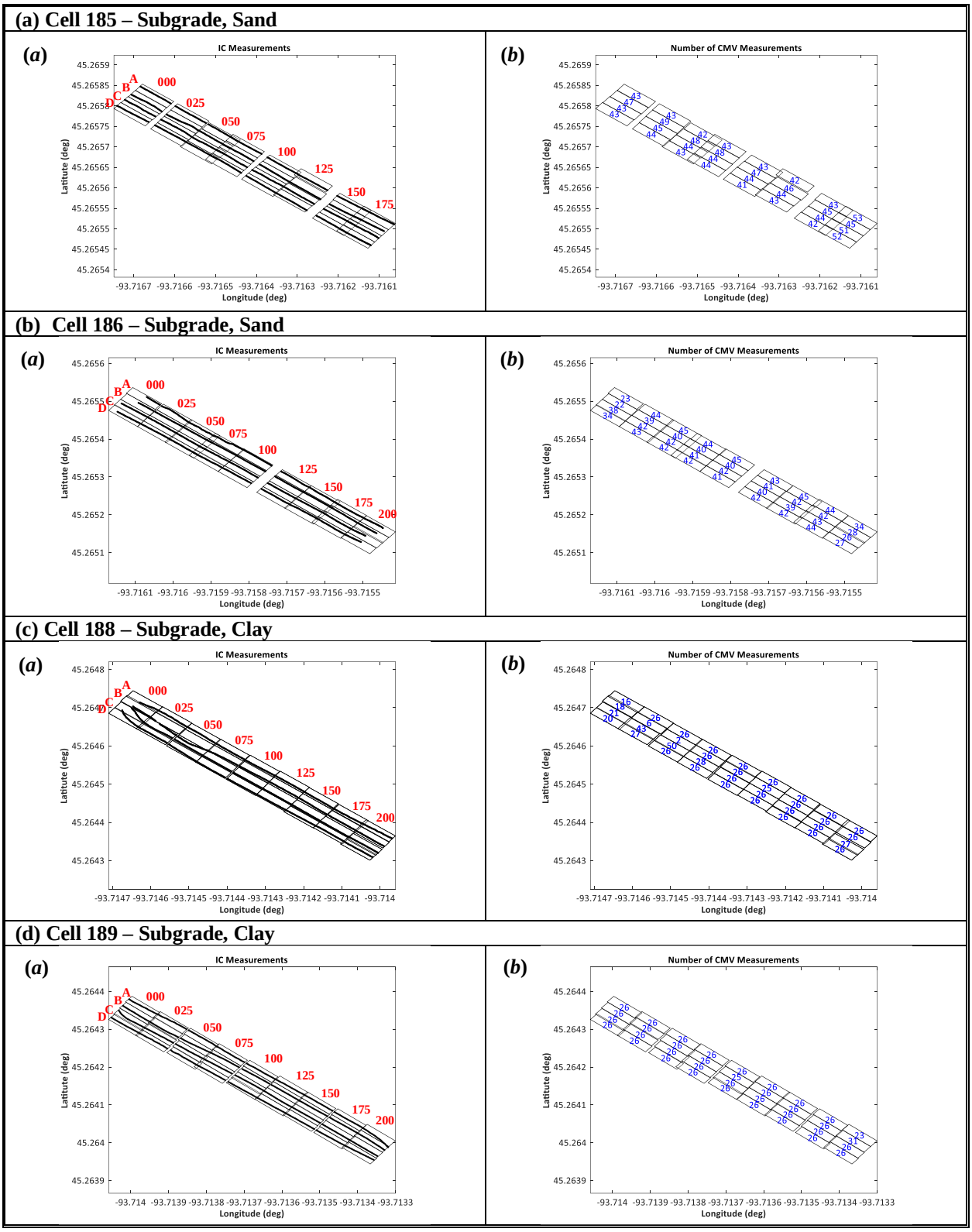

Figure F-19. Roller line passes and number of CMV measurements per rectangular buffer on subgrade on Cells 185, 186, 188, and 189.

Cell 185 – Subgrade, Sand

CMV Color Code

	13 – 17
	18 – 23
	24 – 42

Descriptive Statistics

Mean	24
Std. Deviation	7.2

Chainage

Chainage m	Chainage ft
0	0
7.5	25
15.0	50
22.5	75
30.0	100
37.5	125
45.0	150
52.5	175
60.0	200

CMV

D	C	B	A
23	24	42	19
18	18	25	17
22	23	23	16
21	23	21	13
22	23	25	15
23	28	29	15
27	33	37	14
31	34	38	14

Coefficient of Variation, %

D	C	B	A
18	21	23	7
11	17	16	7
8	12	10	10
7	11	12	14
4	9	11	9
19	18	8	15
15	11	9	10
15	6	20	33

Operating Frequency, Hz

D	C	B	A
28.3	28.3	28.3	28.3
28.3	28.3	28.3	28.3
28.3	28.3	28.3	28.3
28.3	28.3	28.3	28.3
28.3	28.3	28.3	28.3
28.3	28.3	28.3	28.3
28.3	28.3	28.3	28.3
27.8	28.3	27.5	28.1

Speed, mph

D	C	B	A
2.0	2.0	1.8	2.0
2.0	1.9	1.8	2.0
2.0	1.9	1.8	2.0
2.0	2.0	1.8	2.0
2.1	2.0	1.8	2.0
2.0	2.0	1.9	2.0
2.0	1.9	1.9	2.0
1.6	1.7	1.8	1.6

Cell 186 – Subgrade, Sand

CMV Color Code

	13 – 19
	20 – 26
	27 – 46

Descriptive Statistics

Mean	27
Std. Deviation	7

Chainage

Chainage m	Chainage ft
0	0
7.5	25
15.0	50
22.5	75
30.0	100
37.5	125
45.0	150
52.5	175
60.0	200

CMV

D	C	B	A
29	30	27	14
26	32	30	13
24	30	31	13
26	32	29	16
32	34	29	13
34	30	28	15
31	33	30	17
28	30	32	19
33	34	46	28

Coefficient of Variation, %

D	C	B	A
9	19	25	11
10	6	8	14
18	5	4	12
17	5	7	12
18	7	8	8
6	8	6	17
11	6	9	19
11	7	6	21
24	13	40	42

Operating Frequency, Hz

D	C	B	A
28.0	28.0	27.7	28.0
28.3	28.3	28.3	28.3
28.3	28.3	28.3	28.3
28.3	28.3	28.3	28.3
28.3	28.3	28.3	28.3
28.3	28.3	28.3	28.3
28.3	28.3	28.3	28.3
28.3	28.3	28.3	28.3
27.6	27.7	25.2	27.2

Speed, mph

D	C	B	A
2.0	2.0	2.1	1.8
2.0	2.0	2.2	1.9
2.0	2.1	2.2	2.0
2.1	2.1	2.2	2.0
2.0	2.1	2.2	1.9
2.0	2.1	2.1	2.0
2.0	2.2	2.0	1.9
2.0	2.0	2.0	1.9
1.7	1.6	2.0	1.6

Figure F-20. Spatial variation of (a) UTEP DAQ CMVs, (b) coefficient of variation of rectangular buffered areas CMVs, (c) operating frequency, and (d) IC roller speed on sandy subgrade on Cells 185 and 186.

Cell 188 – Subgrade, Clay

CMV Color Code

1.1 – 3.0
3.1 – 4.0
4.1 – 8.2

Descriptive Statistics
Mean 4.1
Std. Deviation 1.8

Chainage		CMV				Coefficient of Variation, %				Operating Frequency, Hz				Speed, mph			
m	ft	D	C	B	A	D	C	B	A	D	C	B	A	D	C	B	A
0	0	8.2	3.9	4.6	4.6	32	41	44	26	28.3	27.8	27.5	27.9	3.3	3.3	3.1	3.2
7.5	25	4.2	4.2	3.6	4.8	42	43	10	22	28.3	28.3	28.3	28.3	3.2	3.3	3.3	3.3
15.0	50	3.9	3.9	2.5	4.3	29	40	10	11	28.3	28.3	28.3	28.3	3.3	3.3	3.4	3.3
22.5	75	3.8	2.1	2.3	6.0	26	39	37	11	28.3	28.3	28.3	28.3	3.3	3.3	3.3	3.3
30.0	100	4.6	3.3	5.1	8.0	23	21	13	18	28.3	28.3	28.3	28.3	3.3	3.3	3.3	3.3
37.5	125	3.9	2.6	6.5	7.6	20	34	17	15	28.3	28.3	28.3	28.3	3.3	3.3	3.3	3.3
45.0	150	1.9	1.1	4.8	4.7	22	59	22	27	28.3	28.3	28.3	28.3	3.3	3.3	3.3	3.3
52.5	175	2.0	1.8	3.1	6.5	33	39	26	20	28.3	28.3	28.3	28.3	3.3	3.3	3.3	3.3
60.0	200	2.6	1.6	3.4	5.6	35	22	24	22	28.3	28.3	28.3	28.3	3.3	3.3	3.3	3.3

Cell 189 – Subgrade, Clay

CMV Color Code

1.2 – 2.0
2.1 – 2.6
2.7 – 8.8

Descriptive Statistics
Mean 2.7
Std. Deviation 1.1

Chainage		CMV				Coefficient of Variation, %				Operating Frequency, Hz				Speed, mph			
m	ft	D	C	B	A	D	C	B	A	D	C	B	A	D	C	B	A
0	0	3.6	3.2	4.3	5.5	17	19	12	22	28.3	28.3	28.3	28.3	3.3	3.4	3.3	3.3
7.5	25	4.8	3.0	4.1	4.3	18	14	9	27	28.3	28.3	28.3	28.3	3.3	3.3	3.3	3.3
15.0	50	4.2	2.5	4.3	3.7	26	25	15	20	28.3	28.3	28.3	28.3	3.3	3.3	3.3	3.3
22.5	75	3.3	1.3	3.8	2.0	28	52	21	34	28.3	28.3	28.3	28.3	3.3	3.3	3.3	3.3
30.0	100	2.0	1.3	2.0	1.5	23	33	19	42	28.3	28.3	28.3	28.3	3.3	3.3	3.3	3.3
37.5	125	2.8	1.2	2.8	1.7	23	49	19	24	28.3	28.3	28.3	28.3	3.3	3.3	3.3	3.3
45.0	150	3.0	1.7	3.5	2.1	26	22	18	26	28.3	28.3	28.3	28.3	3.3	3.3	3.3	3.3
52.5	175	2.5	1.3	2.4	2.1	22	28	12	15	28.3	28.3	28.3	28.3	3.3	3.3	3.3	3.3
60.0	200	2.1	1.3	2.3	1.4	43	41	24	29	28.2	28.3	28.3	28.3	3.3	3.3	3.3	3.3

Figure F-21. Spatial variation of (a) UTEP DAQ CMVs, (b) coefficient of variation of rectangular buffered areas CMVs, (c) operating frequency, and (d) IC roller speed on clayey subgrade on Cells 188 and 189.

Cell 185 – Coarse RCA Base on Top of Sandy Subgrade

CMV Color Code

	36 – 49
	50 – 65
	66 – 85

Descriptive Statistics

Mean	66
Std. Deviation	14

Chainage

Chainage	
m	ft
0	0
7.5	25
15.0	50
22.5	75
30.0	100
37.5	125
45.0	150
52.5	175
60.0	200

CMV

D	C	B	A
75	48	83	62
83	65	60	60
82	63	48	61
79	85	54	58
85	75	55	47
72	77	47	36
83	78	60	49
82	76	64	65

Coefficient of Variation, %

D	C	B	A
9	23	18	17
23	23	5	24
20	11	10	14
11	28	12	16
17	16	8	16
20	25	11	39
29	17	11	29
24	22	27	23

Operating Frequency, Hz

D	C	B	A
25.3	26.6	27.1	24.7
24.3	25.2	28.3	25.1
24.3	26.4	28.3	24.7
25.4	23.7	28.3	24.0
23.8	25.8	28.3	24.5
25.3	25.1	28.3	24.1
24.0	25.7	28.3	24.8
24.6	26.1	27.2	24.2

Speed, mph

D	C	B	A
3.2	3.2	3.3	3.3
3.2	3.2	3.3	3.3
3.3	3.3	3.2	3.3
3.2	3.3	3.3	3.3
3.3	3.3	3.1	3.3
3.3	3.2	3.3	3.3
3.3	3.3	3.2	3.3
3.1	3.0	2.8	3.1

Cell 186 – Fine RCA Base on Top of Sandy Subgrade

CMV Color Code

	35 – 56
	57 – 75
	76 – 100

Descriptive Statistics

Mean	75
Std. Deviation	19

Chainage

Chainage	
m	ft
0	0
7.5	25
15.0	50
22.5	75
30.0	100
37.5	125
45.0	150
52.5	175
60.0	200

CMV

D	C	B	A
73	71	68	89
87	85	51	98
86	76	57	94
95	78	34	74
81	76	56	67
96	89	59	78
98	82	42	81
91	94	35	57
57	97	42	

Coefficient of Variation, %

D	C	B	A
14	20	11	31
22	11	21	17
17	9	29	17
11	20	38	24
30	21	28	17
13	12	34	13
15	13	40	12
27	8	25	35
16	10	32	

Operating Frequency, Hz

D	C	B	A
25.1	26.0	27.6	23.2
24.9	27.1	28.3	23.5
24.7	28.3	28.3	24.5
24.1	28.3	27.9	25.4
25.5	27.7	26.4	25.6
24.8	28.3	24.3	26.1
25.0	28.3	25.4	24.6
24.8	28.3	26.7	24.1
28.1	27.3	26.3	

Speed, mph

D	C	B	A
3.3	3.3	3.3	3.5
3.3	3.3	3.3	3.3
3.3	3.3	3.3	3.4
3.3	3.3	3.3	3.2
3.3	3.3	3.3	3.5
3.4	3.3	3.3	3.5
3.3	3.3	3.4	3.3
3.3	3.3	3.3	3.2
3.1	3.2	3.2	

Figure F-22. Spatial variation of (a) UTEP DAQ CMVs, (b) coefficient of variation of rectangular buffered areas CMVs, (c) operating frequency and (d) IC roller speed on flexible base on sandy subgrade on cells 185 and 186.

Cell 188 – Limestone Aggregate Base Class 6 on Top of Clayey Subgrade

CMV Color Code

3 – 6
7 – 9
10 – 34

Descriptive Statistics

Mean 9.7
Std. Deviation 4.9

Chainage		CMV				Coefficient of Variation, %				Operating Frequency, Hz				Speed, mph			
m	ft	D	C	B	A	D	C	B	A	D	C	B	A	D	C	B	A
0	0	34	14	16	9	61	30	27	44	26.9	28.0	23.6	26.2	3.2	3.2	3.2	3.3
7.5	25	7	6	9	6	27	26	22	36	27.2	28.3	27.8	25.2	3.3	3.3	3.2	3.2
15.0	50	9	9	13	11	34	28	25	13	27.1	28.1	26.3	24.7	3.3	3.3	3.3	3.4
22.5	75	9	9	15	11	51	28	25	28	25.0	28.3	24.5	25.3	3.3	3.3	3.3	3.3
30.0	100	10	11	11	10	13	17	16	21	27.5	28.3	26.5	25.6	3.3	3.3	3.3	3.3
37.5	125	6	6	11	9	19	24	18	27	27.7	28.3	23.5	26.0	3.3	3.3	3.3	3.3
45.0	150	6	7	11	7	26	14	12	26	28.3	28.3	27.3	27.1	3.2	3.3	3.3	3.3
52.5	175	3	9	9	7	39	20	14	26	27.7	28.3	26.0	26.4	3.3	3.3	3.2	3.3
60.0	200	3	6	10	8	40	13	13	42	27.8	28.5	24.3	24.6	3.2	3.2	3.3	3.2

Cell 189 – Recycled Aggregate Base Class 6 on Top of Clayey Subgrade

CMV Color Code

5 – 7
8 – 9
10 – 13

Descriptive Statistics

Mean 9.8
Std. Deviation 2.2

Chainage		CMV				Coefficient of Variation, %				Operating Frequency, Hz				Speed, mph			
m	ft	D	C	B	A	D	C	B	A	D	C	B	A	D	C	B	A
0	0	9	12	8	14	39	16	21	19	24.3	27.4	27.1	27.3	3.3	3.3	3.3	3.2
7.5	25	12	11		9	19	15		13	22.1	27.5		27.8	3.3	3.3		3.3
15.0	50	12	8	5	11	29	21	22	10	22.8	28.1	28.3	28.3	3.3	3.3	3.3	3.3
22.5	75	14	8	9	13	19	9	15	20	23.3	28.3	28.3	26.1	3.3	3.3	3.3	3.3
30.0	100	10	9	10	13	12	12	14	15	28.3	28.3	27.6	26.7	3.3	3.3	3.3	3.3
37.5	125	10	9	11	13	15	19	11	4	26.9	28.1	27.9	28.3	3.3	3.3	3.3	3.3
45.0	150	9	7	7	12	19	19	16	8	24.5	28.1	28.3	28.1	3.3	3.3	3.3	3.3
52.5	175	10	8	10	7	25	12	11	20	24.7	25.1	28.3	25.1	3.3	3.3	3.3	3.3
60.0	200	12	7	7	9	33	34	21	29	23.8	24.8	27.9	24.0	3.4	3.0	3.4	3.5

Figure F-23. Spatial variation of (a) UTEP DAQ CMVs, (b) coefficient of variation of rectangular buffered areas CMVs, (c) operating frequency, and (d) IC roller speed on flexible base on top of clayey subgrade on Cells 188 and 189.

Relationship of ICMV with Modulus-Based Measurements

Figures F-24 through F-27 compares the rectangular buffer averaged CMVs with LWD and FWD moduli obtained at the spot test locations. The FWD moduli were calculated using the same equation for calculating the LWD moduli, by using the deflection directly under the load. Figures F-25 through F-27 show that the mapping of the LWD and FWD moduli are somewhat similar to the mapping of CMV measurements. For instance, for subgrade in cells 185 and 186, lower moduli occurred along Line A, which seem to be consistent with the representative CMVs, as mapped in Figure F-14.

Cell 185 – Subgrade, Sand

Color Code

< 75% of Average Measurement
75% of Average ≤ *x* < Average
≥ Average Measurement

Descriptive Statistics

NDT	Mean	Standard Deviation
CMV	24	7.2
LWD	4.3	1.0
FWD	5.3	1.5

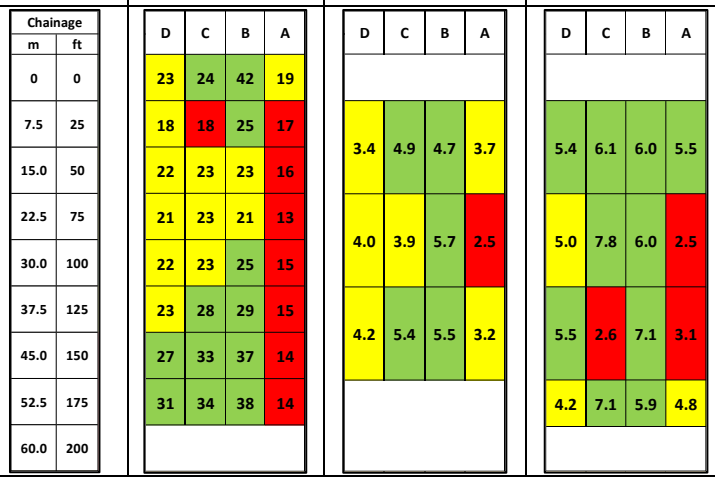

Cell 186 – Subgrade, Sand

Color Code

< 75% of Average Measurement
75% of Average ≤ *x* < Average
≥ Average Measurement

Descriptive Statistics

NDT	Mean	Standard Deviation
CMV	27	7.3
LWD	5.2	1.3
FWD	5.7	1.1

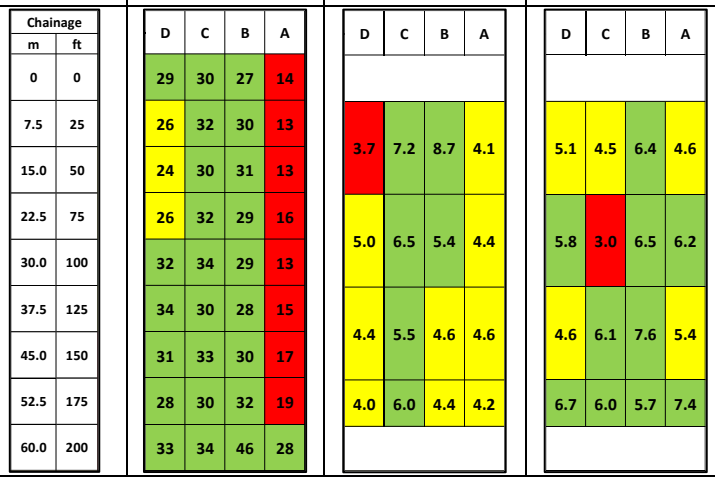

Figure F-24. Spatial variation of (a) UTEP DAQ CMVs, (b) LWD modulus, and (c) FWD modulus on sandy subgrade on Cells 185 and 186.

Cell 188 – Subgrade, Clay

Color Code

< 75% of Average Measurement
75% of Average ≤ *x* < Average
≥ Average Measurement

Descriptive Statistics

NDT	Mean	Standard Deviation
CMV	4.1	1.8
LWD	6.2	2.5
FWD	2.9	0.7

Chainage		CMV				LWD Modulus, ksi				FWD Modulus, ksi			
m	ft	D	C	B	A	D	C	B	A	D	C	B	A
0	0	8.2	3.9	4.6	4.6	8.5	8.4	3.8	9.0	4.2	4.1	2.7	3.3
7.5	25	4.2	4.2	3.6	4.8	6.0	12.5	5.9	8.5	3.7	5.1	3.3	3.2
15.0	50	3.9	3.9	2.5	4.3	6.2	8.5	5.0	5.4	3.0	3.9	3.4	2.8
22.5	75	3.8	2.1	2.3	6.0	7.6	7.8	4.4	7.2	2.2	2.9	2.2	3.4
30.0	100	4.6	3.3	5.1	8.0	10.2	8.2	6.8	8.8	1.9	3.6	2.4	2.4
37.5	125	3.9	2.6	6.5	7.6	2.9	5.3	6.0	8.1	2.0	3.3	3.3	2.6
45.0	150	1.9	1.1	4.8	4.7	1.6	4.2	4.4	6.7	2.1	2.0	2.1	2.7
52.5	175	2.0	1.8	3.1	6.5	8.8	3.7	3.7	5.6	2.7	2.3	2.5	3.5
60.0	200	2.6	1.6	3.4	5.6	1.3	3.6	2.4	6.7	2.6	2.2	2.3	3.3

Cell 189 – Subgrade, Clay

Color Code

< 75% of Average Measurement
75% of Average ≤ *x* < Average
≥ Average Measurement

Descriptive Statistics

NDT	Mean	Standard Deviation
CMV	2.7	1.1
LWD	3.8	1.7
FWD	2.3	0.3

Chainage		CMV				LWD Modulus, ksi				FWD Modulus, ksi			
m	ft	D	C	B	A	D	C	B	A	D	C	B	A
0	0	3.6	3.2	4.3	5.5	3.9	3.0	3.1	4.8	2.1	2.0	2.1	2.8
7.5	25	4.8	3.0	4.1	4.3	3.0	4.5	3.5	3.5	2.0	2.3	2.3	
15.0	50	4.2	2.5	4.3	3.7	2.1	3.8	2.8	5.6		2.3	2.1	2.5
22.5	75	3.3	1.3	3.8	2.0	6.5	2.6	2.2	6.1	2.6	2.1	2.2	
30.0	100	2.0	1.3	2.0	1.5	8.7	2.9	2.7	6.6	2.9	2.2	2.4	2.6
37.5	125	2.8	1.2	2.8	1.7	5.5	2.9	2.5	5.5	2.8	1.9	2.2	2.6
45.0	150	3.0	1.7	3.5	2.1	7.6	4.2	2.4	4.8	3.0	2.3	2.1	2.6
52.5	175	2.5	1.3	2.4	2.1	1.6	2.5	3.3	2.7	2.2	2.3	2.3	2.3
60.0	200	2.1	1.3	2.3	1.4	1.5	3.0	1.8	3.6	3.1	2.0	1.9	2.3

Figure F-25. Spatial variation of (a) UTEP DAQ CMVs, (b) LWD modulus, and (c) FWD modulus on clayey subgrade on Cells 188 and 189.

Cell 185 – Coarse RCA Base on Top of Sandy Subgrade

Color Code

< 75% of Average Measurement
75% of Average ≤ *x* < Average
≥ Average Measurement

Descriptive Statistics

NDT	Mean	Standard Deviation
CMV	66	14
LWD	9.0	1.1
FWD	10.0	2.5

Chainage		CMV				LWD Modulus, ksi				FWD Modulus, ksi			
m	ft	D	C	B	A	D	C	B	A	D	C	B	A
0	0	75	48	83	62	8.5	8.0	9.6	9.0	7.1	11.1	13.5	9.3
7.5	25	83	65	60	60	7.7	8.8	7.9	10.3	10.6	8.9	6.1	10.5
15.0	50	82	63	48	61	8.1	7.9	9.1	7.9	6.9	10.7	8.0	10.1
22.5	75	79	85	54	58	8.7	9.6	9.1	8.7	11.4	10.9	5.8	
30.0	100	85	75	55	47	8.9	8.9	10.7	7.5	12.6	13.3	12.3	7.5
37.5	125	72	77	47	36	7.7	8.9	9.0	8.4	7.4	10.9	16.6	7.8
45.0	150	83	78	60	49	9.9	9.9	12.2	9.8	12.4	12.3	10.4	12.6
52.5	175	82	76	64	65	8.0	10.9	9.3	8.0	8.6	9.6	8.3	6.4
60.0	200												

Cell 186 – Fine RCA Base on Top of Sandy Subgrade

Color Code

< 75% of Average Measurement
75% of Average ≤ *x* < Average
≥ Average Measurement

Descriptive Statistics

NDT	Mean	Standard Deviation
CMV	75	19
LWD	14.4	2.6
FWD	11.1	2.8

Chainage		CMV				LWD Modulus, ksi				FWD Modulus, ksi			
m	ft	D	C	B	A	D	C	B	A	D	C	B	A
0	0	73	71	68	89	16	13	12	14		12	7	9
7.5	25	87	85	51	98	13	21	10	17	10	17	6	13
15.0	50	86	76	57	94	16	17	15	14	12	15	12	7
22.5	75	95	78	34	74	15	21	10	17	14	15	6	
30.0	100	81	76	56	67	16	13	12	15	13	9	9	
37.5	125	96	89	59	78	12	17	12	16	8	11	12	12
45.0	150	98	82	42	81	13	13	13	12	11	11	12	12
52.5	175	91	94	35	57	11	18	14	14	7	11	11	12
60.0	200	57	97	42		13	12	15	13	9	11	6	

Figure F-26. Spatial variation of (a) UTEP DAQ CMVs, (b) LWD modulus, and (c) FWD modulus on flexible base on top of sandy subgrade on Cells 185 and 186.

Cell 188 – Limestone Aggregate Base Class 6 on Top of Clayey Subgrade

Color Code

< 75% of Average Measurement
75% of Average ≤ *x* < Average
≥ Average Measurement

Descriptive Statistics

NDT	Mean	Standard Deviation
CMV	9.7	4.9
LWD	11.3	2.3
FWD	7.2	1.8

Chainage		CMV				LWD Modulus, ksi				FWD Modulus, ksi			
m	ft	D	C	B	A	D	C	B	A	D	C	B	A
0	0	34	14	16	9	12.5	11.5	9.0	11.5	6.7	9.7	7.7	9.5
7.5	25	7	6	9	6	11.4	14.6	7.0	12.1	6.7	8.4	6.0	8.4
15.0	50	9	9	13	11	11.5	12.9	8.4	7.3	6.2	10.1	6.2	7.1
22.5	75	9	9	15	11	10.5	14.7	12.0	13.5	7.0	9.2	6.4	6.8
30.0	100	10	11	11	10	8.9	12.9	13.2	12.5	5.8	8.5	8.7	11.3
37.5	125	6	6	11	9	8.6	13.1	11.4	16.0	4.1	8.4	7.5	9.1
45.0	150	6	7	11	7	7.8	11.7	9.6	14.4	3.5	6.0	7.5	9.9
52.5	175	3	9	9	7	10.4	12.7	10.6	11.0	5.3	6.5	6.0	6.0
60.0	200	3	6	10	8	8.8	10.7	7.8	15.1	5.6		4.1	

Cell 189 – Recycled Aggregate Base Class 6 on Top of Clayey Subgrade

Color Code

< 75% of Average Measurement
75% of Average ≤ *x* < Average
≥ Average Measurement

Descriptive Statistics

NDT	Mean	Standard Deviation
CMV	9.8	2.2
LWD	9.7	2.3
FWD	6.2	5.9

Chainage		CMV				LWD Modulus, ksi				FWD Modulus, ksi			
m	ft	D	C	B	A	D	C	B	A	D	C	B	A
0	0	9	12	8	14	8.0	11.9	8.0	17.1	4.0	7.2	4.3	6.7
7.5	25	12	11		9	7.9	11.9	10.6	11.8	3.4	6.1	6.0	7.2
15.0	50	12	8	5	11	5.9	11.4	9.2	10.2	3.0	7.7	6.2	4.6
22.5	75	14	8	9	13	6.9	10.0	8.6	10.4	3.3	5.5	2.9	6.8
30.0	100	10	9	10	13	8.4	12.1	6.8	13.2	3.7	7.6	5.1	8.7
37.5	125	10	9	11	13	11.8	10.9	9.8	12.0	5.1	5.4	2.4	6.8
45.0	150	9	7	7	12	9.8	10.8	8.2	10.2	4.0	6.3	4.8	6.2
52.5	175	10	8	10	7	7.0	9.5	10.5	8.1	2.9	4.4	35.6	4.0
60.0	200	12	7	7	9	5.4	8.6	7.4	9.6		5.8	5.6	5.1

Figure F-27. Spatial variation of (a) UTEP DAQ CMVs, (b) LWD modulus, and (c) FWD modulus on flexible base on top of clayey subgrade on Cells 188 and 189.

Laboratory Test Results of Base and Subgrade Materials Collected at MnROAD Construction Sites

The engineering properties of six different materials used in the four MnROAD construction sites were determined in the laboratory for purpose of correlating the extracted mechanical properties of compacted geomaterials under field conditions and for calibration of the forward and backcalculation developed models for the estimation of mechanical properties. Samples of the evaluated geomaterials were retrieved from the four different cells, consisting of two subgrades: sand and clay; and four bases: coarse and find recycled concrete aggregates (RCA), limestone aggregate base Class 6 and recycled aggregate base Class 6. The four cells and their respective materials are described in Figure F-5. The tests performed on each geomaterial are listed on Table F-15.

Table F-15. Summary of tests conducted on sampled MnROAD materials.

Material		Sieve Analysis	Atterberg Limits	Moisture Density	Permanent Deformation	Resilient Modulus
Subgrade	Sand	✓	✓	✓	✓	✓
	Clay	✓	✓	✓	✓	✓
Base	Coarse RCA	✓	✓	✓	✓	✓
	Fine RCA	✓	✓	✓	✓	✓
	Limestone Aggregate Class 6	✓	✓	✓	✓	✓
	Recycled Aggregate Class 6	✓	✓	✓	✓	✓

Testing Methodology

Instrumentation

For conducting resilient modulus and permanent deformation tests on the specimens from sample materials, a servo-dynamic MTS® load unit system was used, as shown in Figure F-28(a). Its components are schematically shown in Figure F-28(b). A top actuator was used to apply the dynamic axial loading sequence to the tested specimens. In addition, a rigid triaxial cell was used. The load cell was placed inside the triaxial chamber to minimize the inaccurate load readings due to friction. Linear variable differential transformers (LVDTs) were used to measure deformations of the specimen.

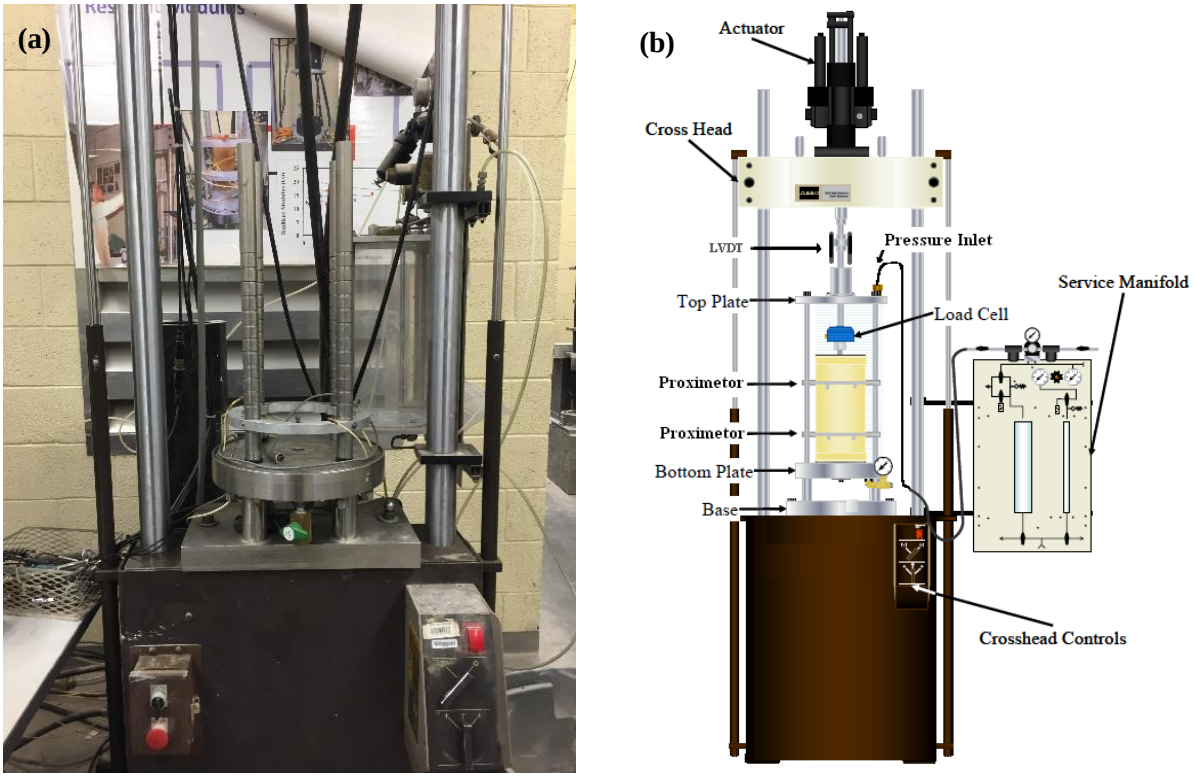

Figure F-28. (a) MTS® load unit system and (b) its components.

Specimen Preparation

Figure F-29 provides a flowchart of the activities involved in specimen preparation. These activities are further illustrated in Figure F-30. As a first step, the material was dried and mixed according to a specified gradation obtained from sieve analysis; water was added to achieve target moisture content. The soil-water mixture was allowed to mellow for 24 hours in a sealed container.

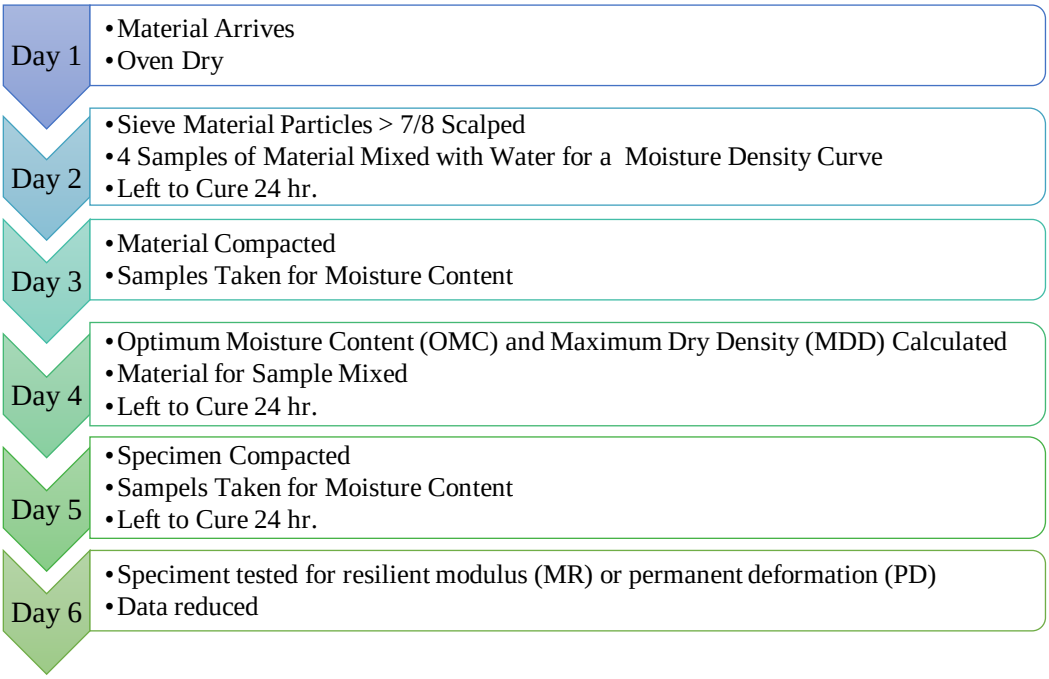

Figure F-29. Specimen preparation process.

For subgrade materials, 100 mm (4 in.) diameter and 200 mm (8 in.) high specimens were compacted following AASHTO T-99, while for base materials, 150 mm (6 in.) diameter and 300 mm (12 in.) high specimens were compacted following AASHTO T-180. The specimen was extruded, measured and weighed to determine its density and was mellowed for another 24 hours while covered with a membrane. The top and bottom platens were attached to the specimen using a Jade stone grout. After the grout cured, vacuum grease was applied to platens to avoid any air intrusion during testing. O-rings were used to seal the membrane.

Laboratory Results of Subgrade Materials

Index Tests

Sandy subgrade material corresponding to Cells 185 and 186 and clayey subgrade material corresponding to Cells 188 and 189 were sampled for laboratory testing. Figure F-31 shows the wet grain size distribution of each subgrade material. Table F-16 summarizes their Atterberg limits. According to the Unified Soil Classification System (USCS):

Sandy subgrade material in cells 185 and 186 was classified as poorly graded sand with non-plastic fines (SP-SM), and

Clayey subgrade material in cells 188 and 189 was classified as inorganic clay of low plasticity (CL) with a plasticity index (PI) of 14.

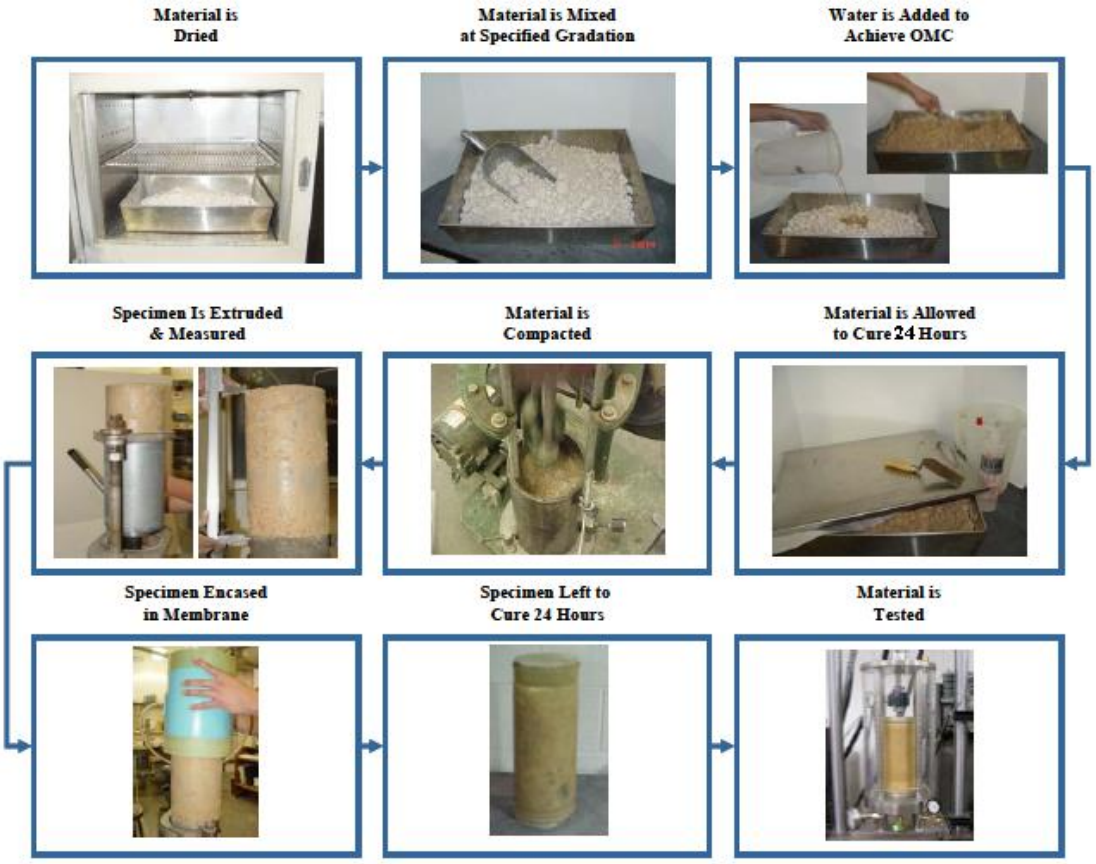

Figure F-30. Specimen preparation.

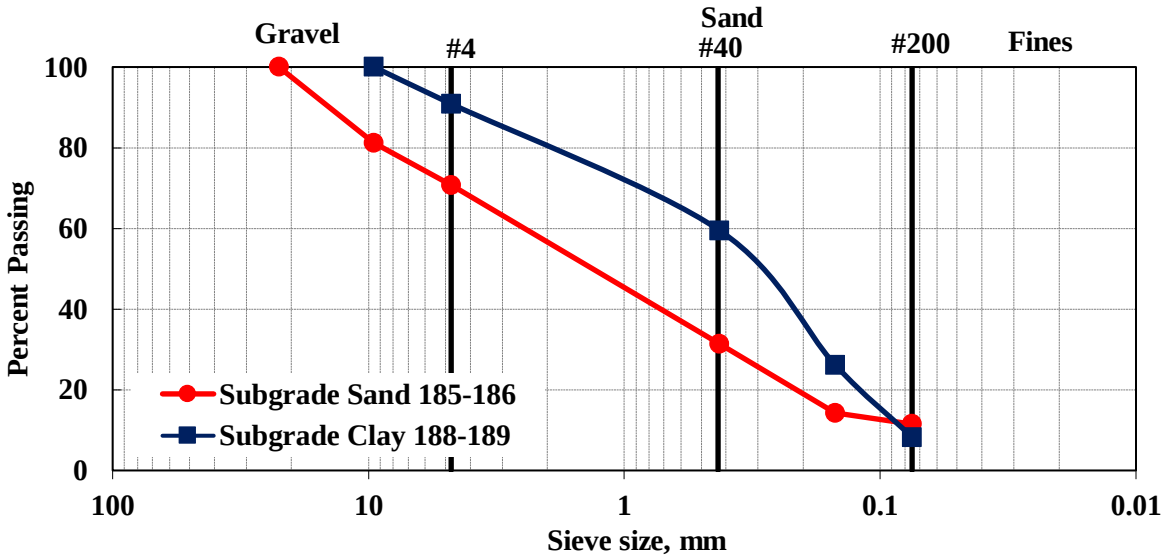

Figure F-31. Wet grain size distribution for subgrade materials.

Table F-16. Summary of Atterberg limits for subgrades in cells 185–186 and cells 188–189.

Property	Test Method	Cells 185–186	Cells 188–189
Liquid limit	AASHTO T 89	NP*	31
Plastic limit	AASHTO T 90	NP*	17
Plasticity index (PI)	AASHTO T 90	NP*	14
Liquid limit	AASHTO T 89	NP*	31

*NP: non-plastic

Figure F-32 shows the moisture-density curves for both subgrades as per AASHTO T-99. Table F-17 summarizes the optimum moisture contents (OMCs) and corresponding maximum dry densities (MDDs) for the sandy and clayey subgrades.

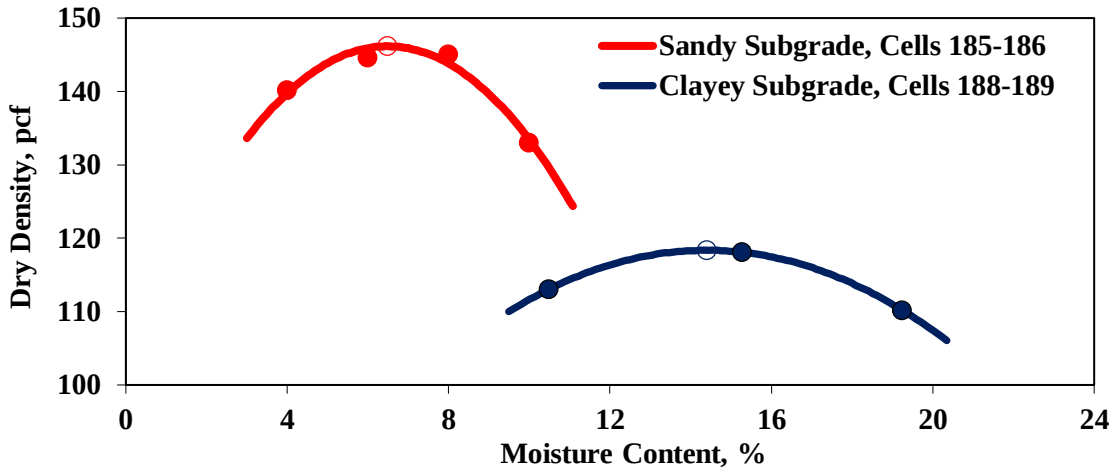

Figure F-32. Moisture density curves for subgrade materials.

Table F-17. Moisture content and maximum dry densities (MDDs) for subgrade materials.

Property	Subgrade Cells 185–186	Subgrade Cells 188–189
Optimum Moisture Content (OMC), %	6.5	14.4
Maximum Dry Density (MDD), pcf	146.2	118.4

Resilient Modulus Tests

Figure F-33 shows the resilient modulus test results for the sandy subgrade material (Figure F-33a) and for the clayey subgrade material (Figure F-33b) at OMC. Detailed laboratory results obtained from the testing of these two materials at different moisture contents are provided in Appendix H. Table F-18 summarizes the measured parameters from the resilient modulus tests performed as per AASHTO T-307 for both types of subgrade. The representative resilient modulus, *MR*, was obtained using the following relationship:

$$MR = k_1' P_a \left(\frac{\theta}{P_a} \right)^{k_2'} \left(\frac{\tau_{oct}}{P_a} + 1 \right)^{k_3'}, \quad \text{(F.2)}$$

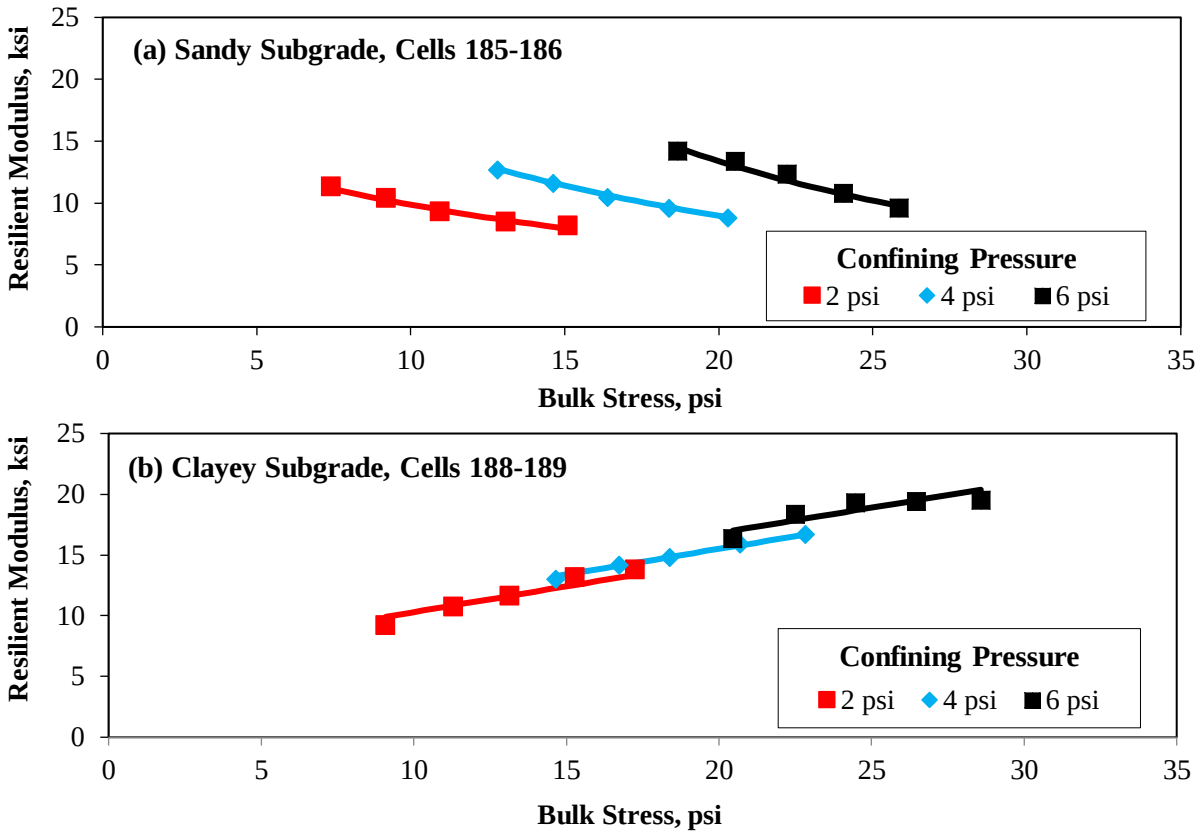

Figure F-33. Resilient modulus test for subgrade materials at OMC.

where k_1, k_2, and k_3 are the nonlinear parameters, P_a is the atmospheric pressure (14.7 psi), and θ and τ_{oct} are the bulk stress and octahedral shear stress, respectively.

The representative resilient modulus of the sandy subgrade of Cells 185 and 186 increased as the samples experienced an increase in moisture until the OMC was reached. The highest *MR* recorded for this material ranged from 11.1 ksi to 11.5 ksi. Specimens that were subjected to saturation conditions above the OMC showed a significant decrease in strength. Unlike the sandy subgrade material, the clayey subgrade of Cells 188 and 189 experienced a decrease in representative resilient modulus as the moisture condition of the specimens increased. At OMC-20%, the specimens exhibited the highest resilient modulus values of 13.8 ksi and 12.1 ksi.

Permanent Deformation

The permanent deformation tests for subgrade specimens were performed as part of the AASHTO T-307 conditioning cycles with a confining pressure of σ_c = 6 psi and a deviatoric stress of σ_d = 4 psi for 1000 cycles. Figure F-34 demonstrates the process of reducing the permanent deformation data. After the deformation is converted to strain, a power function was fitted to the results from cycle 200 onward. Using Equation F.3,

$$y = ax^b \ , \tag{F.3}$$

where the intercept a and slope b were determined. Rutting parameters α and μ are then calculated using Equations F.4 and F.5,

$$\alpha = \frac{ab}{\varepsilon_{res}}, \tag{F.4}$$

Table F-18. Resilient modulus results for Cells 185–186 and 188–189.

Material		Moisture Content, %	Dry Density, pcf	MEPDG Parameters				
				k_1	k_2	k_3	*MR*, ksi	R^2
Cells 185–186	OMC -2%	4.6	142.6	280	1.52	-0.19	10.0	0.98
	OMC -2%	4.9	139.3	299	1.58	-0.39	10.7	0.94
	OMC -1%	5.8	142.7	277	1.57	-0.05	10.5	0.83
	OMC -1%	5.2	142.1	283	1.7	-0.36	11.0	0.99
	OMC	6.7	145.3	355	1.39	-0.5	11.1	0.98
	OMC	6.4	144.4	349	1.43	-0.34	11.5	0.98
	OMC +1%	7.5	142.2	220	1.63	-0.05	8.6	0.93
	OMC +1%	7.8	142.1	220	1.8	-0.64	8.6	0.98
	OMC +2%	8.9	139.1	204	1.53	-0.33	7.1	0.92
	OMC +2%	8.8	138.7	169	1.92	-0.33	7.5	0.95
Cells 188–189	OMC -20%	10.4	114.9	909	0.33	-1.12	13.2	0.96
	OMC -20%	11.4	114.7	810	0.37	-1.13	12.1	0.96
	OMC -10%	13.6	116.8	797	0.42	-1.71	11.0	0.99
	OMC -10%	12.7	117.1	697	0.50	-1.15	11.2	0.98
	OMC	14.1	117.9	690	0.60	-2.51	9.1	0.99
	OMC	14.1	119.3	607	0.65	-2.66	8.1	0.98
	OMC +10%	15.6	116.2	540	0.71	-2.65	7.4	0.98
	OMC +10%	15.6	115.6	484	0.67	-2.11	7.2	0.95
	OMC +20%	17.6	114.3	135	1.21	-3.00	2.3	0.86
	OMC +20%	17.1	114.0	161	1.09	-3.00	2.6	0.89

Note: τ_{oct} and θ values of 3 psi and 12.4 psi for subgrade.

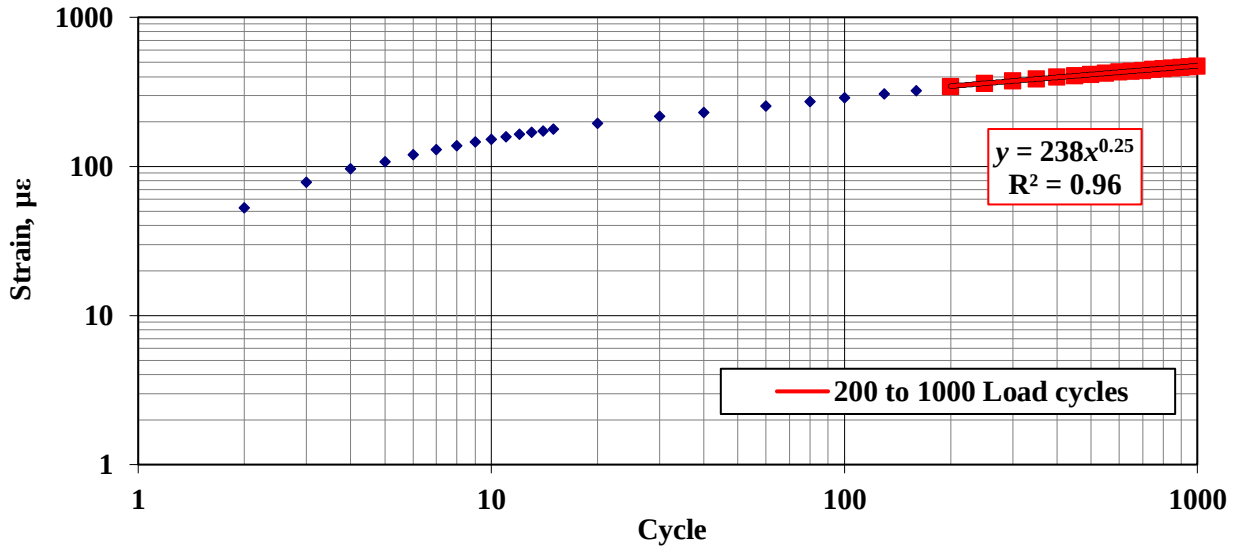

Figure F-34. Typical permanent deformation test results for Cells 185–186.

$$\mu = 1 - b \,. \tag{F.5}$$

Figure F-35 shows the results from the permanent deformation tests for the sandy subgrade of Cells 185–186 (Figure F-35[a]) and the clayey subgrade of Cells 188–189 (Figure F-35[b]), for each moisture content. Table F-19 summarizes the permanent deformations after 1000 cycles for subgrade in cells 185–186 and Cells 188–189.

The resilient strain, defined as the strain at the 200th cycle, ranged from nearly 200 με to 300 με for all tests except the wet specimens for Cells 188–189. On the other hand, both subgrade materials reached the highest permanent strain (1000th cycle) at wet conditions, i.e., at OMC +2% and OMC+20%, for the sandy and clayey subgrade materials, respectively.

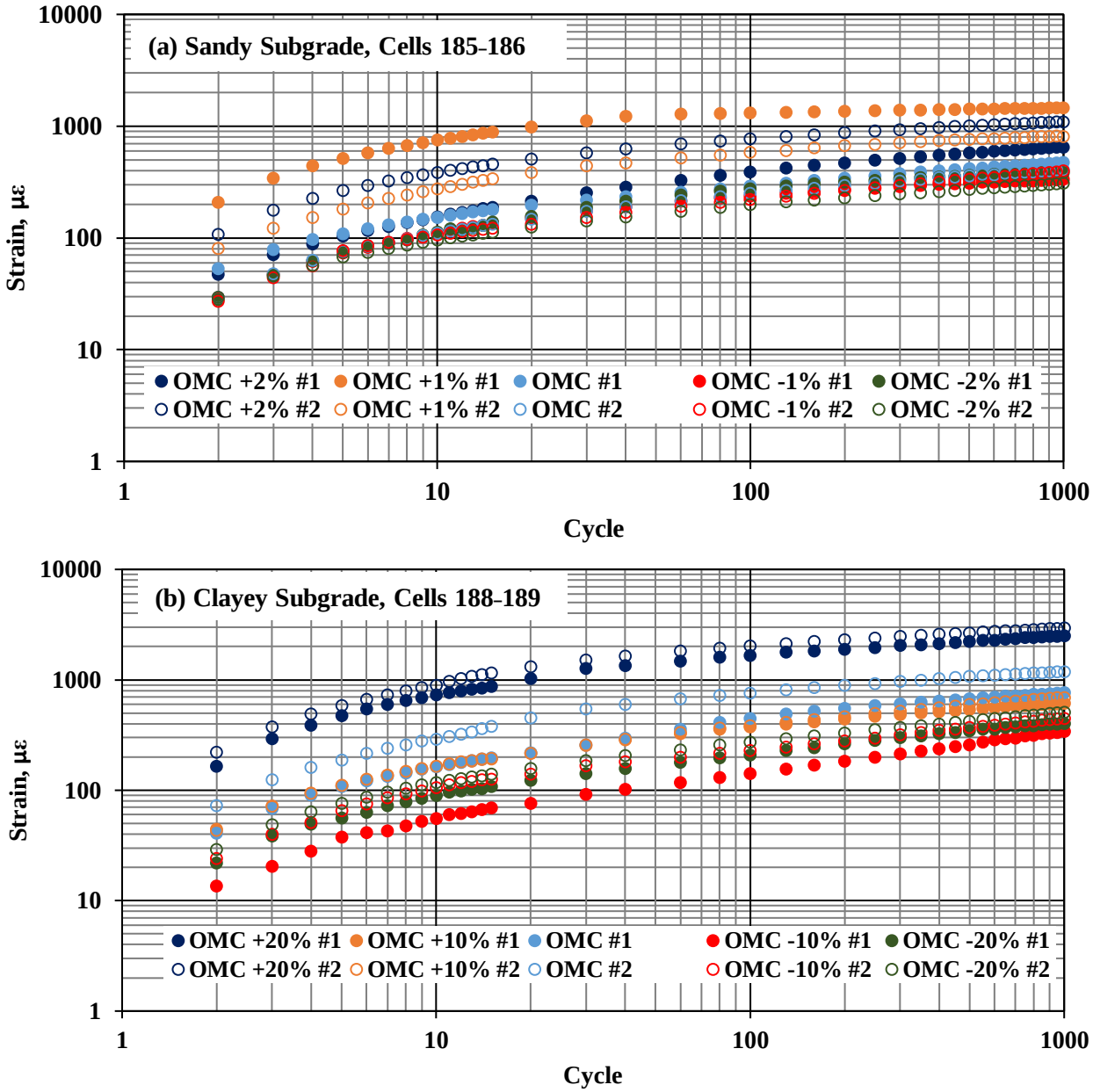

Figure F-35. Permanent deformation analysis results for subgrade material.

Table F-19. Permanent deformation laboratory results for subgrade materials.

Material		Moisture Content, %	Dry Density, pcf	Intercept *a*	Slope *b*	R^2	Resilient Strain ε_{res} ($\mu\varepsilon$)	Permanent Strain ε_{perm} ($\mu\varepsilon$)	Rutting Parameters	
									μ	α
Cells 185–186	OMC -2%	4.6	142.6	0.0002	0.12	0.98	189	382	0.11	0.88
	OMC -2%	4.9	139.3	0.0001	0.18	1.00	217	308	0.07	0.82
	OMC -1%	5.8	142.7	0.0001	0.13	0.99	187	335	0.09	0.87
	OMC -1%	5.2	142.1	0.0001	0.25	1.00	203	396	0.09	0.75
	OMC	6.7	145.3	0.0001	0.20	1.00	205	470	0.12	0.80
	OMC	6.4	144.4	0.0001	0.20	1.00	229	409	0.09	0.80
	OMC +1%	7.5	142.2	0.0011	0.04	1.00	202	1455	0.23	0.96
	OMC +1%	7.8	142.1	0.0004	0.12	0.98	241	809	0.18	0.88
	OMC +2%	8.9	139.1	0.0002	0.20	1.00	282	649	0.12	0.80
	OMC +2%	8.8	138.7	0.0004	0.14	0.99	274	1088	0.21	0.86
Cells 188–189	OMC -20%	10.4	114.9	0.00007	0.26	0.99	276	400	0.06	0.74
	OMC -20%	11.4	114.7	0.00008	0.27	1.00	233	505	0.09	0.73
	OMC -10%	13.6	116.8	0.00002	0.39	1.00	289	338	0.03	0.61
	OMC -10%	12.7	117.1	0.00006	0.29	1.00	289	444	0.06	0.71
	OMC	14.1	117.9	0.00019	0.20	1.00	286	766	0.14	0.80
	OMC	14.1	119.3	0.00035	0.18	0.99	318	1185	0.20	0.82
	OMC +10%	15.6	116.2	0.00015	0.20	1.00	280	613	0.11	0.80
	OMC +10%	15.6	115.6	0.00013	0.25	1.00	329	690	0.09	0.75
	OMC +20%	17.6	114.3	0.00075	0.18	1.00	591	2498	0.22	0.82
	OMC +20%	17.1	114	0.00105	0.15	1.00	753	2933	0.21	0.85

Laboratory Results of Base Materials

Index Tests

Four different base materials, designated as coarse recycled concrete aggregate (RCA), fine RCA, limestone aggregate Class 6 and reclaimed asphalt and concrete aggregate (RAP+RCA) Class 6, were also retrieved from MnROAD facility from Cells 185, 186, 188 and 189, respectively. Figure F-36 shows the grain size distribution of each base material.

According to the Unified Soil Classification System (USCS):

- base materials from Cells 185 and 188 were classified as well graded gravels (GW),
- base material from Cell 186 was classified as poorly graded sand (SP), and
- base material from Cell 189 was classified as poorly graded gravel (GP).

The Atterberg limits tests were performed on each geomaterial to obtain their plasticity indices. All four base materials were classified as non-plastic. Table F-20 summarizes the optimum moisture content (OMC) and maximum dry density (MDD) of the four base materials used in cells 185, 186, 188 and 189 following the AASHTO T-188 Specification.

Resilient Modulus

Resilient modulus tests were also carried out on duplicate specimens at five different moisture contents. Figure F-37 shows the resilient modulus test results for coarse RCA in Cell 185 at OMC. The laboratory results for other materials are included in Appendix H. Table F-21 summarizes all resilient modulus tests

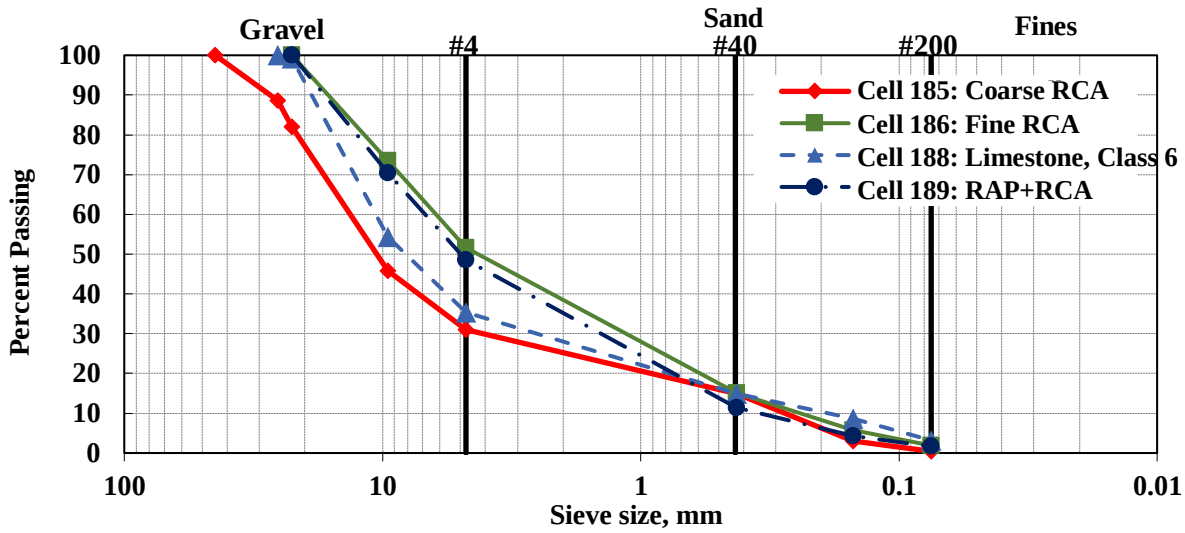

Figure F-36. Grain size distribution for base materials.

Table F-20. Optimum moisture content (OMC) and maximum dry density (MDD) of base materials.

Property	Cell 185	Cell 186	Cell 188	Cell 189
Optimum Moisture Content (OMC), %	10.5	10.9	6.6	10.5
Maximum Dry Density (MDD), pcf	122.5	120.9	142.6	122.9

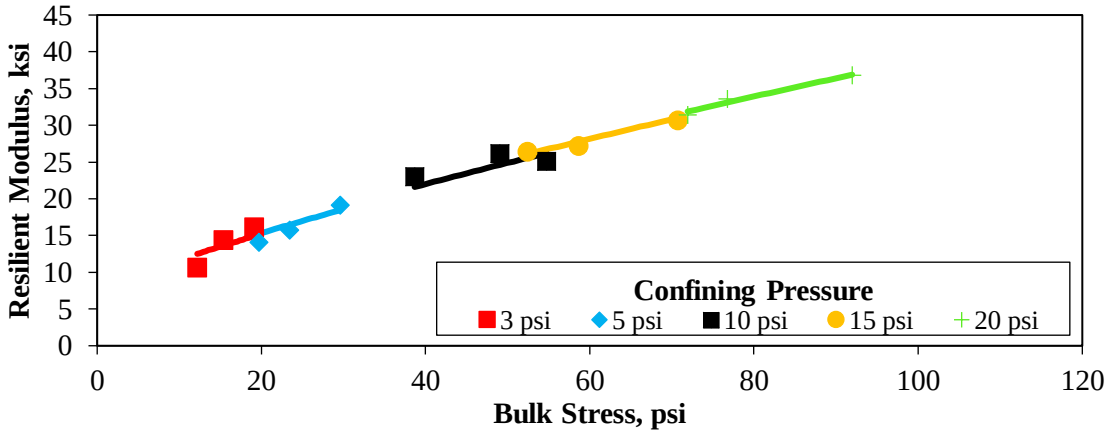

Figure F-37. Resilient modulus test results for coarse RCA base material in Cell 185.

of the four different bases. For all materials, the highest resilient modulus occurred at dry conditions, i.e. at moisture contents below the OMC. Resilient moduli decreased gradually as moisture increased.

Permanent Deformation

Table F-22 summarizes the permanent deformation laboratory results for each geomaterial. For the base materials of Cells 185 and 186, all moisture conditions were evaluated. For base materials of Cells 188 and 189, specimens prepared at OMC+2% experienced premature deformations.

Table F-21. Resilient modulus results for base materials.

Material		Moisture Content, %	Dry Density, pcf	MEPDG Parameters				
				k_1	k_2	k_3	*MR*, ksi	R^2
Cell 185	OMC -2%	8.8	119.1	394	0.90	-0.05	15.75	0.97
	OMC -2%	8.2	119.2	470	0.60	-0.05	13.37	0.67
	OMC -1%	9.5	121.1	611	0.79	-0.05	21.56	0.98
	OMC -1%	9.2	120.5	591	0.76	-0.05	20.15	0.98
	OMC	10.2	122.5	523	0.82	-0.06	19.01	0.98
	OMC	10.3	122.0	500	0.83	-0.07	18.31	0.99
	OMC +1%	11.6	121.7	459	0.82	-0.05	16.75	0.96
	OMC +1%	11.3	121.7	435	0.92	-0.19	16.79	0.99
	OMC +2%	12.7	120.5	466	0.70	-0.05	14.84	0.87
	OMC +2%	12.3	119.8	455	0.84	-0.05	16.99	0.99
Cell 186	OMC -2%	8.9	119.0	682	0.8	-0.22	22.69	0.99
	OMC -2%	9.3	119.2	800	0.63	-0.09	23.15	0.97
	OMC -1%	10.2	120.5	578	0.54	-0.05	15.36	0.58
	OMC -1%	10.3	119.6	514	0.75	-0.05	17.33	0.99
	OMC	10.8	121.4	499	0.83	-0.05	18.42	0.99
	OMC	11.1	121.0	469	0.88	-0.07	18.17	0.99
	OMC +1%	12.0	119.9	441	0.64	-0.05	13.12	0.89
	OMC +1%	11.8	120.4	427	0.8	-0.05	15.24	0.92
	OMC +2%	13.2	119.9	510	0.63	-0.05	15.01	0.83
	OMC +2%	13.1	118.9	501	0.64	-0.05	14.91	0.73
Cell 188	OMC -2%	4.9	138.4	544	0.8	-0.10	19.01	0.98
	OMC -2%	4.9	138.5	553	0.83	-0.12	19.83	0.98
	OMC -1%	5.8	139.7	552	0.54	-0.05	14.67	0.59
	OMC -1%	5.7	139.2	484	0.74	-0.05	16.13	0.92
	OMC	6.3	141.3	501	0.57	-0.05	13.77	0.76
	OMC	6.6	142.3	499	0.63	-0.05	14.68	0.54
	OMC +1%	7.8	140.1	419	0.55	-0.05	11.26	0.71
	OMC +1%	7.9	140.4	397	0.70	-0.05	12.65	0.76
	OMC +2%	Too Wet to Test						
	OMC +2%							
Cell 189	OMC -2%	7.9	119.9	444	0.96	-0.06	18.92	0.99
	OMC -2%	8.2	119.0	421	0.87	-0.05	16.26	0.98
	OMC -1%	9.6	121.8	531	0.90	-0.16	20.28	0.99
	OMC -1%	9.6	122.1	668	0.70	-0.05	21.28	0.97
	OMC	10.6	122.8	418	0.96	-0.14	17.23	0.99
	OMC	10.8	123.0	398	0.97	-0.10	16.87	0.99
	OMC +1%	11.3	121.5	315	0.94	-0.08	13.01	0.98
	OMC +1%	11.2	121.9	327	0.94	-0.05	13.68	0.94
	OMC +2%	Too Wet to Test						
	OMC +2%							

Note: τ_{oct} and θ values of 7.5 psi and 31 psi for base.

Table F-22. Permanent deformation results for base materials.

Material		Moisture Content, %	Dry Density, pcf	Intercept *a*	Slope *b*	R^2	Resilient Strain ε_{res} ($\mu\varepsilon$)	Permanent Strain ε_{perm} ($\mu\varepsilon$)	Rutting Parameters	
									μ	α
Cell 185	OMC -2%	8.8	119.1	0.0004	0.16	0.98	380	1082	0.15	0.84
	OMC -2%	8.2	119.2	0.0002	0.30	0.94	480	1898	0.14	0.70
	OMC -1%	9.5	121.1	0.0004	0.11	0.94	530	831	0.08	0.89
	OMC -1%	9.23	120.5	0.0005	0.13	1.00	432	1312	0.16	0.87
	OMC	10.2	122.5	0.0003	0.15	0.99	393	994	0.13	0.85
	OMC	10.3	122.0	0.0006	0.11	0.97	448	1139	0.13	0.89
	OMC +1%	11.6	121.7	0.0004	0.17	0.99	478	1367	0.15	0.83
	OMC +1%	11.3	121.7	0.0003	0.17	0.99	437	894	0.11	0.83
	OMC +2%	12.7	120.5	0.0000	0.64	0.95	588	3058	0.04	0.36
	OMC +2%	12.3	119.8	0.0006	0.12	1.00	565	1487	0.14	0.88
Cell 186	OMC -2%	8.9	119.0	0.0003	0.12	1.00	378	782	0.11	0.88
	OMC -2%	9.3	119.2	0.0004	0.12	1.00	342	882	0.13	0.88
	OMC -1%	10.2	120.5	0.0007	0.12	1.00	431	1602	0.19	0.88
	OMC -1%	10.3	119.6	0.0001	0.46	0.96	515	2954	0.10	0.54
	OMC	10.8	121.4	0.0004	0.13	1.00	409	966	0.13	0.87
	OMC	11.1	121.0	0.0007	0.15	1.00	493	1822	0.20	0.85
	OMC +1%	12.0	119.9	0.0007	0.18	1.00	615	2336	0.20	0.82
	OMC +1%	11.8	120.4	0.0009	0.18	0.99	700	3090	0.23	0.82
	OMC +2%	13.2	119.9	0.0009	0.16	0.98	525	2836	0.29	0.84
	OMC +2%	13.1	118.9	0.0005	0.31	1.00	655	3818	0.21	0.69
Cell 188	OMC -2%	4.9	138.4	0.0003	0.24	1.00	410	1689	0.19	0.76
	OMC -2%	4.9	138.5	0.0004	0.17	0.99	396	1137	0.15	0.83
	OMC -1%	5.8	139.7	0.0002	0.47	1.00	751	6468	0.15	0.53
	OMC -1%	5.68	139.2	0.0003	0.32	1.00	588	3030	0.18	0.68
	OMC	6.3	141.3	0.0004	0.34	0.99	744	4754	0.20	0.66
	OMC	6.58	142.3	0.0006	0.45	1.00	856	13724	0.32	0.55
	OMC +1%	7.8	140.1	0.0005	0.45	1.00	995	11489	0.23	0.55
	OMC +1%	7.9	140.4	0.0004	0.46	1.00	847	8814	0.20	0.54
	OMC +2%	Too Wet to Test								
	OMC +2%									
Cell 189	OMC -2%	7.9	119.9	0.0008	0.12	1.00	408	1833	0.24	0.88
	OMC -2%	8.2	119.0	0.0008	0.13	1.00	423	1939	0.24	0.87
	OMC -1%	9.6	121.8	0.0006	0.15	0.99	412	1667	0.22	0.85
	OMC -1%	9.6	122.1	0.0002	0.30	0.98	391	1844	0.17	0.70
	OMC	10.6	122.8	0.0006	0.17	1.00	457	2000	0.23	0.83
	OMC	10.8	123.0	0.0011	0.13	0.96	482	2797	0.31	0.87
	OMC +1%	11.3	121.5	0.0012	0.15	1.00	489	3227	0.35	0.85
	OMC +1%	11.2	121.9	0.0014	0.12	0.99	601	3288	0.29	0.88
	OMC +2%	Too Wet to Test								
	OMC +2%									

Note: τ_{oct} and θ values of 7.5 psi and 31 psi for base.

APPENDIX G

Calibration of Models using Field Data

Introduction

Appendix G introduces the calibration procedure for adjusting the relationships between the numerical forward models described in Appendix D and collected field measurements similar to those described in Appendix F. Table G-1 lists the four test sites that were used for the calibration of the forward models. The dataset from Site 1 was collected in 2014 during an FHWA "Every Day Counts" (EDC-2) project entitled "National Deployment of Intelligent Compaction."

Table G-1. Field test sites.

Site	Location	Date	Layer	Dimensions
1	Cleburne, TX	April 17–19, 2014	Clayey subgrade on top of existing embankment	150 m (500 ft) long and 7.5 m (25 ft) wide test section
2	MnROAD Facility	July 20–25, 2017	Cells 185 and 186: sandy subgrade	70 m (226.5 ft) long test section
			Cell 188 and 189: clayey subgrade	
		August 1–2, 2017	Cell 185: 300 mm (12-in.) thick coarse recycled concrete aggregate (RCA) base on top of sandy subgrade	
			Cell 186: 300 mm (12-in.) thick fine RCA base on top of sandy subgrade	
			Cell 188: 300 mm (12-in.) thick limestone aggregate base class 6 on top of clayey subgrade	
			Cell 189: 300 mm (12-in.) thick recycled aggregate base class 6 on top of clayey subgrade	

The LWD moduli measured on top of the subgrade at each site was used as the initial input for simulation of the responses using the linear elastic static FE (SSL) model. Base moduli were backcalculated using the LWD deflections on top of the base and subgrade using an iterative process. The static stationary nonlinear FE (SSN) model then collaborates with the measured field data. The nonlinear k' parameters (determined from fitting the laboratory data to the modified MEPDG model) were introduced to the simulated geosystems. Finally, to more realistically simulate the mapping process and to improve the adjustment factor derived from the comparison of pavement responses obtained from the simulated drum-soil system and corresponding measured field data, vibration was designated to the simulated stationary drum. Table G-2 lists the geomaterial properties of the pavement structures corresponding to the test sites listed in Table G-1. The analysis for calibration purposes from the four test sites is summarized in the following sections.

Table G-2. Geomaterial properties of test sections.

Site	Location		Layer	Properties of Geomaterial					
				Resilient Modulus Results (Modified MEPDG Model)				In-situ Test	
				k'_1	k'_2	k'_3	M_R	E_{LWD}	Modulus*
1	Cleburne, TX		Subgrade	269	0.54	-3	21 MPa (3.1 ksi)	41.8 MPa (6.1 ksi)	---
2	MnROAD	Cell 185	Subgrade	335	1.6	-0.6	79 MPa (12 ksi)	29 MPa (4.3 ksi)	---
			Base	512	0.8	-0.1	129 MPa (19 ksi)	63 MPa (9 ksi)	117 MPa (17 ksi)
		Cell 186	Subgrade	335	1.6	-0.6	79 MPa (12 ksi)	36 MPa (5.2 ksi)	---
			Base	484	0.9	-0.1	126 MPa (18 ksi)	99 MPa (14 ksi)	193 MPa (28 ksi)
		Cell 188	Subgrade	649	0.6	-2.6	59 MPa (8.6 ksi)	43 MPa (6.2 ksi)	---
			Base	500	0.6	-0.1	98 MPa (14.2 ksi)	78 MPa (11.3 ksi)	138 MPa (20 ksi)
		Cell 189	Subgrade	649	0.6	-2.6	59 MPa (8.6 ksi)	26.3 MPa (3.8 ksi)	---
			Base	408	0.9	-0.1	118 MPa (17.1 ksi)	67 MPa (9.7 ksi)	134 MPa (19 ksi)

* Base modulus backcalculated using LWD moduli measured on top of base and subgrade surface.

† Base layer placed on top of stiff subgrade.

Site 1

The first step toward the calibration of the FE model consisted of using the measurements collected by in-ground sensors on a test section near Cleburne, Texas, during the third week of November 2014. The summary of the activities, instrumentation, and calibration results are discussed in the following sections.

The site was located at the junction of US 67-Business and County Road 801B near Cleburne, Texas, as shown in Figure G-1(a). This study focused on pre-mapping the existing embankment and the proof-mapping of a 300 mm (12 in.) compacted clayey subgrade layer. A 150 m (500 ft) long and 7.5 m (25 ft) wide test section was selected on the east bound frontage road to perform the IC data collection as shown in Figure G-1(b).

Caterpillar (CAT), Wirtgen Group-Hamm (HAMM) and Sakai America (SAKAI) participated in this study. Table G-3 summarizes the specifications of the three vibratory rollers utilized in the test section.

The vibration data were collected in the following two conditions:

- Vibratory Stationary at the embedded sensors under the following settings:
  - Low frequency and low amplitude
  - Low frequency and high amplitude
- Vibratory Moving data were recorded by moving the rollers a total distance of 30 m (100 ft), starting 15 m (50 ft) before and ending 15 m (50 ft) after the location of the embedded geophones, as shown in Figure G-2.

The data reduction process for obtaining CMV from the accelerometer measurements, which were documented extensively as part of Appendix I of Phase I report, are omitted here.

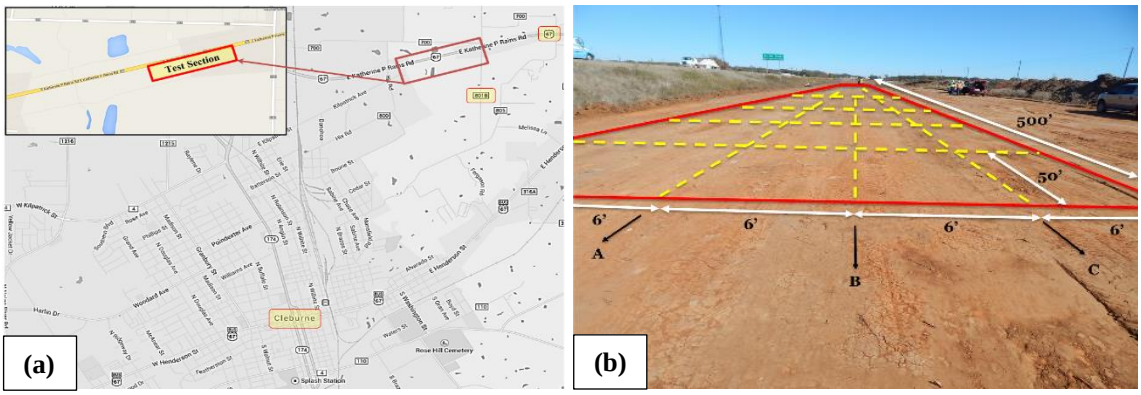

Figure G-1. Location of (a) test site near Cleburne, Texas, and (b) test grid.

Table G-3. Specifications of IC rollers used in Site 1 testing location at US-67, Cleburne, Texas.

Vendor/ Manufacturer	Caterpillar	SAKAI	HAMM/Wirtgen
			
Model	Single-drum IC roller with a padfoot shell kit - CS74B	Single-drum padfoot IC roller (with smooth drum shell kit) - SV540T	HD120 Vibratory Smooth Drum Roller
Compaction Width	2.1 m (82 in.)	2.1 m (82 in.)	2.1 m (82 in.)
Operating Weight	157 kN (35,300 lb)	109 kN (24,500 lb)	110 kN (24,700 lb)
Centrifugal Force	166 – 332 kN (37,300 lb – 74,600 lb)	172 – 255 kN (38,600 lb – 57,300 lb)	171– 246 kN (38,400 lb – 55,300 lb)
Nominal Amplitude	0.99 – 2.1 mm (0.039 – 0.083 in.)	0.94 – 1.93 mm (0.037 – 0.076 in.)	0.84 – 2.03 mm (0.033 – 0.080 in.)
Frequency	23.3 – 28 Hz (1400 – 1680 vpm)	28.3 – 33.3 Hz (1700 – 2000 vpm)	30 – 40 Hz (1800 – 2400 vpm)

Spot tests were also performed using LWD during the pre-mapping of the existing embankment and after the compaction of 300 mm (12 in.) clayey subgrade layer.

Stationary Field Tests

Figure G-3 shows representative vertical displacement time histories measured by the two geophones during the vibration of SAKAI roller at low frequency and high amplitude setting at the stationary condition. Measured displacement in the stable region was averaged to obtain a single representative displacement value. The displacement at the surface was also calculated by double integration of the acceleration measured by the roller accelerometers, as shown in Figure G-4.

Table G-4 summarizes vertical displacement at the surface and at depths of 0.6 m (24 in.) and 1.2 m (48 in.) for different IC rollers.

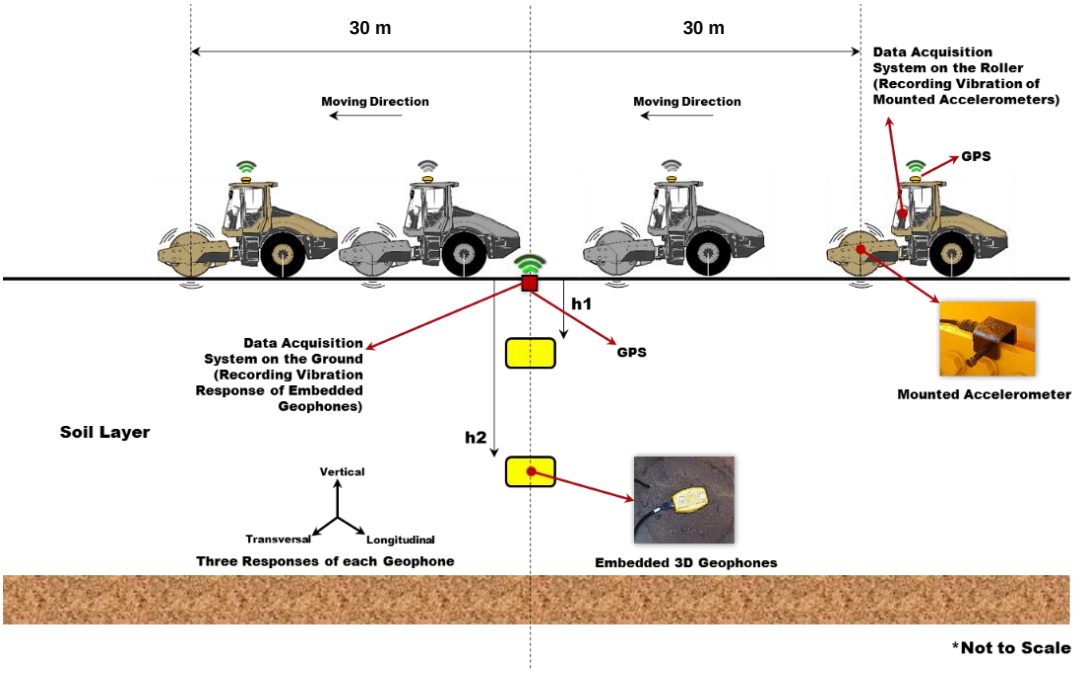

Figure G-2. Data collection during the vibratory moving condition.

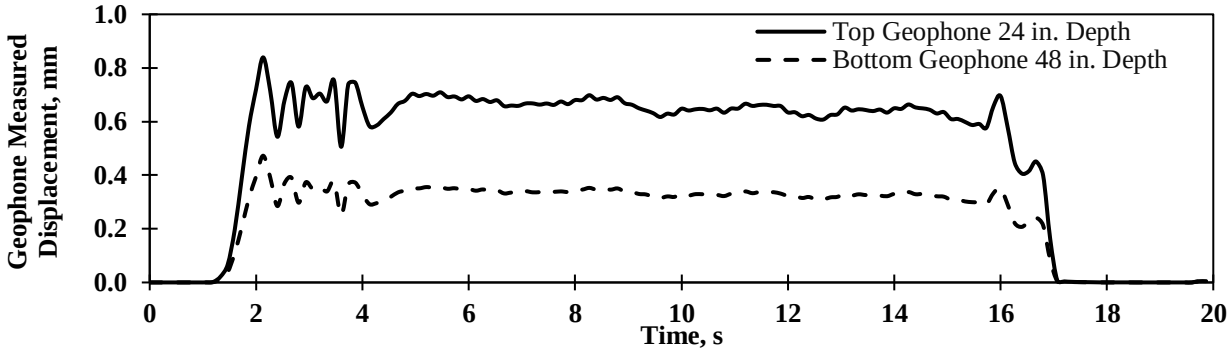

Figure G-3. Displacement measured by embedded geophones during stationary vibratory test on top of embankment using SAKAI roller operating under low frequency and high amplitude.

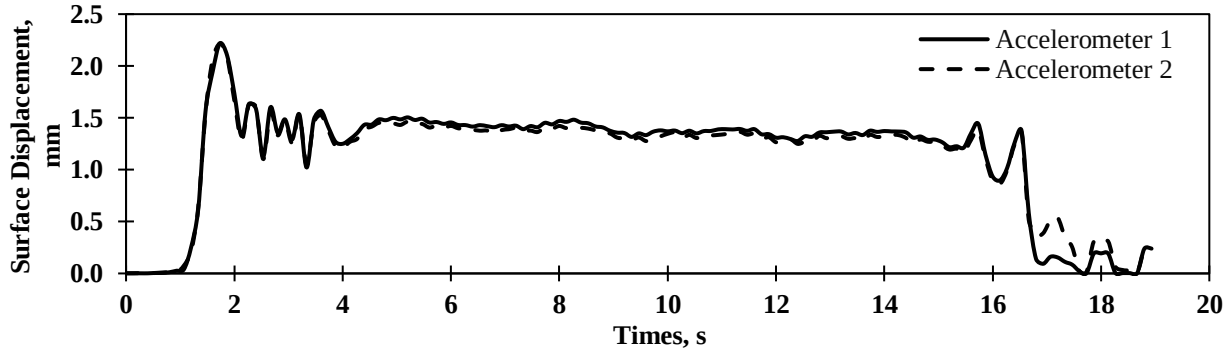

Figure G-4. Surface displacement calculated during stationary vibratory test on top of embankment using SAKAI roller operating under low frequency and high amplitude.

Table G-4. Vertical displacement at different depths for the different IC rollers under stationary vibration tests on top of embankment.

Roller		Caterpillar CS74B		SAKAI SV540T		HAMM HD120	
Operating Settings	Amplitude	High	Low	High	Low	High	Low
	Frequency	Low	Low	Low	Low	Low	Low
		Vertical Displacement (mm)					
Depth	Surface	2.47	1.51	1.57	0.79	3.10	1.38
	0.6 m (24 in.)	1.35	0.74	0.67	0.28	1.05	0.63
	1.2 m (48 in.)	0.74	0.38	0.33	0.16	0.56	0.32

Static Stationary Linear (SSL) FE Model

Figure G-5 compares the measured displacements under vibratory stationary rollers for different rollers and operating settings evaluated with the corresponding displacements obtained from FE SSL model. The two displacements show similar trends but with different amplitudes.

Figure G-6 shows the transfer function between the SSL model responses and the field measurements. The numerical responses are about 2.6 times greater than the corresponding field measurements. Some of the data points fall outside the 25% error lines. The two displacements are correlated with a coefficient of determination of $R^2 = 0.58$ and standard error of estimate, SEE = 0.36 mm.

Static Stationary Nonlinear (SSN) FE Model

The geomaterial responses were evaluated simulating the load imposed by the drum as static and geomaterials simulated as nonlinear (SSN) by introducing the nonlinear k' parameters obtained from the laboratory resilient modulus tests listed in Table G-2. It should be pointed out that the laboratory resilient modulus of the collected samples was used as the initial modulus of the simulated geomaterials in SSN models. Figure G-7 compares the measured field data and the nonlinear FE SSN models. In comparison to the linear FE SSL model, a better correlation between the measured field data and computed nonlinear FE SSN model is made as judged by a higher coefficient of determination, $R^2 = 0.74$, and a lower standard error of estimate, SEE = 0.17 mm; however, the slope of the regression fit line increased by a factor of 2.1 when compared to the linear model. The large difference between the adjustment factors obtained from the comparison of measured field displacements with the corresponding results yielded by both nonlinear and linear FE models can be explained by the difference in stress states and compaction efforts achieved in field and laboratory resilient modulus tests.

To better represent the state of stress and compaction effort achieved in the field and reduce the difference between nonlinear and linear observations, another simulation was attempted using a backcalculated k'_1 (the nonlinear parameter associated with stiffness in the resilient modulus constitutive model proposed by Ooi et al. (2004) described in Equation D.7). To backcalculate k'_1, M_R was substituted by the LWD modulus in Equation B.7, while nonlinear k'_2 and k'_3 parameters were determined from fitting the laboratory data to the proposed MEPDG model. In this approach, stress hardening and cohesiveness (causing softening) of the geomaterials can be properly achieved by nonlinear k'_2 and k'_3 parameters at a desirable compaction effort achieved by the backcalculated k'_1 parameter and E_{LWD}. The summary of the backcalculated k'_1 parameter for the implemented test sections is listed in Table G-5.

Figure G-8 compares the displacements obtained from the field measurements and SSN FE models when k_1' parameter is backcalculated. The SSN FE displacement is about 2.9 greater than the field measurements using the above-mentioned approach.

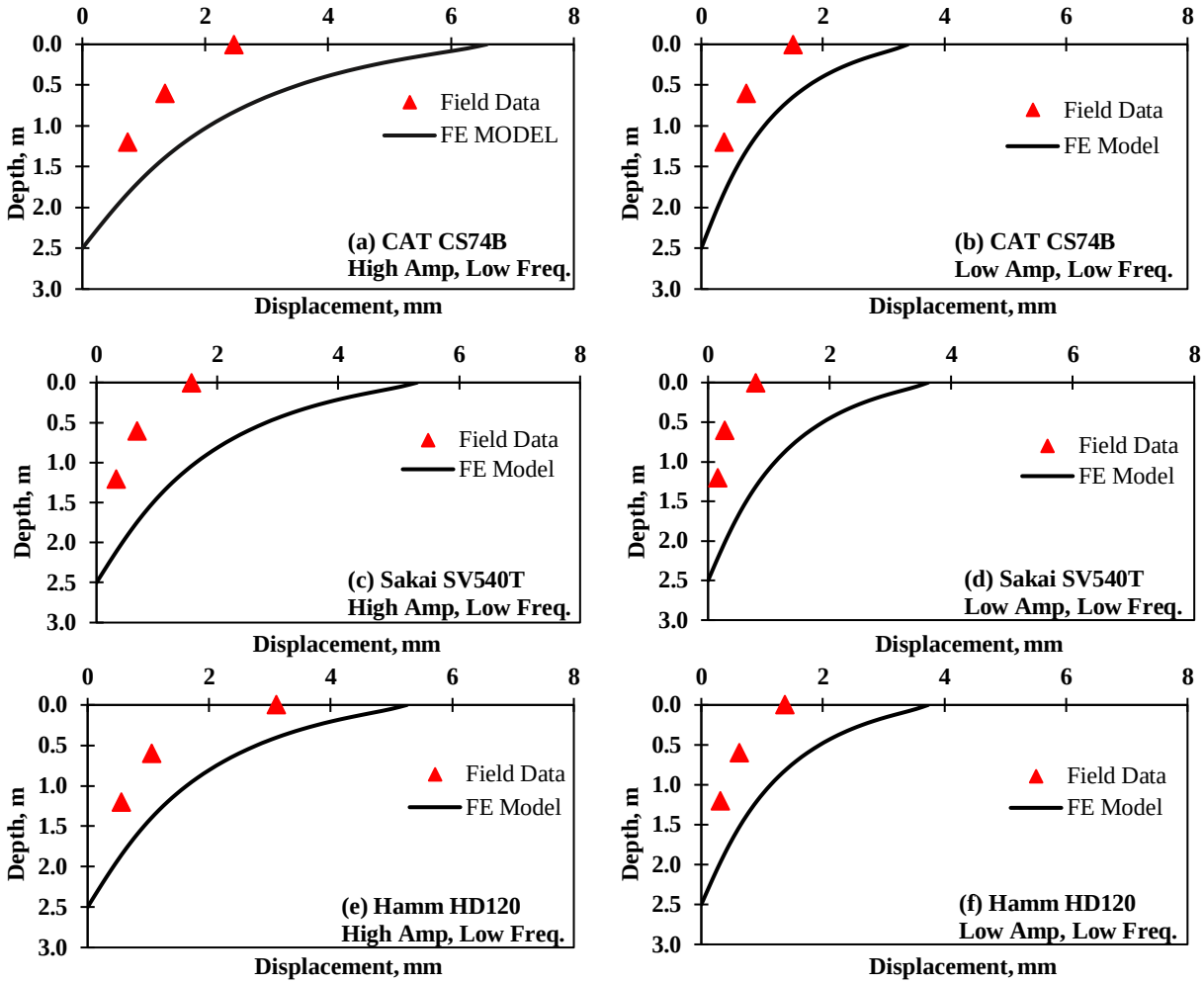

Figure G-5. Vertical displacement at different depths as obtained from FE SSL model and field measurements during stationary vibratory tests on top of embankment at Cleburne, Texas.

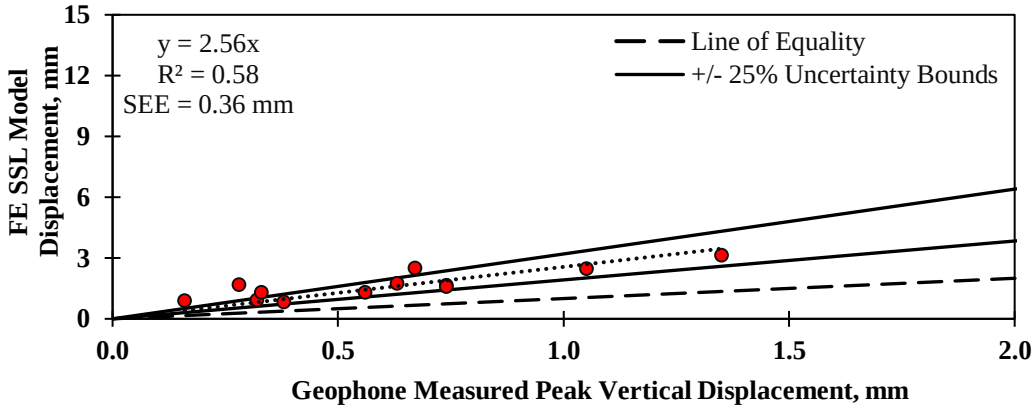

Figure G-6. Relationship between Site 1 field-measured displacements for different vibratory stationary rollers on top of embankment and FE SSL model displacement.

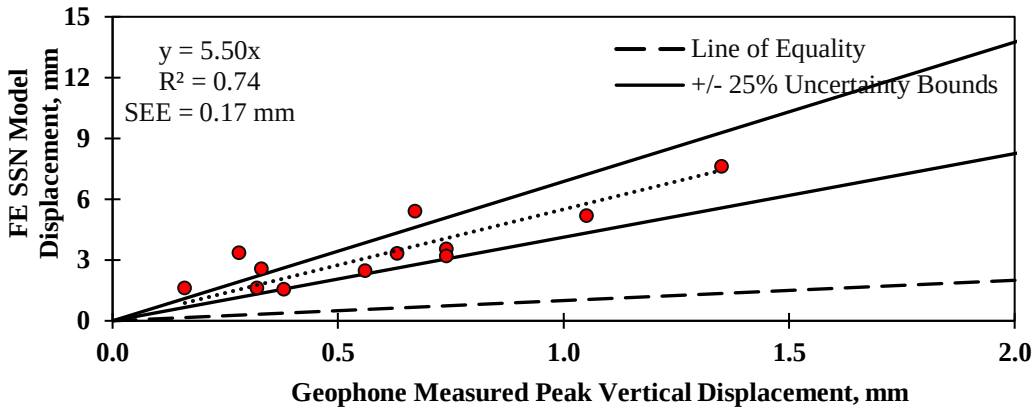

Figure G-7. Relationship between Site 1 field-measured displacements for different vibratory stationary rollers on top of embankment layer and FE SSN model displacement.

Table G-5. Backcalculated k_1' parameter for the implemented test sections.

Site	Location		Backcalculated k'_1 Parameter		
			Embankment	Subgrade	Base
1	Cleburne, TX		499	336	---
2	MnROAD	Cell 185	---	123	467
		Cell 186	---	152	722
		Cell 188	---	462	709
		Cell 189	---	283	470

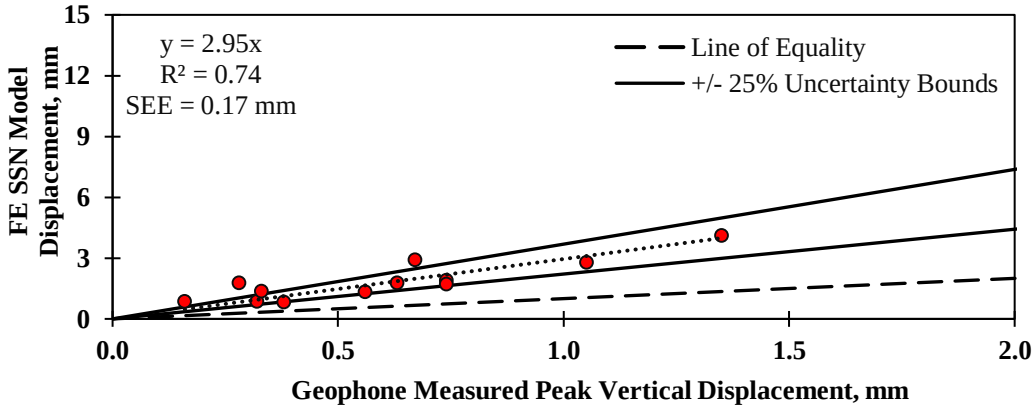

Figure G-8. Relationship between Site 1 field-measured displacements for different vibratory stationary rollers on top of embankment layer and FE SSN model displacement when k_1' is backcalculated using the LWD modulus.

Vibratory Stationary Nonlinear (VSN) FE Model

Considering the applied load as vibratory, as opposed to static, to more realistically simulate the dynamic behavior of the compacted geomaterials under the operating rollers was investigated. The simulation of a vibratory load was comprised of a sinusoidal load at a certain frequency for each of the operating rollers as listed in Table G-3. Similar to SSN model, two approaches were used for simulating the geomaterials

behavior of the vibratory stationary nonlinear (VSN) FE models: (1) the geosystem was simulated using the nonlinear k′ parameters (all obtained from the laboratory resilient modulus tests), and (2) the geosystem was simulated utilizing the nonlinear k′2 and k′3 parameters (obtained from the laboratory tests) while k′1 was backcalculated using the ELWD. Figures G-9 and G-10 show the comparison of displacement field measurements and their corresponding results from VSN FE models considering the aforementioned approaches, respectively. Correlation between the field measurements and the displacements as obtained from the FE models improved when compared to the linear FE SSL model. The adjustment factor of 4.88 shown in Figure G-10 indicates the difference between the compaction efforts employed in the field and laboratory resilient modulus tests. Figure G-11 shows that the VSN model yields promising results as judged by R^2 = 0.75 and SEE = 0.16 mm. Similar to linear FE SSL models, the displacements obtained from the VSN models (when k′1 parameter is backcalculated) is about 2.6 times greater than the field measurements. The summary of the discussed scenarios is reported in Table G-6.

When the displacement is normalized with respect to the corresponding maximum surface displacement, the numerical and measured displacement profiles follow one another quite favorably (see Figure G-11).

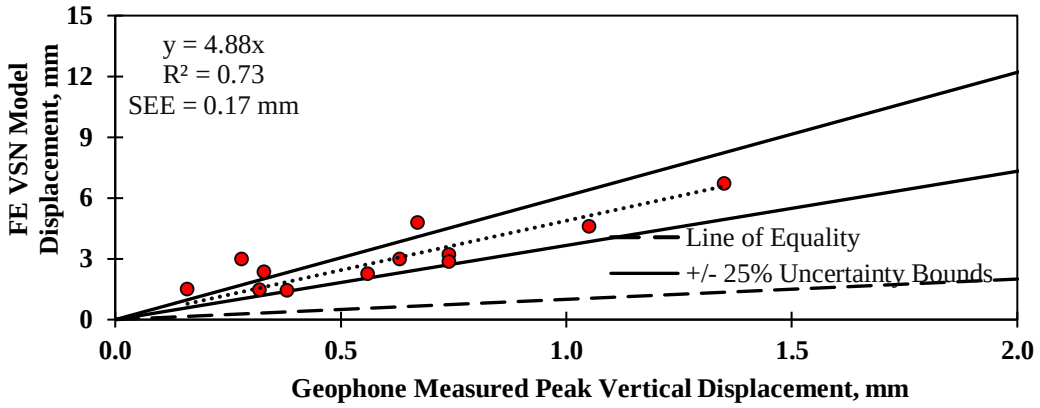

Figure G-9. Relationship between Site 1 field-measured displacements for different vibratory stationary rollers on top of embankment layer and FE VSN model displacement.

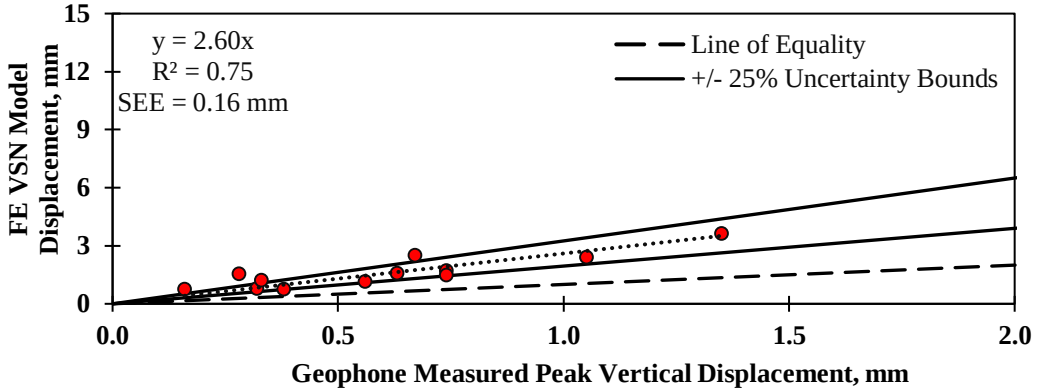

Figure G-10. Relationship between Site 1 field-measured displacements for different vibratory stationary rollers on top of embankment layer and FE VSN model displacement when k_1' is backcalculated using the LWD modulus.

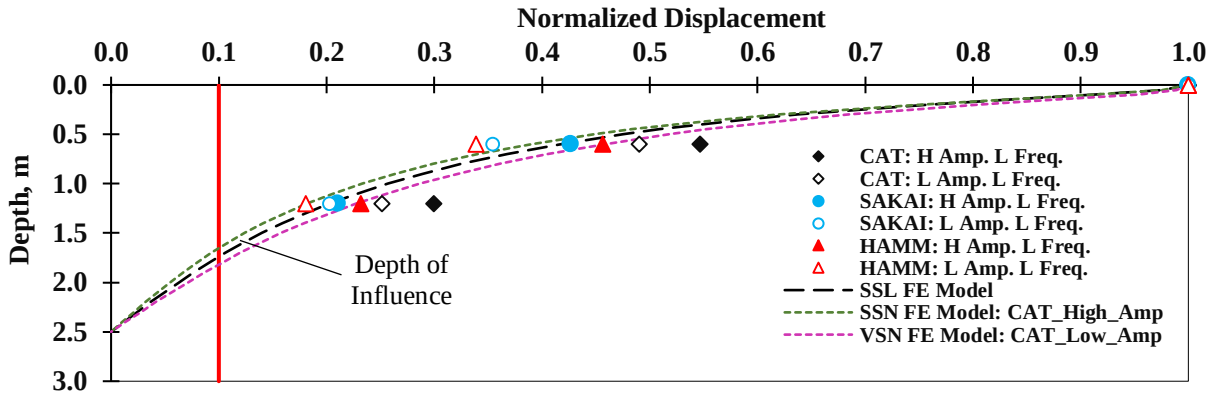

Figure G-11. Comparison of normalized displacement obtained from FE model and Site 1 field data during stationary test on top of existing embankment layer.

Table G-6. Summary of the descriptive relationship of the field-measured displacement under vibratory rollers at stationary condition and different FE scenarios for Site 1.

Descriptive Correlation	SSL FE Model	SSN FE Model		VSN FE Model	
		k'_1: Laboratory Test	k'_1: Backcalculated from E_{LWD}	k'_1: Laboratory Test	k'_1: Backcalculated from E_{LWD}
Adjustment Factor, *S*	2.56	5.50	2.95	4.88	2.60
Coefficient of Determination, R^2	0.58	0.74	0.74	0.73	0.75
Standard Error of Estimate, *SEE*	0.36	0.17	0.17	0.17	0.16

The depths of influence from the experimental data, defined as the depth at which the displacement attenuates to 10% of the maximum surface displacement, can be extrapolated to depths between 1.65 m (65 in.) and 2.10 m (83 in.), while the influence depth for FE models varies from 1.65 m (65 in.) to 1.9 m (75 in.). The higher the amplitude of the roller vibration is, the deeper the depth of influence will become. The results also show that the depth of influence for the VSN FE models are slightly greater than the comparable SSN scenarios.

The summary of the recorded displacements at certain depths at which the geophones are embedded for the simulated rollers on top of the embankment layer with respect to different FE scenarios is reported in Table G-7.

Moving Field Tests

Static Stationary Linear (SSL) FE Model

Figure G-12 compares the displacement basins in the vertical direction for the embedded geophones under the vibratory moving CAT CS74B roller at low frequency and low amplitude settings with the corresponding FE SSL model. The recorded peaks of displacement basins at different depths, i.e., 0.75 m (30 in.) and 1.35 m (54 in.) after the addition of subgrade layer, under different vibratory IC rollers at moving condition are summarized in Table G-8.

Table G-7. Vertical displacements obtained from different FE scenarios at different depths under rollers operating on top of the embankment layer during the stationary tests.

(a) Caterpillar CS74B: FE Model

Roller			Caterpillar CS74B					
Operating Settings		Amplitude	High			Low		
		Frequency	Low			Low		
			Displacement, mm					
Depth			Surface	0.6 m (24 in.)	1.2 m (48 in.)	Surface	0.6 m (24 in.)	1.2 m (48 in.)
FE Scenario	SSL		6.6	3.2	1.7	3.4	1.6	0.8
	SSN	k'_1: Laboratory Test	19	7.6	3.6	7.7	3.2	1.6
		k'_1: Backcalculated	11	4.1	1.9	4.3	1.7	0.8
	VSN	k'_1: Laboratory Test	15	6.7	3.2	6.3	2.9	1.4
		k'_1: Backcalculated	8.5	3.7	1.7	3.4	1.5	0.7

(b) SAKAI SV540T: FE Model

Roller			SAKAI SV540T					
Operating Settings		Amplitude	High			Low		
		Frequency	Low			Low		
			Displacement, mm					
Depth			Surface	0.6 m (24 in.)	1.2 m (48 in.)	Surface	0.6 m (24 in.)	1.2 m (48 in.)
FE Scenario	SSL		5.3	2.5	1.3	3.6	1.7	0.9
	SSN	k'_1: Laboratory Test	13.5	5.4	2.6	8.0	3.4	1.6
		k'_1: Backcalculated	7.6	2.9	1.4	4.5	1.8	0.9
	VSN	k'_1: Laboratory Test	10.6	4.8	2.3	6.5	2.9	1.5
		k'_1: Backcalculated	5.8	2.5	1.2	3.5	1.6	0.8

(c) HAMM HD120: FE Model

Roller			HAMM HD120					
Operating Settings		Amplitude	High			Low		
		Frequency	Low			Low		
			Displacement, mm					
Depth			Surface	0.6 m (24 in.)	1.2 m (48 in.)	Surface	0.6 m (24 in.)	1.2 m (48 in.)
FE Scenario	SSL		5.2	2.4	1.3	3.7	1.8	0.9
	SSN	k'_1: Laboratory Test	12.9	5.2	2.5	8.0	3.3	1.6
		k'_1: Backcalculated	7.3	2.8	1.3	4.4	1.8	0.9
	VSN	k'_1: Laboratory Test	10.1	4.6	2.2	6.4	3.0	1.4
		k'_1: Backcalculated	5.5	2.4	1.2	3.6	1.6	0.8

As shown in Figure G-13, the numerical displacement are about 1.6 times greater than the field measurements with R^2 of 0.39 and SEE of 0.27 mm. Aside from the weakness of the simulation due to simplifying assumptions, some of the variability can be attributed to the lack of uniformity at the site and the lack of uniformity in the operation of some of the rollers.

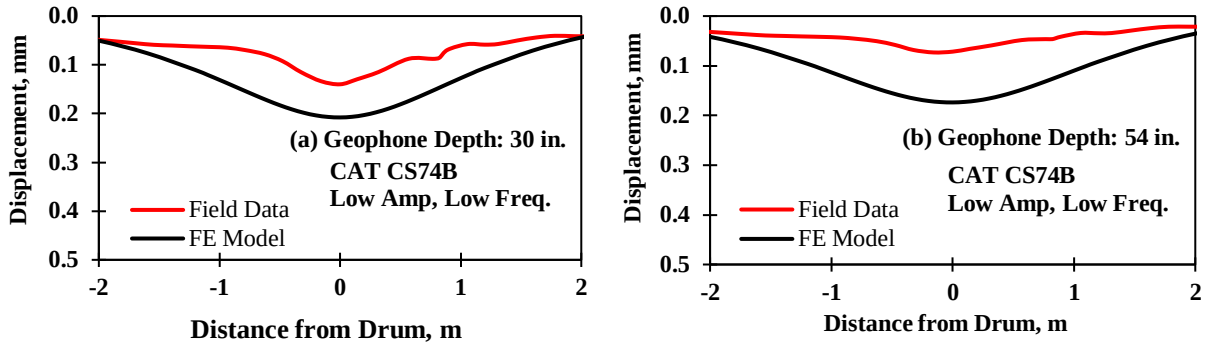

Figure G-12. Displacement basin at different depths as obtained from FE SSL model and Site 1 field measurements during vibratory moving test on top of subgrade.

Table G-8. Vertical displacement at different depths for different IC rollers under vibratory moving tests on subgrade layer.

Roller		Caterpillar CS74B		SAKAI SV540T		HAMM HD120	
Operating Settings	**Amplitude**	High	Low	High	Low	High	Low
	Frequency	Low	Low	Low	Low	Low	Low
		Vertical Displacement (mm)					
Depth	Surface	2.57	1.27	1.13	0.48	1.81	1.07
	0.75 m (30 in.)	0.80	0.27	0.31	0.14	0.46	0.20
	1.35 m (54 in.)	0.31	0.13	0.20	0.07	0.19	0.12

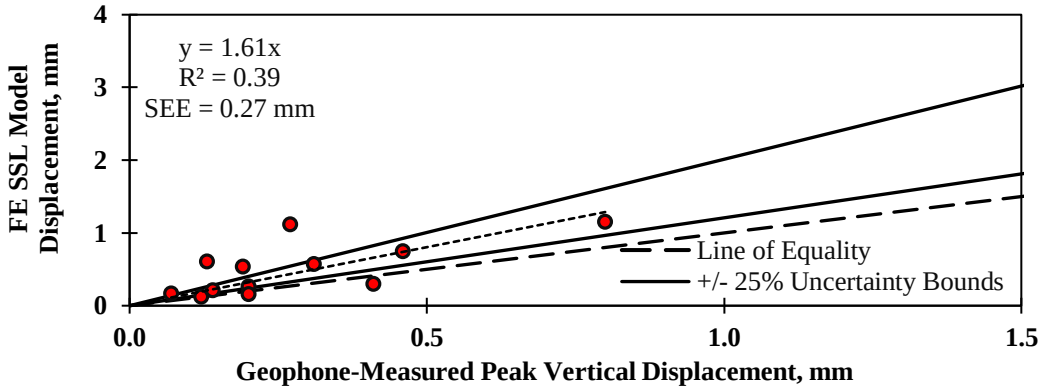

Figure G-13. Relationship between Site 1 field-measured displacements for different vibratory moving rollers on top of subgrade layer and FE SSL model displacement.

Static Stationary Nonlinear (SSN) FE Model

Figure G-14 compares the peak displacements recorded by the embedded geophones with the corresponding results obtained from the static stationary nonlinear (SSN) FE models when k_1' parameter is backcalculated. The R^2 of 0.85 and SEE of 0.23 mm indicate SSN FE model can be appropriately correlated with the field data as compared with the results obtained from linear SSL model.

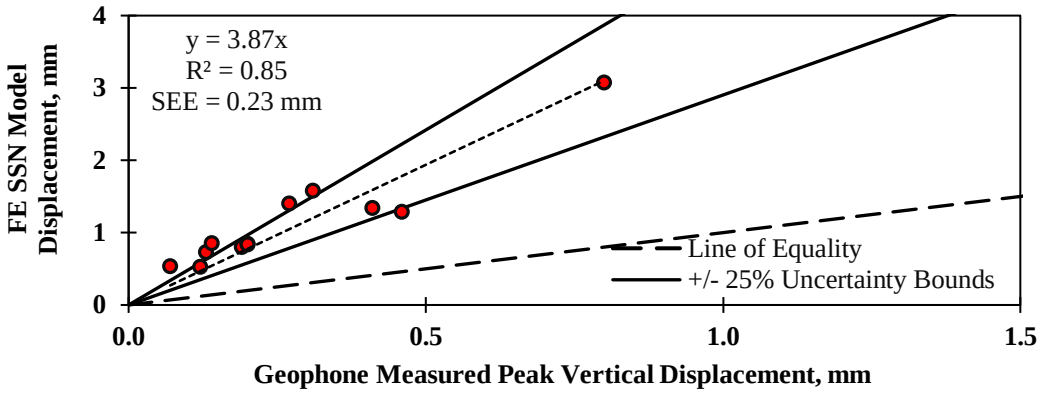

Figure G-14. Relationship between Site 1 field-measured displacements for different vibratory moving rollers on top of subgrade and FE SSN model displacement using backcalculated k'_1.

Vibratory Stationary Nonlinear (VSN) FE Model

Figure G-15 compares the measured field displacements and corresponding results obtained from the vibratory stationary nonlinear (VSN) FE models. Again, k'_1 parameter was backcalculated using the measured LWD modulus. By introducing the vibratory condition and the material nonlinearity into the model, the correlation improved slightly as indicated by a lower SEE = 0.19 mm for the VSN model in comparison to SSN model. Table G-9 summarizes all the attempted FE scenarios.

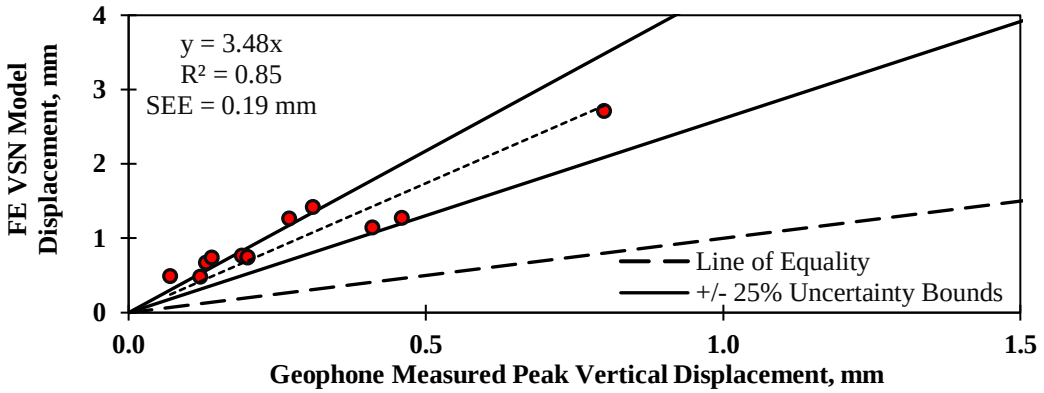

Figure G-15. Relationship between Site 1 field-measured displacements for different vibratory moving rollers on top of subgrade and FE VSN model displacement using backcalculated k'_1.

Table G-9. Summary of the descriptive relationship of the field-measured displacement under vibratory rollers at moving condition and different FE scenarios for Site 1.

Descriptive Correlation	SSL FE Model	SSN FE Model		VSN FE Model	
		k'_1: Laboratory Test	k'_1: Backcalculated from E_{LWD}	k'_1: Laboratory Test	k'_1: Backcalculated from E_{LWD}
Adjustment Factor, *S*	1.61	4.64	3.87	4.46	3.48
Coefficient of Determination, R^2	0.39	0.85	0.85	0.86	0.85
Standard Error of Estimate, *SEE*	0.27	0.34	0.23	0.27	0.19

The measured peak displacements under the moving rollers were normalized with respect to the maximum surface displacement measured from double integration of the recorded accelerations. Figure G-16 shows the normalized displacements for both numerical and field data. Similar to the stationary tests, the FE models are in agreement with the measured field data when the displacement is normalized. The depth of influence varies from 1.4 m (55 in.) to 1.75 m (69 in.) for the moving tests. While the average influence depth for the FE models was determined to be about 1.75 m (69 in.). As depicted in Figure G-16, the influence depth increases with an increase in the load amplitude.

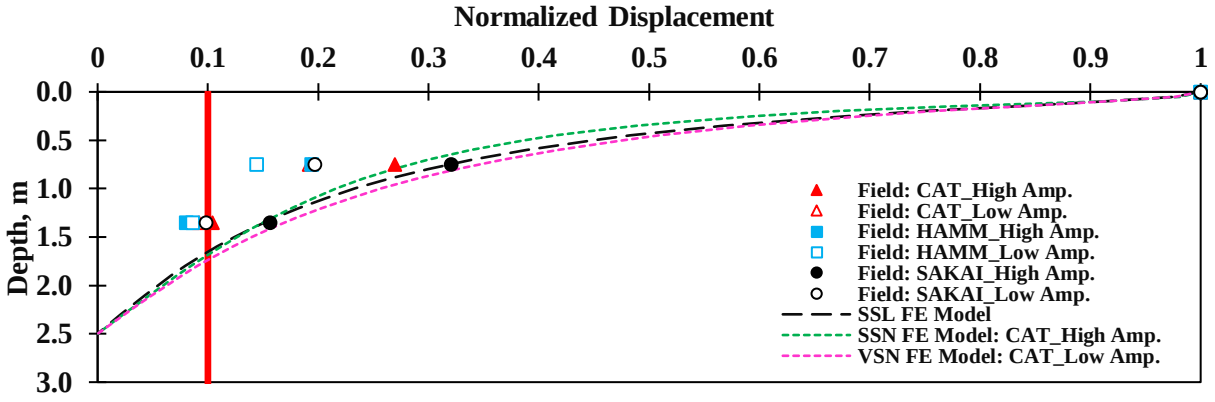

Figure G-16. Comparison of normalized displacement obtained from FE model and Site 1 field-measured data during moving test on top of subgrade layer.

Table G-10 summarizes the recorded displacements at different depths under attempted FE scenarios for the moving tests implemented on top of the subgrade layer for Site 1.

MnROAD (Site 2)

IC Tests on Top of Subgrade

Figure G-17 shows the measured vertical displacements recorded by the embedded geophones during mapping of the subgrade layer by the vibratory moving roller for Cells 185 through 189. The maximum surface displacement is demonstrated for a distance of 30 m (100 ft), starting 15 m (50 ft) before and ending 15 m (50 ft) after the location of the embedded geophones for Cells 185 through 189 as shown in Figure G-18. An abrupt drop is observed in the recorded displacement for Cell 189 indicating the DAQ system was switched off at the end of the test section (Figure G-18d).

Static Stationary Linear (SSL) FE Model

Figure G-19 shows a sample of geophone measurements and comparable SSL FE model when proof-mapping on top of subgrade at depths of 0.15 m (6 in.) and 0.6 m (24 in.) for Cell 188. The summary of the peak displacement measurements after mapping for Cells 185 through 189 on top of the subgrade layer is presented in Table G-11.

Figure G-20 compares the geophone measured peak vertical deformation to the vertical deformation under the roller as predicted by the SSL FE model at two different depths for all four cells' single-layer geosystems. FE model displacement responses were about 3.5 times larger than those measured in the field with R^2 of 0.48 and SEE of 0.53 mm.

Table G-10. Vertical displacements obtained from different FE scenarios at different depths under rollers operating on top of subgrade layer during the moving tests for Site 1.

(a) Caterpillar CS74B: FE Model

Roller			Caterpillar CS74B					
Operating Settings		Amplitude	High			Low		
		Frequency	Low			Low		
			Displacement, mm					
Depth			Surface	0.6 m (24 in.)	1.2 m (48 in.)	Surface	0.6 m (24 in.)	1.2 m (48 in.)
FE Scenario	SSL		3.6	1.2	0.6	3.5	1.1	0.6
	SSN	k'_1: Laboratory Test	19.0	3.7	1.9	7.1	1.7	0.9
		k'_1: Backcalculated	14.5	3.1	1.6	5.7	1.4	0.7
	VSN	k'_1: Laboratory Test	14.9	6.7	3.2	6.3	2.9	1.4
		k'_1: Backcalculated	8.5	3.7	1.7	3.4	1.5	0.7

(b) SAKAI SV540T: FE Model

Roller			SAKAI SV540T					
Operating Settings		Amplitude	High			Low		
		Frequency	Low			Low		
			Displacement, mm					
Depth			Surface	0.6 m (24 in.)	1.2 m (48 in.)	Surface	0.6 m (24 in.)	1.2 m (48 in.)
FE Scenario	SSL		0.9	0.3	0.3	0.6	0.2	0.2
	SSN	k'_1: Laboratory Test	1.4	1.2	0.9	0.9	0.7	0.6
		k'_1: Backcalculated	1.6	1.3	0.8	1.0	0.8	0.5
	VSN	k'_1: Laboratory Test	10.6	4.8	2.3	6.5	2.9	1.5
		k'_1: Backcalculated	5.8	2.5	1.2	3.5	1.6	0.8

(c) HAMM HD120: FE Model

Roller			HAMM HD120					
Operating Settings		Amplitude	High			Low		
		Frequency	Low			Low		
			Displacement, mm					
Depth			Surface	0.6 m (24 in.)	1.2 m (48 in.)	Surface	0.6 m (24 in.)	1.2 m (48 in.)
FE Scenario	SSL		2.3	0.7	0.5	0.5	0.2	0.1
	SSN	k'_1: Laboratory Test	2.9	2.0	1.2	0.9	0.7	0.5
		k'_1: Backcalculated	1.5	1.3	0.8	1.0	0.9	0.5
	VSN	k'_1: Laboratory Test	10.1	4.6	2.2	6.4	3.0	1.4
		k'_1: Backcalculated	5.5	2.4	1.2	3.6	1.6	0.8

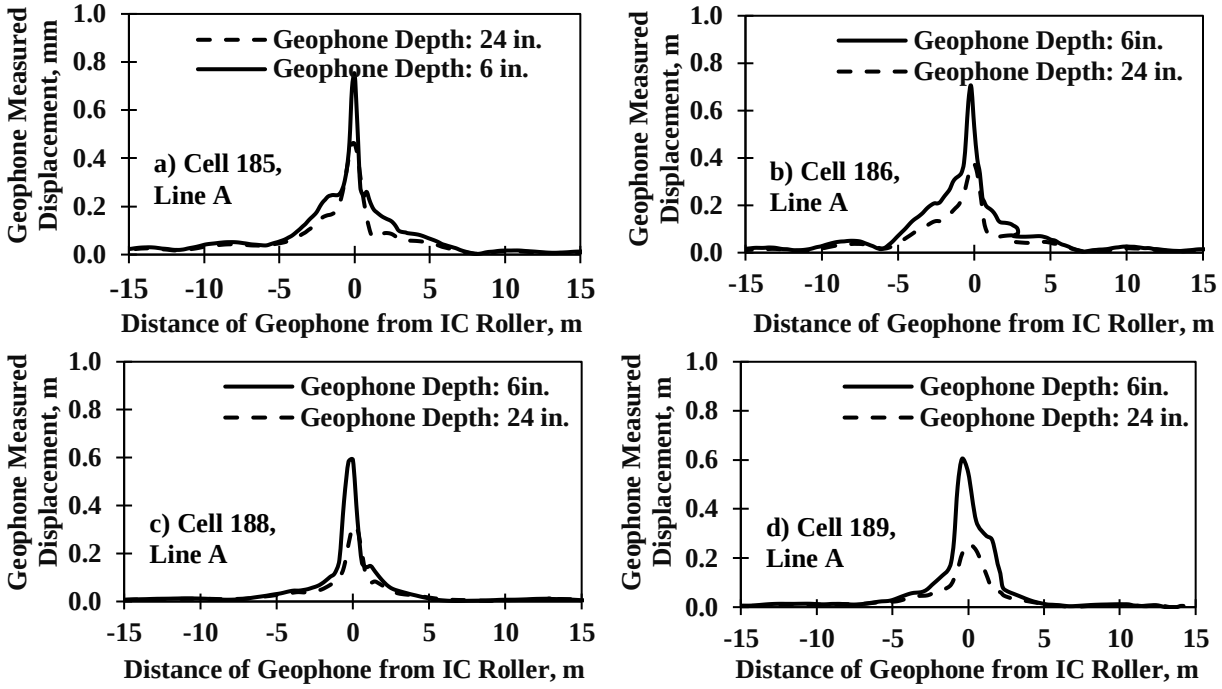

Figure G-17. Displacement measured by embedded geophones during vibratory moving test on top of subgrade at (a) Cell 185, (b) Cell 186, (c) Cell 188, and (d) Cell 189 at MnROAD.

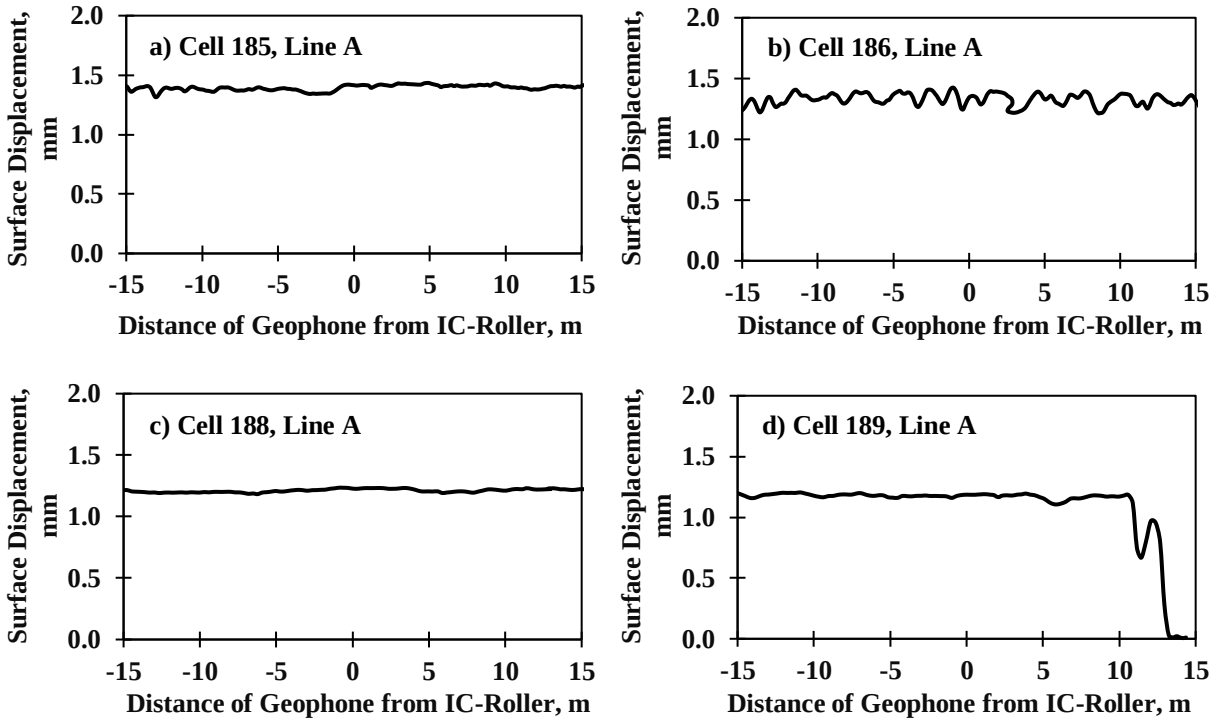

Figure G-18. Surface displacement calculated during vibratory moving test on top of subgrade layer for (a) Cell 185, (b) Cell 186, (c) Cell 188, and (d) Cell 189 at MnROAD.

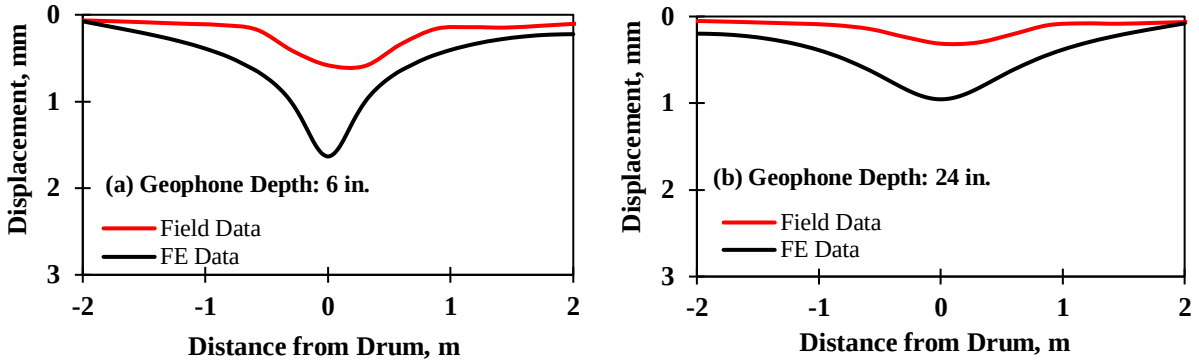

Figure G-19. Displacement basin at different depths as obtained from FE SSL model and field measurements during vibratory moving test on top of subgrade for Cell 188 at MnROAD.

Table G-11. Vertical displacement at different depths for IC roller under moving vibration tests on top of subgrade at MnROAD.

Embedded Geophone Depth		Peak Vertical Displacement (mm)	
		Field	Field
Sandy Subgrade		**Cell 185**	**Cell 186**
Depth	Surface	1.41	1.34
	0.15 m (6 in.)	0.75	0.70
	0.6 m (24 in.)	0.46	0.37
Clayey Subgrade		**Cell 188**	**Cell 189**
Depth	Surface	1.22	1.18
	0.15 m (6 in.)	0.59	0.26
	0.6 m (24 in.)	0.31	0.61

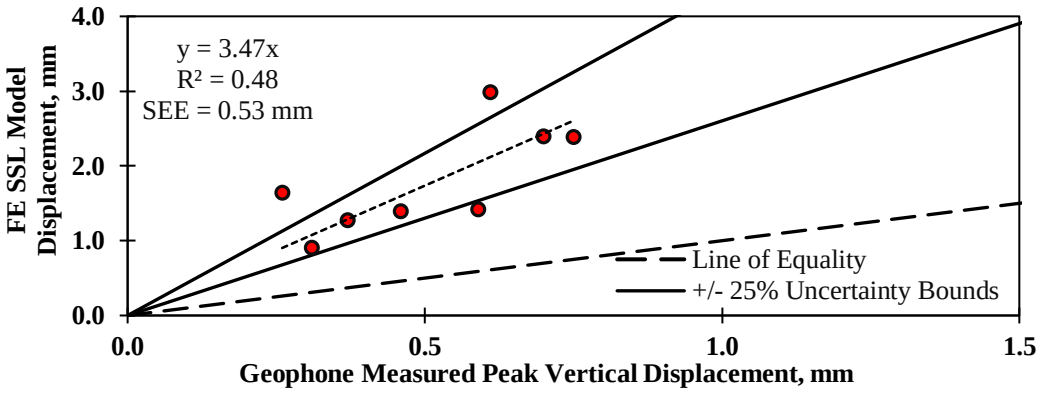

Figure G-20. Relationship between field-measured displacements for vibratory moving roller on top of subgrade layer and FE SSL model displacement at MnROAD.

Static Stationary Nonlinear (SSN) FE Model

By introducing nonlinearity into the FE model, the geomaterials behave more realistically under the imposed load by the roller on top of the subgrade layer. Figure G-21 compares the peak values of the displacement basins recorded by the embedded geophones through Cells 185 to 189 with corresponding results yielded by the SSN FE models. To simulate the geomaterials behavior the nonlinear k'_2 and k'_3

parameters were determined from the laboratory resilient modulus tests, while the parameter k'_1 was backcalculated using the LWD modulus implemented on top of the subgrade. The summary of the resilient modulus tests, as well as the backcalculation of k'_1 parameter for the subgrade materials of the MnROAD Cells, are reported in Tables G-2 and G-5, respectively. As observed in Figure G-21, the nonlinearity makes an improvement to the relationship between the measured field data and the simulated models as compared to linear SSL model so that a higher coefficient of determination and lower SEE can be made.

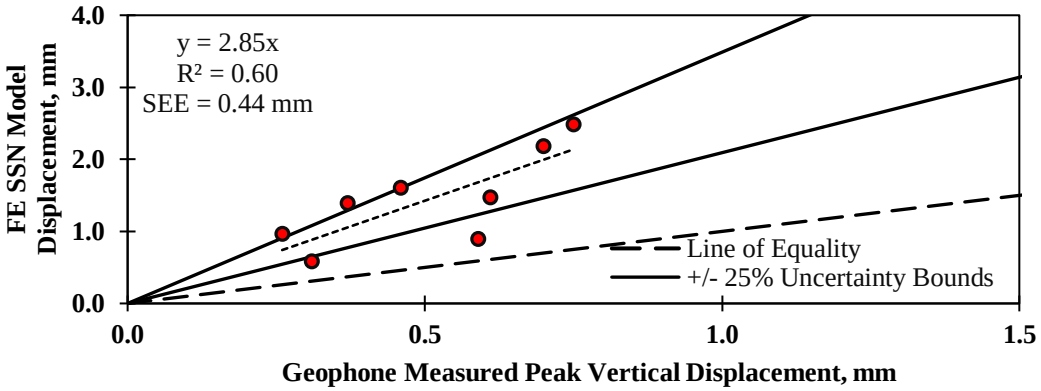

Figure G-21. Relationship between field-measured displacements for vibratory moving roller on top of subgrade layer and FE SSN model displacement at MnROAD: k'_1 is backcalculated using the LWD modulus.

Vibratory Stationary Nonlinear (VSN) FE Model

To further improve the relationship between the measured displacements and the comparable finite element results, the vibration was introduced to the simulated drum on top of the subgrade. Again, the parameter k'_1 was backcalculated using the LWD modulus. The operating load and vibration frequency of the utilized roller has been reported in Table D-2. As shown in Figure G-22, the VSN FE model yields promising results so that the FE model can be correlated with the measured field displacement with R^2 of 0.79 and SEE of 0.41 mm. The transfer function between the VSN FE model and field data was adjusted to be about 4.

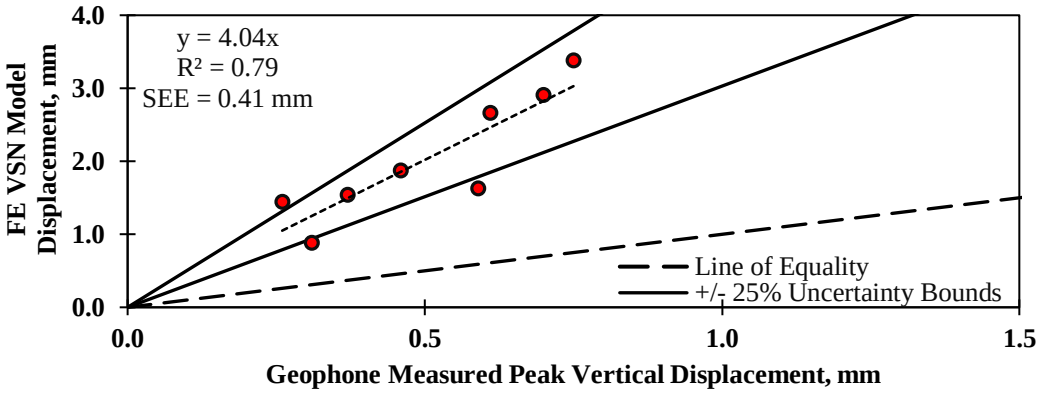

Figure G-22. Relationship between field-measured displacements for vibratory moving roller on top of subgrade layer and FE VSN model displacement at MnROAD: k'_1 is backcalculated using the LWD modulus.

The transfer functions derived from the comparison of measured field displacement and the attempted FE models for single-layer systems are summarized in Table G-12. The difference between the linear and nonlinear FE models can be justified by the difference of stiffness and the compaction effort that the material experiences during the implementation of field and laboratory tests. Since the reconstructed samples during the laboratory test cannot achieve the same state of stress and stiffness that the geomaterial has experienced during the compaction process, we suggest to use nonlinear k'_2 and k'_3 parameters obtained from the laboratory resilient modulus test, and backcalculate k'_1 with respect to LWD modulus for simulating the geomaterial system to properly capture the stiffness of the compacted geomaterials.

Table G-12. Summary of the descriptive relationship of the measured field displacement and different FE scenarios for single-layer systems under vibratory moving rollers for Site 2.

Descriptive Correlation	SSL FE Model	SSN FE Model		VSN FE Model	
		k'_1: Laboratory Test	k'_1: Backcalculated from E_{LWD}	k'_1: Laboratory Test	k'_1: Backcalculated from E_{LWD}
Adjustment Factor, *S*	3.47	1.41	2.85	1.67	4.04
Coefficient of Determination, R^2	0.48	0.48	0.60	0.79	0.79
Standard Error of Estimate, *SEE*	0.53	0.08	0.44	0.13	0.41

Figure G-23 compares the normalized displacement for single-layer soil systems (subgrade only) for both measured field data and attempted FE models. As observed in Figure G-17, the displacement measured by the geophones embedded in the sandy subgrade, Cells 185 and 186, is slightly larger than the values recorded for clayey subgrade. The depth of influence of IC roller for single-layer systems was extrapolated for Cells 185 through 189. The influence depth varies between 1.4 m (55 in.) to 1.9 m (75 in.). The different patterns of the profiles can be attributed to the nonlinear behavior of the geomaterials when subjected to the roller loads. The normalized displacement profiles of different cells obtained from the FE simulations show that the influence depth of cells containing sandy material (185 and 186) is slightly greater than the penetration depth calculated for clayey subgrade (Cells 188 and 189). Owing to the similarity between the normalized displacement profiles of each type of the materials, two profiles representing sandy and clayey materials are depicted in Figure G-23. The influence depth of the SSN FE models is about 2 m (79 in.); while the depth of influence obtained from the vibratory FE models is about 1.8 m (71 in.) which is favorably similar to the field measurement. The normalized displacement profiles of different cells are the same when linear behavior is used for the simulation of the single-layer geosystems. Hence, only a single simulated profile is shown as a representative of the four Cells. The influence depth acquired from the linear SSL model, 1.85 m (73 in.), is a proper indicator of penetration depth for the commercially available regular sized roller with the operating features listed in Table D-2.

The summary of the recorded displacements under the attempted FE models for simulation of single-layer geosystems under vibratory moving rollers at MnROAD facility is listed in Table G-13.

IC Tests on Top of Subgrade

The measured vertical displacements recorded by the geophones embedded within the base layer, i.e., 0.15 m (6 in.), and two geophones embedded in the subgrade layer with 0.45 m (18 in.) and 0.9 m (36 in.) from the surface, are shown in Figure G-24. The shallower the geophone is embedded, the higher the measured displacement is. The base layer attenuates the measured displacement of the embedded geophones in the subgrade layer.

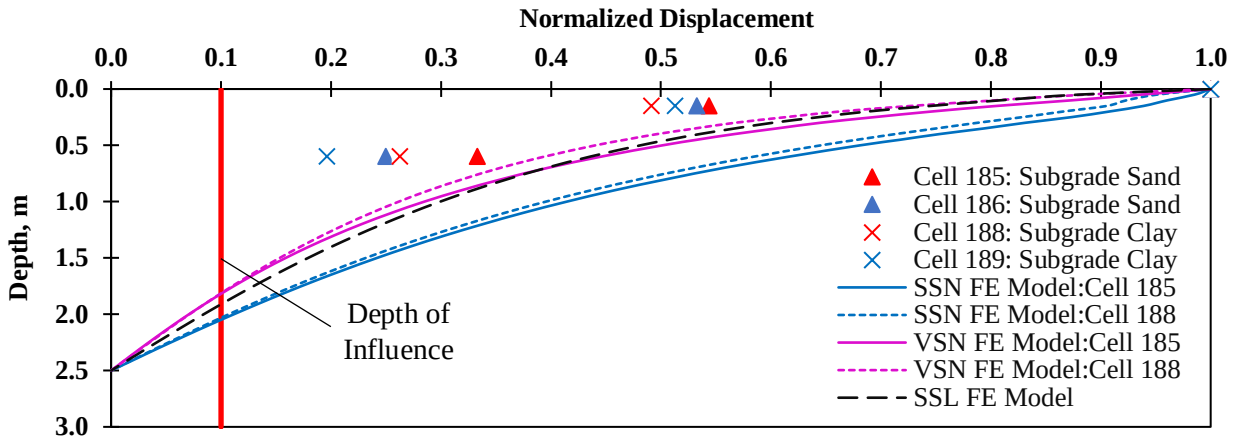

Figure G-23. Comparison of normalized displacement obtained from FE model and field data during vibratory moving test on top of subgrade layer for Cells 185–189 at MnROAD.

Table G-13. Vertical displacements obtained from different FE scenarios at different depths under rollers operating on top of subgrade layer during the moving tests for Site 2.

Embedded Geophone Depth			Vertical Displacement, mm					
Sandy Subgrade			Cell 185			Cell 186		
FE Scenarios	Depth		Surface	0.15 m (6 in.)	0.6 m (24 in.)	Surface	0.15 m (6 in.)	0.6 m (24 in.)
	SSL		3.2	2.4	1.4	3.1	2.4	1.3
	SSN	k'_1: Laboratory Test	1.0	0.9	0.6	1.1	1.0	0.6
		k'_1: Backcalculated	2.7	2.5	1.6	2.4	2.2	1.4
	VSN	k'_1: Laboratory Test	1.5	1.2	0.7	1.5	1.3	0.7
		k'_1: Backcalculated	4.2	3.4	1.9	3.4	2.9	1.5
Clayey Subgrade			Cell 188			Cell 189		
FE Scenarios	Depth		Surface	0.15 m (6 in.)	0.6 m (24 in.)	Surface	0.15 m (6 in.)	0.6 m (24 in.)
	SSL		1.5	1.4	0.9	3.9	3.0	1.6
	SSN	k'_1: Laboratory Test	0.8	0.7	0.5	1.0	0.9	0.6
		k'_1: Backcalculated	1.0	0.9	0.6	1.6	1.5	1.0
	VSN	k'_1: Laboratory Test	0.9	0.8	0.5	1.6	1.2	0.6
		k'_1: Backcalculated	2.2	1.6	0.9	3.6	2.7	1.4

Figure G-25 shows the maximum surface displacements during the vibration of the moving roller on top of the base for Cells 185 through 189. The patterns of the observed displacements indicate a bouncing behavior of the roller due to the stiffer base material as more measurements exhibit more variability when compared to the surface displacement obtained from the mapping on subgrade materials (Figures G-25 and G-17, respectively).

The abrupt drop in the measured displacement for Cell 189 shows where the DAQ system was turned off. For comparison purposes to FE model responses, an average value of the measurements was within a range of ±0.5 m distance from the sensor for each of the records.

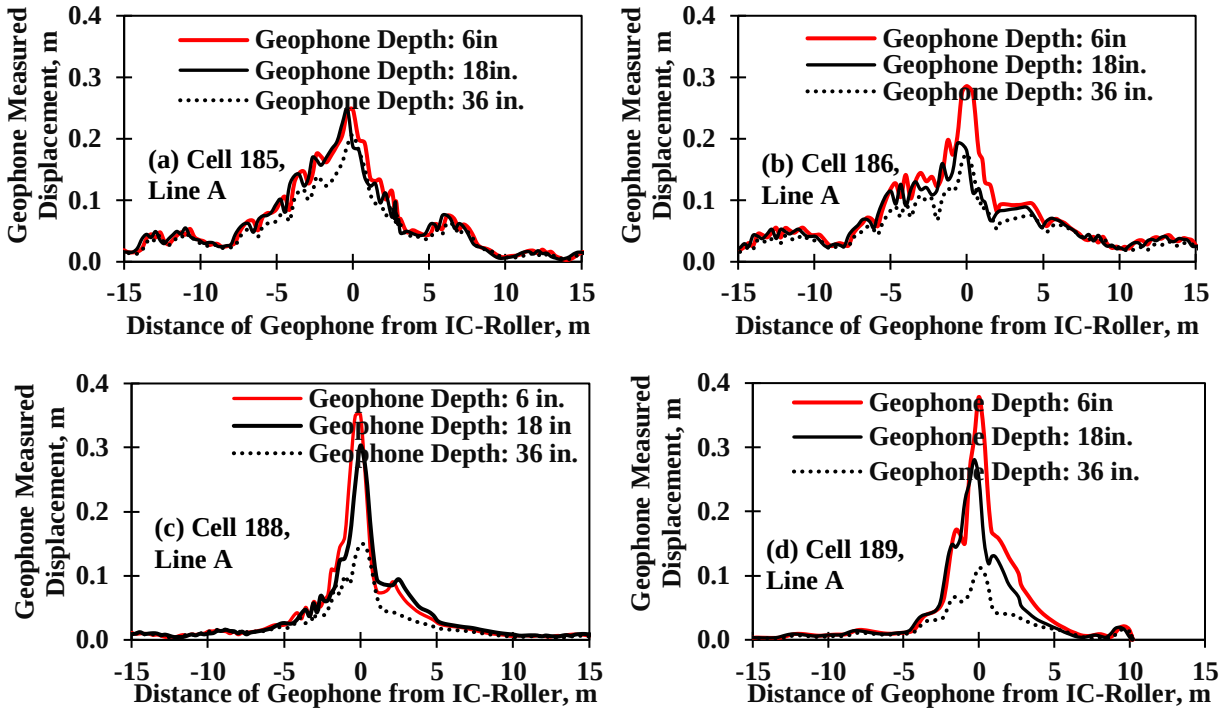

Figure G-24. Displacement measured by embedded geophones during vibratory moving test on top of base layer for (a) Cell 185, (b) Cell 186, (c) Cell 188, and (d) Cell 189 at MnROAD.

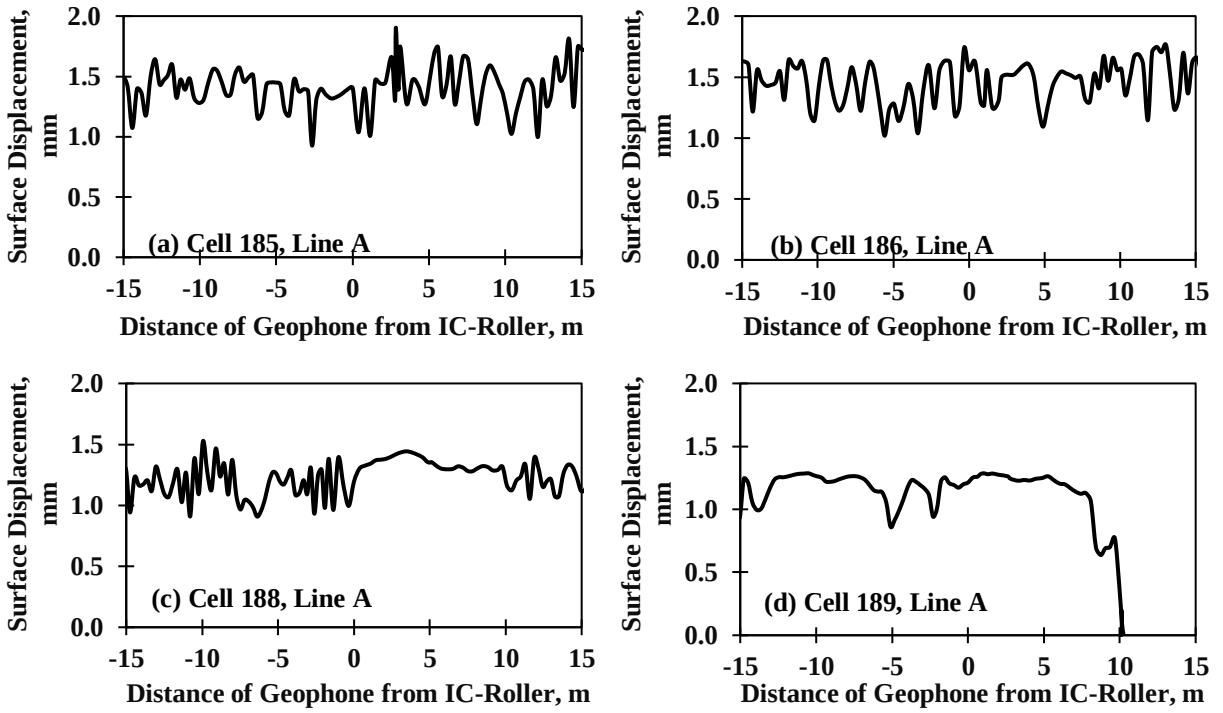

Figure G-25. Surface displacement calculated during vibratory moving test on top of subgrade layer for (a) Cell 185, (b) Cell 186, (c) Cell 188, and (d) Cell 189 at MnROAD.

Figure G-26 illustrates the displacement basin obtained from the simulated FE SSL model and the corresponding measured displacement basin at the three different depths for Cell 188. Displacement basins for the other cells show similar patterns and are omitted. As the roller moves further away from the geophones location, the displacement is attenuated at a faster rate for the FE model in comparison to the field data. However, for the analysis presented hereby, only the peak displacement values of the measurements are used.

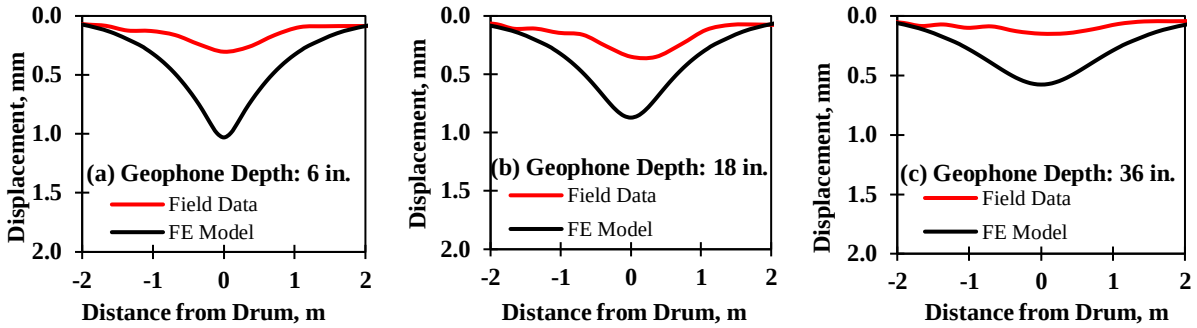

Figure G-26. Displacement basin at different depths as obtained from FE SSL model and field measurements during vibratory moving test on top of base for Cell 188 at MnROAD.

Figure G-27 also shows the variation of displacement with depth for Cell 188. Even though the amplitudes of the displacements obtained from the simulation and field data are different, the similar trend of the two displacement profiles shows that the FE model can yield promising results.

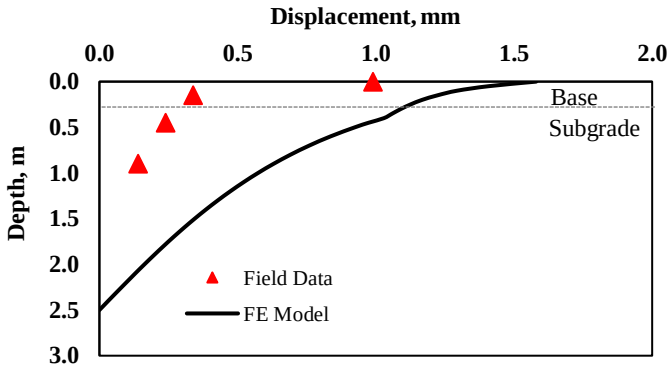

Figure G-27. Vertical displacement at different depths as obtained from FE SSL model and field measurements during vibratory moving test on top of base for Cell 188 at MnROAD.

Table G-14 summarizes the peak displacement values measured as the roller passed directly on top of the geophones for Cells 185 through 189. The peak displacement decreases with depth.

The two shallower geophones at depths of 0.15 m (6 in.) and 0.45 m (18 in.) captured less displacement for the sandy subgrades (i.e., Cells 185 and 186) as compared to the clayey subgrade (Cells 188 and 189). This trend reverses for the deeper geophone indicating that the clayey material exhibits a shallower depth of influence as it attenuates displacement less than the sandy material.

Table G-14. Vertical displacement at different depths for IC roller under moving vibration tests on top of base at MnROAD.

Embedded Geophone Depth		Peak Vertical Displacement (mm)	
		Field	Field
Sandy Subgrade		**Cell 185**	**Cell 186**
Depth	Surface	1.36	1.29
	0.15 m (6 in.)	0.25	0.29
	0.45 m (18 in.)	0.22	0.19
	0.90 m (36 in.)	0.21	0.17
Clayey Subgrade		**Cell 188**	**Cell 189**
Depth	Surface	0.99	1.25
	0.15 m (6 in.)	0.30	0.38
	0.45 m (18 in.)	0.35	0.28
	0.90 m (36 in.)	0.15	0.11

Figure G-28 compares the measured and simulated FE SSL deflections on top of the base layer. A factor of about 5.1 is required for matching the simulated and measured field data tested on top of the base for Cells 185 through 189 as compared to a factor of about 3.5 for the subgrade materials. A coefficient of determination, R^2 = 0.45, and standard error of estimate, *SEE* = 0.26 mm, were determined for the relationship.

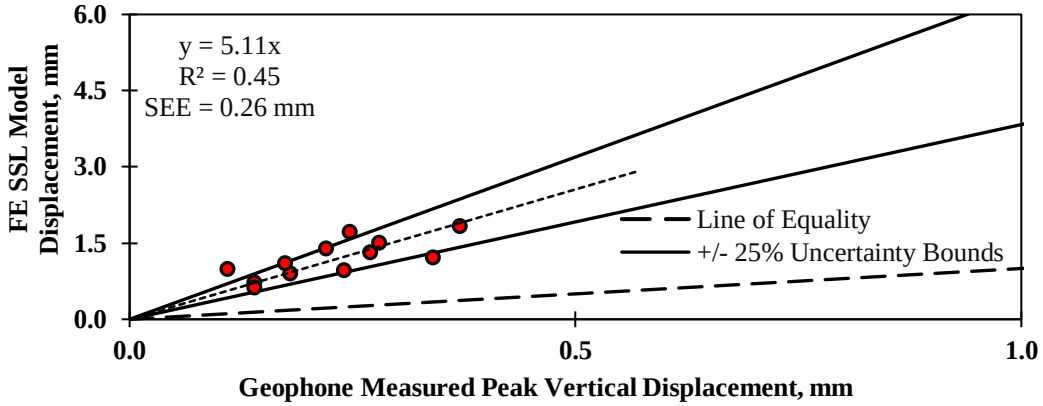

Figure G-28. Relationship between field-measured displacements for vibratory moving roller on top of base layer and FE SSL model displacement at MnROAD.

Similar to the single-layer systems, the measured displacements were computed using different FE models. In this respect, five different scenarios were taken into consideration including linear and nonlinear behaviors for the simulated geomaterials under static and vibratory loading conditions. Table G-15 summarizes the descriptive statistics of the obtained relationships.

The recorded displacements under different FE scenarios at different depths are summarized in Table G-16. The displacements for the nonlinear FE models (SSN and VSN), when the nonlinear parameter k'_1 associated with the backcalculated LWD modulus, get closer to the corresponding displacements captured by linear SSL model. In other words, the variability in the relationships between the field measurements and the simulated displacements decreases as nonlinearity was considered in the geomaterials' constitutive model.

Table G-15. Summary of the descriptive relationship of the field-measured displacement and different FE scenarios for two-layer systems under vibratory moving rollers for Site 2.

Descriptive Correlation	SSL FE Model	SSN FE Model		VSN FE Model	
		k'_1: Laboratory Test	k'_1: Backcalculated from E_{LWD}	k'_1: Laboratory Test	k'_1: Backcalculated from E_{LWD}
Adjustment Factor, *S*	5.11	3.19	5.06	3.55	5.84
Coefficient of Determination, R^2	0.45	0.81	0.54	0.72	0.57
Standard Error of Estimate, *SEE*	0.26	0.08	0.36	0.16	0.58

Table G-16. Vertical displacements obtained from different FE scenarios at different depths under rollers operating on top of base layer during the moving tests for Site 1.

Embedded Geophone Depth			Vertical Displacement, mm							
Sandy Subgrade			**Cell 185**				**Cell 186**			
Depth			**Surface**	**0.15 m (6 in.)**	**0.45 m (18 in.)**	**0.90 m (36 in.)**	**Surface**	**0.15 m (6 in.)**	**0.45 m (18 in.)**	**0.90 m (36 in.)**
FE Scenarios	**SSL**		2.2	1.7	1.4	0.9	1.6	1.3	1.1	0.7
	SSN	**k'_1: Laboratory Test**	1.0	0.9	0.7	0.5	1.0	0.9	0.7	0.4
		k'_1: Backcalculated	2.2	2.0	1.7	1.1	1.6	1.5	1.3	0.9
	VSN	**k'_1: Laboratory Test**	1.5	1.2	0.8	0.5	1.5	1.2	0.8	0.5
		k'_1: Backcalculated	3.0	2.6	2.1	1.3	2.3	2.0	1.6	1.0
Clayey Subgrade			**Cell 188**				**Cell 189**			
Depth			**Surface**	**0.15 m (6 in.)**	**0.45 m (18 in.)**	**0.90 m (36 in.)**	**Surface**	**0.15 m (6 in.)**	**0.45 m (18 in.)**	**0.90 m (36 in.)**
FE Scenarios	**SSL**		1.6	1.2	1.0	0.6	2.3	1.8	1.5	1.0
	SSN	**k'_1: Laboratory Test**	1.3	1.1	0.8	0.5	1.2	1.1	0.8	0.5
		k'_1: Backcalculated	1.4	1.3	1.0	0.7	1.4	1.3	1.1	0.7
	VSN	**k'_1: Laboratory Test**	1.5	1.2	0.8	0.5	1.6	1.2	0.8	0.5
		k'_1: Backcalculated	1.6	1.4	1.0	0.6	1.8	1.4	1.0	0.7

Figure G-29 shows the normalized peak displacements with respect to maximum surface displacement on top of the base layers for Cells 185 through 189. The representative normalized displacement profiles obtained from the corresponding FE models are shown for Cells 185 and 188. FE models of Cells 186 and 189 pavements show similar normalized displacement profiles and are omitted. Cells 185 and 186 (sandy subgrade) have a deeper depth of influence as compared to Cells 188 and 189 (see Figure G-36). The extrapolated depth of influence for tests on top of the two-layer systems varies between 0.9 m (35 in.) to 1.4 m (55 in.). Shallower depths of influence are observed for Cells 188 and 189 (base courses on top clayey subgrade) indicating that the clayey materials attenuate material displacement less than sandy materials. The depth of influence is about 2.0 m (79 in.) for the vibratory FE models, while the penetration depth slightly increases for the static cases (2.1 m or 83 in.).

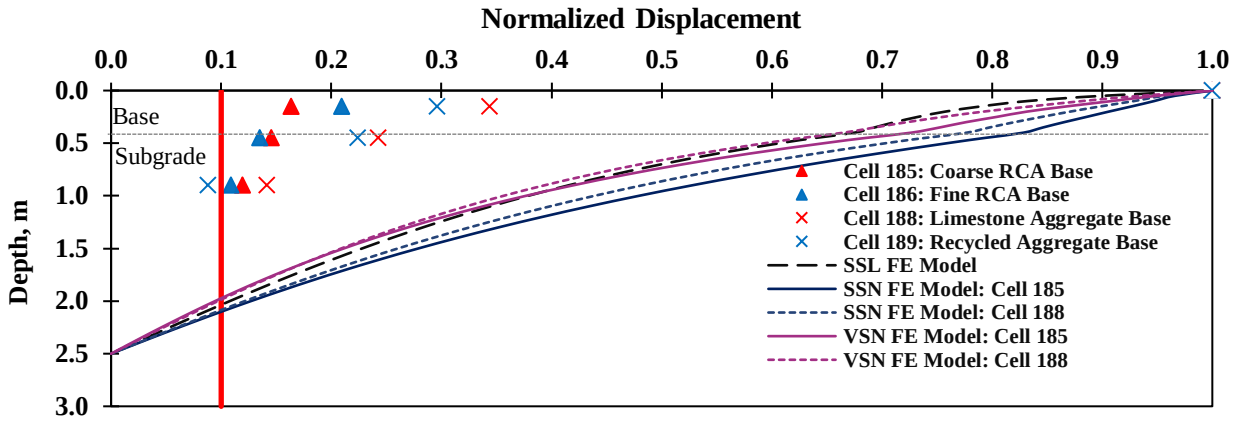

Figure G-29. Comparison of normalized displacement obtained from FE model and field data during vibratory moving test on top of base layer for Cells 185–189 at MnROAD.

Development of Adjustment Factor

Figure G-30 compares the measured and simulated peak displacements directly under the roller at different depths, under both the stationary and moving conditions for all evaluated sites. The compiled results show that the SSL FE model yields displacements that are globally about 2.9 times greater than the field measurements with a coefficient of determination, R^2 = 0.42, and *SEE* = 0.47 mm.

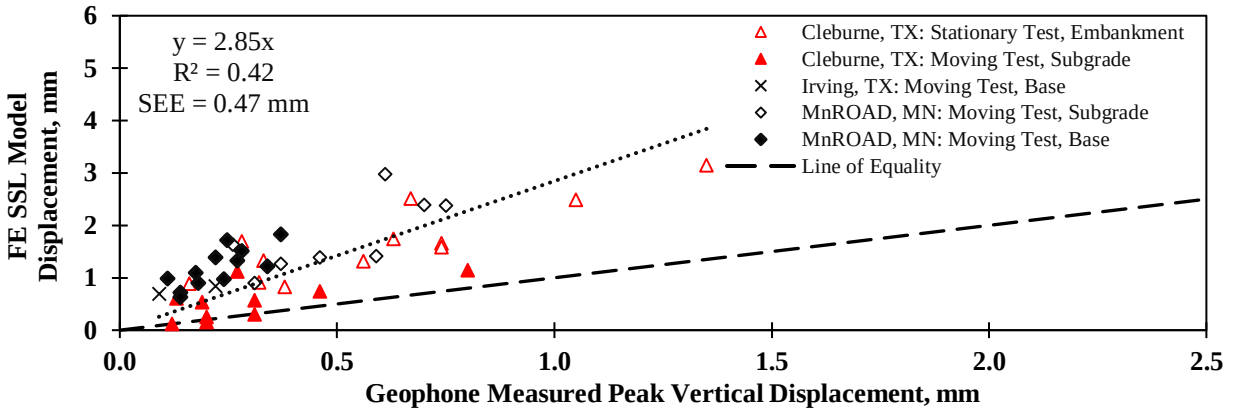

Figure G-30. Relationship between field-measured displacements for vibratory rollers and FE SSL model displacement.

Two scenarios were utilized for each of the nonlinear models (being SSN or VSN): (1) using the laboratory k'_1 as the input variable and (2) adjusting the k'_1 with a proper stress state using LWD modulus to better represent the compaction effort that the geomaterials have experienced in the field. Figure G-31 shows the global relationship of the nonlinear SSN FE model and the corresponding field data when the first approach is taken into account. The data collected from the two test sites can be separated due to the uncertainty in the stress states. In other words, when the laboratory nonlinear k'_1 parameter is employed for simulating the geomaterials behavior, an unreliable stress state might be achieved. This limitation can be solved by backcalculating k'_1 using the LWD modulus implemented on top of the compacted layers.

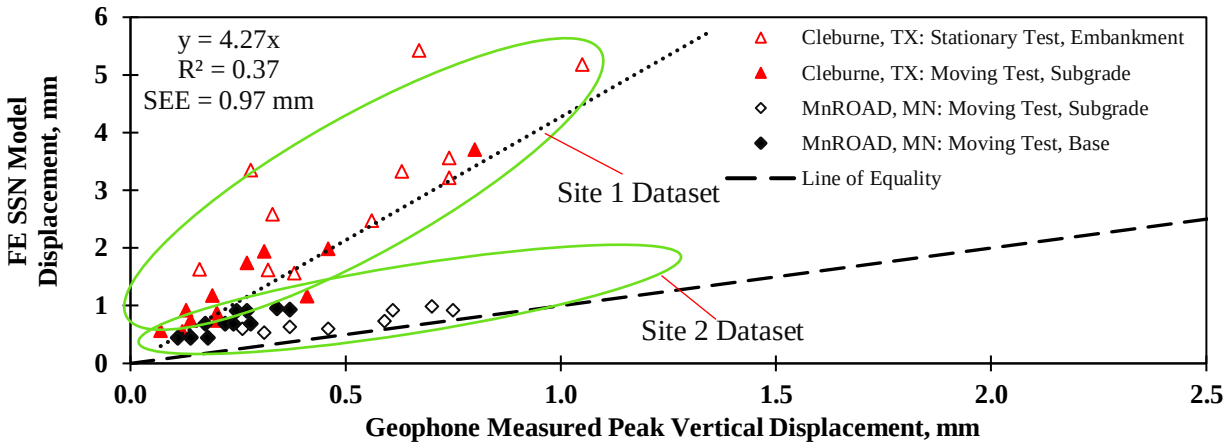

Figure G-31. Relationship between field-measured displacements for vibratory rollers and FE SSN model displacement.

To more realistically simulate the compacted materials, Scenario (2) was taken into consideration for the SSN models. In other words, parameter k'_1 was backcalculated using the field LWD test results. A new transfer function that correlates better the SSN FE model with the measured field displacements is obtained, as shown in Figure G-32. The SSN FE model yields displacements about 3.2 times greater than the embedded geophone measurements. In comparison to SSL FE model, the global relationship improved as judged by a higher coefficient of determination, $R^2 = 0.60$, and a lower standard error of estimate, SEE = 0.41 mm. However, a part of the variation in the observed comparison between the simulated and field data can be attributed to the two-layer geosystems since the addition of stiffer material on top of the subgrade layer can cause an enhancement in the bouncing behavior that the moving roller experiences.

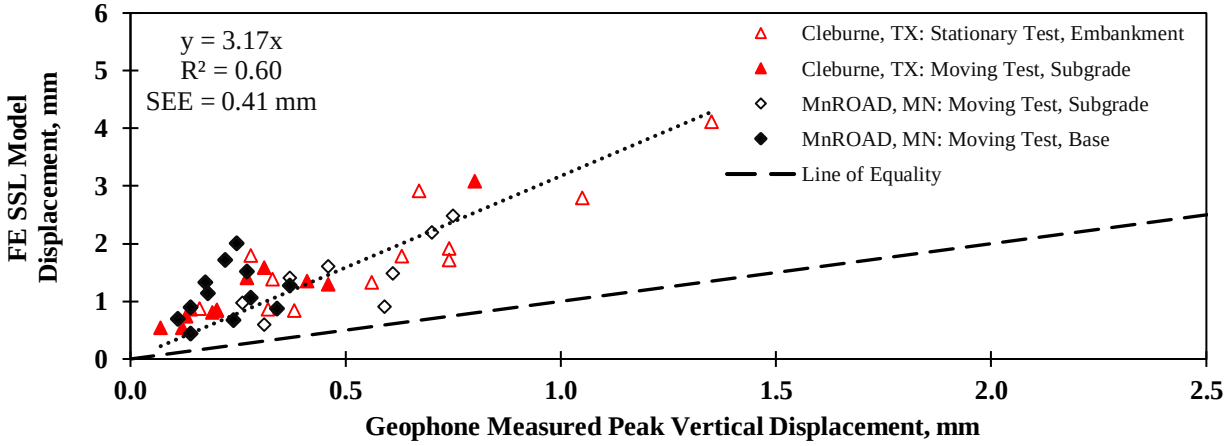

Figure G-32. Relationship between field-measured displacements for vibratory rollers and FE SSN model displacement: k'_1 is backcalculated using the LWD modulus.

Similarly, two scenarios were considered for the FE VSN models. Taking the laboratory nonlinear k'_1 parameter as the input parameter (Scenario 1) may cause a great variation in the global relationship for the two test sites as demonstrated in Figure G-33. Again, the observed separation in the results for the two implemented sites is attributed to the different stress state and confining pressure that the materials have experienced during field and laboratory tests.

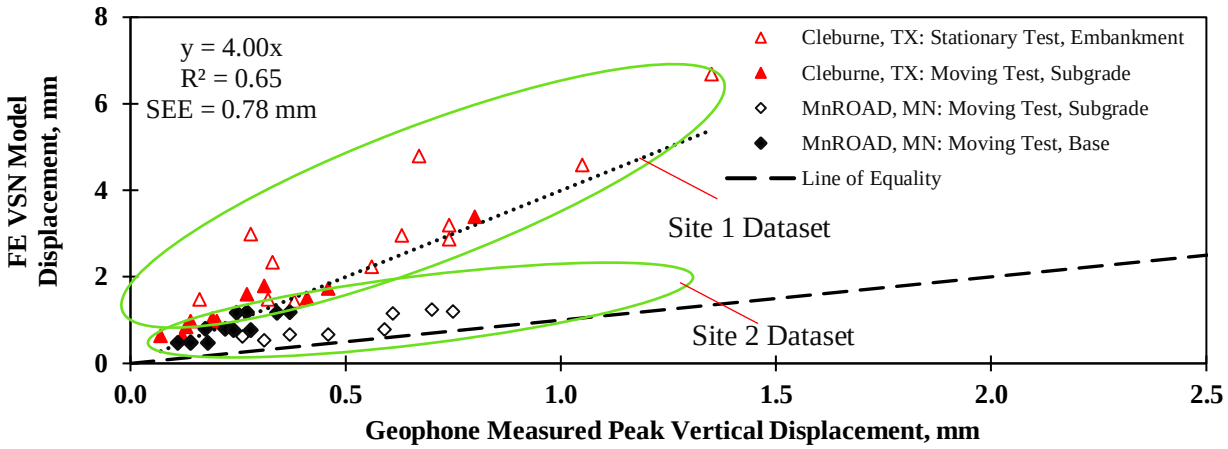

Figure G-33. Relationship between field-measured displacements for vibratory rollers and FE VSN model displacement.

Figure G-34 shows the global relationship between the measured displacements and the simulated VSN FE results.

Similar to the SSN FE model, the backcalculated k'_1 was incorporated into the VSN FE model (Scenario 2) to better simulate the field condition. The best fit regression has a slope of 3.5 with R^2 of 0.71 and SEE of 0.42 mm indicating that the consideration of vibratory conditions and material nonlinearity in the model can make an improvement to the transfer function derived from the above-mentioned comparison (see Figure G-34). Though a part of the variation and uncertainty in the results is inevitable due to the bouncing behavior of the operating roller on the stiffer two-layer systems.

The summary of the derived transfer functions between different FE scenarios employed in this study and the measured field data is listed in Table G-17.

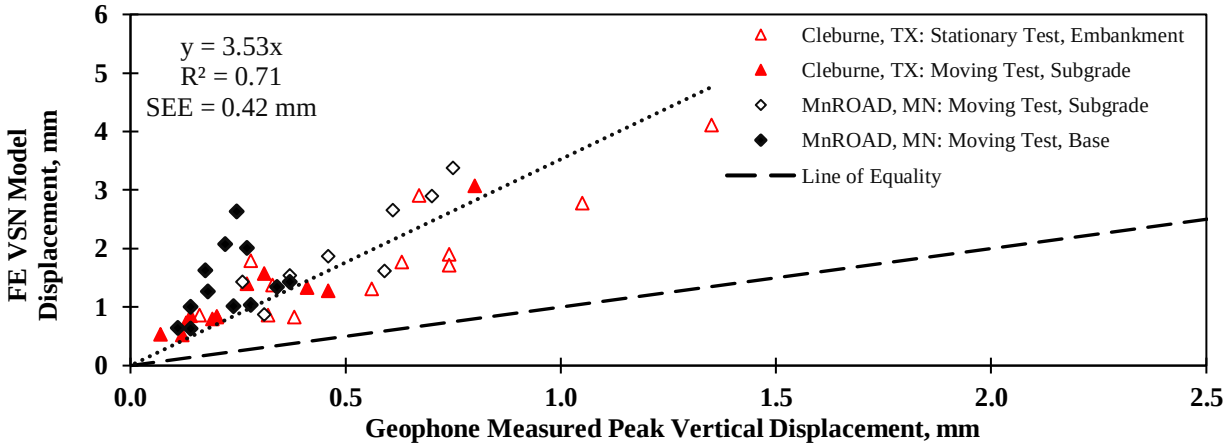

Figure G-34. Relationship between field-measured displacements for vibratory rollers and FE VSN model displacement: k'_1 is backcalculated using the LWD modulus.

Table G-17. Summary of the descriptive relationship of the field-measured displacement and different FE scenarios for two-layer systems under vibratory moving rollers for Site 2.

Descriptive Correlation	SSL FE Model	SSN FE Model		VSN FE Model	
		k'_1: Laboratory Test	k'_1: Backcalculated from E_{LWD}	k'_1: Laboratory Test	k'_1: Backcalculated from E_{LWD}
Adjustment Factor, *S*	2.85	4.27	3.17	4.00	3.53
Coefficient of Determination, R^2	0.42	0.37	0.60	0.65	0.71
Standard Error of Estimate, *SEE*	0.47	0.97	0.41	0.78	0.42

Pressure Cells

Pressure cells were embedded at two different locations, as schematically illustrated by Figure D.5. For every single cell, along Line A, one pressure cell was embedded 0.3 m (12 in.) into the subgrade, while another one was embedded below the base layer, i.e. 0.3 m (12 in.) from the base surface. The measured vertical stress recorded by the pressure cells embedded in Cells 186 and 188 are shown in Figure G-35.

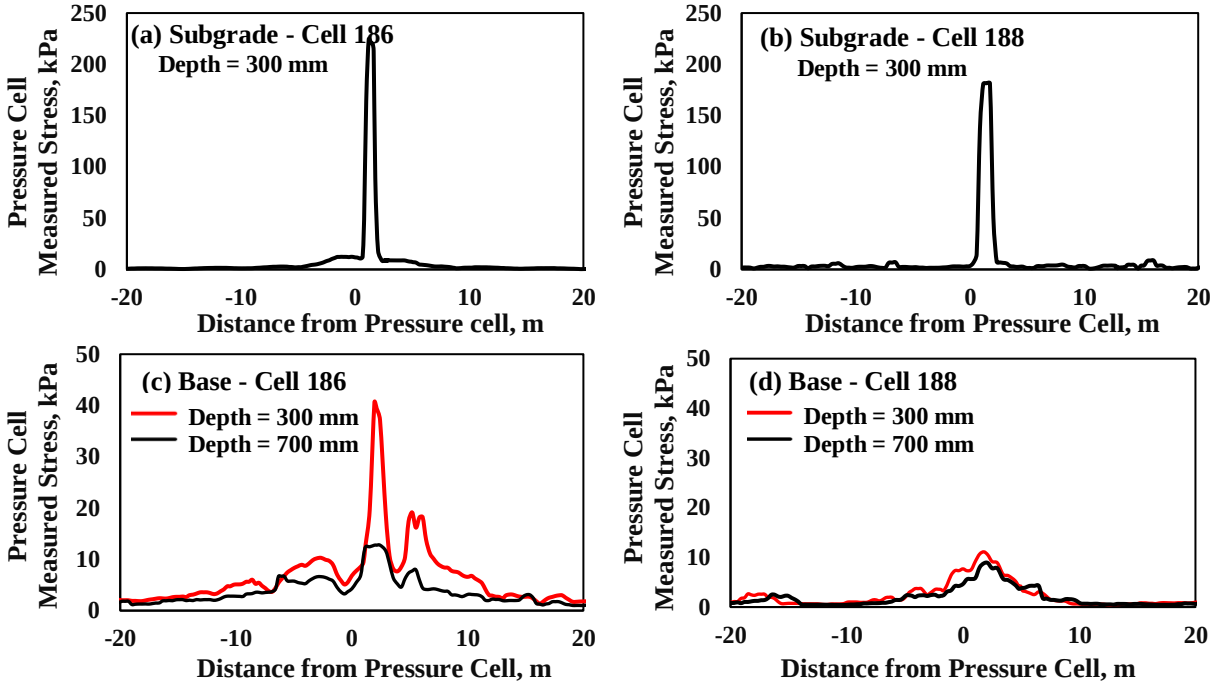

Figure G-35. Stress measured by embedded pressure cells during vibratory moving test on top of subgrade layer for (a) Cell 186 and (b) Cell 188, and on top of base layer for (c) Cell 186 and (d) Cell 188.

Figures G-35a and G-35b show the vertical stress profile constructed as the roller approached and moved away from the pressure cell locations while proof-mapping the subgrade. Peak stresses occurred when the roller was located directly on top of the pressure cell. Likewise, Figures G-35c and G-35d show the vertical stress profile as measured by the pressure cells as the roller proof-mapped the base layer. The shallower the pressure cell is embedded, the higher the measured stress will be. However, the measured stresses attenuated significantly when proof-mapping occurred on top of the base compared to stresses obtained when proof-mapping is performed on subgrade, despite pressure cells being buried at equal depths from the

surface. Moreover, the reconstructed stress profiles exhibit more variability in measurements on mapping of base material than those obtained when mapping subgrade. This can be attributed to bouncing of the drum due to the mapping of a stiffer material.

Peak measured vertical stresses are compared in Figure G-36 with the vertical stresses as obtained from the FE VSN models for subgrade material for Cells 185 through 189. The field-measured stresses vary significantly for different cells indicating that the materials exhibited significant plastic behavior during the mapping process due to the low stiffness of the materials and poor compaction. On the other hand, the FE models of proof-mapping of subgrade provided similar stresses for all geomaterials since the modified MEPDG constitutive model does not capture the plastic response of the materials. This limitation is also seen in Figure G-37 for the base layer.

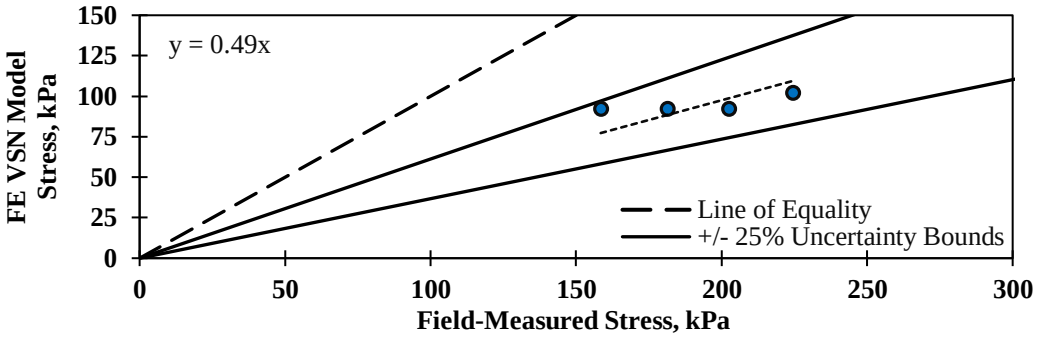

Figure G-36. Relationship between Site 2 field-measured stress for different vibratory moving rollers on top of subgrade layer and FE SSL model stress.

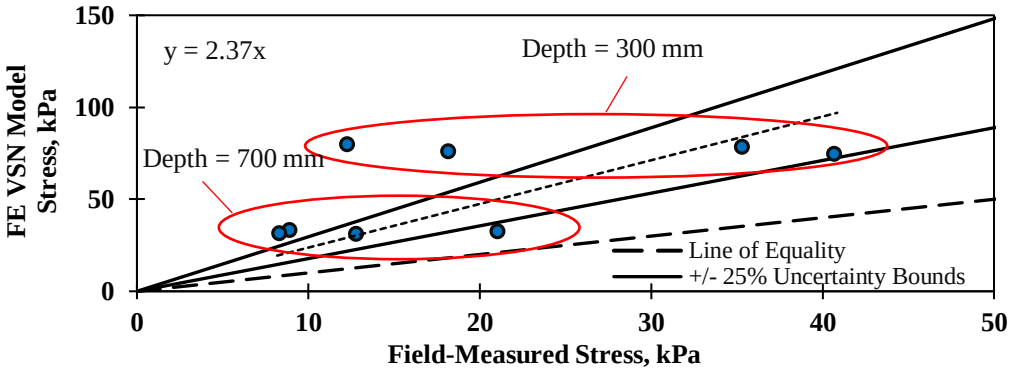

Figure G-37. Relationship between Site 2 field-measured stress for different vibratory moving rollers on top of base layer and FE SSL model stress.

Evaluation of Inverse Algorithms to Extract Layer Mechanical Properties

To extract the mechanical properties of the compacted geomaterials in real time, inverse algorithms were proposed and described in Appendix E. Five inversion scenarios/architectures with different levels of sophistication were evaluated. The more complex the constructed inverse solver is, the more precise the solver will be. However, more complex inverse solvers require greater laboratory efforts to determine the needed input variables. Table G-18 summarizes the inverse model input scenarios described in Appendix C for backcalculating the base modulus. Scenarios 4 and 5 include the parameter k'_1 backcalculated using the implemented LWD modulus to properly represent the stress state and compaction effort employed in the field.

Table G-18. Different inverse scenarios for extracting modulus of base layer.

Scenarios	Input Features	Target
1	h, k'_{2b}, k'_{3b}, d_2, d_1	Base Modulus
2	h, k'_{2b}, k'_{3b}, d_2, $M_{r\text{-}sub}$	Base Modulus
3	h, k'_{2b}, k'_{3b}, d_2, $M_{r\text{-}sub}$ (Representative)	Base Modulus
4	h, $k'_{1b\text{-}back}{}^{*}$, k'_{2b}, k'_{3b}, d_2, d_1	Base Modulus
5	h, $k'_{1s\text{-}back}{}^{*}$, k'_{2s}, k'_{3s}, $k'_{1b\text{-}back}{}^{*}$, k'_{2b}, k'_{3b}, d_2, d_1	Base Modulus

* Note: $k'_{1\text{-back}}$ values backcalculated using E_{LWD}.

Table G-19 lists the collected data required for the evaluation of the above-mentioned scenarios for the four cells of Site 2 (Cells 185 through 189 at MnROAD facility). The modulus at the middle of the base layer was used as a representative of the top layer. The summary of the backcalculated $E_{LWD\text{-}base}$ and resilient modulus for the base material are reported in Table G-2. Prior to feeding the input displacements d_1 and d_2 into the inverse solver, the field-measured displacements were adjusted using the factor $f = 3.2$, determined in Section G.6 for SSN models. The outcome of this study obtained from different scenarios can be summarized in the following manner.

Table G-19. Summary of predictor variables measured for Site 2 (MnROAD).

MnROAD Cells	Base Thickness	Nonlinear Parameters for Subgrade Layer			Nonlinear Parameters for Base Layer			Resilient Modulus of Subgrade Layer		Surface Displacement at	
	h, mm	$k'_{1s\text{-}back.}$	k'_{2s}	k'_{3s}	$k'_{1b\text{-}back.}$	k'_{2b}	k'_{3b}	$M_{R\text{-}sub}$, MPa	$M_{R\text{-}sub\text{-}rep.}$, MPa	Top of Base d_2, mm	Top of Subgrade d_1, mm
Cell 185	300	123	1.6	-0.6	467	0.8	-0.1	79	79	1.36	1.41
Cell 186	300	152	1.6	-0.6	722	0.9	-0.1	79	79	1.29	1.34
Cell 188	300	462	0.6	-2.6	709	0.6	-0.1	59	60	0.99	1.22
Cell 189	300	283	0.6	-2.6	470	0.9	0.1	59	60	1.25	1.18

Scenario 1: h, k'_{2b}, k'_{3b}, d_2, d_1

Scenario 1 is the simplest approach since no in-situ spot test (e.g., LWD test) is required to extract the base modulus. The estimated base moduli of Cells 185 through 189 from the inverse solver are compared with the corresponding base moduli ($E_{LWD\text{-}Base}$) and representative resilient moduli ($M_{R\text{-}Base}$) in Figure G-38. Figure G-45(a) shows that base modulus can be predicted properly using the first scenario as these values fell close to the line of equality and within the 20% upper and lower bounds, though with some uncertainty as judged by the scattering of the results. Figure G-38(b) shows that the average extracted modulus is about 1.3 times greater than the representative resilient moduli of the base materials, revealing that resilient modulus as obtained in the laboratory might not be an appropriate indicator of the stiffness of the compacted layer under a moving roller. This suggests that the confining condition attained in the field due to the compaction effort is not achieved in the laboratory using the reconstructed samples subjected to the resilient modulus tests.

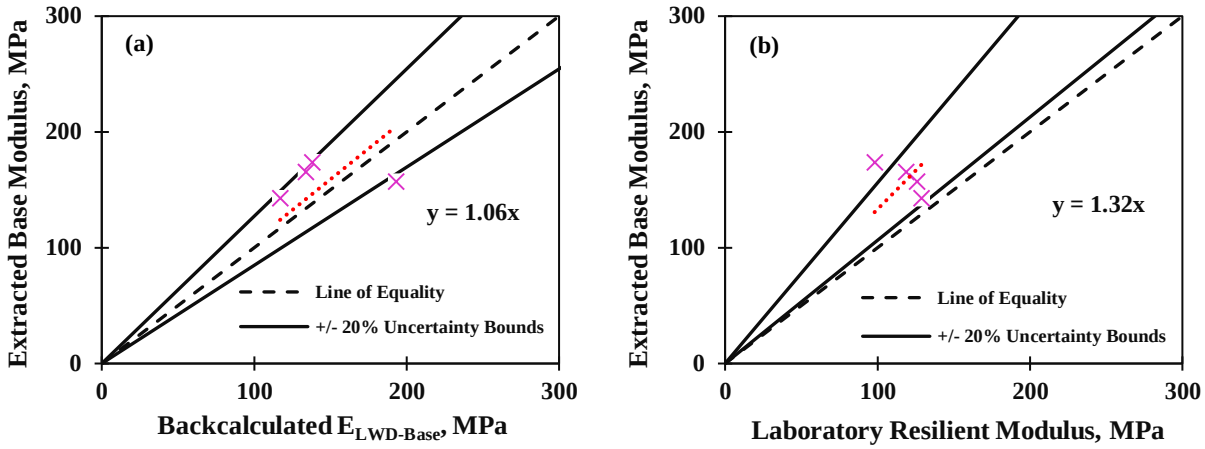

Figure G-38. Comparison of extracted base moduli obtained from Scenario 1 with corresponding (a) backcalculated LWD modulus ($E_{LWD\text{-}base}$) and (b) resilient modulus ($M_{R\text{-}Base}$).

Scenario 2: h, k'_{2b}, k'_{3b}, d_2, $M_{R\text{-}sub}$

As shown in Figure G-39, the data are more scattered in comparison to Scenario 1, as judged by the number of cases falling outside the 20% upper and lower bounds. Figure G-39(a) shows that the average extracted base moduli are slightly greater than the corresponding backcalculated $E_{LWD\text{-}base}$ moduli. While the comparison of the laboratory resilient modulus and the extracted base modulus indicate a factor of about 1.4 (Figure G-39[b]).

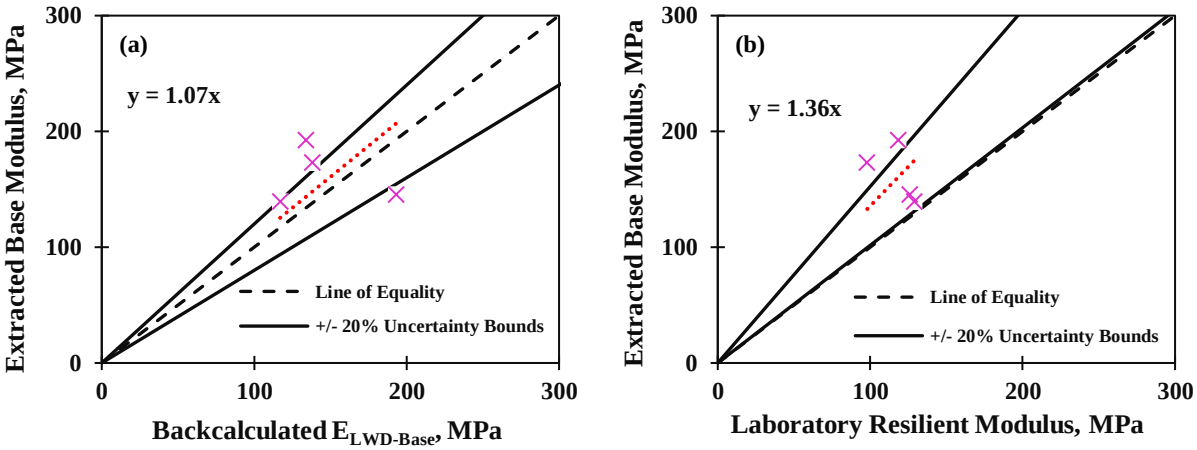

Figure G-39. Comparison of extracted base moduli obtained from Scenario 2 with corresponding (a) backcalculated LWD modulus ($E_{LWD\text{-}base}$) and (b) resilient modulus ($M_{R\text{-}Base}$).

Scenario 3: h, k'_{2b}, k'_{3b}, d_2, $M_{R\text{-}sub}$ (Representative)

Scenario 3 is somewhat comparable to Scenario 2. For Scenario 2, the resilient modulus obtained from the laboratory test was taken as the predictor variable; while Scenario 3 requires the representative resilient modulus as input. Again, the regression fit line laid close to the line of equality when the calculated base moduli were compared to the LWD moduli with some uncertainty (Figure G-40[a]). A factor of 1.3 is obtained when the base moduli are compared to their respective resilient moduli. The scattering and the level of uncertainty can be closely related to the level of sophistication of the employed inverse solver. However, as observed in Appendix E, the prediction power of the inverse solvers improved significantly

by introducing the nonlinear k' parameters of subgrade layer in general and nonlinear k'_1 (related to stiffness) parameter of the base in particular into the model.

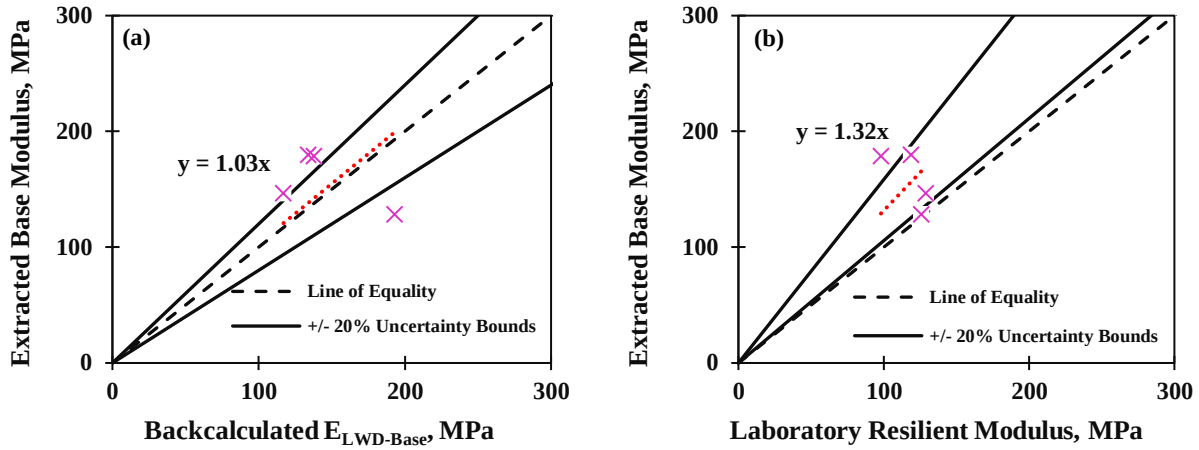

Figure G-40. Comparison of extracted base moduli obtained from Scenario 3 with corresponding (a) backcalculated LWD modulus ($E_{LWD\text{-}base}$) and (b) resilient modulus ($M_{R\text{-}Base}$).

Scenario 4: h, k'_{1b} (Backcalculated using E_{LWD}), k'_{2b}, k'_{3b}, d_2, $M_{R\text{-}sub}$ (Representative)

Parameter k'_{1b} affects the prediction power of the constructed ANN model favorably as observed in Figure G-41. The correlation between the extracted and backcalculated LWD moduli improved noticeably when the parameter k'_{1b} was introduced as one of the predictor variables (Figure G-41[a]). The coefficient of determination $R^2 = 0.92$ and standard error of estimate SEE = 15 MPa indicates how well the two aforementioned values are correlated. The transfer function derived between the extracted modulus of the top (base) layer is about 1.3 times of the backcalculated LWD modulus. Although the prediction power of Scenario 4 has been evidently improved; the use of this inverse model requires in-situ LWD modulus-based spot test to be performed.

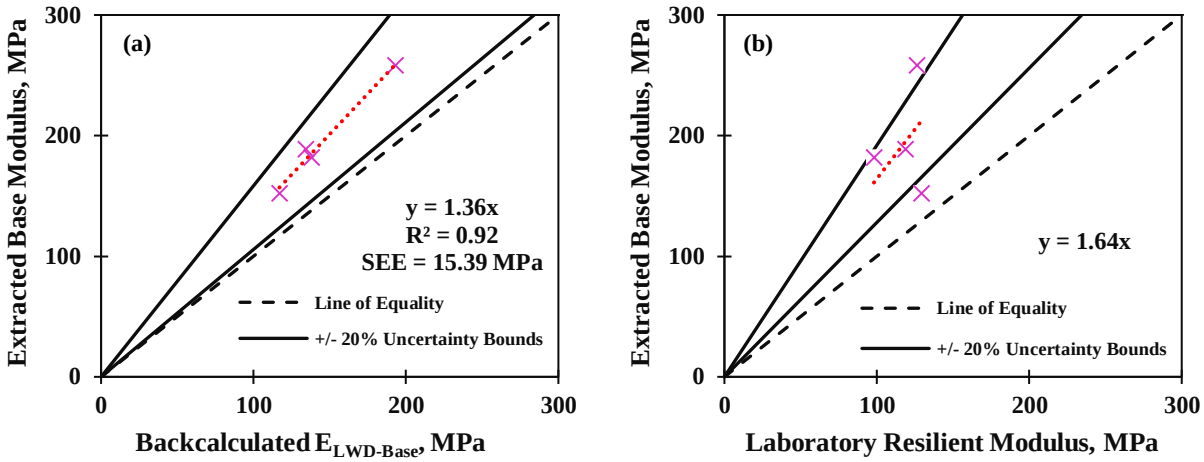

Figure G-41. Comparison of extracted base moduli obtained from Scenario 4 with corresponding (a) backcalculated LWD modulus ($E_{LWD\text{-}base}$) and (b) resilient modulus ($M_{R\text{-}Base}$).

Scenario 5: h, k'_{1s} (Backcalculated using E_{LWD}), k'_{2s}, k'_{3s}, k'_{1b} (Backcalculated using E_{LWD}), k'_{2b}, k'_{3b}, d_2, d_1.

Scenario 5 is the most complicated inverse solver as its construction requires nonlinear k' parameters of both subgrade and base materials as well as the implementation of LWD tests on top of subgrade and base materials (9 input variables in total). As shown in Figure G-42, the best fit regressions are about 1.2 and 1.4 when compared to E_{LWD} and laboratory resilient moduli, respectively.

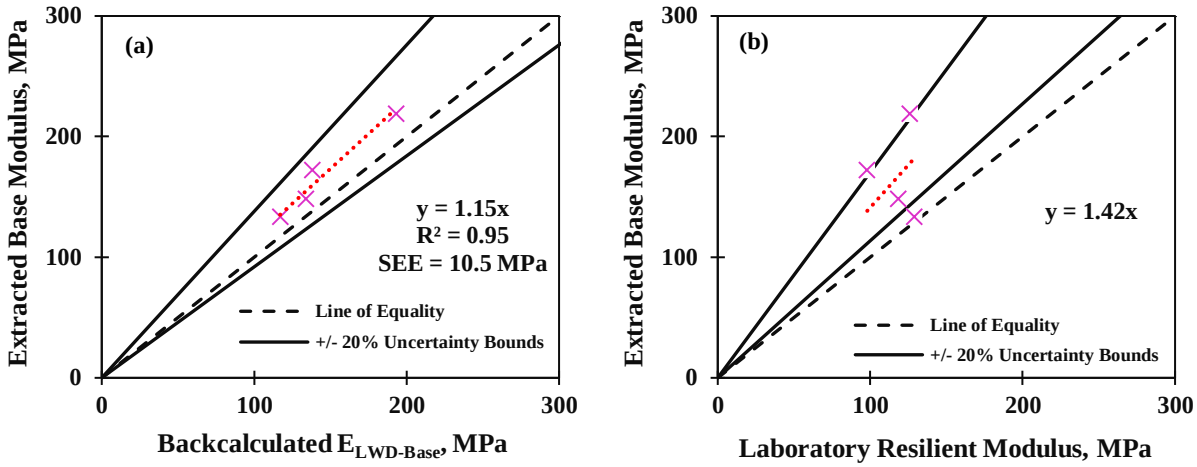

Figure G-42. Comparison of extracted base moduli obtained from Scenario 5 with corresponding (a) backcalculated LWD modulus (ELWD-base) and (b) resilient modulus (MR-Base).

The correlation between the extracted and field LWD moduli improved slightly when compared to Scenario 4, as reflected by an $R^2 = 0.95$ and SEE = 10.5 MPa, as seen in Figure G-42(a). When compared to the laboratory resilient modulus in, the most of the results fall inside the 20% uncertainty bounds, as shown in Figure G-42(b).

APPENDIX H

Mechanical Property Measurements

Introduction

Appendix H introduces the procedure for evaluating the mechanical properties of compacted geomaterials using the roller-mounted accelerometer measurements and includes the resulting mechanical properties maps generated after the analysis of the collected field measurements of the four construction cells studied at the MnROAD facility. The approach, which involved the use of the cyclic surface displacement to calculate a roller-based stiffness, is discussed in this appendix.

The secant soil stiffness, k_s, has been used toward the measurements of a mechanistic, performance-related soil property. This mechanistic measurements can be determined from the force-displacement hysteresis loops built that make use of the acceleration time histories collected by accelerometers installed in the drum. Force-displacement loops are created by plotting the time-varying contact force versus time-varying drum displacement, where contact force is calculated from the vertical response of the drum. Secant soil stiffness, k_s, can be calculated as the gradient of the line passing through the point of zero dynamic displacement to the point representing the maximum dynamic drum displacement.

A data reduction process was implemented to obtain the acceleration time signal necessary for the calculation of the roller-based stiffness. This data reduction process starts with the conversion of the accelerometer time-domain voltage output into time-domain acceleration measurements. To capture the eccentric mass position and acceleration of the roller precisely, data was sampled at a frequency of 10 kHz using blocks with 6,000 data points, for a frequency resolution of 1.67 Hz in the frequency domain. For analysis purposes, such as the calculation of CMV, the acquired acceleration data was decimated and filtered to blocks of 600 data points acquired at a sampling frequency of 1 kHz for a spatial resolution of roller measurements of 0.5 m (1.7 ft) when roller speed was of 3.2 kph (2 mph).

Once the acceleration time-history records were obtained, the deflection was found using a frequency-domain algorithm. This method requires the transformation of the accelerometer measurements, $\ddot{x}(t)$, into the frequency domain by means of a fast Fourier transform (FFT) algorithm (see Figure H-1[a]). Integration in the frequency domain is accomplished by multiplying the function by $j\omega^{-1}$, where $j = \sqrt{-1}$, as described in Equation H.1,

$$X(f) = \frac{\ddot{X}(f)}{(j\omega)^2} = \frac{\ddot{X}(f)}{-\omega^2} \ , \tag{H.1}$$

where $X(f)$ is the displacement in the frequency domain, $\ddot{X}(f)$ the acceleration signal in the frequency domain, and ω is the angular frequency in rad/s. The displacement time signal, $x(t)$, is obtained by using an inverse Fourier transform. Figure H-1(b) shows the displacement time signal obtained by implementing the described approach to the sample acceleration record shown in Figure H-1(a).

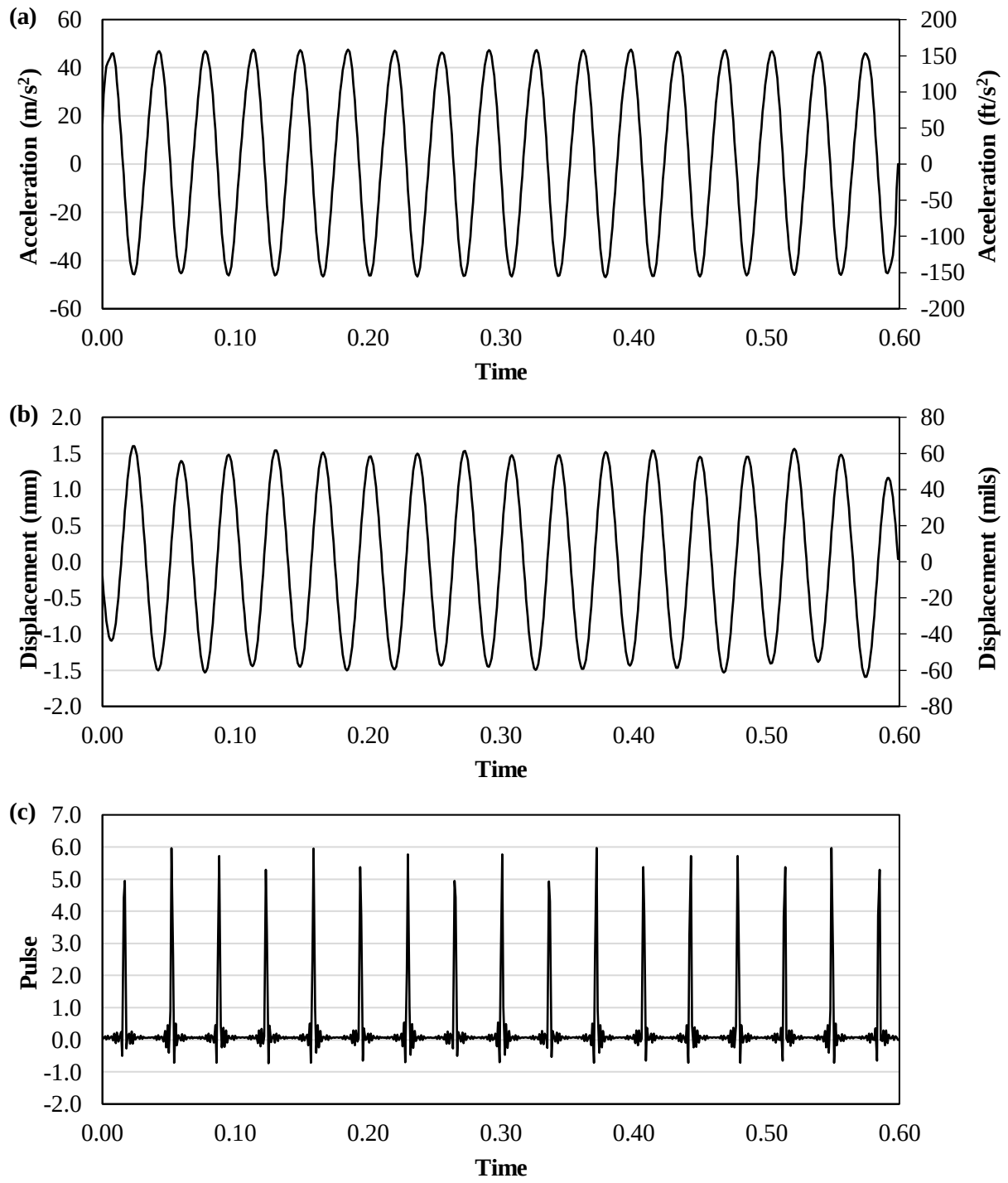

Figure H-1. Time signals: (a) acceleration time signal, (b) deflection time signal obtained after omega arithmetic method, and (c) eccentric mass position indicator pulse signal measurements on sandy subgrade.

The total applied force consists of the machine weight, the eccentric force and the drum and frame inertia, as shown in Equation H.2,

$$F_t = m_D \ddot{x}_D + m_F \ddot{x}_F + \left(m_D + m_F\right) g + m_0 e_0 \omega^2 \cos\left(\omega t + \phi\right), \quad \text{(H.3)}$$

where m_D and m_F are the drum and frame mass, respectively, $\ddot{x}_D$ and $\ddot{x}_F$ are the drum and frame masses accelerations (to calculate inertia), g is the gravity acceleration constant, m_0e_0 is the mass-eccentricity and ϕ is the phase lag. These parameters are listed among the operating features of the roller used at the site, provided in Table F-3. To calculate the applied force, the eccentric force is calculated by measuring the vertical drum acceleration and eccentric mass position, while the frame inertia is neglected.

To record the position of the eccentric mass, a third channel of the data acquisition system was dedicated to record a pulse signal (indicating eccentric mass position) in addition to the two channels that acquired the accelerometer-based measurements. A sample of this signal is shown in Figure H-1(c). This third channel records a pulse that is used to calculate the phase lag necessary to adjust the sinusoidal component of the force caused by the eccentric mass.

Figure H-2 shows the components that comprise the total applied force: (1) force due to drum inertia, $F_D = m_D\ddot{x}_D$, calculated using the vertical component of the accelerometer measurements, (2) force due to rotation of the eccentric mass, $F_{ev} = m_0e_0\omega^2\cos(\omega t + \phi)$, adjusted with the phase shift using the pulse signal indicating the eccentric mass position, and (3) the operating weight, $(m_D + m_F)g$, which can be neglected in the calculation of the stiffness, as the latter is constant and only shifts the force-displacement hysteresis loop. The force components of the time record depicted in Figure H-2 were generated using the acceleration signal and pulse shown in Figure H-1(a) and H-1(c), respectively.

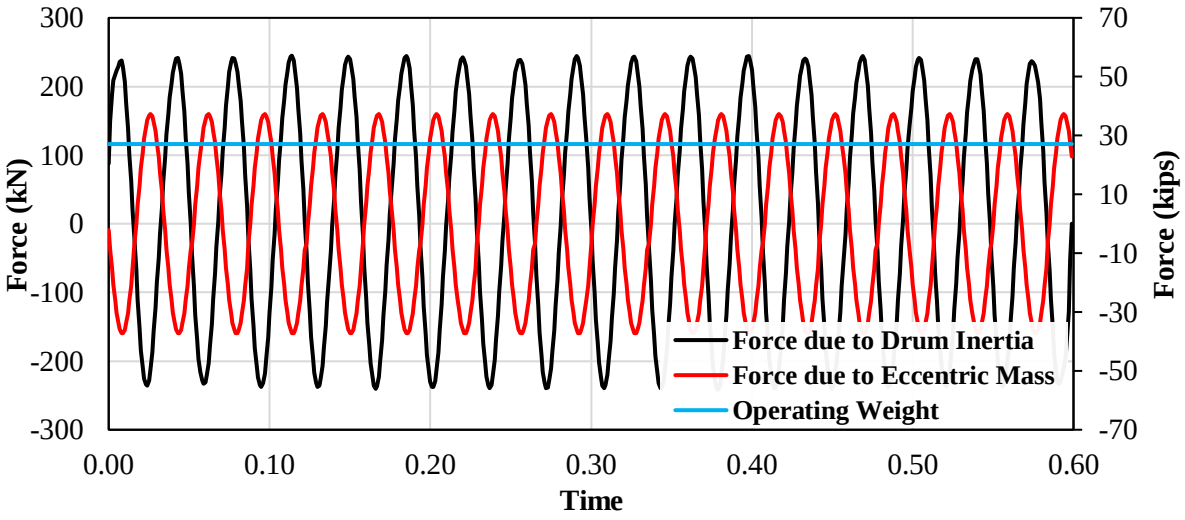

Figure H-2. Components of total applied force.

Using these measurements, the force-displacement hysteresis loops can be developed to obtain the roller-measured stiffness. Figures H-3 and H-4 show the force-displacement hysteresis loops from sample measurements obtained from proof-mapping measurements along one of the passes on top of the two different subgrade materials and on top of one of the base materials, respectively. The pavement structure and dimensions of the four cells are described in Figures F-5 and F-11. Figure H-3 compares the stiffness between sandy and clayey subgrade materials. As expected, higher stiffness values were measured on top of the sandy material. As shown in Figure H-4, when a 300 mm (12 in.) coarse RCA base material was laid on top of the sandy subgrade, the roller-measured stiffness increased in magnitude as compared to the stiffness obtained on top of the sandy subgrade in the same location.

The calculation of the stiffness can also be simplified by obtaining the ratio of the complex amplitudes of the force and displacement records in the frequency domain at the roller's operating frequency. This approach, which rapidly and robustly yields a unique stiffness value for each block of data assigned to a

GPS coordinate, provides a representative stiffness analog to the average stiffness calculated from multiple force-displacement hysteresis loops for that particular block of data points.

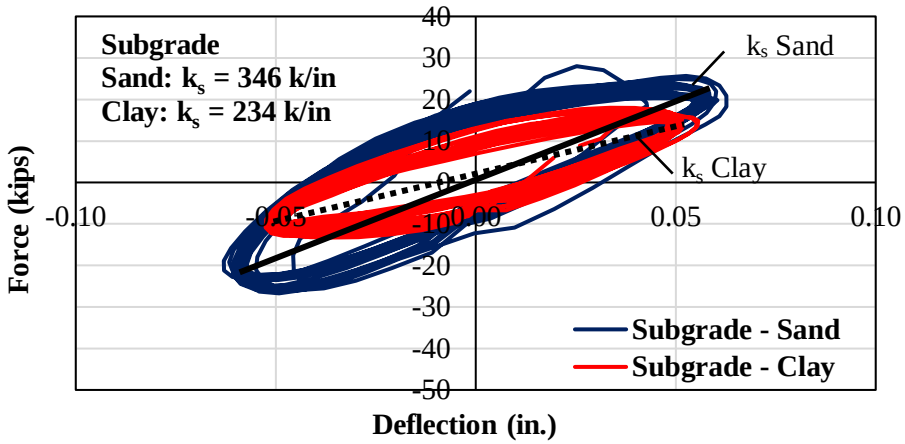

Figure H-3. Force-displacement hysteresis loops for the calculation of stiffness, k_s, obtained from measurements on sandy and clayey subgrade materials on Cells 185 and 188, respectively.

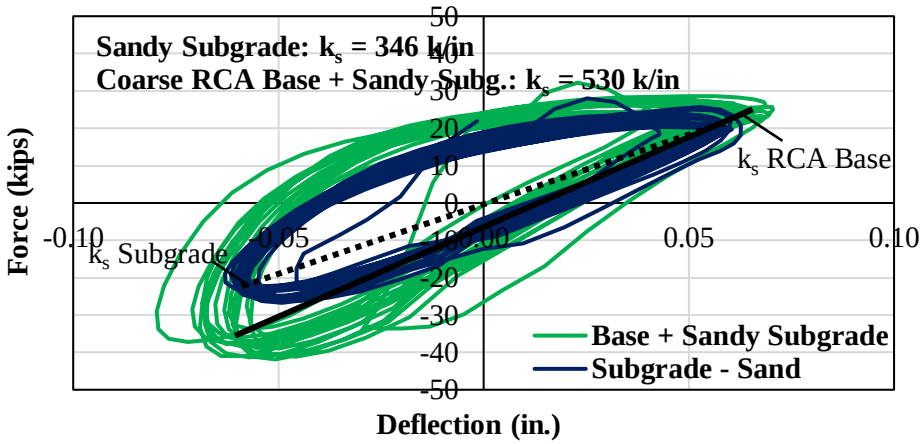

Figure H-4. Force-displacement hysteresis loops for the calculation of stiffness, k_s, obtained from measurements on sandy subgrade and coarse RCA base material on top of sandy subgrade, both on Cell 185.

Integrating this latter approach into the analysis module that processes the measured proof-mapping datasets acquired by the UTEP-developed data acquisition system allowed the development of the maps that make use of the gridding approach described in Appendix F to generate the mapping of the stiffness of geomaterials. Similar to CMV measurements, stiffness measurements were averaged within each rectangular buffered area to provide a unique stiffness value that represents an area that is adequate for rework.

Figures H-5 and H-6 summarize the spatial variation in stiffness obtained by the UTEP DAQ as the roller proof mapped the site. Higher values are obtained for sandy subgrades (Cell 185 and Cell 186) than the clayey subgrade (Cell 188 and Cell 189).

Mapping of the coefficient of variation (COV) of stiffness indicated that the stiffness values were fairly uniform, as few cells barely exceeded a COV of 10%. As the base course layers were laid upon the subgrade

sections, measured stiffness increased between 10% and 20%. Variability in stiffness measurements also increased; however, most measurements remained below a COV of 20%, indicating that the measured stiffness values were generally uniform.

(a) Stiffness (k/in)

Color Code

- < 90% of Average Measurement
- 90% of Average ≤ k_s < Average
- ≥ Average Measurement

Cell	185	186	188	189
Material	Sand	Sand	Clay	Clay

Chainage m	Chainage ft	185 D	185 C	185 B	185 A	186 D	186 C	186 B	186 A	188 D	188 C	188 B	188 A	189 D	189 C	189 B	189 A
0	0	414	417	474	408	462	474	438	421	316	309	324	295	226	239	282	271
7.5	25	387	388	441	402	440	466	441	408	315	311	302	273	248	256	303	266
15.0	50	424	426	426	385	436	457	450	415	302	307	307	271	233	242	305	253
22.5	75	421	437	424	375	455	470	447	427	293	315	291	288	254	240	307	249
30.0	100	421	429	430	385	479	477	441	407	296	309	292	283	238	241	318	260
37.5	125	400	443	446	399	492	459	436	418	282	289	293	290	247	248	320	259
45.0	150	426	489	476	407	475	493	456	437	262	286	283	283	236	240	311	247
52.5	175	444	497	458	402	461	476	461	444	259	291	280	275	238	239	311	245
60.0	200					464	464	447	452	252	284	272	275	246	244	283	246
Mean (k/in)		425				451				290				263			
Std. Deviation (k/in)		30.4				21.8				14.5				29.0			

(b) Coefficient of Variation (COV) of Stiffness (%)

Color Code

- > 35%
- 25% ≤ COV < 35%
- ≤ 25%

Cell	185	186	188	189

Chainage m	Chainage ft	185 D	185 C	185 B	185 A	186 D	186 C	186 B	186 A	188 D	188 C	188 B	188 A	189 D	189 C	189 B	189 A
0	0	6	6	5	3	1	3	4	2	10	7	4	10	10	6	4	8
7.5	25	4	4	5	2	2	3	4	3	5	5	2	4	4	4	2	5
15.0	50	3	4	2	2	3	2	3	3	2	6	1	4	7	4	3	4
22.5	75	3	2	3	2	5	2	3	3	2	4	4	4	8	2	3	6
30.0	100	2	5	3	2	4	2	3	2	2	2	3	3	5	3	2	4
37.5	125	8	7	4	3	1	3	5	3	2	3	2	2	5	2	1	4
45.0	150	4	3	3	4	4	2	3	3	6	3	3	7	5	2	2	3
52.5	175	4	2	3	4	3	3	3	3	5	4	4	5	5	2	1	3
60.0	200					2	7	3	4	3	3	3	3	11	5	11	3

Figure H-5. Spatial variation of (a) stiffness (k_s) and (b) coefficient of variation (COV) of rectangular buffered areas stiffness measurements on subgrade.

(a) Stiffness (k/in)

Color Code

- < 90% of Average Measurement
- 90% of Average ≤ k_s < Average
- ≥ Average Measurement

Cell	185	186	188	189
Material	Coarse RCA Base	Fine RCA Base	Limestone Aggregate Base Class 6	Recycled Aggregate Base Class 6

Chainage m	Chainage ft	185 D	185 C	185 B	185 A	186 D	186 C	186 B	186 A	188 D	188 C	188 B	188 A	189 D	189 C	189 B	189 A
0	0	487	448	543	474	510	525	503	472	406	370	338	368	317	326	311	375
7.5	25	481	465	522	447	497	550	458	492	335	352	362	341	254	308	300	339
15.0	50	485	503	492	443	507	533	470	513	326	366	347	323	278	294	255	351
22.5	75	510	481	513	416	484	549	435	497	337	378	323	348	300	309	265	322
30.0	100	498	518	530	421	511	515	478	473	342	385	358	380	336	300	289	344
37.5	125	499	497	507	380	520	557	403	528	337	360	301	391	338	310	332	374
45.0	150	507	532	530	441	524	550	400	471	330	340	341	376	314	296	267	348
52.5	175	542	548	512	473	504	565	437	435	322	359	342	357	308	284	266	303
60.0	200					516	556	452		322	349	318	352	291	281	283	284
Mean (k/in)		489				495				349				307			
Std. Deviation (k/in)		40.1				44.1				21.1				30.3			

(b) Coefficient of Variation (COV) of Stiffness (%)

Color Code

- > 35%
- 25% ≤ COV < 35%
- ≤ 25%

Cell	185	186	188	189

Chainage m	Chainage ft	185 D	185 C	185 B	185 A	186 D	186 C	186 B	186 A	188 D	188 C	188 B	188 A	189 D	189 C	189 B	189 A
0	0	3	7	3	3	4	4	4	5	10	5	10	4	6	5	3	8
7.5	25	5	6	2	6	5	6	5	4	5	4	4	5	13	5	4	5
15.0	50	5	2	3	4	5	9	7	4	5	5	6	7	6	12	12	4
22.5	75	2	6	5	4	10	3	6	5	11	5	12	5	6	5	7	13
30.0	100	7	2	2	7	7	6	6	16	4	3	4	5	5	10	12	5
37.5	125	3	4	3	5	5	3	8	3	4	4	14	5	5	7	13	2
45.0	150	5	3	4	7	5	3	10	9	4	2	3	5	4	9	6	4
52.5	175	3	4	5	9	8	2	7	5	4	3	5	4	10	9	6	6
60.0	200					5	4	8		7	4	21	7	14	16	10	17

Figure H-6. Spatial variation of (a) stiffness (k_s) and (b) coefficient of variation (COV) of rectangular buffered areas stiffness measurements on base layer.